

FORSCHUNGSZENTRUM KARLSRUHE
Technik und Umwelt

Wissenschaftliche Berichte
FZKA 6472

Proceedings of the Workshop ANI 99

Current Topics of Cosmic Ray Research
with EAS Observations

Nor-Amberd Station of the Mt. Aragats Cosmic Ray
Observatory
Armenia
May 29 – June 3, 1999

Editors: A.A. Chilingarian¹, A. Haungs, H. Rebel, Kh.N. Sanosyan¹

Institut für Kernphysik

¹*Yerevan Physics Institute, Cosmic Ray Division, Yerevan, Armenia*

Forschungszentrum Karlsruhe GmbH, Karlsruhe
2000

Preface

The present proceedings compile the presentations during the workshop ANI 99, held in the Cosmic Ray Observatory of the Yerevan Physics Institute in Nor-Amberd (Armenia), May 29 - June 3, 1999. The workshop has been thematically focused to investigations of Extensive Air Showers (EAS), the EAS parameter estimation from experimental observations both of the KASCADE and ANI experiments, and the inference of spectra and composition of the primary cosmic ray flux, in particular around the knee in the primary spectrum. The collaborative groups of the Yerevan Physics Institute (ANI) and Forschungszentrum Karlsruhe (KASCADE) discussed in an informal and fruitful atmosphere various approaches and methodological aspects of the current analyses and updated the present knowledge about the main goals of the experimental efforts. Special emphasis has been put on the presentation of modern analysis methods of non-parametric multivariate distributions, comparing the experimental distributions with the patterns predicted by Monte Carlo simulations. It has been stressed that such type of analyses (for which rather sophisticated program packages ANI and CORSIKA have been developed) need also a careful account for the detector efficiencies and response, as exercised by the CRES program for the KASCADE experiment and by ARES under development for the ANI experiment. An interesting aspect arises from the fact that the intrinsic fluctuations of the EAS development are minimised for observations in high mountain altitudes, which encourages combined analyses of the KASCADE and ANI data. A step in this direction has been demonstrated by considerations of the zenith angle dependence of the MAKET ANI (on Mt. Aragats at 3250 m a.s.l.) and KASCADE (110 m a.s.l.) EAS size spectra, towards an understanding of the longitudinal EAS development and of the EAS attenuation length. The significance of the observation muon arrival time and EAS age distributions for the EAS understanding has been also emphasised. Related to studies of the longitudinal development is the question of the dependence of the simulated EAS pattern from the hadronic interaction models, used as generators of the Monte Carlo simulations. The model dependence needs also a specific consideration with the efforts to isolate by the advanced statistical methods mononuclear beams from event-by-event EAS observations. We would like to thank all colleagues who did contribute to the pleasant discussions with scientific ideas to the discussed topics. We acknowledge the generous support of all sponsors who in fact enabled a valuable meeting of scientists of different laboratories, and we thank, in particular, the staff of the Yerevan Physics Institute and of the Nor Amberd station for preparing a helpful infrastructure with a pleasant atmosphere, including a visit of the Ashtarak wine factory.

Yerevan - Karlsruhe, April 2000

The editors



PARTICIPANTS

IK - KASCADE, Forschungszentrum Karlsruhe, Germany

A. Haungs
H.-J. Mathes
H. Rebel

Centre d'Etudes Nucléaires de Bordeaux - Gradignan, France

J. Procureur

National Institute for Physics and Nuclear Engineering, Bucharest, Romania

H. Bozdog

Yerevan Physics Institute, Armenia

T.L. Asatiani	E.V. Korkotyan
K. Bakhshetyan	R.M. Martirosov
A.A. Chilingarian	L.G. Melkumyan
A.V. Daryan	S.V. Safaryan
A.P. Garyaka	Kh.N. Sanosyan
G.V. Gharagozyan	K.E. Sogoyan
A.S. Hairapetyan	S.M. Sokhoyan
A.P. Hovhanissyan	A.A. Vardanyan
G.G. Hovsepyan	O. Vardanyan
V.A. Ivanov	M.Z. Zazyan



Proceedings of the Workshop ANI 99

Current Topics of Cosmic Ray Research with EAS Observations

Nor-Amberd Station of the Mt. Aragats Cosmic Ray Observatory, Armenia,

May 29 – Juni 3, 1999

Editors: A.A. Chilingarian, A. Haungs, H. Rebel and Kh.N. Sanosyan

CONTENT

- Preface iii
- Participants v
- What tell us Extensive Air Shower Observations about Hadronic Interactions at Ultrahigh Energies?
H. Rebel for the KASCADE Collaboration – Forschungszentrum Karlsruhe 1
- Towards Target-type Experiments with Mononuclear Cosmic Ray Beams
A. Chilingarian, M. Roth and A. Vardanyan for the KASCADE Collaboration – Yerevan Physics Institute and Forschungszentrum Karlsruhe 11
- On the Possibility of Selecting Pure Nuclear Beams from Measurements of the KASCADE Experiment
A. Vardanyan, A. Chilingarian and M. Roth for the KASCADE Collaboration – Yerevan Physics Institute and Forschungszentrum Karlsruhe 23
- Methods for the Reconstruction of the Primary Energy Spectrum at the KASCADE Experiment
A. Haungs for the KASCADE Collaboration – Forschungszentrum Karlsruhe 31
- Determination of the EAS Attenuation Length from Data of the ANI Experiment
A.A. Chilingarian, G.V. Gharagyozyan, S.S. Ghazaryan, G.G. Hovsepyan, E.A. Mamidjanyan, L.G. Melkumyan, S.H. Sokhoyan – Yerevan Physics Institute 43
- The Dependence of the Age Parameter from EAS Size and Zenith Angle of Incidence
A.A. Chilingarian, G.V. Gharagyozyan, S.S. Ghazaryan, G.G. Hovsepyan, E.A. Mamidjanyan, L.G. Melkumyan, S.H. Sokhoyan – Yerevan Physics Institute 53

- Lateral Distribution Functions for EAS Charged Particles
A. Haungs for the KASCADE Collaboration – Forschungszentrum Karlsruhe 59
- Lateral Distributions of EAS Muons at Different Threshold Energies, Bundles and Horizontal Muon Events
A.A. Chilingarian, A.V. Darian, V.S. Eganov, V.A. Ivanov, N.M. Nikolskaya, V.A. Romakhin, V.V. Subbotin – Yerevan Physics Institute and Lebedev Institute Moscow..... 69
- Simulation Study of the Lateral Distributions of the Muon and Electromagnetic EAS Components on Mt. Aragats Altitude
J.-N. Capdevielle and Kh.N. Sanosyan – College de France and Yerevan Physics Institute 75
- The EAS Electron Lateral Distribution as observed with the MAKET-ANI Setup
A.A. Chilingarian, G.V. Gharagyozyan, S.S. Ghazaryan, G.G. Hovsepyan, L.G. Melkumyan, S.H. Sokhoyan – Yerevan Physics Institute 83
- Experimental Studies of the Characteristic Features of the Soft EAS Component with the GAMMA Array
V.S. Eganov, A.P. Garyaka, E.V. Korkotian, R.M. Martirosov, J. Procureur, H. Sogoyan, M.Z. Zazyan – Yerevan Physics Institute and Centre d’Etudes Nucléaires Bordeaux 87
- EAS Muon Characteristics in the Knee Region Measured with the GAMMA Array
A. Chilingarian, A.V. Darian, V.S. Eganov, A.P. Garyaka, V.A. Ivanov, E.A. Mamidjanian, R.M. Martirosov, N.M. Nikolskaya, J. Procureur, V.A. Romakhin, M.Z. Zazyan – Yerevan Physics Institute, Lebedev Institute Moscow and Centre d’Etudes Nucléaires Bordeaux..... 91
- The Aragats Event Simulation Tool ARES
A. Haungs, A.F. Badea, M.Z. Zazyan – Forschungszentrum Karlsruhe, NIPNE Bucharest and Yerevan Physics Institute 95
- ARES Simulations for the GAMMA Muon Underground Detector
A.F. Badea, H. Bozdog, I.M. Brancus, A. Haungs, H.J. Mathes, H. Rebel, A.A. Chilingarian, M.Z. Zazyan – NIPNE Bucharest, Forschungszentrum Karlsruhe and Yerevan Physics Institute 99
- The Response of the EAS Muon Component in the GAMMA Detector Array
M.Z. Zazyan, A.F. Badea, A.P. Garyaka, A. Haungs, R.M. Martirosov, H. Rebel – Yerevan Physics Institute, NIPNE Bucharest and Forschungszentrum Karlsruhe 105
- Calibration of Scintillation Detectors for the Aragats EAS Installations
S.V. Blokhin, V.A. Romakhin, G.G. Hovsepyan - Lebedev Institute Moscow and Yerevan Physics Institute 111

- The Role of Arrival Time and Angle-of-Incidence Measurements in EAS Observations
H. Rebel – Forschungszentrum Karlsruhe..... 115

- Investigation of Relative Arrival Time Distributions of EAS Electron and Muon Component with the KASCADE Central Detector
W. Hafemann, R. Haeusler, F. Badea, I.M. Brancus, H. Rebel, H.-J. Mathes for the KASCADE Collaboration – Forschungszentrum Karlsruhe and NIPNE Bucharest..... 127

- Linsley’s Approach to infer the Elongation Rate and Fluctuations of the EAS Maximum Depth from Muon Arrival Time Distributions
A.F. Badea, H. Rebel, M.Z. Zazyan, I.M. Brancus, A. Haungs, J. Oehlschläger – NIPNE Bucharest, Forschungszentrum Karlsruhe and Yerevan Physics Institute 133

- Collaborations 139



What tell us Extensive Air Shower Observations about Hadronic Interactions at Ultrahigh Energies?

H.Rebel^{1*} for the KASCADE Collaboration[†]

¹*Institut für Kernphysik, Forschungszentrum Karlsruhe, Germany*

The interpretation of extensive air shower (EAS) observations needs a sufficiently accurate knowledge of the interactions driving the cascade development in the atmosphere. While the electromagnetic and weak interaction parts do not provide principal problems, the hadronic interaction is a subject of uncertainties and debates, especially in the ultrahigh energy region extending the energy limits of man made accelerators and experimental knowledge from collider experiments. Since the EAS development is dominantly governed by soft processes, which are presently not accessible to a perturbative QCD treatment, one has to rely on QCD inspired phenomenological interaction models, in particular on string-models based on the Gribov-Regge theory like QGSJET, VENUS and SYBILL. Recent results of the EAS experiments KASCADE are scrutinized in terms of such models used as generators in the Monte Carlo EAS simulation code CORSIKA.

1 Introduction

In cosmic ray investigations, in addition to the astrophysical items of origin, acceleration and propagation of primary cosmic rays, there is the historically well developed aspect of the interaction of high-energy particles with matter. Cosmic rays interacting with the atmosphere as target (on sea level it is equivalent to a lead bloc of 1m thickness) produce the full zoo of elementary particles and induce by cascading interactions intensive air showers (EAS) which we observe with large extended detector arrays distributed in the landscapes, recording the features of different particle EAS components. The EAS development carries information about the hadronic interaction (but it has to be disentangled from the unknown nature and quality of the beam). When realizing the present limits of man made accelerators, it is immediately obvious why there appears a renaissance of interest in cosmic ray studies from the point of view of particle physics. EAS observations of energies 10^{15} eV represent an almost unique chance to test theoretical achievements of very high energy nuclear physics.

Actually the astrophysicist is faced with the situation that reliable interpretations of the features of the secondary particle production, and of their relation to the characteristics of the primary particle are necessarily related to our understanding of the hadronic interactions. This aspect is particularly stimulating for high-energy physicists, since there is not yet an exact way to calculate the properties of the bulk of hadronic interactions.

This lecture is directed to review some relevant aspects of hadronic interactions affecting the EAS development, illustrated with recent results of EAS investigations of the KASCADE experiment [1], especially of studies of the hadronic EAS component using the iron sampling calorimeter of the KASCADE central detector.

*corresponding author: rebel@ik3.fzk.de

†full collaboration list see at the end of these proceedings

2 EAS development and hadronic interactions

The basic ingredients for the understanding of EAS are the total cross sections of hadron air collisions and the differential cross sections for multiparticle production. Actually our interest in the total cross section is better specified by the inelastic part, since the elastic part does not drive the EAS development. Usually with ignoring coherence effects, the nucleon-nucleon cross section is considered to be more fundamental than the nucleus-nucleus cross section, which is believed to be obtained in terms of the first. Due to the short range of hadron interactions the proton will interact with only some, the so-called wounded nucleons of the target. The number could be estimated on basis of geometrical considerations, in which size and shape of the colliding nuclei enter. All this is mathematically formulated in the Glauber multiple scattering formalism, ending up with nucleon-nucleus cross sections. Looking for the cross features of the particle production, the experiments show that the bulk of it consists of hadrons emitted with limited transverse momenta ($\langle P_t \rangle \sim 0.3 \text{ GeV}/c$) with respect to the direction of the incident nucleon. In these "soft" processes the momentum transfer is small. More rarely, but existing, are hard scattering processes with large P_t -production.

It is useful to remind that cosmic ray observations of particle phenomena are strongly weighted to sample the production in forward direction. The kinematic range of the rapidity distribution for the Fermilab proton collider for 1.8 TeV in the c.m. system is equivalent to a laboratory case of 1.7 PeV. Here the energy flow is peaking near the kinematical limit. That means, most of the energy is carried away longitudinally. This dominance of longitudinal energy transport has initiated the concept, suggested by Feynman: The inclusive cross sections are expressed by factorizing the longitudinal part with an universal transverse momentum distribution $G(P_t)$ and a function scaling with the dimensionless Feynman variable x_F , defined as the ratio of the longitudinal momentum to the maximum momentum. Though this concept, expressing the invariant cross sections by

$$E \cdot d^3\sigma/dp^3 \sim x_F \cdot d^3\sigma/dx_F dp_T \quad (1)$$

provides an orientation in extrapolating cross sections, it is not correct in reality, and the question of scaling violation is a particular aspect in context of modeling ultrahigh-energy interactions.

3 Hadronic interaction models as generators of Monte-Carlo simulations

Microscopic hadronic interaction models, i.e. models based on parton-parton interactions are approaches, inspired by the QCD and considering the lowest order Feynman graphs involving the elementary constituents of hadrons (quarks and gluons). However, there are not yet exact ways to calculate the bulk of soft processes since for small momentum transfer the coupling constant α_s of the strong interaction is so large that perturbative QCD fails. Thus we have to rely on phenomenological models which incorporate concepts from scattering theory.

A class of successful models are based on the Gribov-Regge theory. In the language of this theory the interaction is mediated by exchange particles, so-called Reggeons. At high energies, when non-resonant exchange is dominating, a special Reggeon without colour, charge and angular momentum, the Pomeron, gets importance. In a parton model the Pomeron can be identified as a complex gluon network or generalised ladders i.e. a colourless, flavourless multiple (two and more) gluon exchange. For inelastic interactions such a Pomeron cylinder of gluon and quark loops is cut, thus enabling colour exchange ("cut cylinder") and a re-arrangement of the quarks by a string formation. Fig.1 recalls the principles by displaying some parton interaction diagram's.

- The interacting valence quarks of projectile and target rearrange by gluon exchange the color structure of the system (the arrow indicates the colour exchange by opening the cylinder). As a consequence, constituents of the projectile and target (a fast quark and slow di-quark e.g.) for a colour singlet string with partons of large relative momenta. Due to the confinement the stretched chains start to fragment (i.e. a spontaneous $q\bar{q}$ -production) in order to consume the energy within the string. We recognize a target string (T) and a projectile string (P), which are the only chains in pp collisions. In multiple collision processes in a nucleus, sea quarks are additionally excited and may mediate nucleon-A interactions. While in the intermediate step the projectile diquark remains inert, chains with the sea quark of the projectile are formed.
- Most important are diffractive processes, signaled in the longitudinal momentum (x_F) distribution by the diffractive peak in forward directions. Here the interacting nucleon looks like a spectator, in some kind of polarisation being slowed down a little bit due to a soft excitation of another nucleon by a colour exchange with sea quarks (quark-antiquark pairs spontaneously created in the sea).
- There is a number of such quark lines, representing nondiffractive, diffractive and double diffractive processes, with single and multiple colour exchange.

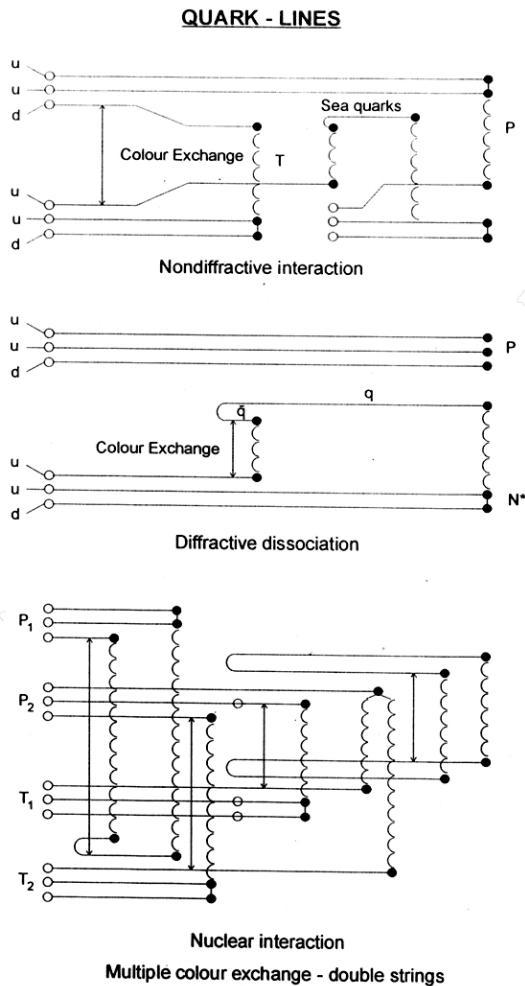


Figure 1: Parton interaction lines.

The various string models differ by the types quark lines included. For a given diagram the strings are determined by Monte Carlo procedures. The momenta of the participating partons are generated along the structure functions. The models are also different in the technical procedures, how they incorporate hard processes, which can be calculated by perturbative QCD. With increasing energy hard and semihard parton collisions get important, in particular minijets induced by gluon-gluon scattering.

In summary, the string models VENUS [2], QGSJET [3] and DPMJET [4] which are specifically used as generators in Monte-Carlo EAS simulations are based on the Gribov-Regge theory. They describe soft particle interactions by exchange of one or multiple Pomerons. Inelastic reactions are simulated by cutting Pomerons, finally producing two color strings per Pomerons which subsequently fragment into color-neutral hadrons. All three models calculate detailed nucleus-nucleus collisions by tracking the participants nucleons both in target and projectile. The differences between the models are due to some technical details in the treatment and fragmentation of strings. An important difference is that QGSJET and DPMJET are both able to treat hard processes, whereas VENUS, in the present form, does not. VENUS on the other hand allows for secondary interactions of strings which

are close to each other in space and time. That is not the case in QGSJET and DPMJET. SYBYLL [5] and HDPM [6] extrapolate experimental data to high energies guided by simple theoretical ideas. SIBYLL takes the production of minijets into account. These models are implemented in the Karlsruhe Monte Carlo simulation program CORSIKA [6, 7] to which we refer in the analyses of data. An extensive comparison of the various models and studies of their influence on the simulated shower development and EAS observables have been made in ref.[8]. There are distinct differences in the average multiplicities and the multiplicity distributions generated by different models. Nevertheless the variations in the average longitudinal development, though visible, appear to be relatively small. It should be noted that when inspecting the development of single showers with identical initial parameters, instead of average quantities, we get impressed by the remarkable fluctuations and sometimes unusual EAS developments. A further aspect which affects the accuracy of the simulations are the tracking algorithms propagating the particles through the atmosphere. In devising the CORSIKA code great care has been taken on this aspect, since the outcome for arrival time and lateral distributions could be significantly influenced by the tracking procedures.

4 The KASCADE apparatus

From the very beginning, when planning the KASCADE experiment [1] the setup of an calorimeter for efficient studies of the hadronic component in the shower center has been foreseen with the intention of checking the predictions of hadronic interaction models.

The KASCADE detector array consists of an field array of 252 detector stations, arranged in a regular way in an area of $200 \cdot 200 \text{ m}^2$, and of a complex central detector with a sampling calorimeter for hadron detection. The field detectors identify the EAS event, they provide the principal trigger (a

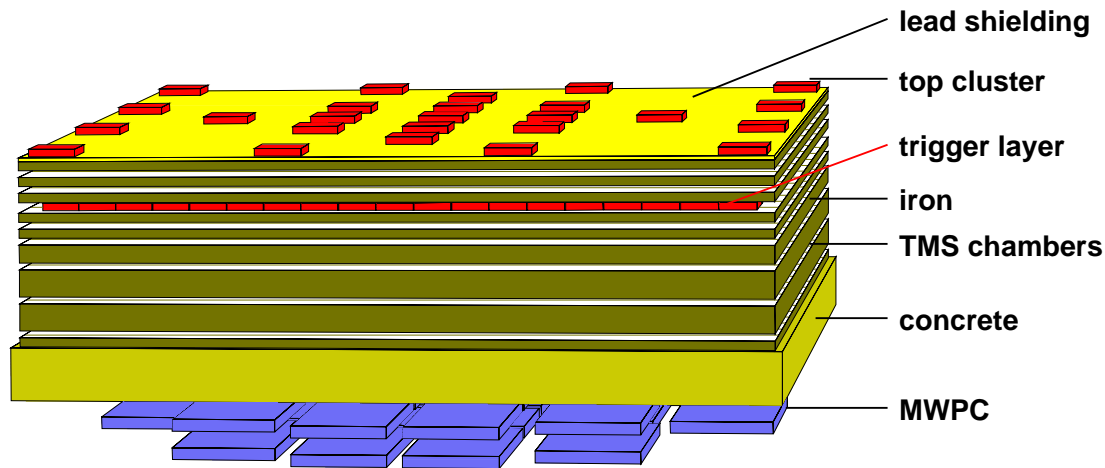


Figure 2: *Scheme of the KASCADE central detector.*

coincidence in at least eight stations), the basic characterisation (angle of incidence, shower axis and core location) and do sample the lateral distribution of the electron-photon and muon component from which the shower size and quantities characterising the intensity and muon content of the showers are determined. In the array stations the muon detectors are positioned directly below the scintillators of the electron-photon detectors, shielded by lead and iron corresponding to 20 radiation lengths,

imposing a energy detection threshold of about 300 MeV.

The central detector combines various types of detector installation with with an iron sampling calorimeter of eight layers of active detectors.

The iron absorbers are 12-36 cm thick, increasingly in the deeper parts of calorimeter. Therefore the energy resolution does not scale as $1/\sqrt{E}$, but is rather constant, slowly varying from $\sigma\sqrt{E} = 20\%$ at 100 GeV to 10% at 10 TeV. In total (including the concrete ceiling) the calorimeter thickness corresponds to 11 interaction lengths ($\lambda_I = 16.7$ cm Fe) for vertical muons. On top, a 5 cm lead layer absorbs the electromagnetic component to a sufficiently low level.

The active detectors are 10.000 ionisation chambers using room temperature liquids tetramethylsilan (TMS) and tetramethylpentane (TMP) operated with a large dynamical range ($5 \cdot 10^4$). This ensures that the calorimeter measures linearly the energy of single hadrons up to 15 TeV. The third layer of the calorimeter setup is an "eye" of 456 plastic scintillator, which deliver a fast trigger signal. Independently from hadron calorimetry, it is used as additional muon detector and as timing facility for muon arrival time measurements. In the basement of the iron calorimeter there are position sensitive multiwire proportional chamber (MWPC) installed for specific studies of the structure of the shower core and of the EAS muon component with an energy threshold of 2 GeV.

The energy calibration of the energy deposit of single ionisations chambers is made by means of the through-going muons, and the transition curves, i.e. the longitudinal profiles of the energy deposition are compared with simulations (using the detector simulation code GEANT [9] with the FLUKA description).

5 Test of EAS observables

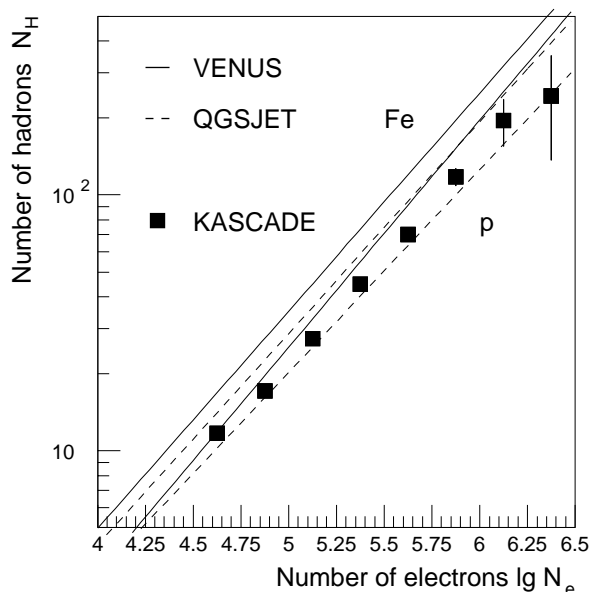


Figure 3: *Hadron number N_H - shower size N_e correlation.*

- The muon content N_μ^{tr} which the number of muons obtained from an integration of the lateral distribution in the radial range from 40 to 200 m. It has been shown that this quantity is approximately an mass independent energy estimator for the KASCADE layout, conveniently used for a first energy

The general scheme of the analysis of EAS observations involves Monte Carlo simulations constructing pseudo experimental data which can be compared with the real data [10]. The king-way of the comparison is the application of advanced statistical techniques of multivariate analyses of nonparametric distributions [11].

The mass composition of cosmic rays in the energy region above 0.5 PeV is poorly known. Hence the comparison of simulation results based on different interaction models has to consider two extreme cases of the primary mass: protons and iron nuclei, and the criteria of our judgment of a model is directed to the question, if the data are compatible in the limits of the predicted extremes of protons and iron nuclei. We consider the hadronic observables [12], in dependence from shower parameters which characterize the registered EAS, in particular indicating the primary energy:

- The shower size N_e , i.e. the total electron number

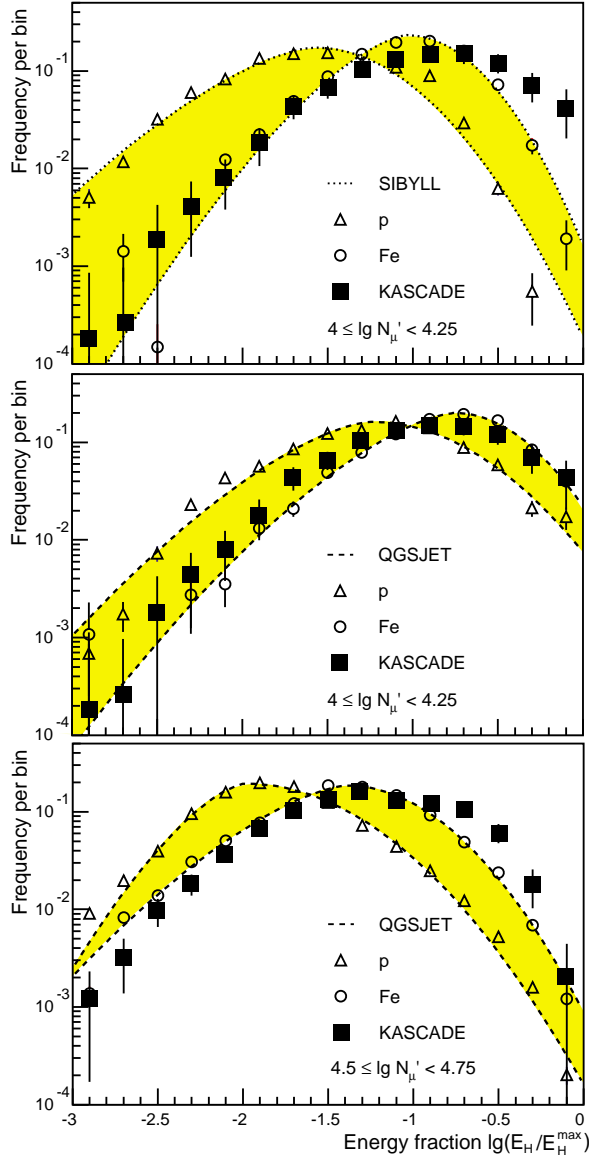


Figure 4: *Distribution of the energy fraction of the EAS hadrons.*

- At energies well above the knee (about 12 PeV) also the QGSJET exhibits discrepancies, at least in the energy distribution of the hadrons of the shower core. Other observables like lateral distribution and the total number of hadrons, however are appear more compatible with the model.

How to interpret this results? Tentatively we may understand that in the simulations E_H^{max} , the energy of the leading hadrons is too large. Lowering E_H^{max} would lead to a redistribution of the E/E_H^{max} distribution shifting the simulation curves in direction of the data.

A further test quantity is related to the spatial granularity of hadronic core of the EAS. The graph (Fig.5 left) shows the spatial distribution of hadrons for a shower induced by a 15 PeV proton. The size of the points represents the energy (on a logarithmic scale).

classification of the showers [13].

First, the dependence of the average number of hadrons N_H with an energy $E_H > 100$ GeV from the shower size is shown and compared with the predictions of the VENUS and QGSJET model. The energy range covers the range from 0.2 PeV to 20 PeV. The result shows some preference for the QGSJET model, and such an indication is corroborated by other tests.

There is another feature obvious. When shower observables are classified along the electromagnetic shower sizes N_e , a proton rich composition is displayed. This effect is understood by the fact that at the same energy protons produce larger electromagnetic sizes than iron induced showers, i.e. with the same shower size iron primaries have higher energies, where the steeply falling primary induces the dominance of protons in the sample.

Another example considers the frequency distributions of the energy of each single hadron E_H with respect to the energy of the most energetic hadron E_H^{max} . The data are compared with predictions of SYBILL and QGSJET for iron and proton induced showers.

- For a primary proton one expects that the leading particle is accompanied by a swarm of hadron of lower energies. For a primary iron nuclei the energy distribution appears narrowed.
- The two upper curves display the case for a primary energy below the knee (about 3 PeV). The deficiencies of SYBILL are obvious and have been also evidenced by other tests, especially with the muon content [12]. SYBILL seems to produce a wrong EAS muon intensity, and it fair to mention that just this observation has prompted the authors to start a revision of the SYBILL model.

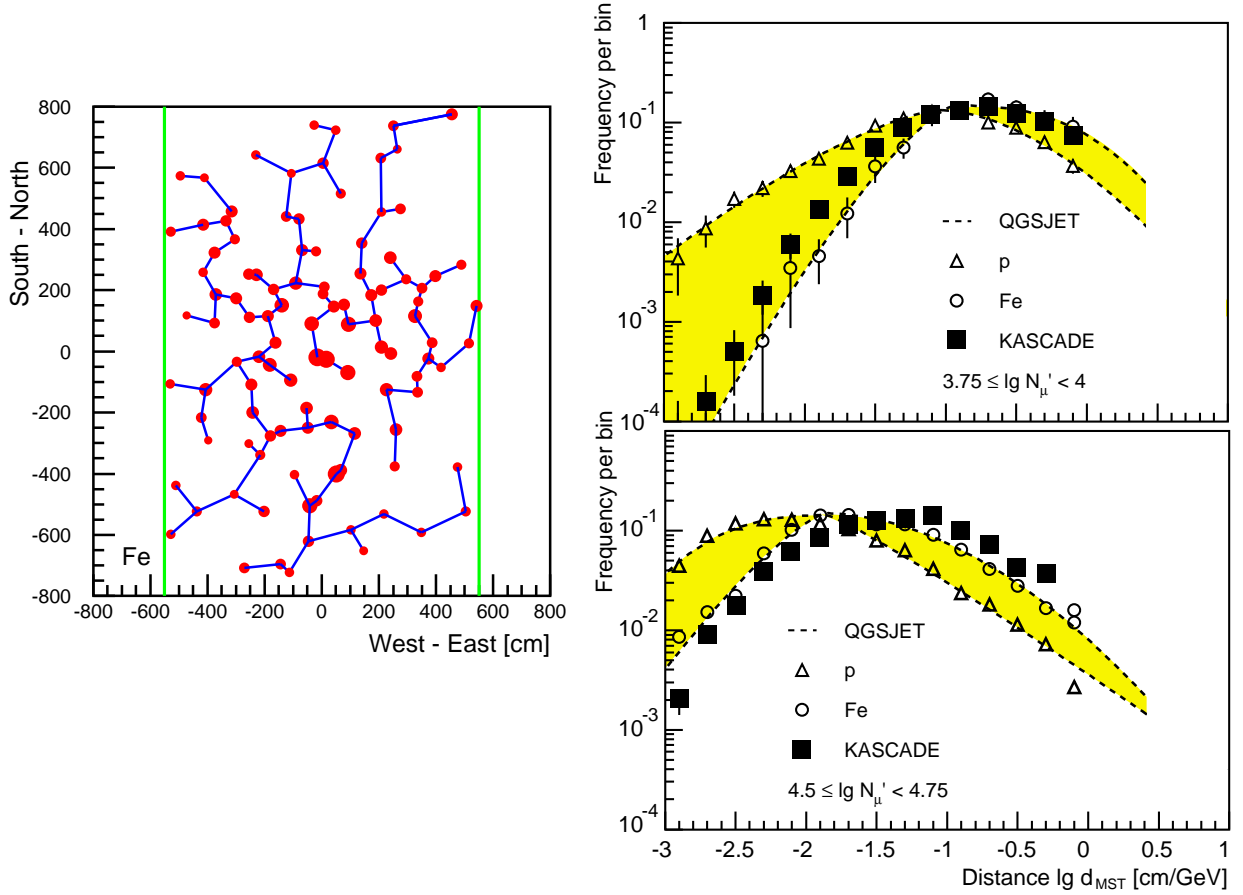


Figure 5: *Left: Example of a hadronic core observed in the calorimeter (top view). Right: Frequency distributions of the distances of the minimum-spanning-tree.*

For a characterisation of the pattern a minimum spanning tree is constructed. All hadron points are connected by lines and the distances are weighted by the inverse sum of energies. The minimum spanning tree minimizes the total sum of all weighted distances. The test quantity is the frequency distribution of the weighted distances d_{MST} . Results are shown for two different bins of the truncated muon size or of the primary energy (2 and 12 PeV), respectively (Fig.5 right). Again we are lead to the impression that either the distribution pattern is not reproduced or the high-energy hadrons are missing in the model.

Tentatively we may deduce from these indications, that the transfer of energy to the secondaries - what we phenomenologically characterize with the not very well defined concept of the inelasticity of the collision - appears to be underestimated.

In order to underline this feature we may inspect the variation of some other observables with the quantity $\log_{10}(N_{\mu}^{tr}) \propto \log_{10}(E_{prim})$: The so-called shower age s , which characterizes the stage of the EAS development, the number of observed hadrons N_h with $E_H > 100$ GeV, the energy sum $\sum E_h$ of this hadrons and the energy of the highest energy hadrons E_H^{max} . Fig.6 compares with predictions with the QGS model (with the limit $\log N_{\mu}^{tr} < 4.6$). The predictions of the VENUS display the same features. Globally we realize the tendency that the experimental data approach the predictions for iron induced showers, i.e. for faster developed EAS. But this may be hardly interpreted as consequence of a heavier mass composition, rather as arising from a larger inelasticity of the hadronic collisions e.g..

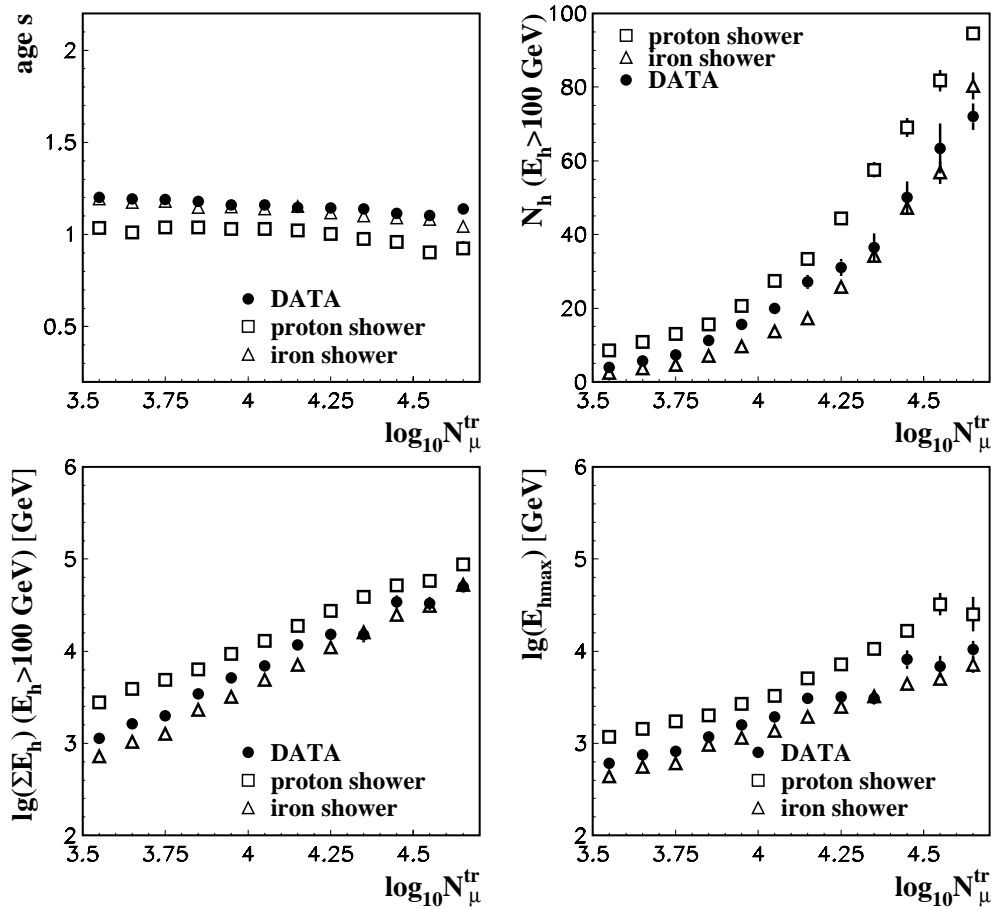


Figure 6: Comparison of various experimentally accessible EAS variables with predictions of the the QGSJET model. [14]

6 Concluding remarks

From the investigation of a series EAS observables and comparisons with different hadronic interaction models, en vogue for ultrahigh energy collisions, we conclude with following messages:

- The model SYBILL, in the present release, has problems, in particular when correlations with the muon content of the showers are involved.
- The model VENUS is in fair agreement with the data, but it indicates also some problems at high energies, when correlations with the shower sizes are considered.
- In the moment the model QGSJET, which includes the minijet production - in contrast to VENUS - reproduces sufficiently well the data, though it underestimates the number of high energy hadrons for high energies.
- In general there are tentative indications that the inelasticity in the fragmentation region is underestimated especially with increasing energy.

All models are in a process of refinements. Actually somehow triggered by the experimental indications, there is a common enterprise of VENUS and QGSJET towards a combined model descriptions: NEXUS [15]. That is a unified approach combining coherently the Gribov-Regge theory and perturbative QCD. Faced with the experimental endeavour to set up giant arrays for astrophysical observations at extremely high energies, the Monte Carlo simulations need certainly a safer ground of model generators. Hence our efforts in KASCADE are directed to extend the array and to refine the present studies with results towards primary energies of 10^{17} eV.

Acknowledgement

The experimental results are based on a KASCADE publication [12]. In particular, I would like to thank Dr. Andreas Haungs for contributions and clarifying discussions.

References

- [1] H.O. Klages et al. - KASCADE Collaboration, Nucl.Phys.B(Proc.Suppl.) **52B** (1997) 92
- [2] K. Werner, Phys.Rep. **232** (1993) 87
- [3] N.N. Kalmykov and S.S. Ostapchenko, Phys.At.Nucl. **56** (1993) 346
- [4] J. Ranft, Phys.Rev. D **51** (1995) 64
- [5] R.S. Fletcher et al., Phys.Rev. D **50** (1994) 5710
- [6] J.N. Capdevielle et al., KfK Report 4998 (1992), Kernforschungszentrum Karlsruhe
- [7] D. Heck et al., FZKA Report 6019, Forschungszentrum Karlsruhe 1998
- [8] J. Knapp, D.Heck, G.Schatz, FZKA Report 5828, Forschungszentrum Karlsruhe 1996
- [9] GEANT 3.15, Detector Description and Simulation Tool, CERN Program Library Long Writeup W5015, CERN (1993)
- [10] H. Rebel, in FZKA Report 6215, Forschungszentrum Karlsruhe 1998
- [11] A. Chilingarian, "ANI - Nonparametric Statistical Analysis of High Energy Physics and Astrophysics Experiments", Users Guide, 1998; M. Roth, FZKA Report 6262, Forschungszentrum Karlsruhe 1999
- [12] T. Antoni et al. - KASCADE Collaboration, Journal of Physics G: Particles and Nuclei (in press)
- [13] R. Glasstetter for the KASCADE Collaboration, 25th ICRC(Durban, South Africa) Vol 6, 157
- [14] A. Haungs, private communication
- [15] H.J. Drescher et al., preprint hep-ph/9903296 (March 1999)



Towards Experiments with Mononuclear Cosmic Ray Beams

A.Chilingarian^{1*}, M.Roth² and A.Vardanyan¹ for the KASCADE Collaboration[†]

¹*Yerevan Physics Institute, Cosmic Ray Division, Armenia*

²*Institute für Kernphysik, Forschungszentrum Karlsruhe, Germany*

The KASCADE experiment measures a large number of EAS observables with an improved degree of sampling of the electron-photon and muon components, with additional information about the hadronic core. It provides accurate data for an event-by-event analysis of the primary cosmic ray flux in the energy range of $10^{14} - 10^{16}$ eV. Nonparametric procedures for the estimation of the energy spectrum and mass composition are described. The possibility of studies with quasi-mononuclear beams are discussed.

1 Introduction

The idea to use advanced statistical techniques of multivariate analyses [1] for isolating certain classes of Extended Air Showers (EAS) stems from an early proposal of A. Chilingarian and H. Zazyan [2, 3] to prepare quasi-mononuclear beams by mass discriminative analyses of event-by-event EAS observations, planned for the ANI experiment [4] in context of investigations of inelastic cross sections of very-high-energy cosmic ray interactions e.g. . The realisation of this proposal has become realistic by the recent results of the multi-detector experiment KASCADE [5] which provide an accurate experimental basis of event-by-event data of many EAS observables. In the contribution of A. Vardanyan [6] the classification procedure using KASCADE data ($N_e, N_\mu^{tr}, \text{age}, \dots$) is described and the purity of the prepared proton and iron beams, the bias and accuracy of the mass and energy estimates are discussed. The claimed results of ca. 70% purity of the beams exceed the expectations inferred from the considerations of the situation of the ANI-experiment [4].

This approach appears to be very promising with the aspect of refined tests of current interaction models and to pave the way to a consistent description [7] of the hadronic interaction at extremely high energies by experimental road signs. Still the results of the KASCADE experiments concerning the energy spectrum and mass composition of primary cosmic rays are considerably affected by a model error, estimated for the energy slope to be 10 times larger than the statistical uncertainty [8]. The present report gives a brief description of the techniques of multivariate classification and Monte Carlo statistical inference and introduces in the use of the options of the ANI program package.

2 Monte Carlo Statistical Inference

2.1 Nonparametric Classification

In cosmic ray physics the main technique of physical analysis is the Monte Carlo Statistical Inference (MCSI), the detailed simulation of the CR traversal through the atmosphere and the response of the experimental installation with a following comparison of the multivariate simulation and experimental data. Actually, an algorithm is constructed, which describes EAS development and registration

*corresponding author: e-mail: chili@yerphi.am

†full collaboration list see at the end of these proceedings

of its different components at the observation level, which is based on a certain family of models of the physical processes investigated.

MCSI requires some specifications (basic physics, experimental techniques, data analysis techniques), it generates families of models to meet this specifications and it synthesizes *a priori* knowledge and experimental results to create new knowledge. Complexity of the MCSI is determined by its multi-functionality, adaptability and flexibility - attributes that one best realized in Neural Network models. Neural models captures the statistics of processes directly from data vectors - collection of "pseudo-experimental" variables, corresponding to all significant variations of the model input parameters. Herein lies MCSI flexibility. It allows the input vectors to be formed directly from initial measurements or from reconstructed EAS parameters.

Neural methods are universal and can deal with very big input vectors. A common complaint about nonparametric techniques is the dependence of the results on the purity and finiteness of training sets (small training samples effects). However, due to the inherent robust characteristics of Neural Network (generalization ability), results from neural analyses are relatively insensitive to modest impurities in the training sets.

MCSI incorporates and uses such advanced nonparametric methods as Fuzzy Analysis, Adaptive Multivariate Density Estimation, Fractal Dimensionality Analysis, etc, For net training the Evolutionary Algorithms are used, Stopping Rules, based on the Prediction Error estimation and Committee method provide high level of generalization, avoiding overtraining errors. For the training of very big networks hardware accelerators (neurochips) are used.

The overall scheme of learning from examples can be defined as following [10]:

1. random event generator, drawn independently from a fixed but unknown distribution mixture;
2. a supervisor (absolute decision rule) that returns an output vector for every input vector, according to a unknown, but also fixed conditional distribution function;
3. a learning machine (algorithm) capable to implement a number (may be infinite) of different approximation functions.

The problem of learning is that of choosing the appropriate set of functions, and then particular member of this family, which predicts the supervisor's response in the best way (optimal decision rule). The selection is based on the training set (sample), of independent and identically distributed observations presented to the supervisor.

Let us consider the stochastic mechanism $(\mathcal{A}, \mathcal{P})$ which generates the observations \mathbf{v} in a multivariate feature space - \mathcal{V} , \mathbf{v} is a d -dimensional vector of EAS parameters measured experimentally. We assume that observations are random and can be described by some conditional probability density function depending on the primary particle type. The feature space \mathcal{V} covers possible acceptable values of EAS parameters including cuts on shower age and size, etc. . . .

The basic states space \mathcal{A} consists of different primary nucleus. The appropriate statistical model describing EAS initiated by various primaries is the probability mixture model:

$$p(\mathbf{v}) = \sum_{k=1}^L P_k p(\mathbf{v}/\mathcal{A}_k). \quad (1)$$

The proportions (frequencies) of the probability mixture P_k of events in each category \mathcal{A}_k , determine the mass composition of the primary flux. Unfortunately, we don't know the full statistical description (conditional probability density functions $p(\mathbf{v}/\mathcal{A}_k)$) of how nature produces EAS from incident primaries, that is why, to determine the mutual probability measure on the direct product of \mathcal{A} and \mathcal{V} spaces, the total Monte-Carlo simulation of the EAS development in the atmosphere

and in detectors is performed, including experimental data registration and reconstruction of EAS parameters for different primaries and alternative strong interaction models in a wide energy range. The problem is how to introduce the probability measure in the primary particle parameters space \mathcal{T} (K-dimensional metric space). Usually following parameters are used as input for Monte-Carlo simulation program:

- primary type;
- primary energy;
- angle of incident;
- strong interaction model (one of the CORSIKA alternatives [12]).

Of course, we have to implement the physical restriction and define the bounded subspace of \mathcal{T} , from which we randomly take the mesh points $(\mathbf{t}_i, i = 1, M)$, M is number of simulation trials. The primary particle classes will be restricted by 5 groups, including all primaries from proton to iron. The set of corresponding d -dimensional $(\mathbf{u}_i, i = 1, M)$ vectors obtained in simulations is an analog of the experimentally measured values of $(\mathbf{v}_i, i = 1, M_{exp})$, where M_{exp} , is the number of detected events. But, as opposed to experimental data, it is exactly known which primary particle was used in simulations. These, *labeled* events include *a priori* information about dynamics of the EAS development and registration with inherent fluctuations. All statistical variability of events belonging to the definite class is expressed in a nonparametric form, in form of simulation trials. The sequence $(\mathbf{u}_i, t_j), i = 1, M_j, j = 1, L, t-$ is the class index, and is generated with the CORSIKA simulation program [12] and consists of L classes each containing M_j simulation trials. This "controlled" stochastic mechanism we denote by $(\mathcal{A}, \tilde{\mathcal{P}})$ and will refer to it as training sample (TS). The training sample is the basis of all statistical procedures in applied Bayesian and neural approaches. Usually we denote a TS by \mathcal{A}_k or explicitly by the primary group - P, O, ..., Fe. The corresponding distribution mixture model takes the form:

$$\hat{p}(\mathbf{v}) = \sum_{k=1}^L \hat{P}_k \hat{p}(\mathbf{v}/\mathcal{A}_k) \quad (2)$$

Of course this substitution of unknown conditional density function $p(\mathbf{v}/\mathcal{A}_k)$ by "simulation" analog $\hat{p}(\mathbf{v}/\mathcal{A}_k)$, estimated by means of the training sample $\{\mathbf{u}_i, t_j\}$, is only valid if the used model is adequate. And validation of the model remain the most crucial and yet unsolved problem for EAS data analysis.

For reliable estimation of conditional densities we'll need significant amount of training trials to cover all intrinsic variations of measurable EAS parameters and completely represent all categories (primary nucleus). Since both physical processes of particle production and those of registration are stochastic, only by careful measurement of probabilities we can gain an understanding of the EAS phenomena. We can't expect simple solutions, as multidimensional distributions of EAS parameters overlap significantly and any decision on primary particle type and it's energy will contain uncertainty. The only thing we can require when classifying a distribution mixture is to minimize the losses due to incorrect classification to some degree and to ensure the use of a priori information completely. Such a procedure is the *Bayes decision rule with nonparametric estimation of the multivariate probability density function*.

2.2 Bayesian Decision Rules

The Nonparametric Bayesian decision rule have a form [13]

$$\tilde{\mathcal{A}} = \eta(\mathbf{v}, \mathcal{A}, \tilde{\mathcal{P}}) = \operatorname{argmax}_i \{C_i \hat{p}(\mathcal{A}_i/\mathbf{v})\}, \quad i = 1, \dots, L. \quad (3)$$

where c_i are the losses connected with $\tilde{\mathcal{A}}$ decision, $\hat{p}(\mathcal{A}_i/\mathbf{v})$ is the nonparametric estimate of the *a posteriori* density, connected with conditional ones by the Bays theorem:

$$\hat{p}(\mathcal{A}_i/\mathbf{v}) = \frac{\hat{P}_i \hat{p}(\mathbf{v}/\mathcal{A}_i)}{\hat{p}(\mathbf{v})}. \quad (4)$$

Finally, substituting the *a posteriori* densities by the conditional ones we get the Bayesian decision rule in the form

$$\tilde{\mathcal{A}} = \operatorname{argmax}_i \{C_i P_i \hat{p}(\mathbf{v}/\mathcal{A}_i)\}, \quad i = 1, \dots, L. \quad (5)$$

Provision is made to avoid statistical decision if all classes are very far from experimental events (outliers problem). If

$$\hat{p}(\mathbf{v}/\mathcal{A}_i) < ST \text{ for all } i = 1, \dots, K, \quad (6)$$

then the "outliers message" is send to output stream. *ST* is, so called, Strangeness Criteria, usually set to a small number.

The Nonparametric Likelihood Ratio for classes \mathcal{A}_1 , \mathcal{A}_2 and experimental event \mathbf{v} can be represented as:

$$LR(\mathbf{v}) = \frac{\hat{p}(\mathbf{v}/\mathcal{A}_1)}{\hat{p}(\mathbf{v}/\mathcal{A}_2)}. \quad (7)$$

The nonparametric Log-likelihood function for k -th class takes the form:

$$\mathcal{L}_k = \sum_{i=1}^M \ln \hat{p}(\mathbf{v}_i/\mathcal{A}_k), \quad k = 1, L, \quad (8)$$

where M is number of experimental events. The negative of the Log-Likelihood function is also calculated; the smaller values will correspond to the most probable model.

2.3 Nonparametric Probability Density Estimators

To estimate conditional densities, we use Parzen kernel [14, 15] and K Nearest Neighbors (KNN) methods [16, 17] with an automatic adaptation of the method parameter (kernel width - for Parzen estimate, and number of neighbors - for KNN estimate)[18]. Several probability density estimates corresponding to different values of parameters are calculated simultaneously. Then the obtain sequence is ordered and the median of this sequence is chosen as final estimate. Depending on the intrinsic probability density in the vicinity of point \mathbf{v} , where the density is estimated, due to stabilizing properties of the median, each time the best estimate will be chosen [19]. The Parzen kernel probability density is estimated by:

$$\hat{p}(\mathbf{v}/\mathcal{A}_i) = \frac{|\Sigma_i|^{-0.5}}{(2\pi)^{d/2} h^d} \sum_{j=1}^{M_i} e^{-r_j^2/2h^2} \omega_j, \quad i = 1, \dots, L, \quad \sum_{j=1}^{M_i} \omega_j = 1 \quad (9)$$

where d is the feature space dimensionality, M_i is the number of events in the i -th TS, r_j is the distance from experimental event \mathbf{v} to the j -th event of the TS in the Mahalanobis metric

$$r_j^2 = (\mathbf{v} - \mathbf{u}_j)^T \Sigma_i^{-1} (\mathbf{v} - \mathbf{u}_j), \quad (10)$$

where Σ_i is the sampling covariance matrix of the class to which \mathbf{u}_j belongs, ω_j are the event weights, h is the kernel width (parameter controlling the degree of the "smoothness" of an estimate). The K nearest neighbors estimate takes the form:

$$\hat{p}(\mathbf{v}/\mathcal{A}_i) = \frac{k-1}{M_i V_k(\mathbf{v})}, \quad (11)$$

where $V_k(\mathbf{v})$ is the volume of a d -dimensional hypersphere containing the k nearest neighbors to the experimental event \mathbf{v} ,

$$V_k(\mathbf{v}) = V_d |\Sigma_i|^{1/2} r_k^d, \quad V_d = \frac{\pi^{d/2}}{\Gamma(d/2 + 1)}, \quad (12)$$

where r_k is the distance to the k -th nearest neighbor of \mathbf{v} , $\Gamma(\cdot)$ is the gamma function. $|\Sigma_i|$ is the determinant of the covariance matrix of the class to which the k -th neighbor belongs.

2.4 Bayes Error Estimation

The classification methods, like all the statistical ones, include a procedure quality test as a necessary element. The most natural measure for quality test is the error probability which depends on both, the degree of overlapping of alternative multivariate distributions and the decision rule being used:

$$R^B = E\{\theta[\eta(\mathbf{v}, \mathcal{A}, \mathcal{P})]\} = \int \mathbf{v} p(\mathbf{v}) d\mathbf{v}, \quad (13)$$

where

$$\theta[\eta(\mathbf{v}, \mathcal{A}, \mathcal{P})] = \begin{cases} 0 & , \text{ for correct classification,} \\ 1 & , \text{ otherwise} \end{cases} \quad (14)$$

The mathematical expectation is taken over the whole d -dimensional feature space \mathcal{V} . In other words the Bayes error is a measure of the overlapping of alternative distributions in the feature space \mathcal{V} , e.g. the expected proportion of the "incorrect" classification. Since we do not know to which class experimental vectors belong, we obtain an estimate of R^B via the TS:

$$\hat{R}^B = E\left\{\frac{1}{M_{TS}} \sum_{i=1}^{M_{TS}} \theta[\eta(\mathbf{u}_i, \mathcal{A}, \tilde{\mathcal{P}})]\right\}, \quad (15)$$

i.e. we classify the $\{\mathbf{u}_i\}, i = 1, M_{TS}$ and check the correctness of the classification over the index of the class $t_j, j = 1, L$. The expectation is taken over all possible samples of the space M_{TS} . However, as numerous investigations have shown (e.g. [20]), this estimate is systematically biased and hence, a one-leave-out-for-a-time estimate is preferable:

$$\hat{R}^e = \frac{1}{M_{TS}} \sum_{i=1}^{M_{TS}} \theta\{\eta(\mathbf{u}_i, \mathcal{A}, \tilde{\mathcal{P}}_{(i)})\}, \quad (16)$$

where $(\mathcal{A}, \tilde{\mathcal{P}}_{(i)})$ is a TS with a removed i -th element, which is classified and then "returned" to the sample. This estimate is unbiased and has an essentially smaller m.s. deviation compared with other estimators [21]. The advantage of \hat{R}^e is especially notable when the feature space has a high dimensionality. Note, that we have the possibility to estimate the error probability of various types by classifying various TS classes - $\{\mathbf{u}_i, t_j\}, j = 1, L$. By R_{ij}^e (or simply R_{ij}) we denote the probability of classifying the i -th class events as belonging to the j -th class (misclassification). By R_{ii} the "true"

classification probability will be denoted. For EAS classification according to 5 primary groups, each element of the "classification matrix" have to be determined, using the Bayes risk estimate (16).

$$\begin{pmatrix} R_{p \rightarrow p} & R_{p \rightarrow \alpha} & R_{p \rightarrow o} & R_{p \rightarrow si} & R_{p \rightarrow fe} \\ R_{\alpha \rightarrow p} & R_{\alpha \rightarrow \alpha} & R_{\alpha \rightarrow o} & R_{\alpha \rightarrow si} & R_{\alpha \rightarrow fe} \\ R_{o \rightarrow p} & R_{o \rightarrow \alpha} & R_{o \rightarrow o} & R_{o \rightarrow si} & R_{o \rightarrow fe} \\ R_{si \rightarrow p} & R_{si \rightarrow \alpha} & R_{si \rightarrow o} & R_{si \rightarrow si} & R_{si \rightarrow fe} \\ R_{fe \rightarrow p} & R_{fe \rightarrow \alpha} & R_{fe \rightarrow o} & R_{fe \rightarrow si} & R_{fe \rightarrow fe} \end{pmatrix}$$

This matrix presents the accumulated a-priori knowledge on the possibility of data classification into 5 categories. We introduce a separability index G , reflecting the "goodness" of the classification:

$$G = \left(\prod_{i=1}^L R_{ii} \right)^{1/L}. \quad (17)$$

This averaged product of diagonal elements represents the "mean" probability of true classification into L categories. The separability index, of course, is directly connected with the Bayes error.

2.5 Feed-Forward Neural Networks

Feed-Forward Neural Networks (FFNN) represent very simple structures composed of processing elements (nodes) and connections (weights). FFNN belongs to the general class of non-parametric methods that do not require any assumption about the parametric form of the statistical model they use. The central issue of FFNN is the implementation of the bounded mapping [22]:

$$\mathbf{f} : \mathcal{U} \subset \mathbf{R}^{n1} \rightarrow \mathbf{R}^{n2}, \quad (18)$$

from a bounded subset \mathcal{V} of $n1$ dimensional Euclidean space to a bounded subspace $\mathbf{f}[\mathcal{V}]$ of $n2$ -dimensional Euclidean space (usually $n1 > n2$). The special case of such mapping when $n1 = 1$, constitutes the classification problem. Of course, for real live problems it is impossible to define non-overlapping division of \mathcal{V} corresponding to different categories, but using the examples of mapping action, a Network configuration can be tuned to minimize the misclassification errors near to minimal achievable Bayes error (13).

The net architecture consists of L layers each having K nodes. The first layer consists of $N1$ elements that simply accept the components of input vector \mathbf{v} and distribute them, without modification, to all of the nodes of the second layer. The nodes of the second layer calculate a weighted sum of all inputs and then transform it to some nonlinear (sigmoid) function. This output is distributed again to all nodes of the third layer, and so on till the output layer with $N2$ nodes is reached. The output of a FFNN can be used directly for classification, in this case mapping takes a special form with aim to "shift" different classes of TS from each other as much as possible.

Therefore the "goal" output $O_k^{goal}(k)$ for events of the k -th category could be chosen as follows:

$$O_k^{goal} = \frac{k-1}{K-1}, \quad k = 1, K. \quad (19)$$

where K is total number of classes. For the multi-way classification one can define a set of non-overlapping bounded intervals in $(0-1)$ for each category. This sequence of bounded non-overlapping sets $\mathcal{O}_k, k = 1, K$, along with the chosen "goal" values (located within corresponding subsets), will determine the mapping into the K class labels:

$$\mathbf{O}(\mathbf{u}) \subset \mathcal{O}_k \rightarrow \mathbf{u} \text{ belongs to } k_{th} \text{ category.} \quad (20)$$

The objective (error) function to be minimized is simply the discrepancy of apparent and target outputs over all training samples (so called classification score):

$$Q = \sum_{k=1}^K \sum_{j=1}^{M_k} w_k \left(O_k^j - O_k^{\text{goal}} \right)^2, \quad \sum_{k=1}^K w_k = 1. \quad (21)$$

where O_k^j is the actual output value for the j -th training event, belonging to the k -th class, and the O_k^{goal} is the target value for the k -th class output, where K is number of categories and M_k is the number of examples for the k -th class.

The w_k weight coefficients controls the "contribution" of each particular class of TS to the overall error function. For the identification of the primary type by EAS observables, usually intermediate nucleus (oxygen class) with masses between the lightest (proton class) and heaviest with significant abundance (iron class) are trained worse compared with edge classes. There are two possibilities of checking the classification accuracy of middle categories. First of all we can enlarge the category acceptance region $\mathcal{O}_{\text{middle}}$, (*a posteriori* solution) (20). And, second, the corresponding weight value in the error function could be enhanced before starting net training (*a priory* solution) (21).

2.6 Neural Estimation (Learning Regression Function)

Above we consider the classification mode of the neural mapping (18). The recovering of the unknown functional dependence is another realization of neural mapping possibilities implemented by FFNN. This problem is of vital importance for EAS experiments for constructing the energy spectra of the primary CR flux. And if the classification statistical model is appropriate for mass composition studies, the learning of the regression function is more appropriate for energy estimation.

Our fundamental assumption will be that we can generate examples of mapping $\mathbf{f}(\mathcal{V})$ by detailed Monte-Carlo simulation of multidimensional random variables ($\mathbf{u}_i, i = 1, M$), in accordance with assigned probability measure on \mathcal{T} initial parameters space (as described in section 2.1). The bounded subspace of \mathcal{T} e.g. simulated primary energies, will be determined by the installation threshold and acceptance and flux intensity (the information on the steeply fallen energy spectra will also be incorporated in preparing of simulation trials).

A primary advantage of mapping networks over classical statistical regression analysis is that the FFNN have more general (algorithmic) functional forms than classical statistical methods can effectively deal with [22]. FFNN's are free from depending on linear superpositions or orthogonal functions and can mimic sophisticated stochastic mechanism whereby the Nature generate the data. Therefore, in contrast with classical regression problem, we've to specify not the particular member of known analytic family of functions, rather the non-parametric algorithm (estimator), which generalizes the unknown mapping rule, implementing learning strategy on the training sample. The regression learning strategy will be based on the fundamental notion of the *generalization*.

The most common drawback in FFNN performance is the limited number of training and test samples. Usually, in CR physics applications we can't simulate enough simulation trials, especially for most interesting ultra-high energies. And, therefore, we never can be sure that we use sufficient number of examples to learn a general problem and not the specific training data set.

As we are not sure that the used training samples reflect all variability of physical processes, learning of a particular training sample "too good" is also not desirable. What we need is to generalize from the used training set to the entire problem. Therefore, the strategy, checking the expected performance of FFNN during training is of crucial importance. The strategy, proposed in [23] is connected with the *Prediction Risk* as performance measure. In general, particular FFNN model can

be specified (indexed) by the λ parameter:

$$\lambda \subset \Lambda \equiv (\mathbf{V}, \mathbf{G}, \mathbf{W}), \quad (22)$$

- where $\mathbf{V} \subset \mathcal{V}$ notes a chosen subset of variables from the set of all possible variables \mathbf{V} ;
- \mathbf{G} is a selected architecture from the class of possible architectures \mathcal{G} ;
- and W is the set of net parameters (weights).

The *prediction risk* $P(\lambda)$ is defined as expected net performance on a finite test set:

$$P(\lambda) \approx E\left\{\frac{1}{M} \sum_{i=1}^M (t_j^* - O_\lambda(u_j^*))^2\right\}, \quad (23)$$

where (t_j^*, u_j^*) weren't used in training, O_λ - is the trained network output. The strategy exists in the selection of the particular λ from the model space Λ , which minimizes an estimate of the prediction risk.

The procedure of the prediction risk estimation, which reuse data and gives unbiased estimate for small sample sets, is connected with the generalization of one-leave-out-for-the-time estimate used for the Bayes risk estimation (16). The *k-fold cross-validation*, introduced by Geisser [24] and Wahba [25], instead of leaving only one event, delete larger subsets from training sample. Let the training sample $(\tilde{\mathcal{P}} \equiv (t_j, u_j), j = 1, M)$ be divided into k randomly selected disjoint subsets of the equal size $M_k = M/k$, denoted by \tilde{p} . And the $\tilde{\mathcal{P}}_i$ will denote the training sample with deleted i -th subsample \tilde{p}_i . Then the crossvalidation mean square error (MSE) for the selected subset \tilde{p}_i is defined as

$$MSE_{\tilde{p}_i}(\lambda) = \frac{1}{M_k} \sum_{(t_j, u_j) \in \tilde{p}_i} (t_j - O_{\lambda, \tilde{p}_i}(u_j))^2, \quad (24)$$

and

$$MSE(\lambda) = \frac{1}{k} \sum_{j=1}^k MSE_{\tilde{p}_i}(\lambda). \quad (25)$$

Typical choices of k are 5 and 10. An useful modification of cross-validation mean square error, penalizing complicated networks comprising many hidden units, is the Akaike's final prediction error [26]. For large enough training sets it takes following form:

$$P(\lambda) \equiv MSE(\lambda) \left(1 + 2 \frac{NTOT}{M}\right), \quad (26)$$

where *NTOT* is total number of networks weights. Just this expression is recommended by authors of [23] as an estimate of prediction risk. Estimates of the prediction risk offer a sound basis for assessing the generalization performance of the model and can be used as a tool for architecture selection and constructing the stopping rule. Therefore, it is important to check the training results not with the "training error", but with the "generalization error", represented by the prediction risk.

The above described technique with an appropriate defined error function was used for the simultaneous estimation of the primary energy and mass. The following function have to be minimized

$$Q = \sum_{j=1}^M \omega_j \cdot g(\mathbf{t}_j - \mathbf{O}_j), \quad \sum_{j=1}^M \omega_j = 1, \quad (27)$$

where, \mathbf{O}_j is the vector output of the FFNNs last layer (*note, that sigmoid function is not implemented for the nodes in the output layer!*) and \mathbf{t}_j is the vector of parameters used in simulation (primary mass and energy of "pseudo-experimental" event). ω_j is the event weight (usually the highest energy events get higher weights).

A weighted quadratic metric is used as measure of discrepancy of actual and "true" regression function values:

$$g(.) \equiv \alpha(\widehat{mass}(\mathbf{u}_j) - mass(\mathbf{u}_j))^2 + (1 - \alpha)(\hat{E}(\mathbf{u}_j) - E(\mathbf{u}_j))^2 \quad (28)$$

The α coefficients are changing during training cycles to provide stable and reliable recovery of both energy and mass. Setting α value to 0 and 1 we have the possibility to estimate first energy, and then, primary mass or vice-versa.

2.7 Net Training

The only information to "train" network for "nonlinear" mapping is contained in a priori given pairs - $(t_i, u_i), i = 1, M$, where M is the number of training events. During the minimization procedure the calculated differences between the actual network output and the desired output are used to adjust the weights.

The back-propagation (BP) algorithm of neural network training is one of the most important historical developments in neurocomputing. The simple rule (based on gradient descent) of weights updating after processing of one or more training examples in principle will lead to arbitrary small mean square error of function approximation. The family of BP algorithms is realized in numerous packages, with the Jetnet package being most popular in HEP community [27].

Generic Algorithms (GA) and Evolutionary Programming (EP) are both search techniques based on an simulation of the evolutionary processes. The challenge is to find "good solutions" (chromosomes) in very large search spaces. GA employ the successive reproduction among an assembly (pool) of best parents using genetic operations such as crossover, inversion, mutation and selection with predefined rules for constructing next generations. Different m:n scenarios (m - number of parents, n - number of offsprings) can be realized. The current best chromosome (parent) undergoes the zero-mean phenotypic mutation (realized by the random search algorithm with return at an unsuccessful step). This kind of net training has been proved to be much more effective than simple random search algorithms. The MULTI and SINGLE modes of the ANI program package [9] are designed for random search correspondingly in all net parameter space and - to make random change of also randomly chosen net parameter. Different net training scenarios combine different search modes with various search parameters.

For fast scanning of the net weights space a deterministic algorithm is implemented. The error function is calculated in each point of the multidimensional quasi-random sieve [28] uniformly filling the N-dimensional cube. Positioning the sieve center at the previously found best point, and subsequently decreasing sieve size, we'll arrive to the best net. Very essential question of scale invariance can be addressed by changing value of step in the above described SOBOL mode [9].

3 High energy muons and hadrons detected with the KASCADE Central Detector

The multivariate statistical technique has been used for isolating mononuclear beams from the KASCADE data. Applying the energy estimation procedure and subsequently the 3-way classification using only KASCADE array information, beams with rather good "purity" have been obtained (the detailed beam characteristics are given in ref. [14]).

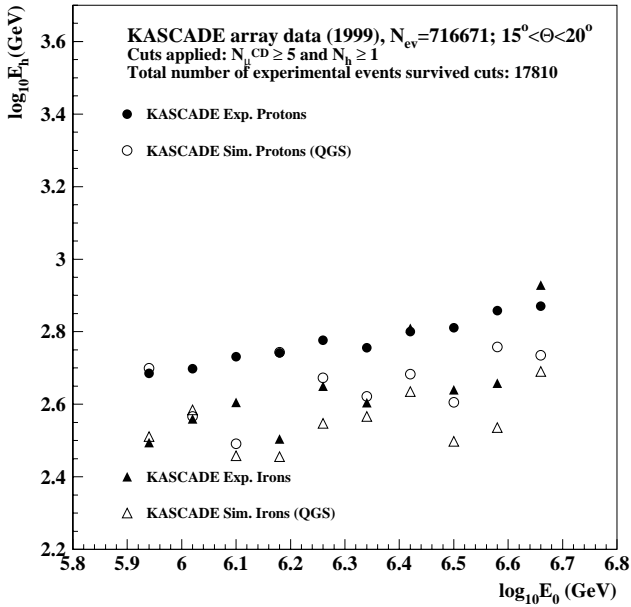


Figure 1: *Energy dependence of the reconstructed energy of the most energetic hadron in the CD for proton and iron primaries.*

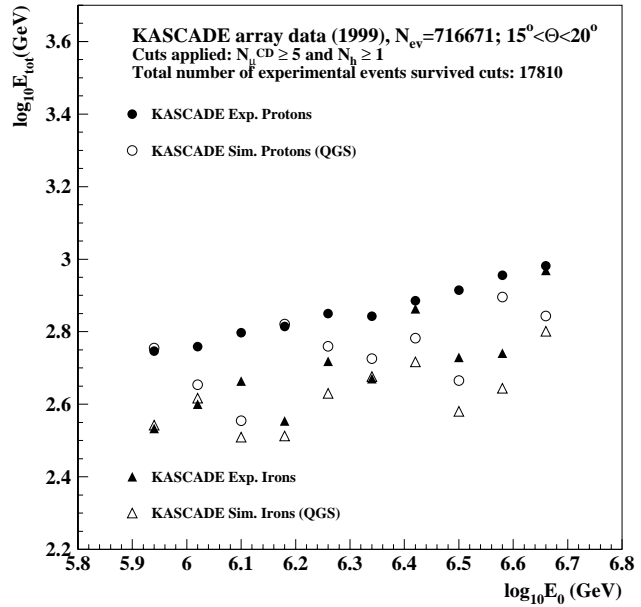


Figure 2: *Energy dependence of the reconstructed total hadronic energy for proton and iron primaries.*

In the present illustration a first attempt to analyze the hadron and muon distributions is given based on data of the KASCADE Central Detector (CD). The estimated purity of the obtained beams and the accuracy of the energy estimation suggests to consider the hadron component of EAS. Comparisons of predictions from CORSIKA simulations invoking the QGSJET model [29], with KASCADE data are displayed in Figures 1-4. The event selection procedure is equivalently done. The simulated and experimental data samples require at least one hadron (with energy larger than 100 GeV) and 5 muons (with energy larger than 2 GeV). The distance of the shower core of the EAS are restricted to < 91 m. The used event selection criteria suppress the selection efficiency of lower-energy events, but significantly enlarge the number of more interesting high-energy events.

Due to the large statistical accuracy the experimental distributions of the hadronic parameters of the showers originating from the primary protons demonstrate a rather smooth variation increasing with the energy. On the other hand the corresponding distributions, originating from the primary iron nuclei do less agree. However, in general, the overall dependences are in agreement with QGSJET simulations [29]. It is worth to note, that contamination of both proton and iron induced events by the intermediate nuclei has been ignored. The results in Figures 3-4 can be compared with ref. [30]. But in the present case the primary energy is determined event-by-event. If we take into account the limited efficiency ($\approx 90\%$) of the muon detecting facility, the agreement of the experimental data with the predictions is rather remarkable.

An improved statistical accuracy for simulation data is required, and the result are model-dependent. Nevertheless, we emphasize that the advocated approach is the only one which takes into account the shower fluctuations properly and is able to specify in a transparent way, how conclusive the results of the inference methods in the CR physics do appear.

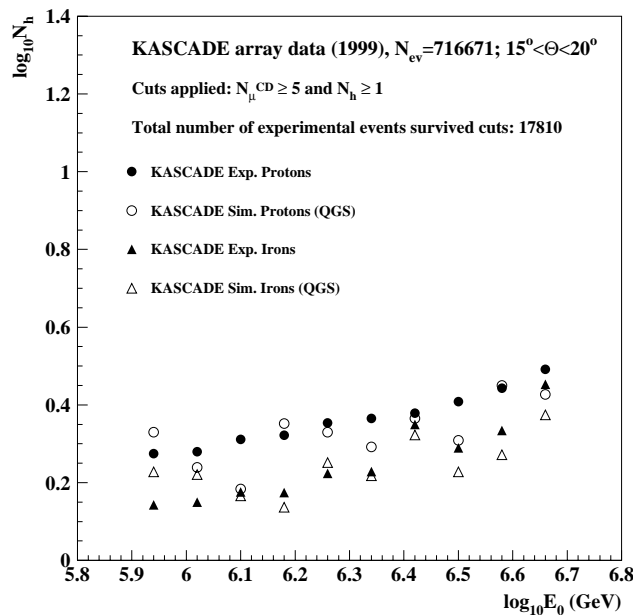


Figure 3: *Energy dependence of the number of reconstructed hadrons for proton and iron primaries.*

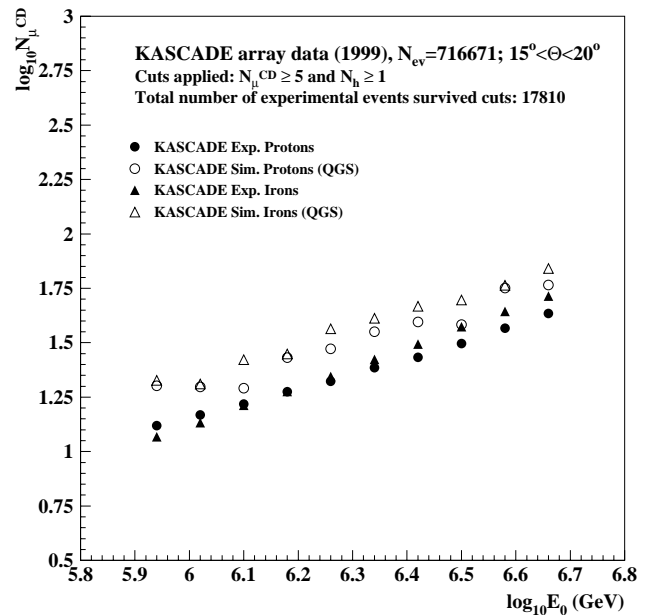


Figure 4: *Energy dependence of the number of muons for proton and iron primaries. The muon detection efficiency of the measurements estimated to about 90% is not taken into account.*

Acknowledgement

We thank S.Ostapchenko for encouraging interest and useful discussions. The work has been partly supported by the ISTC project A116.

References

- [1] A.A. Chilingarian, Computer Physics Communications **54** (1989) 381
- [2] A.A. Chilingarian and H.Z. Zazyan, Yad.Fiz. **54** (1991) 128
- [3] A.A. Chilingarian and H.Z. Zazyan, Il Nuovo Cimento **14C** (1991) 555
- [4] ANI Collaboration, Nucl.Instr.Meth **A323** (1992) 104
- [5] K-H. Kampert et al. - KASCADE Collaboration, Proc. 26 ICRC (Salt Lake City), **3** (1999) 159
- [6] A. Vardanyan et al. - KASCADE Collaboration, ANI Workshop 1999, these proceedings, p.23
- [7] H.J. Drescher et al., preprint hep-ph/9903296 (March 1999)
- [8] A.A. Chilingarian et al. - KASCADE Collaboration, Proc. 26 ICRC (Salt Lake City), **1** (1999) 226

- [9] A.A. Chilingarian, Analysis and Nonparametric Inference in High Energy Physics and Astrophysics Experiments, Reference Manual, 1998, <http://crdtx5.yerphi.am/proj/ani>
- [10] V.N. Vapnik IEEE Trans. on NN **10** (1999) 988
- [11] W. Edwards, H. Lindman, L.J. Savage, *Bayesian Statistical Inference, in Robustness of Bayesian analyses*, Elsevier Science Publishers, 1984
- [12] D. Heck et.al., FZKA-Report 6019, Forschungszentrum Karlsruhe 1998
- [13] F.A. Aharonyan et al., Nucl.Instr.Meth **A302** (1991) 522
- [14] L. Devroye, L. Gyorfi, *Nonparametric density estimation. The L1 view*, John Wiley and Sons, New-York, 1985
- [15] E. Parzen, Ann. Math. Stat. **33** (1962) 1065
- [16] D.O. Lofsgaarden and C.D. Quesenberry, Math. Stat. **36** (1965) 1049
- [17] R.A. Tapia and J.R. Thompson, *Nonparametric probability density estimation*, The John Hopkins University Press, Baltimore and London, 1978
- [18] A.A. Chilingarian and S.Kh. Galfayan, *Stat. Problems of Control, Vilnius* **66** (1984) 66
- [19] B. Efron, Canadian J. Statist. **9** (1981) 139
- [20] G.T. Toussaint, 1974, *IEEE Trans. on Information*, **IT-20**, 472
- [21] S.M. Snappin and J.D. Knoke, Technometrics **26** (1984) 371
- [22] R. Hecht-Nielsen, *Neurocomputing*, Addison-Westly Publishing Company, Reding, MA, 1990
- [23] A. Barron, *Predicted Squared Error: a Criterion for Automatic Model Selection, in Self-Organizing Methods in Modeling*, ed. S.Farlow, Marsel Dekker, New York, 1984
- [24] S. Geisser, JASA, **70** (1975) 350
- [25] G. Wahba, *Spline Models for Observational Data, Regional Conf. Series in Appl.Math.* **59**, SIAM press, Philadelphia, 1990
- [26] H. Akaki, Ann.Inst.Statist.Math. **122** (1970) 203
- [27] C. Petersen, T. Rognvaldsson, L. Lonblad, LU TP 93-29, CERN-TH.7135/94
- [28] I.M. Sobol, SIAM J. Number. Anal. **16** (1979) 790
- [29] N.N. Kalmykov, S.S. Ostapchenko, A.I. Pavlov, Nucl.Phys.B (Proc. Suppl) **52B** (1997) 17
- [30] T. Antoni et al. - KASCADE Collaboration, J.Phys G: Nucl. Part. Phys. **25** (1999) 2161

On the Possibility of Selecting Pure Nuclear Beams from Measurements of the KASCADE Experiment

A. Vardanyan^{1*}, A.A. Chilingarian¹, M. Roth² for the KASCADE Collaboration[†]

¹*Yerevan Physics Institute, Cosmic Ray Division, Armenia*

²*Institute für Kernphysik, Forschungszentrum Karlsruhe, Germany*

The possibility to select proton and iron induced extensive air shower (EAS) events is scrutinized. After classifying the KASCADE experimental data into three nuclear groups (light, intermediate, heavy), the observables used for the classification are compared with those of simulated EAS data. The achieved purity of the proton and iron EAS classification is about 70%, keeping approximately 50% efficiency of event selection. Energy spectra of three groups of primary nuclei are deduced.

1 Introduction

The determination of astrophysical sources of high-energy particles and acceleration mechanisms requires an accurate knowledge on the primary CR flux spectra and mass composition in the knee region [1]. The KASCADE experiment [2] measuring a large number of Extensive Air Shower (EAS) observables in a wide energy range with high accuracy, as well as the availability of detailed Monte Carlo simulations [3] of EAS along with accurate calculations of the detector response provide the possibility to make an event-by-event analysis of experimental data. The nonparametric statistical methods implemented in ANI statistical analysis package, developed at the Cosmic Ray Division of the Yerevan Physics Institute [4, 5] enables the application of advanced multivariate statistical procedures to obtain reliable results on the primary particle type and energy. In our previous paper [6] a tendency of increasing mean mass above the knee was reported. In the present paper the possibility of a precise and detailed description of three groups of primary masses (light, intermediate, and heavy) and their energy spectra is investigated.

The selected ca. 710.000 experimental events within zenith angles from 15° to 20° in the energy range of $5 \cdot 10^{14} - 10^{16} eV$ are analysed on event-by-event basis, using more than 21000 simulated events per primary particle. The simulations have been performed with the QGSJet model [7] in the energy range $10^{14} - 3 \cdot 10^{16} eV$ using the CORSIKA code [3]. The core of the EAS is within a circle of 91m around the center of the KASCADE field stations. The response function of the KASCADE detectors is calculated in great detail using the GEANT code [8].

2 Primary energy estimation

The multi-layered perceptron (MLP) algorithm is used to analyze the mass composition and the energy spectrum of the primary cosmic rays (PCR) in the knee region. This method gives the possibility of primary energy estimation as well as primary mass classification into multiple categories. The basics of neural regression and classification are described in [9, 10, 11]. Further developments of the neural regression and classification techniques are described by A.A.Chilingarian [12].

For the estimation and classification tasks the same EAS observables are used. These are observables

* corresponding author: aro@crdlx5.yerphi.am

† full collaboration list see at the end of these proceedings

of the electromagnetic and muonic components measured by the KASCADE filed array detector installation:

- N_e : number of electrons in the EAS and
- the shower age parameter s , both associated with a Molière radius of 89m,
- N_μ^{tr} : truncated number of muons ($N_\mu^{tr} = 2\pi \int_{40m}^{200m} \rho_\mu(r)rdr$)

Restricting these observables is justified by following reasons:

- It is assumed that the electromagnetic and muonic component of EAS are described by the MC models with sufficient accuracy (a partially insufficient knowledge about the hadronic component is illustrated in [13, 14]).
- Due to the larger statistical accuracy the uncertainties caused by strong EAS fluctuations are eliminated as compared with hadronic information of EAS.
- The KASCADE Central Detector (CD) information can be used independently, after having performed the estimates.

The energy estimates are performed using two sets of observables: (N_e, N_μ^{tr}) and (N_e, N_μ^{tr}, s) . The results on the energy estimates, displayed in Figures 1-2 are obtained by applying the trained network, obviously by adding the observable s the accuracy of the energy estimate is enhanced. Indeed, the correlation of the N_e and N_μ^{tr} with primary energy is strong [6], and added the s parameter is correlated with primary mass (see Table 1). Hence the use of all 3 parameters, "fixing" in some sense the primary type, enlarges the overall accuracy of the energy estimate for all 3 groups of nuclei.

Another important characteristic is the bias of the estimator. Only if the bias is small, energy spectra and "knee position" can be adequately reconstructed. In Figures 1 2 the relative error of the energy estimation is shown. For both sets of observables an almost unbiased estimate in the full energy range (except at the lowest and highest energies) is apparent. Therefore we use a wider energy interval for simulated events to avoid over- and underestimation of primary energies at the boundaries.

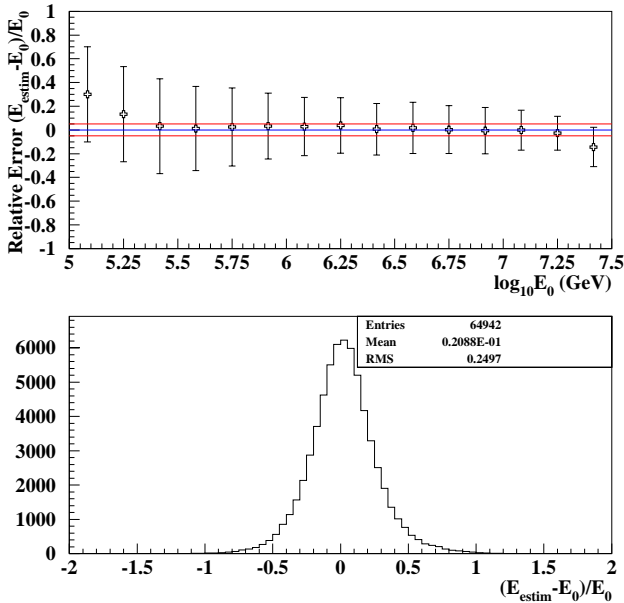


Figure 1: The accuracy of the energy determination displayed by the relative deviation $(E_{est} - E_0)/E_0$ for the 3 observables: N_e , N_μ^{tr} and s .

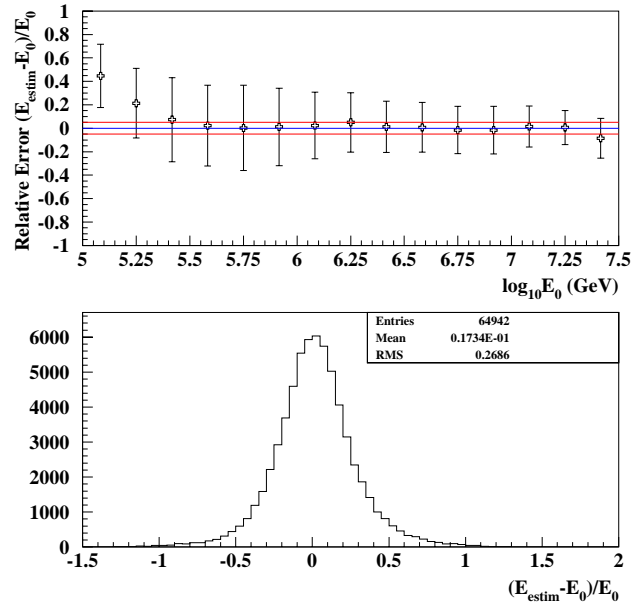


Figure 2: The accuracy of the energy determination displayed by the relative deviation $(E_{est} - E_0)/E_0$ for the 2 observables: N_e and N_μ^{tr} .

3 Primary mass determination

After performing the energy estimation, each EAS event is classified as being induced by light (H,He), intermediate (CNO) or heavy (Si-Fe) nuclei (we will refer these groups as "proton", "oxygen", and "iron"). The parameters of experimental events, classified as initiated from protons and iron nuclei, are afterwards compared with those of simulated ones. The results are given in Figures 3-4. A very good agreement for simulated and experimental proton and iron induced events is obvious.

As shown in Figure 5 the experimental mean shower age is shifted as compared with the simulated data in the full energy interval, but there is still a clear difference between proton and iron events. Although simulations do not describe correctly the observable s , the s parameter is nevertheless a good signature of the primary mass. However the systematic bias of the s parameter can be misleading. For example, a neural net (NN) trained by N_e , N_μ^{tr} and s may result in a heavier mass composition, when applying for experimental data classification. A smaller s value corresponds to lighter nuclei for simulated and experimental data. But the absolute values differ significantly and thus, in mean, proton initiated events could be classified as being of iron type with large probability

In Table 1 where the correlations between primary energy E_0 and measured EAS parameters are presented, a negative correlation of s with the primary energy is revealed. Applying a trained neural network for energy estimation, the data sample have systematically larger values of s as compared with the training sample. Therefore, the s parameter will lead to a systematic underestimation of

Table 1: *Correlations between primary mass A_0 and primary energy E_0 with EAS observables.*

	A_0	E_0	N_e	N_μ^{tr}	s
A_0	-	0.00	-0.19	0.07	0.31
E_0	0.00	-	0.95	0.98	-0.47
N_e	-0.19	0.95	-	0.94	-0.58
N_μ^{tr}	0.07	0.98	0.94	-	-0.47
s	0.31	-0.47	-0.58	-0.47	-

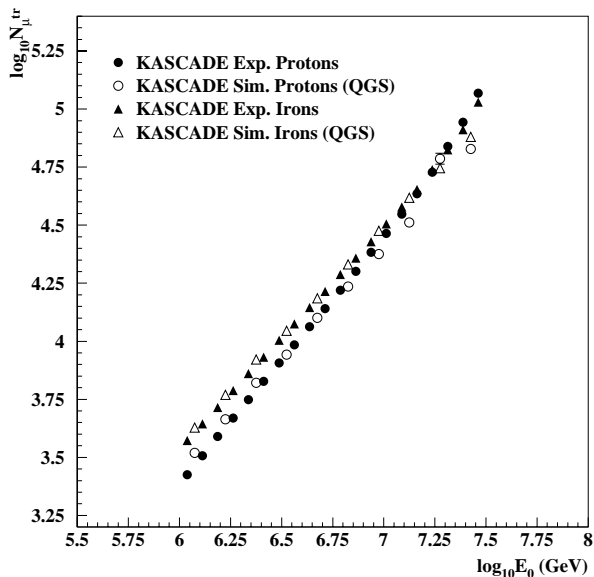


Figure 3: N_μ^{tr} versus E_0 for simulated and experimental proton and iron events (the primary energy is estimated by neural regression method). Used observables: N_e and N_μ^{tr} .

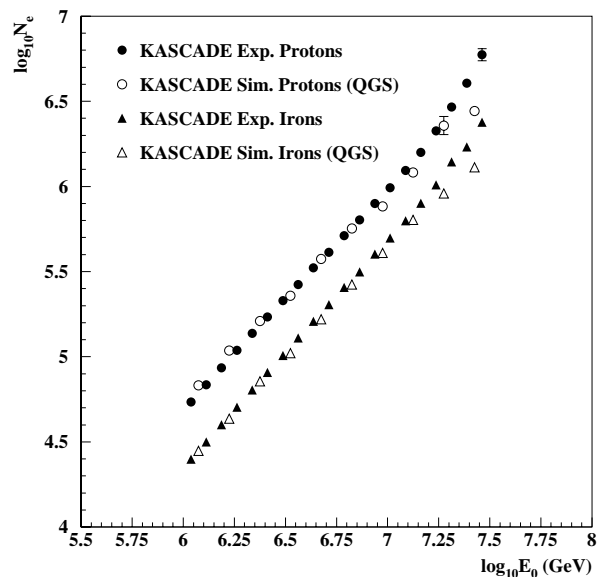


Figure 4: N_e versus E_0 for simulated and experimental proton and iron events (the primary energy is estimated by neural regression method). Used observables: N_e and N_μ^{tr} .

Table 2: *Purity of classified events. Used observables: N_e , N_μ^{tr} and s*

$P_{i \rightarrow j}$	j=p [%]	j=O [%]	j=Fe [%]
p	77	22	1
O	18	63	19
Fe	3	28	69

Table 3: *Purity of classified events. Used observables: N_e and N_μ^{tr}*

$P_{i \rightarrow j}$	j=p [%]	j=O [%]	j=Fe [%]
p	80	18	2
O	19	58	23
Fe	2	23	75

higher energies and correspondingly to a bias of the energy spectrum. For that reason, we use for energy estimation only N_e and N_μ^{tr} , which rather good agreement for simulated and experimental samples.

After estimating the misclassification rates, the possibility to select nuclear beams of maximum pure[†] has been investigated. The used neural network allows to decrease the contamination of misclassified events in each class of nuclei. Of course, the efficiency[‡] of the classification is simultaneously reduced.

The purification has been done in the following way: the neural network (NN) performs a non-linear mapping of the multidimensional characteristics of the EAS observables to the real number interval $[0, 1]$. Particular assignments for the classification in three classes are subintervals like $[0. - 0.33]$, $[0.33 - 0.66]$ and $[0.66 - 1.]$. The misclassification matrices for this intervals are given in Tables 2 and 3. If the NN is trained well enough to have generalization capabilities, the NN output distributions for different classes are overlapping at the boundaries of the subintervals. Therefore by shrinking the ranges of the subintervals a large proportion of misclassified events can be removed, but losing a part of the true classified events.

Figure 6 shows the purity versus the efficiency. The purity of proton and iron beams are larger than 90% with a remaining efficiency of not less than 50%.

Purity estimates were obtained by classifying 4000 control events (not used for the training) per class. For a given purity value the efficiency of proton events classification is always larger than the efficiency of iron event classification. Thus the purification of proton events turns out to be easier, than the purification of iron events. Due to the larger spread of the EAS observables for proton primaries the contamination of protons in the “iron beam” is larger than vice-versa.

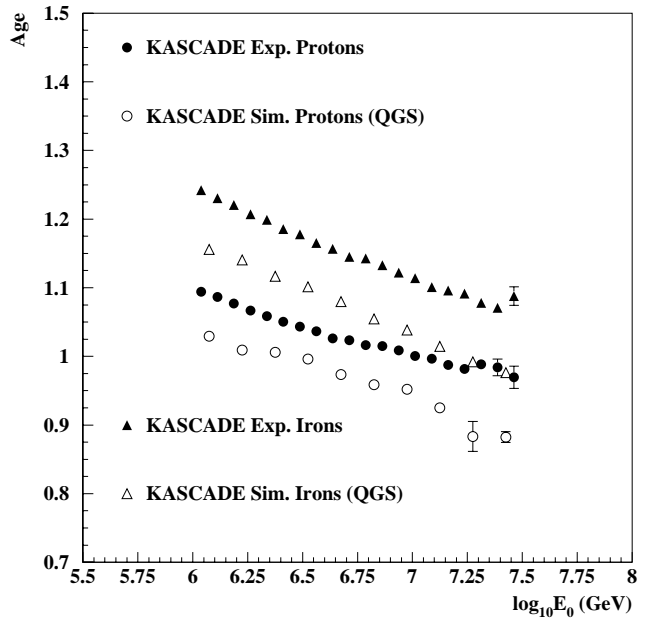


Figure 5: *Shower age s versus E_0 for simulated and experimental events (the primary energy is estimated by neural regression method). Used observables: N_e and N_μ^{tr} .*

[†]purity: fraction of true classified events in actual number of events assigned to a given class

[‡]efficiency: fraction of true classified events in total number of events of a given class

4 Discussion of the results

The inference of mass composition and energy spectra of purified nuclear beams needs an investigation of the efficiency of the classification of different nuclear groups. Because of differing abundances of primary nuclei in the CR flux, it is necessary to measure the influence of purification on all categories in terms of efficiency reductions. Furthermore, the dependence of such influences from the primary energy should be investigated as well, in order to avoid a distortion of the energy spectra caused by nonuniform changes of classification efficiencies.

Figures 7-8 display the relative abundances of three group of nuclei for different energies and the differential energy spectra, respectively, using N_e , N_μ^{tr} and s parameters. Figure 7 shows the energy dependence of the mass composition of the CR flux resulting from the analysis of all three observables: the relative abundance of light nuclei group appears to be decreasing when approaching the knee, while the behavior of intermediate and heavy groups of nuclei is just opposite. Figure 8 demonstrates the knee feature in the all-particle

and light nuclei spectra. A conclusion on the energy spectrum of the intermediate and heavy nuclei is uncertain, due to the relatively large misclassification rates in these groups (see Table 2).

Figures 9 and 10 present the relative abundances and the energy spectra of three group of nuclei obtained by using only the N_e and N_μ^{tr} parameters. Although the same quantitative variation of the relative abundances on the primary energy is observed, the relative fraction of heavy and intermediate nuclei is altered.

In both cases the knee feature is clearly seen for the all-particle and light nuclei spectra. For the spectrum of intermediate nuclei group the difference of the slopes is negligible and there is no evidence for a change in the spectral indices. An inverse knee as observed in the spectrum of the heavy group of nuclei originates most probably from insufficient correction of the misclassification.

The main difference, which has to be seriously taken into account, is that the s parameter leads significantly to smaller values of the spectral indices below the knee. Additionally the knee position gets shifted to the lower energies for the all-particle and light nuclei energy spectra, too. The fits of the energy spectra in both cases were done by a method described in ref. [15].

The indicated aspects of isolating pure nuclear beams from the EAS observables has to be further studied by extending the set of EAS observables and with improved interaction models.

Acknowledgment

We would like to thank Dr. S. Sokhoyan for making fits of the energy spectra and Dr. S. Ostapchenko for his interest to the present paper and useful discussions.

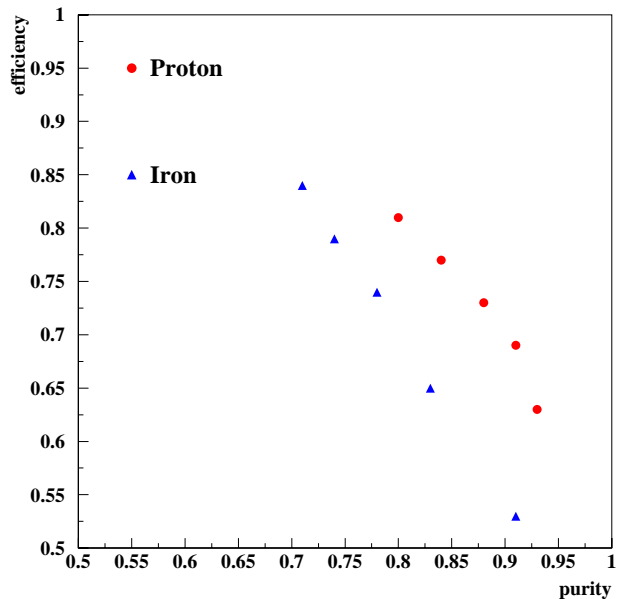


Figure 6: *Event selection efficiency vs purity for proton and iron events (obtained by the classification of the control samples). Used observables: N_e and N_μ^{tr} .*

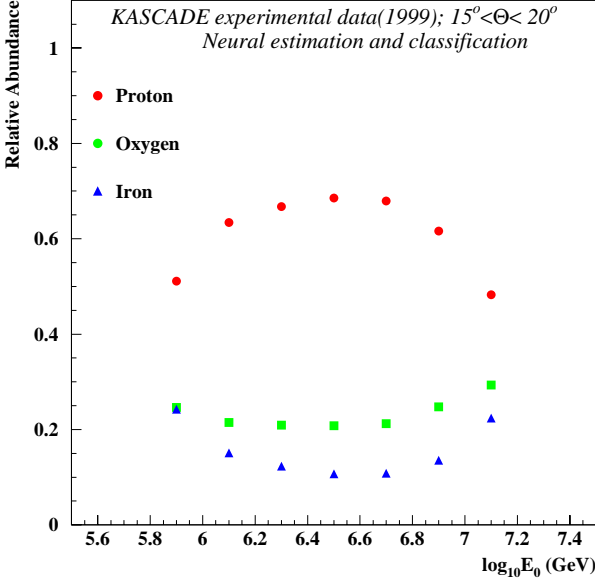


Figure 7: *Relative abundances of different mass groups as a function of energy. Used observables: N_e , N_μ^{tr} and s .*

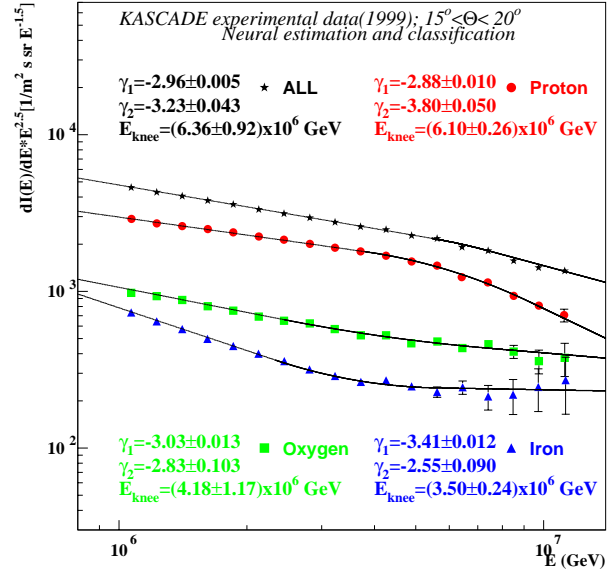


Figure 8: *Differential energy spectra of three mass groups and the all-particle spectrum. Used observables: N_e , N_μ^{tr} and s . The spectra of the different mass groups are obtained without correction with respect to the misclassifications.*

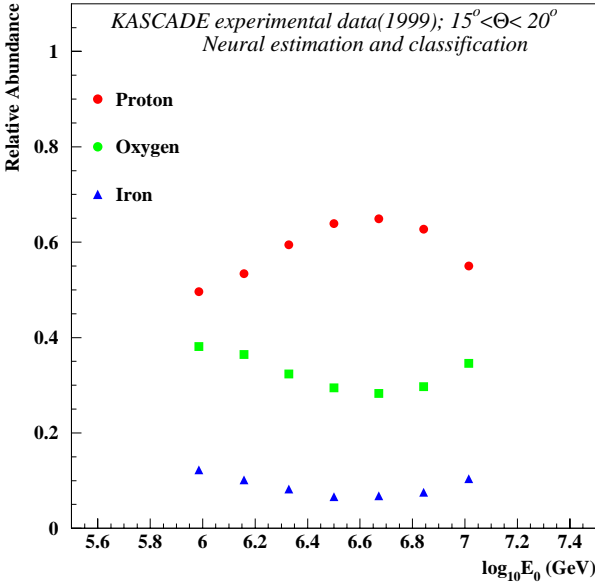


Figure 9: *Relative abundance of different mass groups as a function of energy. Used observables: N_e , N_μ^{tr} .*

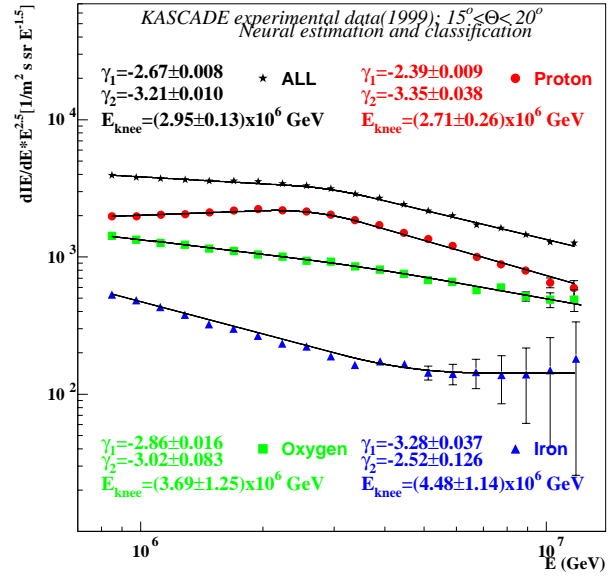


Figure 10: *Differential energy spectra of three mass groups and the all-particle spectrum. Used observables: N_e , N_μ^{tr} . The spectra of the different mass groups are obtained without correction with respect to the misclassifications.*

References

- [1] B.G. Kristiansen et al., *Cosmic Rays of Superhigh Energies (in Russian)*, Atomizdat (1975)
- [2] H.O. Klages et al., Nucl. Phys. B (Proc. Suppl.) **52B** (1997) 92
- [3] D. Heck et al., FZKA-Report 6019, Forschungszentrum Karlsruhe (1998)
- [4] A.A. Chilingarian, Analysis and Nonparametric Inference in High Energy Physics and Astroparticle Physics, Reference Manual (1998), unpublished
- [5] A.A. Chilingarian, Comp. Phys. Com. **54** (1989) 381
- [6] A.A. Chilingarian, M. Roth, A. Vardanyan for the KASCADE Collaboration, Nucl. Phys. B (Proc. Suppl.) **75A** (1999) 302
- [7] N.N. Kalmykov, S.S. Ostapchenko and A.J. Pavlov, Nucl. Phys. B **52R** (1997) 17
- [8] CERN Program Library Long Writups W5013 (1993)
- [9] A.A. Chilingarian, Neurocomputing **6** (1994) 497
- [10] A.A. Chilingarian, Pattern Recognition Letters **16** (1995) 333
- [11] A. Chilingarian, S. Ter-Antonyan, A. Vardanyan, Nucl. Instr. and Meth. A **1063** (1997) 230
- [12] A.A. Chilingarian et al.-KASCADE Collaboration, ANI Workshop 1999, these proceedings, 11
- [13] J.R. Hörandel, FZKA-Report 6015, Forschungszentrum Karlsruhe (1998)
- [14] M. Roth, FZKA-Report 6262, Forschungszentrum Karlsruhe (1999)
- [15] S.H. Sokhoyan for the ANI Collaboration, Proc. of the Workshop ANI 98, eds. A.A. Chilingarian, H. Rebel, M. Roth, M.Z. Zazyan, FZKA-Report 6215, Forschungszentrum Karlsruhe (1998) 55



Methods for the Reconstruction of the Primary Energy Spectrum at the KASCADE Experiment

A. Haungs^{1*} for the KASCADE Collaboration[†]

¹*Institut für Kernphysik, Forschungszentrum Karlsruhe, Germany*

One of the main goals of the KASCADE experiment is the determination of the primary energy spectrum around the so-called "knee". Due to the multi detector arrangement, KASCADE is able to measure raw spectra in different EAS observables like shower size, muon numbers at different energy thresholds, or hadronic parameters. Methods for the reconstruction of the primary energy spectrum from this raw spectra, as well as a nonparametric approach for the determination of the energy spectrum are discussed and results compared. With help of classification scenarios to separate the cosmic rays in different mass groups a determination of the chemical composition is additionally possible and will be presented.

1 Introduction

The all particle cosmic ray spectrum follows over roughly 11 orders of magnitude (10^9 eV - 10^{20} eV) a steeply falling power law with some disturbances in between. These are sun modulations at the lowest energies; the so-called "knee" with a steepening of the spectrum around $5 \cdot 10^{15}$ eV; and a flattening at highest energies may produced by a cutoff mechanism [1].

The source of the "knee" is still a unsolved question; several theoretical approaches of astrophysical explanations exist, like a changing of the source composition may in combination with a transition of the standard acceleration mechanisms of supernovae remnants to somewhat different. Further the knee can also be a result of an energy dependent transport mechanism of the particles in the Galaxy (rigidity model). An exact knowledge of the position and structure of this "knee", as well as the energy dependent primary mass composition would allow to distinguish these models or theoretical approaches.

In the energy region of the knee direct measurements on the top of the atmosphere or in space are impossible due to the low integral flux (≈ 1 particle per m^2 and year) of the cosmic rays. But the primary particle produce an Extended Air Shower (EAS) in the Earth's atmosphere, leading to a particle disc containing more than a million of secondaries (mainly electrons and gammas, with a few percent of muons and some remaining hadrons in the shower center) on the surface. Measuring these discs in different shower observables allows the reconstruction of raw spectra, but unfortunately not directly of the energy spectrum. For the conversion or transformation of the measured spectrum (usually the total number of charged particles N_{ch} measured by an array of small detectors) to the energy spectrum, assumptions of the chemical composition and of the "observable-primary energy"-dependence from a more or less detailed Monte Carlo simulation have to be taken into account (for a review see e.g. [2]).

The KASCADE experiment [3, 4, 5] with its multi detector setup has now the possibility to measure simultaneously spectra in observables of different secondary particle components: electrons, muons and hadrons. The CORSIKA EAS simulation tool [6] consisting of detailed (and different) high-energy interaction models and and a precise three dimensional shower development handling allows

*corresponding author: haungs@ik3.fzk.de

†full collaboration list see at the end of these proceedings

at least a reduction of the uncertainties of the conversion due to the Monte Carlo. Different ways to estimate the primary energy spectrum are used in the analysis of the KASCADE data and will be described in this article. Special attention will be given to the principal methods, its assumptions and the succeeded uncertainties and problems of the methods.

2 The KASCADE Experiment

The idea of the KASCADE experiment is to measure as much as possible observables in each of the three main components of EAS: the electromagnetic, the muonic and the hadronic component. The KASCADE array consists of 252 detector huts in a $200 \times 200 \text{ m}^2$ rectangular grid containing unshielded liquid scintillation detectors (e/γ -detectors) and below 10 cm steel and 4 cm lead plastic scintillators as muon-detectors. The total sensitive areas are 490 m^2 for the e/γ - and 622 m^2 for the muon-detectors. In the center of the array a hadron calorimeter ($16 \times 20 \text{ m}^2$) consists of c.

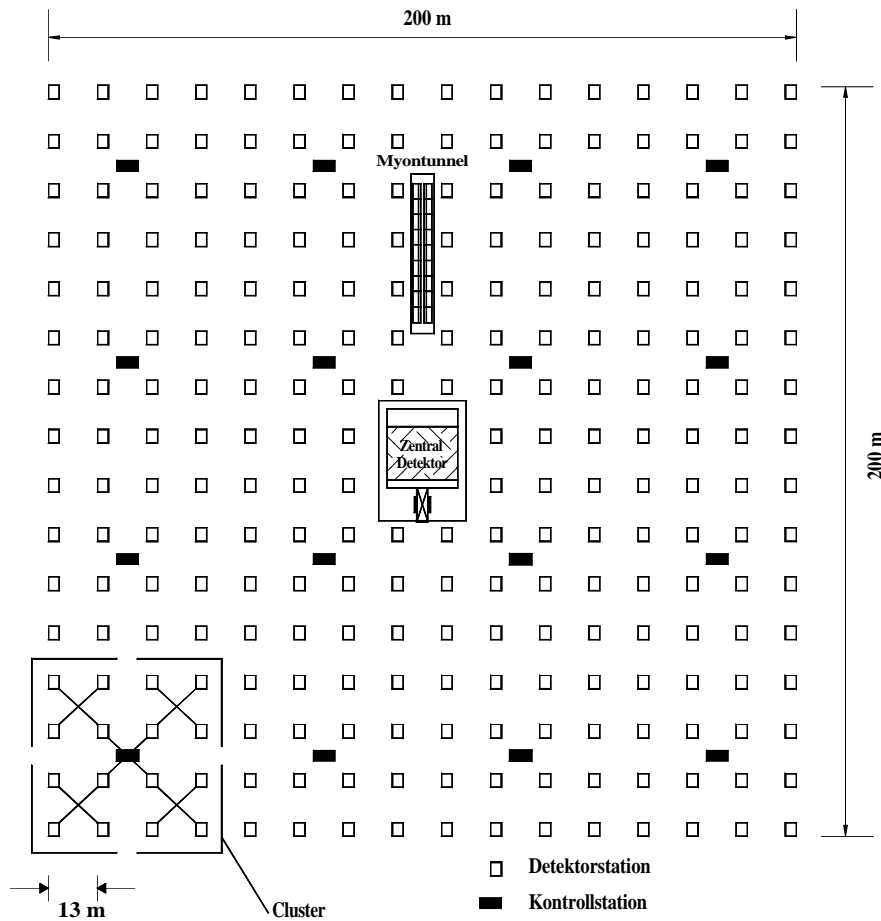
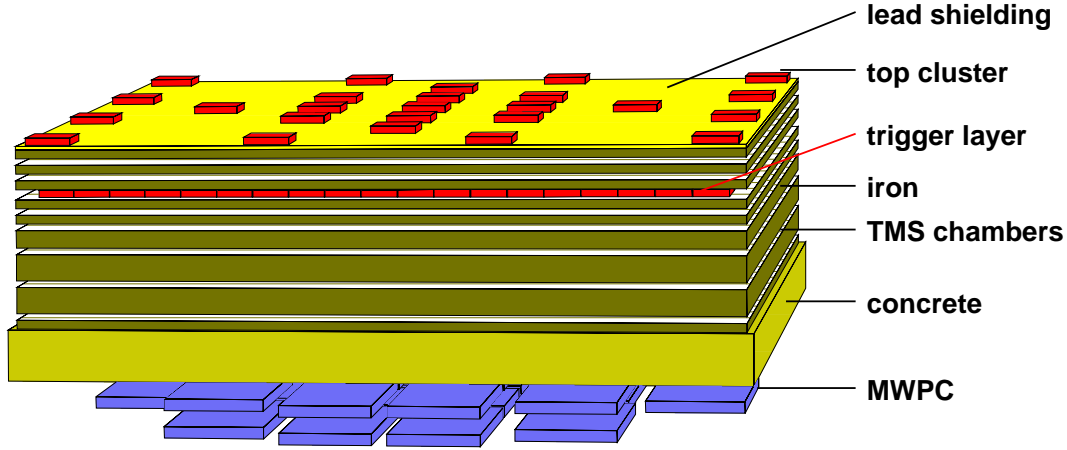


Figure 1: Schematic view of the KASCADE experiment consisting of 252 array detector stations, a central detector and a 50 m muon tunnel.

40000 channels in 8 layers of liquid ionisation material is built up. Below the calorimeter a setup of position sensitive multiwire proportional chambers in two layers measures muons in the shower with an energy larger than 2 GeV. Observables for which spectra are reconstructed or which are relevant for the described analyses are listed in Table 1.

Θ, Φ	shower direction	array, e/γ -detectors
X_0, Y_0	shower core position	array, e/γ -detectors
N_e	shower size (total electron number)	array, e/γ -detectors
N_μ^{tr}	muon size (muon number in 40-200m)	array, muon-detectors
N_H	hadron size (hadron number in 0-24m, $E_h > 50$ GeV)	central detector, calorimeter
N_h^*	reconstructed hadron number, $E_h > 100$ GeV	central detector, calorimeter
E_h	sum of the reconstructed hadronic energy of N_h^*	central detector, calorimeter
E_{hmax}	energy of the "leading" hadron	central detector, calorimeter
N_μ^*	reconstructed muon number	central detector, MWPC
ρ_μ^*	local muon density	central detector, MWPC

Table 1: *List of reconstructed observables of the KASCADE experiment.*Figure 2: *Schematic view of the KASCADE Central Detector.*

3 Methods of the Energy Reconstruction

In the following six subsections different methods for the estimation of the energy spectrum (and sometimes in parallel for the chemical composition) used in the KASCADE experiment will be presented. Special attention is given to the method, the results will be summarized in the conclusions. The methods can be classified in following way:

1. spectrum of one measured observable + observable-energy relation calculated by Monte Carlo simulations including an a-priori assumed chemical composition \rightarrow conversion to the all particle energy spectrum.
2. one observable for the mass discrimination and in parallel a linear approximation of two observables for the energy conversion + observable-energy relation calculated by Monte Carlo simulations for each primary mass group \rightarrow conversion to single mass group energy spectra.
3. spectra of two observables + combined fit of energy and chemical composition (2 groups) with a kernel function obtained by Monte Carlo calculations \rightarrow all particle energy spectrum, single mass group spectra, and composition.

4. one observable for the energy spectrum and independent observable for the mass classification + observable-energy relation calculated by Monte Carlo simulations → conversion to the single mass group energy spectra.
5. multivariate analysis (5 observables) for estimating the mass of single EAS + method 1 for spectra of different observables + observable-energy relation calculated by Monte Carlo simulations → all particle and single mass group energy spectra
6. multivariate analysis (3 or more observables) for estimating the primary energy of single EAS (needs Monte Carlo), and independent similar analysis for the chemical composition → all particle and single mass group energy spectra.

3.1 Hadron Number Spectrum

The conventional way to estimate the primary energy spectrum with help of an EAS experiment is to reconstruct a "shower size" [2]. For the spectrum of the integrated particle number (usually number of all charged particles N_{ch} , often simply called as N_e) a power law dependence from the primary energy is assumed. Additionally an a-priori knowledge of the chemical composition is required to converse the reconstructed spectrum to the energy spectrum.

An example of this method is the estimation of the energy spectrum via the reconstructed hadron number spectrum measured at KASCADE. It is the first time that in the hadronic part of EAS the knee could be confirmed (Fig.3) [7]. N_H is the integrated hadron number in the measured EAS between 0 and 24 m estimated from the number of reconstructed hadrons with energies larger than 50 GeV and with help of the measured average hadron lateral distribution. Only central EAS (core inside the central detector) are taken into account for this analysis.

The conversion from the fitted slopes and knee position of the measured spectrum to the indices and knee position in the energy spectrum is done using the relation $\frac{dN}{dE_0} = \frac{dN}{dN_H} \frac{dN_H}{dE_0} \propto E^{-\gamma}$ assuming power laws in both spectra (hadron number and energy spectra) and for the observable-energy relation. The latter one is calculated by Monte Carlo with a given chemical composition: $N_H \propto E_0^{0.98}$. Due to the limited size of the calorimeter and the concentration of the hadronic part of the EAS in the center, the statistics of the raw spectrum is low and it need some more years of data taking for a final result.

3.2 $N_e - N_\mu^{tr}$ Ratio

Since long time it is known that the muon-electron ratio is the most powerful mass classifier in EAS [8]. This ratio (indeed the ratio of the logarithms of the shower sizes: $\log(N_\mu^{tr})/\log(N_e)$) is used as the mass sensitive parameter in the following analysis [9]. Specific for the KASCADE experiment it

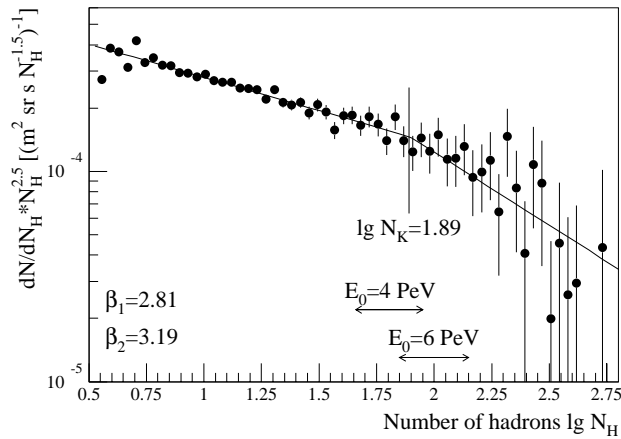


Figure 3: *Reconstructed hadron number spectrum from data of the KASCADE hadron calorimeter. The β 's are the indices of fitted power laws to the spectrum.*

was found that the truncated muon number N_μ^{tr} , i.e. integrated number in the core distance range of 40 m to 200 m, is a good energy estimator because of the nearly mass independent index δ of the relation $N_\mu^{tr} \propto E_0^\delta$. Therefore for different N_μ^{tr} -ranges the $\log(N_\mu^{tr})/\log(N_e)$ -ratio distribution (in a

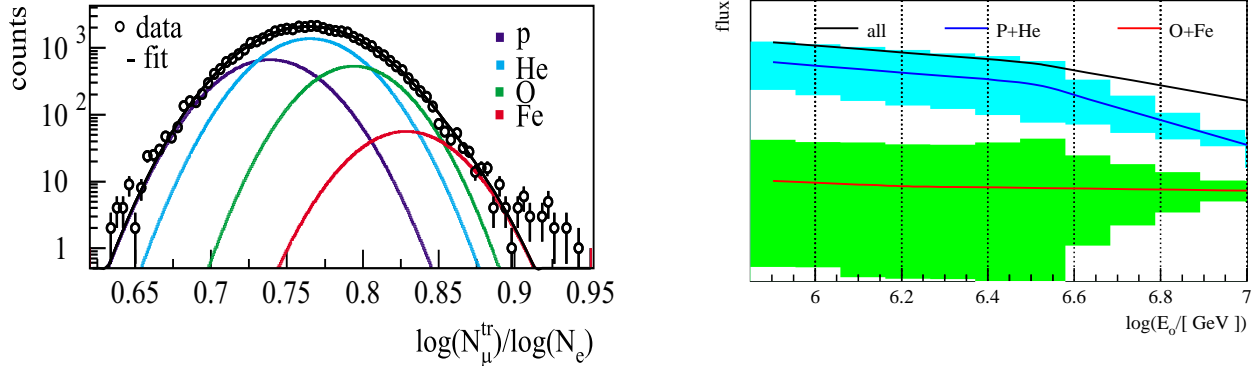


Figure 4: Measured $\log(N_\mu^{tr})/\log(N_e)$ for a N_μ^{tr} -range just before the knee (left). Right: Sketch of the resulting energy spectra for the light and heavy part of the cosmic rays. The ordinate is multiplied by a factor of $E_0^{2.5}$.

certain zenith angular range, $18^\circ < \Theta < 25^\circ$) is fitted with a set of Gaussian distributions (Fig.4, left). This set is obtained by fitting Monte Carlo distributions of the ratio for different mass groups. The resulting mass composition for each N_μ^{tr} -range is converted with the relation $\lg(E)$ as a function of $\lg(N_e)$, $\lg(N_\mu^{tr})$ obtained from Monte Carlo simulations separately.

Regarding the right panel of Fig.4, it should be stressed, that this analysis is optimized to find the chemical composition in the knee region, (whereas the largest methodical problem is the validation of a Gaussian function as parameterization of the observable); the resulting energy spectra are only welcome byproducts.

3.3 $N_e - N_\mu^{tr}$ Spectra

The KASCADE experiment with its special design give the possibility to estimate the total number of electrons N_e and the truncated muon number N_μ^{tr} simultaneously in each single event. The idea of the present method to estimate primary energy spectra is the combination of both observed spectra for a global fit with the restriction to the chemical composition of two primary mass groups, only. This fit leads to the spectra of the (two) single mass groups and therefore to the relative abundances of these mass groups in dependence of the energy and the all particle energy spectrum. The requirement that both measured spectra have to lead to the same energy spectrum and composition is the methodical idea behind this analysis [10]. The fit function is an integral of Fredholm form with a kernel function obtained by Monte Carlo:

$$dJ_A/d\lg N_{e,\mu} = \int dJ_A/d\lg E \cdot p_A(\lg E \rightarrow \lg N_{e,\mu}^s) \cdot d\lg E.$$

The kernel function p_A describes the probability that a primary of energy E leads to reconstructed shower sizes $N_{e,\mu}$ including shower development, detector sampling, reconstruction and all fluctuations in between. Free parameters of the fit are the slopes γ_1 , γ_2 , the knee position E_k , and the flux j_k of the "proton"-part, and $\gamma_1 = \gamma_2$ and the flux j_k of the heavy part of the spectrum. The final fit was performed with this six parameters, whereas fits with more free parameters has never shown a knee in the heavy part. Fig.5 show both measured spectra for showers of a certain angular range including

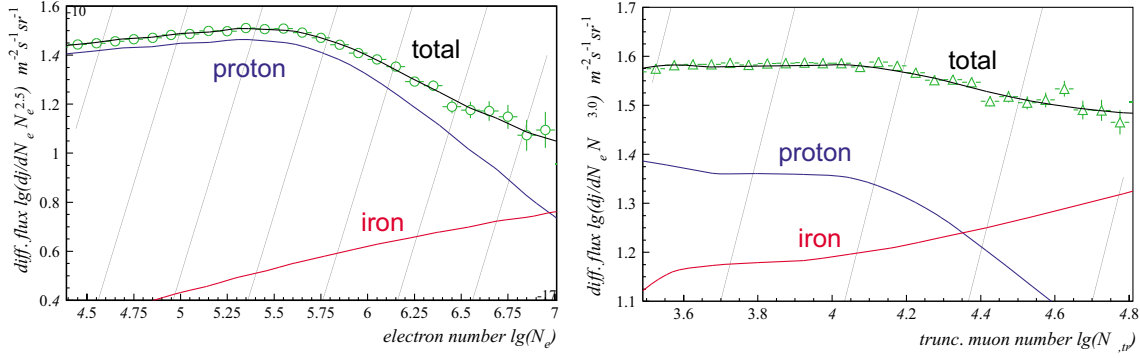


Figure 5: N_e and N_μ^{tr} spectra ($18^\circ < \Theta < 25^\circ$) fitted simultaneously with a two-component composition.

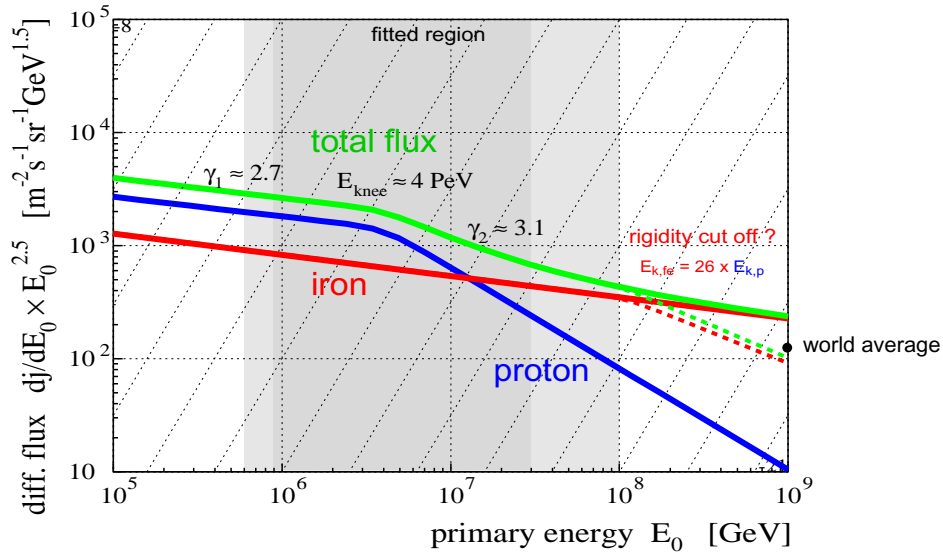


Figure 6: Resulting energy spectra from the simultaneous fit of the N_e and N_μ^{tr} spectra. The shaded part shows the energy range of the fit.

the relative abundances of proton and iron induced showers as estimated by the fit. The resulting spectra (free parameters of the fit) is shown in Fig.6.

The crucial point of this very detailed method are uncertainties due to the model dependence of the Monte Carlo simulations and the uncertainties of the amount of fluctuations described in the simulations. Additionally, the method have to be checked with other or more observed spectra, other zenith angular ranges, and other or more primary mass groups. Never the less this method is promising for the estimation of the "true" primary energy spectrum; because it handles the not negligible uncertainty due to the large fluctuations of EAS observables which are even gained by the steeply fallen spectrum.

3.4 Muon Density Spectrum

All of the three methods before use total particle numbers (shower size) estimated per single shower. This includes uncertainties due to the fit of the NKG-function to the measured particle densities. The idea of the muon density spectrum is to use the measured observable directly. For

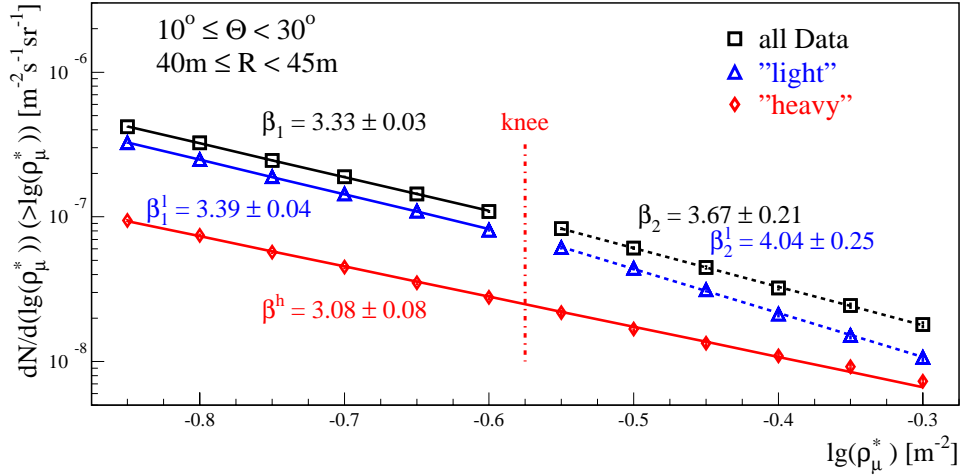


Figure 7: *Integral muon density spectra measured by the MWPC for all showers for enhanced "light" and for enhanced "heavy" showers. The vertical line assigns the position of the knee in the muon density spectra estimated for "all" EAS.*

each shower we estimate a local muon density with help of the MWPC system at the central detector [11]. The resulting spectrum for showers of a certain core distance and zenith angular range shows a power law dependence with a clear kink on a certain muon density (Fig.7, upper spectrum). The conversion of the measured spectra to the primary energy spectra is conventional done (see section 3.1) with help of energy-observable relations (Fig.8) but different core distances are combined. This combination can be used not only for a reduction of statistical uncertainties, it is additionally a check of the Monte Carlo model (at least of the lateral distributions of the muons): the resulting energy spectrum have to be the same for all core distances.

Independent shower observables (here the shower size ratio $\log(N_\mu^{tr})/\log(N_e)$ estimated from data of the array detectors) can be used for a classification in different mass groups. The conversion procedure described above applied to this single mass spectra (Fig.7) leads to the energy spectra for different primaries. Due to the dividing of all showers in different core distance ranges a problem of the method is of statistical nature. Additionally the Monte Carlo statistics plays an important role as a detailed detector simulation is required.

Advantages of the method are the saving of systematic uncertainties due to the fit and integration of measured densities to reveal the shower size.

3.5 Core Structure Investigation

A multivariate analysis of the KASCADE data are applied for the investigation of the core structure of EAS. The MWPC system of KASCADE measures not only high-energy muons which are

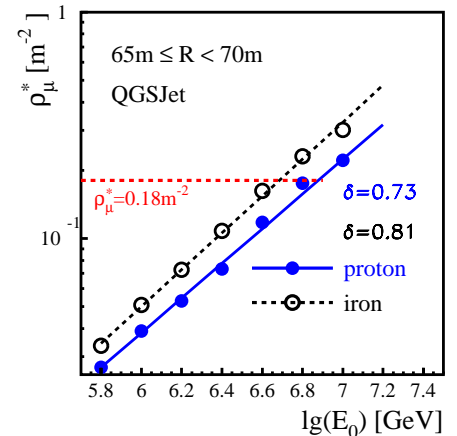


Figure 8: *Example of the dependence of the local muon density on the primary energy for different primaries (CORSIKA simulations including full detector simulations).*

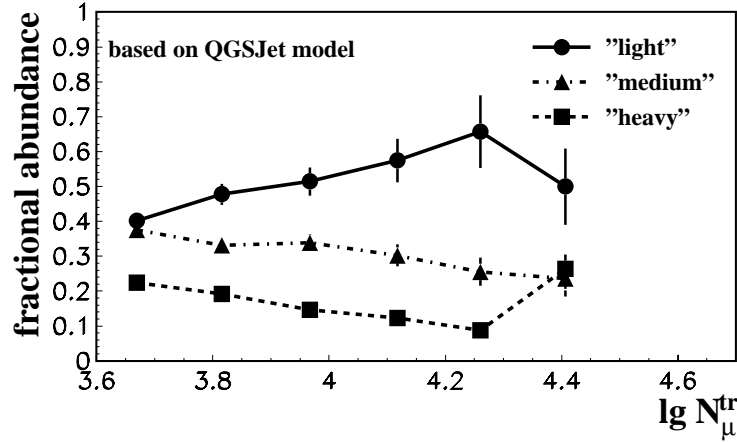


Figure 9: *Relative abundances of different mass groups of primary cosmic rays in the energy region around the knee ($\lg N_\mu^{tr} \approx 4.1$), analyzed on the basis of the interaction model QGSJet [12]. The error bars contain the statistics of both, data and simulations.*

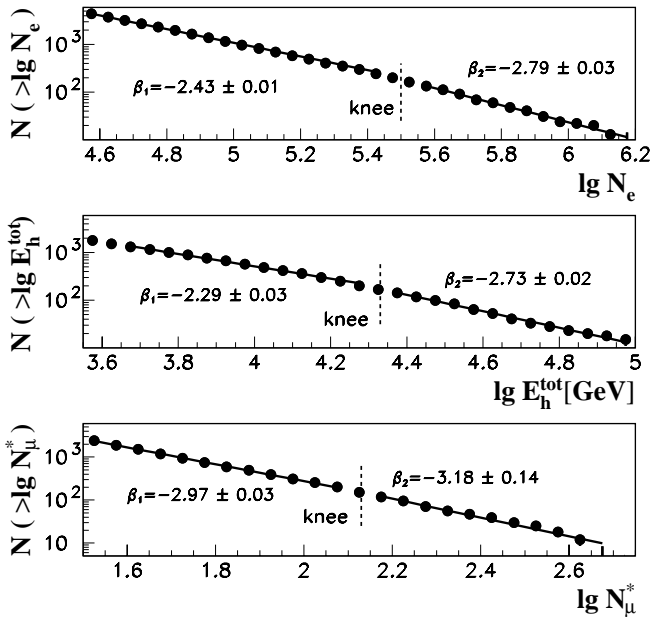


Figure 10: *Integral Spectra of different observables for the central showers of KASCADE. The indicated knee is found at the same flux for spectra at all EAS particle components.*

reconstructed as tracks, but additionally low-energy secondaries produced in the absorber material of the calorimeter, especially at central fallen EAS. This hit pattern reflects the hadron and muon spatial and energy distributions in the center of the shower. The hit pattern can be analysed in terms of multifractal moments leading to two more observables per shower, the so-called generalized multifractal dimensions D_6 and D_{-6} . A detailed Monte Carlo simulation has shown, that these dimensions improve the mass separation of the KASCADE EAS signals [13]. An artificial neural net analysis with five parameters per shower (N_e , N_μ^* , D_6 , D_{-6} , and Θ) estimates a mass probability for each single EAS. With a misclassification matrix obtained by Monte Carlo simulations relative abundances of different mass groups are reconstructed (Fig.9) [14]. For this sample of central showers with the "known" mass for each single EAS, integral spectra in different observables can be reconstructed (N_e , E_h^{tot} , N_μ^* , N_μ^{tr} , N_h^* , E_h^{max} , for examples see Fig.10). These spectra show "knees" in all observables (and therefore at all shower particle components) at the position of the same integral flux above the knee. More, this knee is seen in all "light" induced spectra, too, but not in the spectra of the "heavy" induced showers. The fact, that the position of the knee is found at the same flux in observables

of each particle component is of importance: it gives a strong hint of a astrophysical source of the "knee" (at a fixed primary energy), and make a change of the interaction procedure in the atmosphere implausible.

Assuming the uncertainties in the measurements (fluctuations, etc.) are low and constant for each observable, and assuming the Monte Carlo simulations describes the shower development exactly right, a conversion of each integral spectra should lead to the same indices of the primary energy spectrum before and after the knee, at least for the separated spectra of the light and heavy primary component. The one dimensional conversion of the spectrum measured with the Observable O to the energy spectrum is estimated via the formula: $\frac{dN}{dE_0} = \frac{dN}{dO} \frac{dO}{dE_0} \propto E_0^{-\gamma}$, with $\frac{dN}{dO} \propto O^{-\beta}$ and $O \propto E_0^\delta$. Than γ can be calculated, if β is measured and δ obtained by simulations (including detector simulation and reconstruction uncertainty of the observable). The results of this procedure shows large differences in the resulting indices. This is based mainly on statistical uncertainties since only very central showers can be used, but it can be also interpreted as a insufficient simulation of the balance of the energy and particle numbers of the different EAS components. This gives a first hint to the uncertainties of the Monte Carlo model (here QGSJet).

3.6 Multivariate Analysis of the Energy

Measuring several observables per single EAS makes it possible to estimate the primary energy of each single shower with a nonparametric multivariate analysis directly [15]. Fig.11 shows the energy resolution of this method in the relevant energy range and for different primaries. A large statistics in the Monte Carlo simulations allows the well trained net to calculate the energy of each measured shower in a relatively mass independent way. The results are checked by using different techniques (Bayesian Classifier, Neural Network, k-Nearest-Neighbors), different samples of EAS (central showers with more different observables and showers with core inside the array with a high statistics) and by using different sets of observables (see Tab.1). Fig.12 shows the result of a neural net analysis using N_e , N_μ^{tr} and the shower age as input parameters. As multivariate methods based on a-priori

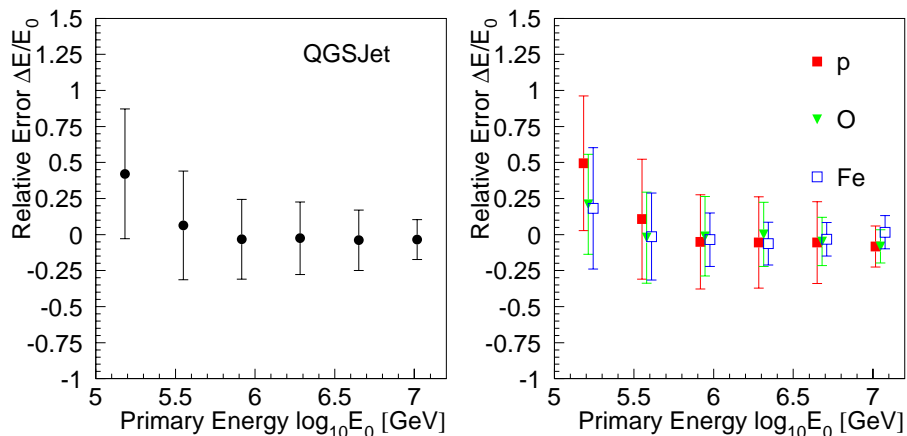


Figure 11: *Energy resolution obtained by a neural net analysis. Left the general resolution is given, where on the right panel the resolution for different primaries is shown.*

knowledge won by Monte Carlo simulations, the model dependent uncertainty is the largest problem of the method but it help to understand the physics and differences of the high-energy interaction

models. Nevertheless only with such an analysis different observables can be combined leading to a useful result. It should be remarked that this is the only method to obtain the energy per single primary particle.

Similar analysis are done for an estimation of the chemical composition of the primary cosmic rays around the knee [16].

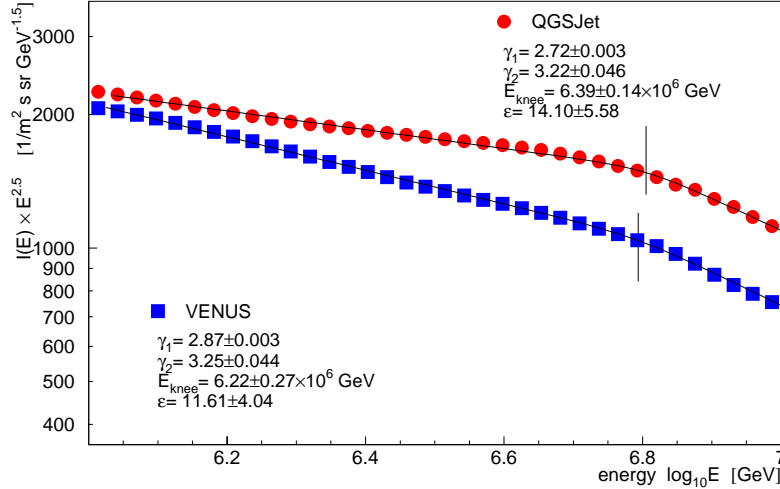


Figure 12: *Energy spectrum obtained by a neural net analysis for two different high-energy interaction models. The fit function is of the type $f(E) = c \cdot E^{-\gamma_1} (1 + (E/E_{\text{knee}})^\epsilon)^{\frac{\gamma_1 - \gamma_2}{\epsilon}}$, where ϵ describes the "smoothness" of the knee.*

4 Results and Conclusions

The main aims of the KASCADE experiment, i.e the estimation of the chemical composition and the primary energy spectrum of the high-energetic hadronic cosmic radiation around the "knee", are tried to achieve in several directions. The different principal methods are explained in a short way in the last chapter. All methods are based on Monte Carlo simulations (CORSIKA with different high-energy interaction models plugged in), but studying the different approaches using different EAS observables will put strong constraints on the interaction models.

Fig.13 shows the chemical composition obtained by different methods at the KASCADE experiment compared with other EAS experiments and the mean of direct measurements. Large differences, especially using different EAS particle components (e.g. only hadronic observables or only electromagnetic observables) give a strong hint for a unrealistic description of the balance of the electromagnetic, muonic and hadronic energy part and/or particle numbers at the different interaction models. The two multivariate methods, using several observables in a nonparametric way, show reasonable medial mean masses, though this is not a hint for the "true" mean mass. Promising is the fact that all methods show the same tendency: The part of heavy primaries increase at energies above the "knee".

Fig.14 compares the results of the six above described methods for the reconstructed spectral indices below and above the "knee" of the all particle energy spectrum and the obtained positions of the knee. Even due to the different ways of estimating the given uncertainties, all the results are close together.

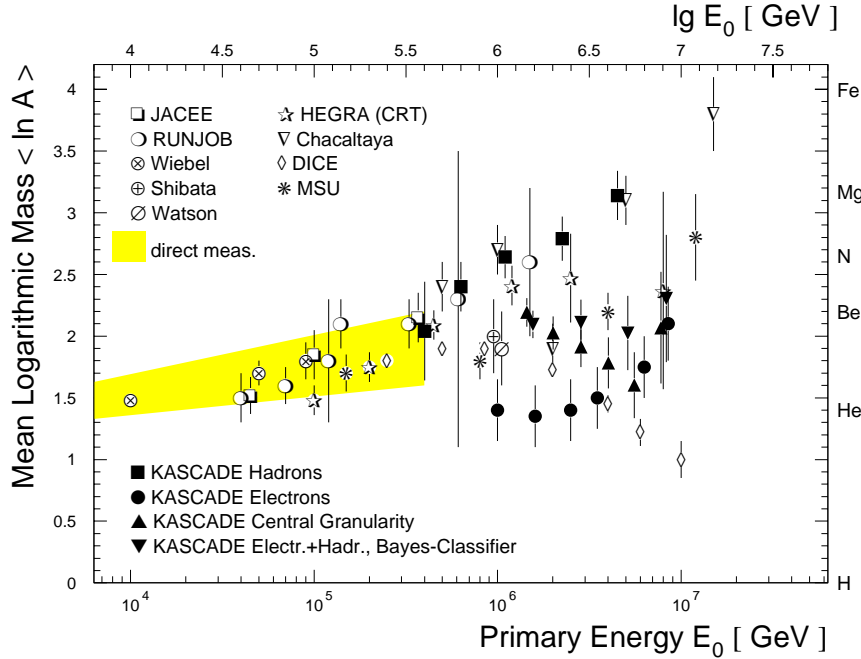


Figure 13: Comparison of experimental results of the mean logarithmic mass vs. primary energy. The shaded area represents direct measurements, compiled by Wiebel-Sooth [17]. JACEE, RUNJOB and other measurements are compiled by Shibata [18] and Watson [19]. HEGRA [20], Chacaltaya [21], DICE [22], MSU [23].

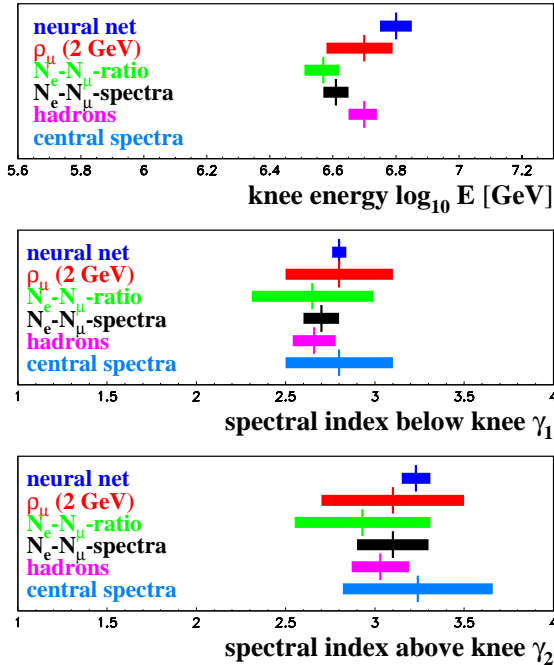


Figure 14: Compilation of the KASCADE results on the position of the "knee" and on the spectral indices below and above the "knee" obtained by the different methods described above.

For my personal opinion the variations of the results are more due to the different observables used than due to systematics of the methods. Combining composition and energy spectra like it is done for the analysis of the N_μ^{tr} - and N_e -size spectra show a sharper knee for the "light" primary particles than the all-particle spectrum, and show a very smooth or no knee in the "heavy" part of the cosmic rays. This is consistent with an increasing "heavy" part regarding the results of analysing the chemical composition independently of the energy reconstruction.

Conclusions of the discussed results of the KASCADE experiment can be summarized as

- The observation of a "knee" in all EAS particle components is a clear indication that the kink is not produced in the atmosphere, i.e. it is of astrophysical source.

- The transition from a light into a "more heavy" chemical composition seems to be established due to the consistent tendencies of the energy dependence of the composition for

different methods.

- None of the existing high-energy interaction models can fit all results in a consistent way at an absolute scale. An improved model is under development. It will be a new and more detailed theoretical approach to the high-energy nucleus-nucleus interaction based on the Gribov-Regge theory as used in QGSJet and VENUS [24]. The model will be named neXus, for further information see [25].

Acknowledgement

The author would like to thank Ashot Chilingarian and all his colleagues for their hospitality and friendship during my first visit of Armenia.

References

- [1] P.Bhattacharjee and G.Sigl, Physics Reports, submitted, (preprint: astro-ph/9811011)
- [2] N.N.Kalmykov, G.B.Khristiansen, Journal Phys. **G 21** (1995) 1279
- [3] H.O.Klages et al. - KASCADE Collaboration, Nucl.Phys.B (Proc.Suppl.) **52B** (1997) 92
- [4] G.Schatz et al. - KASCADE Collaboration, Nucl.Phys.B (Proc.Suppl.) **60B** (1998) 151
- [5] H.O.Klages et al. - KASCADE Collaboration, Proc. 25th ICRC (Durban) **8** (1997) 297
- [6] D.Heck et al., FZKA 6019, Forschungszentrum Karlsruhe 1998
- [7] J.R.Hörandel et al.-KASCADE Collaboration, Proc.26th ICRC (Salt Lake City) 1999, HE 2.2.41
- [8] A.Haungs et al. - KASCADE Collaboration, FZKA 6263, Forschungszentrum Karlsruhe 1998
- [9] J.H.Weber et al. - KASCADE Collaboration, Proc. 26th ICRC (Salt Lake City) 1999, HE 2.2.42
- [10] R.Glasstetter et al.-KASCADE Collaboration, Proc.26th ICRC (Salt Lake City) 1999, HE 2.2.03
- [11] A.Haungs et al. - KASCADE Collaboration, Proc. 26th ICRC (Salt Lake City) 1999, HE 2.2.02
- [12] N.N. Kalmykov and S.S. Ostapchenko, Yad. Fiz. **56** (1993) 105
- [13] A.Haungs et al., Nucl. Instr. Meth. A **372** (1996) 515
- [14] A.Haungs et al. - KASCADE Collaboration, Proc. 26th ICRC (Salt Lake City) 1999, HE 2.2.39
- [15] A.Chilingarian et al.-KASCADE Collaboration, Proc.26th ICRC (Salt Lake City) 1999, HE 2.2.04
- [16] M.Roth et al. - KASCADE Collaboration, Proc. 26th ICRC (Salt Lake City) 1999, HE 2.2.40
- [17] B.Wiebel, P.L.Biermann, H.Meyer, A&A, 330 (1998) 389
- [18] T.Shibata, Nucl.Phys.B (Proc.Suppl.) **75A** (1999) 22
- [19] A.A.Watson, Proc. 25th ICRC (Durban) **8** (1997) 257
- [20] K.Bernlöhr et al., Astrop. Phys. **8** (1998) 253
- [21] Y.Shirasaki et al., Proc. 25th ICRC (Durban) **4** (1997) 53
- [22] S.P.Swordy et al., Proc. 16th ECRS (Alcala) (1998) 265
- [23] Y.A.Fomin et al., Proc. 16th ECRS (Alcala) (1998) 261
- [24] K. Werner, Phys. Rep. **232** (1993) 87
- [25] D.Heck et al., Proc. 26th ICRC (Salt Lake City) 1999, HE 2.2.28

Determination of the EAS Attenuation Length from Data of the ANI Experiment

A.A. Chilingarian, G.V. Gharagozyan, S.S. Ghazaryan, G.G. Hovsepyan,
E.A. Mamidjanyan, L.G. Melkumyan, S.H. Sokhoyan*
Yerevan Physics Institute, Cosmic Ray Division, Armenia

Using the EAS size spectra measured with the MAKET ANI array on Mt. Aragats, Armenia (3200m a.s.l.- 700g·cm⁻²) in the range of $N_e = 10^5 - 10^7$ for different angles-of-incidence, the EAS attenuation length has been determined applying different analysis methods. The analysis is based on a data sample of $2.5 \cdot 10^6$ events collected in the period of June, 97 - April, 99. The results are compared with results deduced from data of the EAS TOP and KASCADE experiments.

1 Introduction

The intensity of Extensive Air Showers (EAS) with fixed shower sizes N_e is assumed to decrease exponentially with increasing atmospheric depth of the observation level. This is considered to be due to the absorption of the particles of the EAS cascade following an exponential law

$$N_e(X) = N_e(X_0) \exp\left(-\frac{X - X_0}{\Lambda}\right), \quad \text{with } X \geq X_0. \quad (1)$$

X_0 is a definite initial atmospheric depth after the maximum of the longitudinal development where the number of (charged) particles is $N_e(X_0)$ and further decreasing exponentially, $N_e(X)$ is the number of particles of the EAS at the slant depth X [g·cm⁻²].

The quantity Λ controls the attenuation of particles of the individual cascade [1] (*size attenuation length*). It is related to the inelastic cross sections (to the mean free path length λ_A) of the interaction of the primary cosmic ray particles with air nuclei. The attenuation of the flux intensity of Extensive Air Showers is characterized by a related quantity λ_N (*intensity attenuation length, absorption*), which can be directly measured by cosmic rays detector arrays. Thus measurements of the attenuation of the EAS intensity in the atmosphere are considered to be an interesting source of information about hadronic interactions, especially if extended to the ultrahigh energy region expected from the forthcoming LHC and TESLA accelerators. In addition due to the sensitivity of the cross sections to the mass of the primary, alterations of the attenuation length with the energy may be indicative for the variations of the mass composition. Measured results imply tests of the energy dependence of the extrapolated cross sections used for Monte Carlo simulations.

The investigations of the present paper are based on an EAS sample measured 1997-1999 with the MAKET ANI array [2, 3] on Mt. Aragats station (Armenia) and registered for different angles-of-incidence in the zenith angle interval $\Theta = 0 - 45^\circ$. The data basis of the analysis can be enlarged by published data from KASCADE (1046 g·cm⁻²) [4] and EAS TOP (810 g·cm⁻²) [5] experiments. Spectra measured by EAS TOP are given in Ref. [6]. Data and zenith angle dependence for KASCADE results are obtained by scanning the spectrum plots communicated by the KASCADE collaboration [7].

We apply different procedures to deduce the attenuation. First we consider the degradation of the

*corresponding author: e-mail: serg@crdlx5.yerphi.am

EAS flux with fixed shower size N_e with increasing zenith angle i.e. increasing atmospheric thickness of the shower development (characterized by the intensity attenuation length (λ_N) [8]). Differently the technique of the constant intensity cut (CIC) [9] considers the intensity spectrum of EAS events and relates equal intensities observed at different atmospheric depths.

There is the tacit assumption that the shower size reflects the energy of the primary. The procedure can be refined by using the knee position in the N_e spectrum as a bench mark for a well defined energy, so far we may associate the knee phenomenon to a feature of the primary energy spectrum of cosmic radiation.

2 Experimental spectra

The experimental basis of the present investigations are measurements of shower size spectra in the knee region and their zenith-angle dependence performed with the MAKET ANI array of the Mt. Aragats Cosmic Ray Station (3200 m a.s.l.) in Armenia. Details of the measurements and the experimental procedures taking into account the detector response are given elsewhere [10, 11]. For a detailed description of the knee region the traditional approximation with two different spectral indices below and above the knee, defining the knee position as intersection of two lines in a logarithmic presentation, appears to be insufficient. Hence a more sophisticated method has been applied with parameterization of the slope of the spectra (see Ref.[12]).

Tab.1 compiles the characteristics of the size spectra measured with the MAKET ANI installation, the changes of the slopes in the knee region (ΔN_{e_k}), expressed by different spectral indices below (γ_1) and above (γ_2) the knee position N_{e_k} for the zenith-angle range of $\Theta = 0 - 45^\circ$. For the display and the analysis of the zenith-angle dependence, the size spectra are determined in 5 angular bins of equal $\Delta \sec \Theta$ widths. The accuracy of the zenith angle determination is estimated to be about 1.5° [10]. A correction due to barometric pressure changes, which lead to small fluctuations of the atmospheric absorption, has not been made. Figure 1 displays the spectra of mean values of each atmospheric depth bin and compares with the results from EAS-TOP [6] and KASCADE [7] experiments.

$I(10^5 < N_e < 1.15 \cdot 10^6)$	$(8.95 \pm 0.18) \cdot 10^{-11} (N_e/10^5)^{\gamma_1}$
$I(N_e > 2.56 \cdot 10^6)$	$(3.23 \pm 0.40) \cdot 10^{-13} (N_e/10^6)^{\gamma_2}$
γ_1	-2.54 ± 0.012
γ_2	-2.94 ± 0.042
$\Delta(N_{e_k})$	$(1.15 \pm 0.034) \cdot 10^6 - (2.56 \pm 0.063) \cdot 10^6$
N_{e_k}	$(1.75 \pm 0.05) \cdot 10^6$
$I(N_{e_k})$	$(5.83 \pm 0.14) \cdot 10^{-14}$

Table 1: *Flux* [$m^{-2}s^{-1}sr^{-1}$] and knee region parameters of the size spectra measured with the MAKET ANI array.

Following fixed intensities of the experimental spectra (see sect.3.2) the average N_e cascade development can be immediately reconstructed as shown in Figure 2. Note that the results in the range of the slant depth observed with the ANI array deviate from the exponential decrease (eq.1). That is an interesting feature which can be revealed more clearly when combining spectra accurately measured on different altitudes. In the present paper we base the formulation of the procedures estimating the attenuation on the exponential decrease (eq.1). It is our interest to explore, if this assumption applied to the ANI and KASCADE data lead to consistent results.

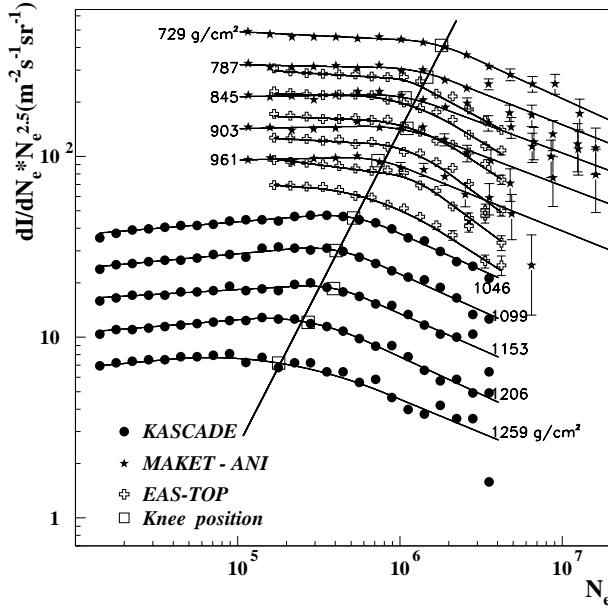


Figure 1: *Differential size spectra for different zenith angles ranges observed with MAKET ANI array, compared with spectra reported by the KASCADE [7] and the EAS TOP [6] collaborations.*

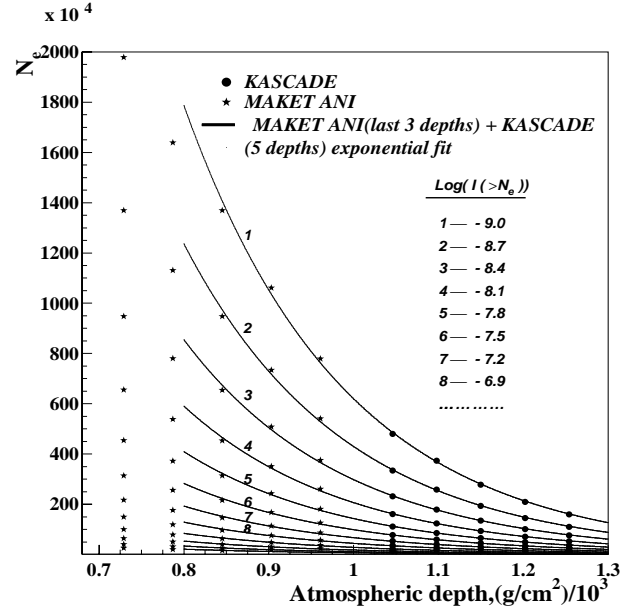


Figure 2: *N_e cascade in the observed range of the atmospheric slant depth.*

3 Procedures for inference of the attenuation length from size spectra

We consider the differential and integral size spectra $I(N_e, X)$ and $I(> N_e, X)$, respectively. In addition to the basic assumption of exponential attenuation of N_e (eq.1) a power-law dependence of the size spectrum

$$I(N_e, X) \propto N_e^{-\gamma}, \quad (2)$$

with the spectral index γ is adopted.

3.1 Attenuation of the intensity of fixed N_e : absorption length

For different fixed values of shower size N_e , on different depths in the atmosphere or/and different zenith angles of incidence, from measured spectra (see vertical dotted lines on Figure 3) we obtain several values of corresponding intensities from the equivalent depths from 700 till 1280 $g \cdot cm^{-2}$. Fitting the depth dependence of the intensities by the straight line (in logarithmic scale) according to equation:

$$I(N_e, X) = I(N_e, X_0) \exp\left(-\frac{X - X_0}{\lambda_N}\right) \quad (3)$$

we obtain the estimate of the absorption length λ_N . The absorption length can be estimated both by integral and differential spectra.

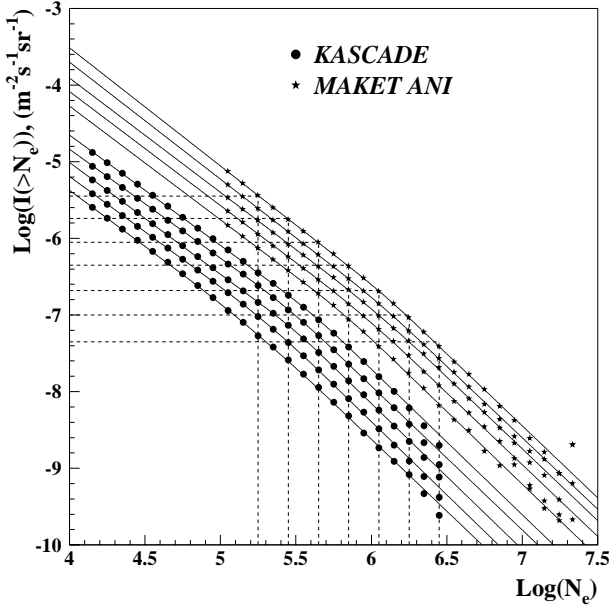


Figure 3: Integral size spectra for different zenith angles ranges observed with MAKET ANI array, compared with spectra reported by the KASCADE [7]: illustration of the procedures for absorption and attenuation length estimates.

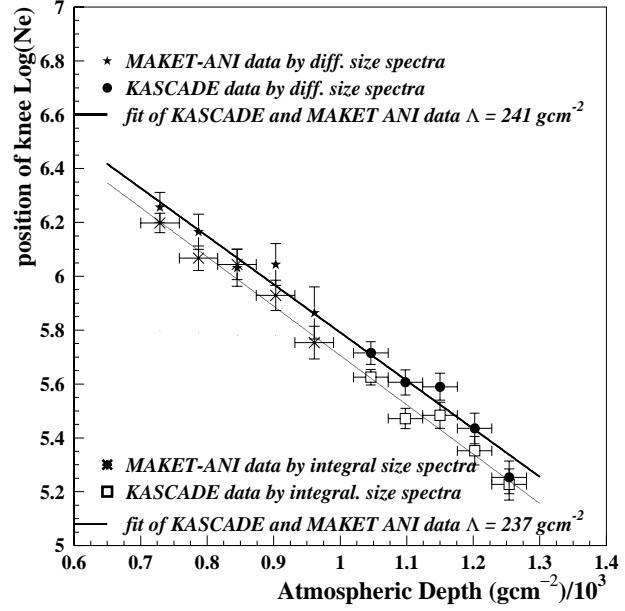


Figure 4: The variation of the knee position with the atmospheric depth.

3.2 Constant intensity cut

The basic idea of this procedure is to compare the average size of showers which have the same rate (showers per $m^2 \cdot s \cdot sr$) in the different bins of the zenith angle of shower incidence and different slant depth, respectively [9].

Considering two different depths in atmosphere $X_1, X_2 > X_0$ the expressions of differential intensities $I(N_e, X)$ has the form

$$N_e(X_1)^{-\gamma} \exp \left[-(\gamma - 1) \frac{X_1 - X_0}{\Lambda} \right] = N_e(X_2)^{-\gamma} \exp \left[-(\gamma - 1) \frac{X_2 - X_0}{\Lambda} \right] \quad (4)$$

With simple transformations we obtain:

$$\Lambda_{diff}(I) = \frac{\gamma - 1}{\gamma} \frac{X_2 - X_1}{\ln \left(\frac{N_e(X_1)}{N_e(X_2)} \right)} \quad (5)$$

The attenuation lengths, obtained by integral spectra do not depend explicitly on spectral index:

$$\Lambda_{int}(I) = \frac{X_2 - X_1}{\ln \left(\frac{N_e(X_1)}{N_e(X_2)} \right)} \quad (6)$$

Practically the estimate of the attenuation length is obtained by fitting the N_e dependence on the depth in atmosphere by the straight line according to the equation (1). The sequence of N_e values is obtained according to the fixed values of the flux intensity, selected from the interpolation of the differential or integral size spectra.

For each N_e value, the slope index γ used in equation 5, is obtained by averaging over all used slant depths. Selecting equal intensities (\approx primary energies) corresponding to different shower sizes N_e and different depths the value of $\Lambda_{diff}(I)$ is estimated. Intensity values from 10^{-9} to $5 \cdot 10^{-6}$ were used for CIC method.

3.3 Attenuation of the size of the knee

A special variant of the constant intensity cut is to follow the decrease of the shower size at a constant primary energy in the size spectrum. Assuming that the knee phenomenon reflects a feature of the primary flux, the variation shower size at the knee with the zenith angle provides the possibility to extract the attenuation length.

Considering the assigned knee position of the data from various experiments, differences within 30% are noticed for all X-bins.

The knee positions obtained by the differential and integral spectra are a bit shifted to the smaller N_e values (see Figure 4). The shift is approximately uniform over all investigated depths interval, therefore the estimates of the attenuation length by the differential and integral size spectra are very close to each other.

3.4 The relation between the absorption and attenuation length

We consider the quantity $I(N_e, X)dN_e$ - the number of EAS at the depth X which comprise N_e to $N_e + dN_e$ particles:

$$I(N_e, X)dN_e \sim N_e^{-\gamma} \exp \left[-(\gamma - 1) \frac{X - X_0}{\Lambda} \right] dN_e \quad (7)$$

With eq.3 we obtain:

$$\Lambda_{diff}(N_e) = (\gamma(N_e) - 1)\lambda_N, \quad (8)$$

where, $\gamma(N_e)$ is the differential size spectra index (here we indicate the N_e dependence of the slope index explicitly). For the integral spectra:

$$\Lambda_{int}(N_e) = \gamma(N_e)\lambda_N, \quad (9)$$

where, $\gamma(N_e)$ is integral size spectra index.

For the evaluation of the inelastic cross section and for comparison of the three methods described above we propose to use the calculated values of the attenuation length Λ (instead of using absorption length λ_N). The attenuation of the number of particles in the individual cascade is more directly connected with the characteristics of the strong interaction and is independent from the parameters of the cosmic ray flux incident on the atmosphere. In turn the absorption length, i.e. the attenuation of the CR flux intensity, reflects also characteristics of the primary flux and is dependent on the change of the slope of the spectra.

3.5 Estimate of the inelastic cross section

The inelastic cross sections, of the primary nuclei with atmosphere nuclei is related by [9]:

$$\sigma_{A-air}^{inel} (mbarn) = \frac{2.41 \cdot 10^4}{\lambda_A (g \cdot cm^{-2})}, \quad (10)$$

where A denotes the primary nuclei. The quantity λ_A is the *interaction length* of the A-nucleus in the atmosphere (note: in some publications the interaction length is denoted by λ_N , where N is

primary nuclei, in contrast in this paper N is reserved for the shower size). The interaction length λ_A is related with the absorption length Λ_A by

$$\lambda_A = K(E) \cdot \Lambda_A \quad (11)$$

The $K(E)$ coefficient reflects peculiarities of the strong interaction model used for simulation. The value of the parameter K has to be determined by simulations of the EAS development in the atmosphere. Such studies require the development of procedures for the selection of EAS initiated by primaries of a definite type (see for example in [13, 14]).

4 Application to the data

The mean values of the attenuation lengths obtained by various methods from data of the ANI and KASCADE installations, as well as for the joint ANI & KASCADE data by the differential (Λ_{dif}) and integral spectra (Λ_{int}) are compiled in the Tables 2,3,4.

Min.depth	MAKET ANI		ANI+KASCADE		KASCADE	
$X_0, g \cdot cm^{-2}$	Λ_{int}	Λ_{dif}	Λ_{int}	Λ_{dif}	Λ_{int}	Λ_{dif}
700	248 ± 27	247 ± 42	203 ± 10	203 ± 13	—	—
758	236 ± 32	237 ± 51	195 ± 8	196 ± 12	—	—
816	211 ± 43	218 ± 70	186 ± 9	188 ± 13	—	—
1020	—	—	—	—	181 ± 14	182 ± 23

Table 2: Attenuation lengths for the data from the MAKET ANI and KASCADE installations estimated by the CIC method from differential and integral size spectra

Min.depth	MAKET ANI		ANI+KASCADE		KASCADE	
$X_0, g \cdot cm^{-2}$	Λ_{int}	Λ_{dif}	Λ_{int}	Λ_{dif}	Λ_{int}	Λ_{dif}
700	239 ± 14	240 ± 15	191 ± 11	193 ± 13	—	—
758	232 ± 13	228 ± 19	186 ± 10	184 ± 17	—	—
816	213 ± 14	219 ± 27	179 ± 11	181 ± 24	—	—
1020	—	—	—	—	181 ± 7	183 ± 11

Table 3: Attenuation lengths for the data from the MAKET ANI and KASCADE installations estimated by the recalculation from the absorption length for differential and integral size spectra

Min.depth	MAKET ANI		ANI+KASCADE		KASCADE	
$X_0, g \cdot cm^{-2}$	Λ_{int}	Λ_{dif}	Λ_{int}	Λ_{dif}	Λ_{int}	Λ_{dif}
700	302 ± 71	295 ± 83	241 ± 17	237 ± 15	—	—
758	272 ± 51	263 ± 42	242 ± 20	221 ± 17	—	—
816	—	—	225 ± 21	225 ± 19	—	—
1020	—	—	—	—	232 ± 26	222 ± 28

Table 4: Attenuation lengths for the data from the MAKET ANI and KASCADE installations, estimated by the "attenuation of knee position" method from differential and integral size spectra

The alternative estimates of the attenuation length reflect the inherent uncertainties of the methods and the statistical errors, as well as the fluctuations of cascade development in the atmosphere, the

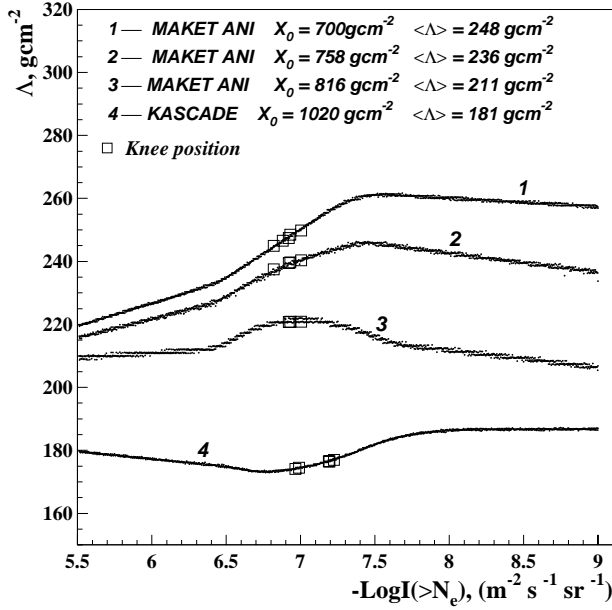


Figure 5: Attenuation Length dependence on Spectra Intensity (Primary Energy).

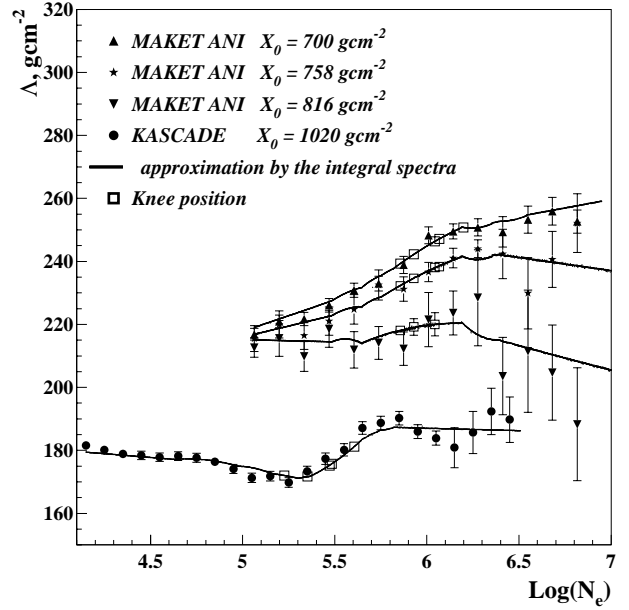


Figure 6: Attenuation Length dependence on the Shower Size N_e .

energy dependence of the inelastic cross section and possible changes in mass composition. As obvious in Figure 2, the values corresponding to the minimal equivalent depths of used MAKET ANI data, deviate significantly from the exponential decrease. The observations reflects the flattening of the cascade curve just after the shower maximum in the altitude $500 - 600 \text{ g} \cdot \text{cm}^{-2}$. Due to these features the attenuation lengths calculated by MAKET ANI data appear to be significantly larger than those derived for the KASCADE data (Tables 2, 3).

Therefore, for the combined analysis of the KASCADE and ANI data we omitted the first and the second zenith angle bins of MAKET ANI and calculate the attenuation lengths by the remaining 9 (minimal equivalent depth $758 \text{ g} \cdot \text{cm}^{-2}$) and 8 (minimal equivalent depth $816 \text{ g} \cdot \text{cm}^{-2}$) angular bins. The dependences of estimated values of attenuation length on the shower size and flux intensity for different amount of the angular bins used, are displayed in Figures 5 (note, that higher intensities on the X axes correspond to the lower primary energies) and 6.

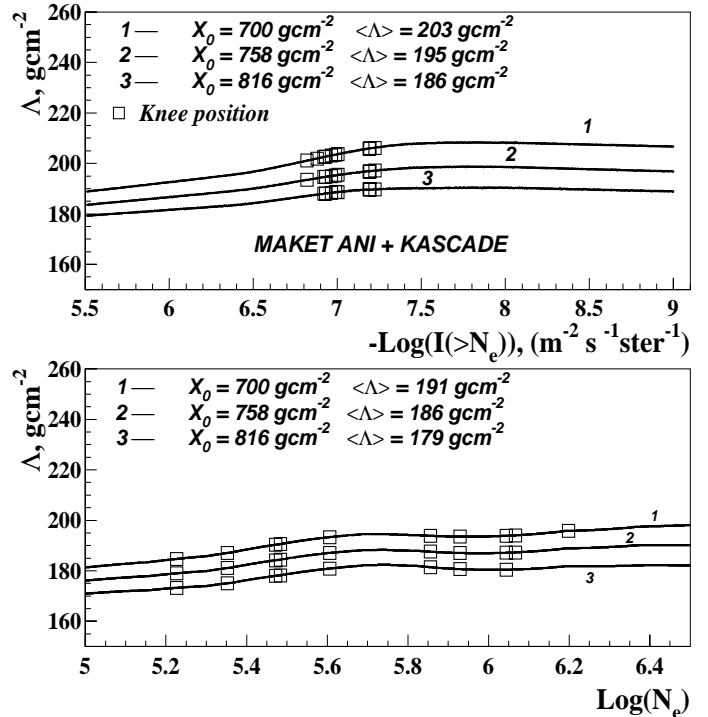


Figure 7: Attenuation length obtained by joint analysis of the MAKET ANI and KASCADE data.

The attenuation length estimates obtained from the differential and integral spectra agree fairly well. The results of both CIC and recalculation from absorption length agree within the error bars. The results obtained by the "attenuation of knee position" are larger for MAKET ANI and KASCADE. As pointed out by S. Ostapchenko [15] it is the consequence of the large EAS fluctuations with the tendency to shift the knee position to the lower energies (and correspondingly to higher fluxes) in a way to "slow down" the cascade curve attenuation.

Well below the shower development maximum starting from $816g \cdot cm^{-2}$ KASCADE and MAKET ANI data could be fitted with one decay parameter (see Figure 7). There is a concentration of the knee positions on the curve showing the dependence of the attenuation of the flux intensity (\approx primary energy). In turn, the curve displaying the dependence of the attenuation length on the shower size demonstrates a rather large dispersion of the "knee positions". These observations in size and energy scales may be interpreted as an indication of the astrophysical nature of the knee phenomenon.

5 Conclusion

Experimental studies of EAS characteristic like the depth of the shower maximum X_{max} , the elongation rate $dX_{max}/d\log_{10}E$ and the attenuation length Λ are of particular importance, since they map rather directly basic features of the hadronic interaction. Strictly, however, the interpretation of these quantities in terms of hadronic cross sections cannot bypass the necessity of detailed calculations of the shower development. Nevertheless these type of EAS quantities, if compared with Monte Carlo simulation results, provide stringent tests of the interaction model ingredients of the simulations.

The recent results of various experimental installations are sufficiently accurate to enable relevant studies of this kind, and combining the data from arrays situated on different altitudes (like MAKET ANI and KASCADE) allows a large span in the atmospheric slant depth for reconstructing the development of the charge particle size. In fact such studies, if using a sufficiently large data sample, could be continued in a more detailed manner by separating the muon component and taking into account the deviations from the exponential shape of the cascade decline. The penetrating muon component contributes with smaller attenuation to the development of the considered charged particle component, but hardly with an exponential degrading (according to eq.1). Actually by use of methods in progress to isolate different primary groups ("pure nuclear beams") of the size spectra [14, 16], these kind of interaction studies would get of extreme interest.

Acknowledgment

This publication is based on experimental results of the ANI collaboration. The MAKET ANI detector installation has been set up as collaborative project of the Yerevan Physics Institute, Armenia and the Lebedev Institute, Moscow. The continuous contributions and assistance of the Russian colleagues in operating the detector installation and in the data analyses are gratefully acknowledged. In particular, we thank S. Nikolski and V. Romakhin for their encouraging interest and useful discussions.

First perspectives of combined considerations of the KASCADE and ANI experimental data have been discussed in 1998 during the ANI-98 workshop in the cosmic ray observatory station Nor-Amberd of Mt. Aragats (Armenia). The MAKET ANI group would like to thank the German colleagues for stimulating discussions and encouragement, in particular H. Rebel for his numerous valuable comments and interesting suggestions to the topic of this paper. We acknowledge the useful discussions with K.-H. Kampert, H. Klages and R. Glasstetter. The suggestions of S. Ostapchenko are highly appreciated.

The work has been partly supported by the research grant No.96-752 of the Armenian Government

and by the ISTC project A116. The assistance of the Maintenance Staff of the Aragats Cosmic Ray Observatory in operating the MAKET ANI installation is highly appreciated.

References

- [1] S. Hayakawa, *Cosmic Ray Physics*, Interscience Monographs and Texts in Physics and Astronomy, V. 22, Wiley-Interscience, 1969
- [2] V.V. Avakyan et al., *Jadernaya Fiz.* **56** (1993) 182
- [3] G.G. Hovsepyan for the ANI Collaboration., Proc. of the Workshop ANI 98, eds. A.A. Chilingarian, H.Rebel, M. Roth, M.Z. Zazyan, FZKA 6215, Forschungszentrum Karlsruhe 1998, 45
- [4] H.O. Klages et al. - KASCADE Collaboration, *Nucl. Phys. B (Proc. Suppl.)* **52B** (1997) 92
- [5] M. Aglietta et al., *Nucl. Instrum. and Meth.* **A336** (1993) 310
- [6] M. Aglietta et al., *Astropart. Phys.* **10** (1999) 1
- [7] R. Glasstetter et al. - KASCADE Collaboration, Proc. 16th ECRS (Alcala, 1998), 564
- [8] G.B. Khristiansen, G. Kulikov, J. Fomin, *Cosmic Rays of Superhigh Energies*, Verlag Thiemig, München, 1979
- [9] M. Nagano et al., *Journ. Phys. G: Nucl. Phys.* **10** (1984) L235;
Gaisser T.K, *Cosmic Rays and Particle Physics*, Cambridge Univ. Press, 1992
- [10] G.V. Gharagozyan for the ANI Collaboration, Proc. of the Workshop ANI 98, eds. A.A. Chilingarian, H.Rebel, M. Roth, M.Z. Zazyan, FZKA 6215, Forschungszentrum Karlsruhe 1998, 51
- [11] S.V. Blokhin, V.A. Romakhin and G.G. Hovsepyan, ANI Workshop 1999, these proceedings, p.111
- [12] S.H. Sokhoyan et al. - ANI Collaboration, Proc. of the Workshop ANI 98, eds. A.A. Chilingarian, H.Rebel, M. Roth, M.Z. Zazyan, FZKA 6215, Forschungszentrum Karlsruhe 1998, 55
- [13] A.A. Chilingarian, H.Z. Zazyan, *Yad. Fiz.* **54** (1991) 128
- [14] A. Vardanyan et al. - KASCADE Collaboration, ANI Workshop 1999, these proceedings, p.23
- [15] S. Ostapchenko , private communication, 1999
- [16] A.A. Chilingarian et al., ANI Workshop 1999, these proceedings, p.53



The Dependence of the Age Parameter from EAS Size and Zenith Angle of Incidence

A.A. Chilingarian, G.V. Gharagozyan*, S.S. Ghazaryan, G.G. Hovsepyan,
E.A. Mamidjanyan, L.G. Melkumyan, S.H. Sokhoyan
Yerevan Physics Institute, Cosmic Ray Division, Armenia

The quality of the MAKET-ANI detector installation in view of the uniformity of the registration efficiency is demonstrated. Based on a data sample collected by the MAKET-ANI array in the period of June 1997 - March 1999, the dependencies of the age parameter on the zenith angle and the EAS size ($10^5 - 10^7$) are studied. The variation of the age parameter with the shower size can be approximately related to the elongation rate.

1 Introduction

The lateral distribution of the charged particle component of extensive air showers (EAS) carries information about the height of maximum of the EAS development. In NKG type parameterizations of the lateral distribution this information is associated with the so-called age parameter s , originally introduced by the analytic description of purely electromagnetic cascades for characterizing the actual stage of the EAS development.

In EAS experiments this parameter is usually extracted from fitting the distribution measured on observed level, assuming that this lateral parameter reflects the actual longitudinal EAS stage. Investigations of the parameter s have been performed on various altitudes, with the aim to gain information on the longitudinal EAS development and on the composition of primary cosmic rays [1-7]. For example, from the analysis of the zenith angle dependence of the average value of s it has been concluded that the mass composition gets either heavier primary energies larger than 10^{15} eV or the multiplicity of secondary particle production in hadronic interactions is unexpectedly increasing. In the present contribution experimental age distributions, dependent on the zenith angle θ of EAS incidence and of the shower size N_e as extracted from an actual data set of the MAKET-ANI array, are communicated. As compared to earlier results [4] the statistical accuracy of the data is considerably improved thanks to various modernizations of the installation [5]. The variation of the age parameter with the observation depth X is considered by a simplified approach.

2 Some characteristics of the data selection

With an effective running time of ca. 8000 h the array triggered for $2.6 \cdot 10^6$ showers. From this set 177066 showers have been selected with following criteria: $N_e \geq 1 \times 10^5$, $\theta < 45^\circ$, $0.3 \leq s \leq 1.7$. The procedures of data selection and further analyses are given in Ref. [5]. The effective area for EAS registration, varying from $28 \cdot 14m^2$ for $N_e \geq 10^5$ to $64 \cdot 32m^2$ for $N_e \geq 10^6$. With Monte Carlo simulations and experimental considerations of the angular accuracy following uncertainties of the reconstructed EAS parameters were obtained: core location: $\delta R \simeq 1.5$ m, $\delta N_e \simeq 15\%$ for $N_e < 10^6$, $\delta N_e \simeq 10\%$ for $N_e > 10^6$, $\delta s \simeq 7\%$, $\delta\theta < 1.5^\circ$ and $\delta\varphi < 5^\circ$.

Figures 1 and 2 display the good uniformity of the EAS registration; the maximum intensity results

*corresponding author: gagik@crdlx5.yerphi.am

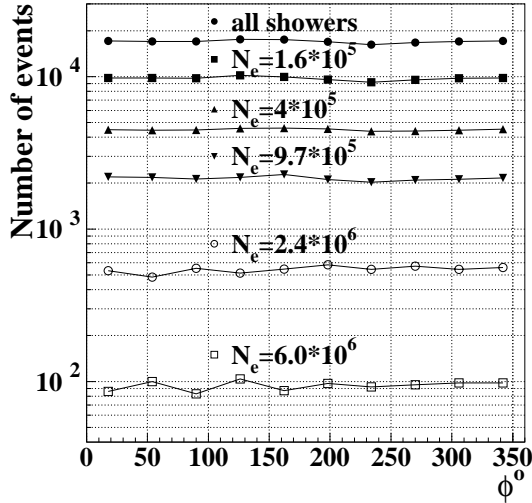


Figure 1: *Distributions of the EAS azimuth angles φ for different EAS sizes.*

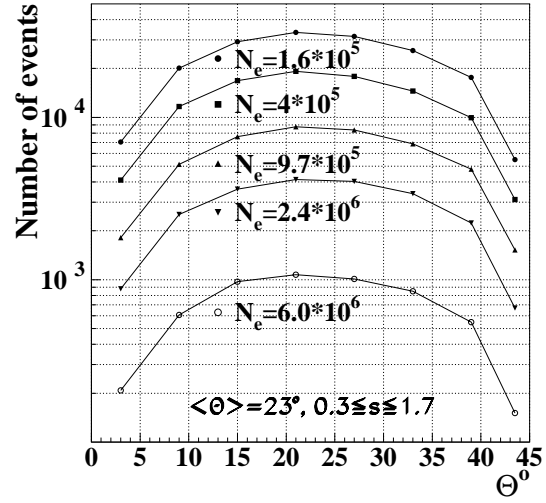


Figure 2: *Distributions of the EAS zenith angles for different EAS sizes.*

from the zenith angle of $\bar{\theta} \simeq 23^\circ$. For more detailed analyses the EAS sample is divided in three classes: "young" showers with $0.3 < s < 0.8$, "mature" showers with $0.8 < s < 1.1$, and "old" showers with $1.1 < s < 1.7$.

Figure 3 display the uniform efficiency of the age selection of the procedures.

3 Age parameter distributions

The distributions of the age parameter values for various EAS sizes are shown in Figure 4, displayed for different ranges of the zenith angles of EAS incidence. The distributions get narrower and show decreasing variances with increasing N_e in agreement with Ref. [1]. This can be understood that small size showers penetrating in the deeper atmosphere show larger fluctuations in s . The average age is slightly, but systematically shifted to higher values with increasing atmospheric depth.

For a consideration of the dependence of the average age from N_e and zenith angle a finer binning of the total angular range has been applied. As examples in Figure 5 the dependence of the mean age is shown for selected angular bins (representing "vertical", "inclined" and all showers). The results are compared with the Norikura data [1],

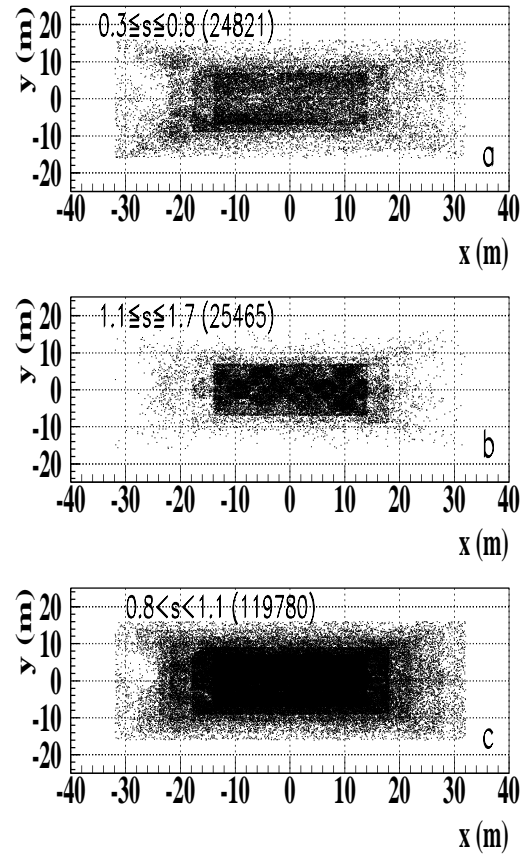


Figure 3: *Distribution of the core locations of different age classes of showers.*

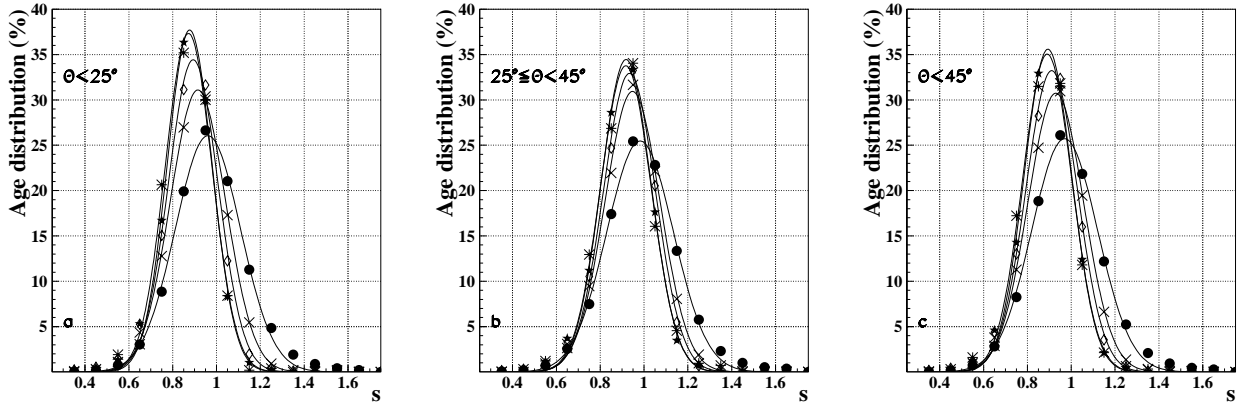


Figure 4: Age parameter distributions for various EAS sizes and angular ranges of EAS incidence: a- vertical, b- inclined, c- all showers. $N_e = \bullet - 1.6 \cdot 10^5$, $\times - 4.0 \cdot 10^5$, $\diamond - 9.7 \cdot 10^5$, $\star - 2.4 \cdot 10^6$, $* - 6.0 \cdot 10^6$.

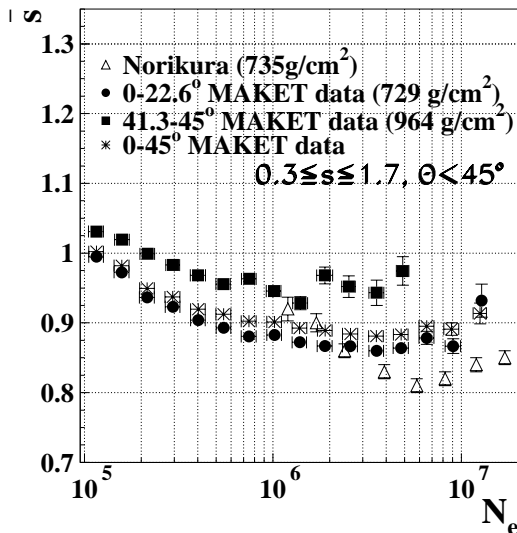


Figure 5: \bar{s} dependence of the shower size.

be increasing monotonously. Hence the shallow slope of the average age for $N_e > 10^6$ may indicate a faster EAS development due to an increasing multiplicity of the secondary production and a heavier composition, respectively.

4 EAS size spectra of different ages

Figure 6 shows the integral size spectra for "young", "mature" and "old" showers for two different angular ranges of shower incidence. While the young and mature shower spectra exhibit the knee feature, a knee is not evident for old showers, which show obviously a different variation with the shower size. This behavior results also from an analysis of KASCADE data classified along various types of primaries by methods of advanced statistical analysis [10]. The old showers are tentatively associated to iron-like showers with a different knee position.

which show similar tendencies, but shifting the global features to larger and younger EAS. It is not clear if this finding is due methodical effects of different evaluation procedures in both experiments. The results of MAKET-ANI agree with the observations Ref. [7], if taking into account the different observation levels, but disagrees with the data of the MSU group [3], the latter claiming an almost constant mean age for EAS of $N_e = 10^5 - 10^6$. There are results of EAS simulations, based on the QGSJET model as generator [8], which show fair agreement [9].

The variation of the average age is affected by the primary energy spectrum, by the change of the chemical composition and the hadronic interaction characteristics, governing the EAS development. As long as there is no noticeable change, the average depth of the shower maximum is expected to

The lower part of Figure 6, taken from Ref. [2], where the showers have been classified by an analysis of the appearance of the shower core, shows a good consistency. There are, however some differences with the Tien-Shan data (given in Ref.[11]). While the slopes are identical for mature showers and equal for old showers, the young showers do not display a knee in the data of Ref. [11]. Whether these differences can be explained by the particular analysis procedures, is not yet clarified.

Figure 7 presents the spectra for different values of the age parameters and characterized by the spectral indices given Table 2 (extracted by the procedures of Ref. [12]). With increasing age values the spectral slope gets flatter before the knee as also evidenced by the KASCADE data [13]. Old showers exhibit a quite different slope.

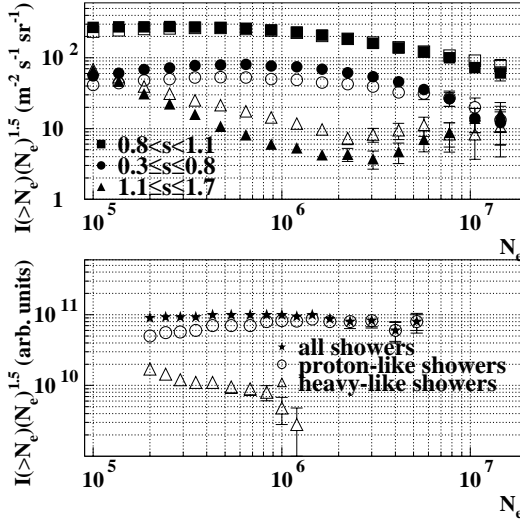


Figure 6: Integral EAS size spectra for two different ranges of the zenith angles (closed symbols: $\theta = 0^\circ - 25^\circ$, open symbols: $\theta = 25^\circ - 45^\circ$ for young, mature and old showers. The lower part of the figure is taken from Ref. [2] for comparison.

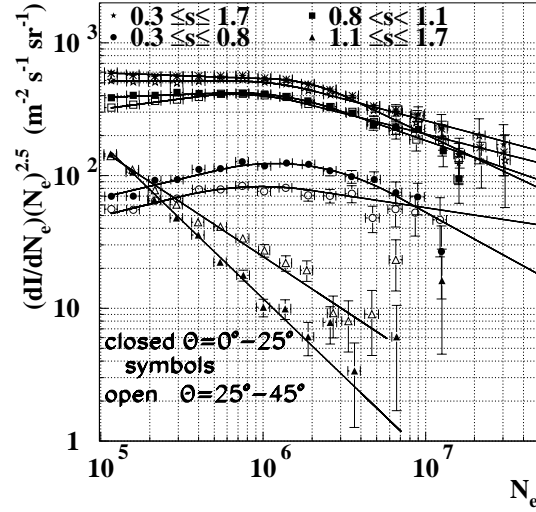


Figure 7: Differential EAS size spectra for different angular and age ranges.

Table 1: Average age values and variances for different zenith angles ($\theta < 25^\circ$, $25^\circ \leq \theta < 45^\circ$, $\theta < 45^\circ$) and EAS sizes together with the values of the parameters A and $s(\theta = 0)$ of the parameterization of the $\sec \theta$ dependence.

N_e	$\theta < 25^\circ$		$25^\circ \leq \theta < 45^\circ$		$\theta < 45^\circ$		A	$s(0)$
	\bar{s}	σ_s	\bar{s}	σ_s	\bar{s}	σ_s		
1.6×10^5	0.96	0.15	0.98	0.15	0.97	0.15	$0.126 \pm .002$	$0.968 \pm .001$
4.0×10^5	0.92	0.13	0.95	0.13	0.93	0.13	$0.194 \pm .004$	$0.902 \pm .005$
9.7×10^5	0.89	0.11	0.93	0.12	0.91	0.12	$0.241 \pm .006$	$0.872 \pm .007$
2.4×10^6	0.88	0.10	0.92	0.11	0.89	0.11	$0.274 \pm .008$	$0.855 \pm .009$
6.0×10^6	0.87	0.11	0.92	0.12	0.89	0.11	$0.316 \pm .2$	$0.852 \pm .032$
$\geq 10^7$	0.93	0.14	0.96	0.14	0.94	0.14	$0.161 \pm .002$	$0.934 \pm .001$

Table 2: Spectral slopes ($dI/DN_e \propto N_e^{-\gamma}$) and knee positions for different ranges of the age parameter values.

θ	s	γ_1	γ_2	$\log(N_e^{knee})$
$0^\circ - 25^\circ$	0.3 - 1.7	2.54 ± 0.03	3.08 ± 0.03	6.30
	0.8 - 1.1	2.45 ± 0.03	2.92 ± 0.07	6.13
	0.3 - 0.8	2.21 ± 0.03	3.17 ± 0.14	6.31
	1.1 - 1.7	3.68 ± 0.08		
$25^\circ - 45^\circ$	0.3 - 1.7	2.50 ± 0.02	2.82 ± 0.04	6.08
	0.8 - 1.1	2.34 ± 0.03	2.81 ± 0.05	5.93
	0.3 - 0.8	2.20 ± 0.02	2.70 ± 0.07	5.91
	1.1 - 1.7	3.31 ± 0.07		

5 Variation of the age with the observation depth

Figure 8 shows the dependence of the mean age $\bar{s}(\theta)$ of particular EAS sizes from the zenith angle θ , as linear dependence from $\sec \theta$.

The parameters $\bar{s}(0)$ and A, adjusted to the $\sec \theta$ dependence are given in Table 1.

With increasing N_e the slope A increases while $\bar{s}(0)$ is decreasing. There is a good agreement with the values of Ref. [1] obtained for $N_e = 2.4 \cdot 10^6$. The values averaged over all EAS sizes are $A = 0.161 \pm 0.002$ and $\bar{s}(0) = 0.934 \pm 0.001$. With the approximate relation $\sec \theta = X/X_v$ where X_v is depth of the observation level and X the transverse atmospheric thickness (grammage) A can be related to the change $d\bar{s}/dX$ of the average age with X. With the average value of A inferred from the data for the observation level $X_v = 700 \text{ g/cm}^2$ a value $d\bar{s}/dX = 2.3 \cdot 10^{-4} \text{ cm}^2/\text{g}$. This result can be compared with $d\bar{s}/dX = 3.4 \cdot 10^{-4} \text{ cm}^2/\text{g}$ given in [1]. A compilation [1] of the data from the literature yields a range $d\bar{s}/dX = (1.9 - 4.3) \cdot 10^{-4} \text{ cm}^2/\text{g}$. Associating the depth of the shower maximum X_m with $\bar{s} = 1$, we reach the relation

$$\bar{s} - 1 = \frac{d\bar{s}}{dX} \cdot (X - X_m), \quad (1)$$

Thus an evaluation of the N_e dependence of $\Delta X = (X - X_m)$ carries some information about the elongation rate, as already indicated by Linsley [14].

6 Concluding Remarks

The present results deduced from the data of the MAKET-ANI array are in good agreement with theoretical expectations. The analyses reveal that:

- Average age parameter gradually decreases with increasing shower size from 10^5 to 10^6 , and for

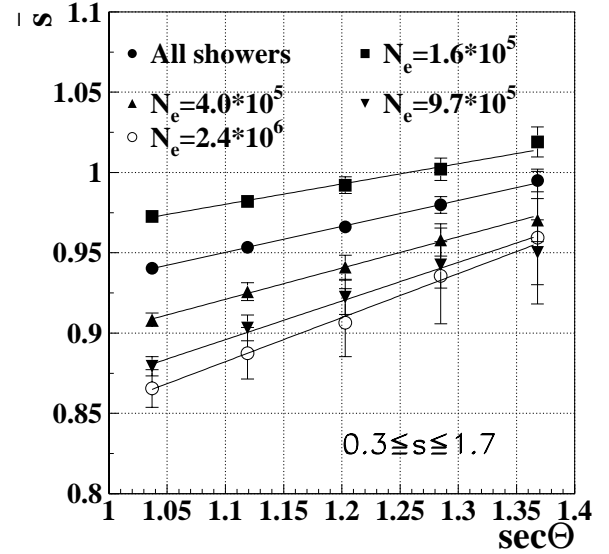


Figure 8: The dependence of the mean age \bar{s} from the zenith angle of EAS incidence for various shower sizes.

$N_e > 10^6$ it becomes almost constant.

- The knee of "young" showers is sharper than knee of the all particle spectra.
- The size spectra classified by different ages show different attenuation.
- The change of age parameter with the zenith angle of EAS incidence can be related to the change of the EAS maximum with N_e .

Acknowledgment

The report is based on scientific results of the ANI Collaboration. The MAKET-ANI installation on Mt. Aragats has been setup as a collaboration project of the Yerevan Physics Institute (Armenia) and the Lebedev Physics Institute (Moscow). The continuous contributions and assistance of the Russian colleagues in operating of the installation and in the data analyses are gratefully acknowledged. In particular, we thank Prof. S. Nikolski and Dr. V. Romakhin for their encouraging interest to this work and useful discussions.

We would like to thank Prof. Dr. H. Rebel pointing on the importance of the elongation rate estimation, Dr. A. Haungs and Dr. Kh. Sanosyan for useful remarks. Corrections and suggestions made by Dr. S. Ostapchenko are highly appreciated. The assistance of the Maintenance Staff of the Aragats Cosmic Ray Observatory in operating the MAKET-ANI installation is highly appreciated. The work has been partly supported by the ISTC project A116.

References

- [1] S. Miyake et al., Proc. 16th ICRC (Kyoto) **13** (1979) 171
S. Miyake et al., Proc. 17th ICRC (Paris) **11** (1981) 293
B.S. Acharya et al., Proc. 17th ICRC (Paris) **9** (1981) 162
- [2] J. Kempa and M. Samorski, J.Phys. G: Nucl. Part. Phys. **24** (1998) 1039
- [3] G.B. Khristiansen et al., Proc. AS USSR, Phys. **35** (1971), 2107 (in Russian)
G.B. Khristiansen et al., Proc. 17th ICRC (Paris) **6** (1981) 39
N.N. Kalmykov et al., Proc. 25th ICRC (Durban) **6** (1997) 277
- [4] V.V. Avakian et al., Soviet J. Nucl. Phys. **56** (1993) 183 (in Russian)
- [5] G.V. Gharagozyan for the ANI Collab., Proc. of the Workshop ANI 98, eds. A.A. Chilingarian, H.Rebel, M. Roth, M.Z. Zazyan, FZKA 6215, Forschungszentrum Karlsruhe 1998, p.51
- [6] A.A. Chilingarian et al., ANI Workshop 1999, these proceedings, p.83
- [7] K. Asakimori et al., Proc. 17th ICRC (Paris) **11** (1981) 301
T. Hara et al., Proc. 17th ICRC (Paris) **6** (1981) 52
K. Asakimori, Proc. 21st ICRC (Adelaide) **3** (1990) 129
- [8] N.N. Kalmykov, S.S. Ostapchenko and A.J. Pavlov, Nucl. Phys. B (Proc.Suppl.) **52B** (1997) 17
- [9] S.S. Ostapchenko, private communication
- [10] A. Vardanyan et al. - KASCADE Collaboration, ANI Workshop 1999, these proceedings, p.23
- [11] S.I. Nikolsky, Proc. 25th ICRC (Durban) **6** (1997) 105
- [12] A.A. Chilingarian et al., ANI Workshop 1999, these proceedings, p.43
- [13] R. Glasstetter et al. - KASCADE Collaboration, Proc. 25th ICRC (Durban) **6** (1997) 157
- [14] J. Linsley, Proc. 15th ICRC (Plovdiv) **12** (1977) 89

Lateral Distribution Functions for EAS Charged Particles

A. Haungs^{1*} for the KASCADE Collaboration[†]

¹*Institut für Kernphysik, Forschungszentrum Karlsruhe, Germany*

Since the first measurements of extended air showers the lateral distributions of the charged particles are most frequently considered observables and starting point of further analyses like the estimation of a total number of muons and electrons in the showers or toward the determination of the chemical composition. A historical overview on the different functional forms used for fitting the measurements will be given. The differences and similarities of the distributions for different particle components are discussed in context of actual applications at the KASCADE experiment.

1 Introduction

Cosmic Rays with energies larger than $\approx 10^{14}$ eV are measurable only indirectly by Earth bounded experiments through secondary particle detection of an extended air shower (EAS). EAS are produced in the Atmosphere by a cascading process of interactions of the primary cosmic ray and its subsequently successors with air molecules (Fig.1). The resulting measurable particle components of an EAS are the electromagnetic, the hadronic and the muonic part. In general electromagnetic and muonic particles are added to the so-called charged component of the EAS. As the atmosphere can be regarded as a calorimeter, measurements of the total number of particles at a certain observation level is strongly correlated with the primaries energy. As most of the charged particles are electrons (with $\approx 10\%$ muons at sea level) the electron or charged number was the experimental access to the energy in most of the Earth bounded experiments. The estimation of the particle number in the EAS requires spot tests of densities in a (as large as possible) certain range of the lateral extinction of the EAS. Arrays of detector stations fulfill

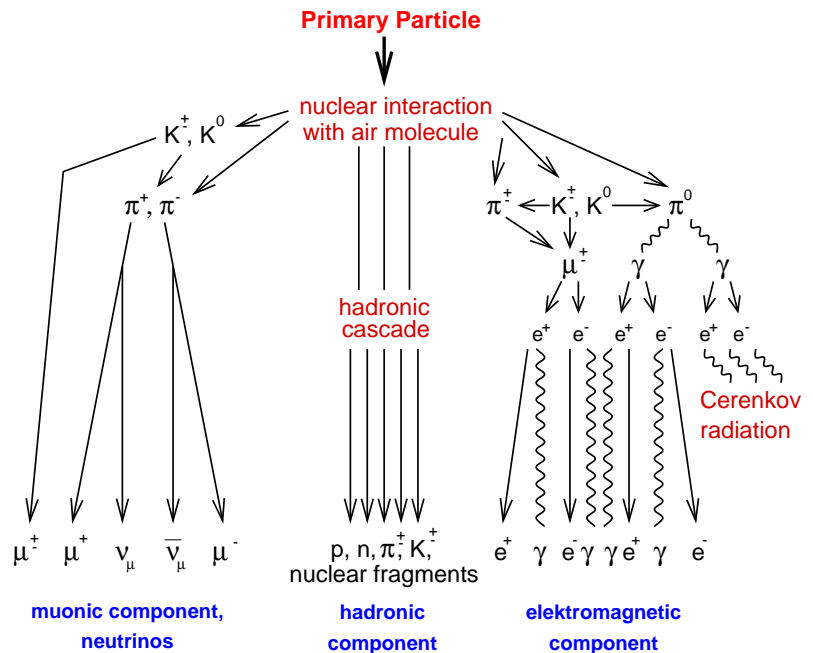


Figure 1: *Schematic view of EAS development at the Atmosphere.*

* corresponding author: haungs@ik3.fzk.de

[†] full collaboration list see at the end of these proceedings

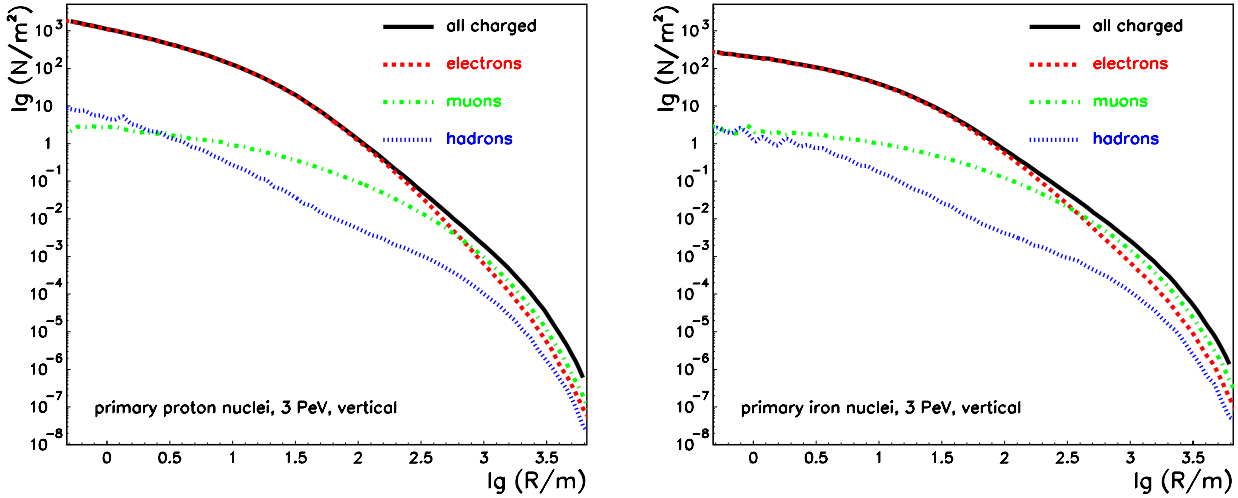


Figure 2: Mean lateral distributions of charged particles in proton and iron induced showers of same energy and zenith angle. The distributions are obtained by CORSIKA [1] simulations (QGSJET [2]).

these requirements; detector size,

observation level and grid size quantify the accessible primary energy range. Additional informations about the muon content measured by underground or shielded detectors are usually used for the mass determination of the cosmic rays.

Taken these spot tests of densities, a well fitting functional dependency to the lateral density distribution is searched (Fig.2). An Integration over the total range of core distance of this LDF results in the so-called shower size, i.e. total number of particles. Beneath the energy range of the primaries different questions intend the LDF: Which secondary EAS component are measured by the used detectors? What is the energy threshold of the measured particles? What kind of detectors are used? In which range of the core distances are the detectors placed?

The experiences of a half of century of earthbound EAS experiments shows the difficulties to find a global function for all experiments, the whole energy range, or for all zenith angles of the primaries. After a historical overview on used functions in the past, the situation of the LDF's at KASCADE will be explained and discussed.

2 Historical Overview

2.1 Electrons, Charged Particles

The shapes of the lateral distributions of different charged particles in showers are described mainly by functions which led to the first type Euler integrals (plus some modifications) or by exponential functions.

For the density function of charged particles there were:

-) The Nishimura–Kamata–Greisen approximation [3, 4]

$$\rho_{ch}(r)dr = \frac{N_{ch}}{2\pi r_0^2} \cdot C \cdot \left(\frac{r}{r_0}\right)^{s-2} \cdot \left(1 + \frac{r}{r_0}\right)^{s-4.5} dr, \quad (1)$$

where

s - so called age parameter which describes the shape of the particle distribution,

r_0 - Moliere unit (= 79 m at the sea level)

N_{ch} - total number of charged particles,

$C = \frac{\Gamma(4.5-s)}{\Gamma(s)\Gamma(4.5-2s)}$, Γ - gamma function.

This approximation is widely used in cosmic ray experiments; for electrons only and for charged particles. The NKG function is based on a theoretical approach to describe a pure electromagnetic shower in the atmosphere. It was very soon known that this function cannot describe a hadronic shower in perfect, therefore the search for a more global function was motivated.

-) Greisen approximation [5, 6, 7]

$$\rho_{ch}(r)dr = \frac{N_{ch}}{2\pi r_0^2} \cdot C_1 \cdot \left(\frac{r}{r_0}\right)^{s-2} \cdot \left(1 + \frac{r}{r_0}\right)^{s-4.5} \cdot \left(1 + C_2 \left(\frac{r}{r_0}\right)^d\right) dr, \quad (2)$$

where $C_1 = [B(s, 4.5 - 2s) + C_2 B(s + d, 4.5 - d - 2s)]^{-1}$, and in Greisen's paper $C_2 = 1/11.4$ and $d = 1$; B is the Euler-function.

-) function, which was used for the investigations of large showers in Akeno [8]

$$\rho_{ch}(r)dr = \frac{N_{ch}}{2\pi r_0^2} \cdot C_3 \cdot \left(\frac{r}{r_0}\right)^{s-2} \cdot \left(1 + \frac{r}{r_0}\right)^{s-4.5} \cdot \left(1 + \beta \frac{r}{r_0}\right)^\nu dr, \quad (3)$$

for which a general integral from zero to infinity does not exist.

-)Some Russian experiments (e.g. [9]) used the following approximation:

$$\begin{aligned} \rho_{ch}(r)dr &= \frac{1.75 \cdot 10^{-3} N_{ch}}{r} \exp -\frac{r}{80} dr & ; & \quad \text{for } r = 3 - 140 \text{ m} \\ \rho_{ch}(r)dr &= 2.25 \cdot N_{ch} r^{-2.8} dr & ; & \quad \text{for } r = 140 - 1000 \text{ m} \end{aligned}$$

For the majority of early investigations the so called total electron number was accepted as a total number of charged particles $N_e \approx N_{ch}$. A modification was introduced by Greisen 1960 [5] to formula (1) in attempt to take into account the role that muons play at large distances from the axis in EAS. Some attempts were also made at mountain level (Chacaltaya 5.2 km asl) to modify the formula (1) in order to obtain a better description of average lateral distributions of charged particles in showers [10]:

$$\begin{aligned} \rho_{ch}(r)dr &= \frac{1.03 \cdot N_{ch} \cdot C_1}{2\pi r_0^2} \cdot \left(\frac{r}{r_0}\right)^{s-2} \cdot \left(1 + \frac{r}{r_0}\right)^{s-4.5} \cdot \\ &\quad \left(1 + C_2 \left(\frac{r}{r_0}\right)^2\right) \cdot \left(1 - 0.2 \cdot \exp \frac{-\left(\ln \frac{r}{r_0} + 0.3\right)^2}{0.5}\right) dr, \end{aligned} \quad (4)$$

where C_1 and C_2 are constants, their values obtained from the best experimental fit.

The formula (4) is the best illustration of the problems which were met by experimental physicists when they made attempts to describe the lateral distribution of charged particles in showers by one universal function - a function describing the lateral distribution of all charged particles in showers.

2.2 Muon Component

The shape of the function of the lateral distribution of muon density in the showers with both different total number of particles N_{ch} and different threshold energies of muons E_μ (GeV) was given by Greisen 1960 [5]:

$$\rho_\mu(r)dr = \frac{14.4 \cdot r^{-0.75}}{\left(1 + \frac{r}{320}\right)^{2.5}} \cdot \left(\frac{N_\mu}{10^6}\right)^{0.75} \cdot \frac{51}{E_\mu + 50} \left(\frac{3}{E_\mu + 2}\right)^{0.14r^{0.37}} dr, \quad (5)$$

where E_μ describes the muon energy threshold in GeV.

Following functional form has also been used for an approximation of the lateral distribution of muons in different experiments [11, 12]:

$$\rho_\mu(r) \propto r^{-\alpha} \exp - \frac{r}{r_0} dr. \quad (6)$$

More or less complicated factors are added depending on the experimental setup (e.g. observation level, muon threshold energy and range of investigated core distance). For example at Tien-Shan [13]:

$$\rho_\mu(r) = 5.95 \cdot 10^{-4} r^{-0.7} \exp - \frac{r}{80} dr.$$

2.3 Hadrons

Lateral distributions of hadrons in EAS with energies greater than a threshold energy E_h are usually approximated by the function:

$$\rho_h(r)dr = A \cdot \exp - \left(\frac{r}{r_0}\right)^\kappa dr. \quad (7)$$

Or in some experiments (e.g. [14]) simply by

$$\rho_h(r)dr = A \cdot \exp - \frac{r}{r_0} dr. \quad (8)$$

In the region of a threshold energy of $E_h = 100 \text{ GeV} - 10 \text{ TeV}$ a coefficient κ may change in the interval $\kappa = 1.0 - 0.25$ [15]. At the threshold 100 GeV the value $\kappa = 0.8$ was obtained from the very first measurements in KASCADE [16] for the showers initiated by primary nuclei with energy about $E_0 = 10^{14} \text{ eV}$. It is characteristic for hadrons that for energies above 100 GeV they concentrate near the shower axis and their density at the distance of about 10 m decreases almost three orders of magnitudes with respect to the densities measured in the shower core area. The observed densities of charged particles in this region of showers may be overestimated considering local interactions of hadrons in (or over) the detector which may lead to a production of secondary particles.

3 LDF at KASCADE

The experimental setup of KASCADE [17, 18] was chosen to optimize the estimation of the electron and muon number simultaneously for each single triggered shower. Detailed Monte Carlo simulations (including detector simulations) were used to search the best functions for the determination of the shower size N_e and the muon number N_μ at the EAS. Nevertheless averaged lateral distributions of the different particle components (electrons and hadrons and muons with different energy detection thresholds) are used for verifications and for comparisons with other experimental results.

3.1 Single Showers

Figure 3 shows an example of a single shower as measured by the KASCADE array detectors. Each point shows the reconstructed density of electrons or muons in the detector stations. The estimation of these densities are the result of an iterative process: as the muon detectors are placed directly below the electron detectors, a first rough estimation of the muon density is used for the reduction of the charged particle density leading to an electron density. Additionally by help of lateral correction functions won by Monte Carlo simulations a correction of punch-through effects of the EAS gamma component is performed.

The function used for the lateral fit is for both particle components the NKG function. The total number of electrons, the shower age and the core position are the resulting parameters of the procedure for the electrons. Fitting the distribution of the muon component the age of the NKG function is fixed to roughly 0.75 with a small dependence from N_e . The Moliere unit is chosen 79 m for the electron LDF and 420 m for the muon LDF, respectively. The lateral distribution of the electron component is fitted for the core distance range between 10 m and 200 m and integrated from zero to infinity. For the muon component it was found by simulations, that the largest differences of the lateral distribution between different masses are at far core distances, where is anyway no experimental excess. On the other hand the muon content (N_μ^{tr}) between 40 m (above the uncorrectable punch-through of electrons and hadrons in the muon detectors) and 200 m is independent from the primary mass, but roughly linear with the primaries energy [19]. Both numbers, N_e and N_μ^{tr} , can be estimated with an uncertainty of less than 8% in the PeV region.

3.2 Average LDF

To reveal general shower properties lateral density distributions in average for a large sample of showers are estimated for all different particle components [20].

In the case of the KASCADE experiment (electron identification, observation at sea-level, primary PeV region, measurement of electron densities up to 250 m core distance) the NKG function represents the electron lateral density distribution very well in all angular ranges (Fig.4). At PeV showers below 10 m core distance the mean lateral distributions are affected by saturation effects in spite of the large dynamical range of the detectors. At 10 PeV the saturation affects the distribution up to 40m core distance.

With help of the large hadron calorimeter of the KASCADE experiment it is possible to measure

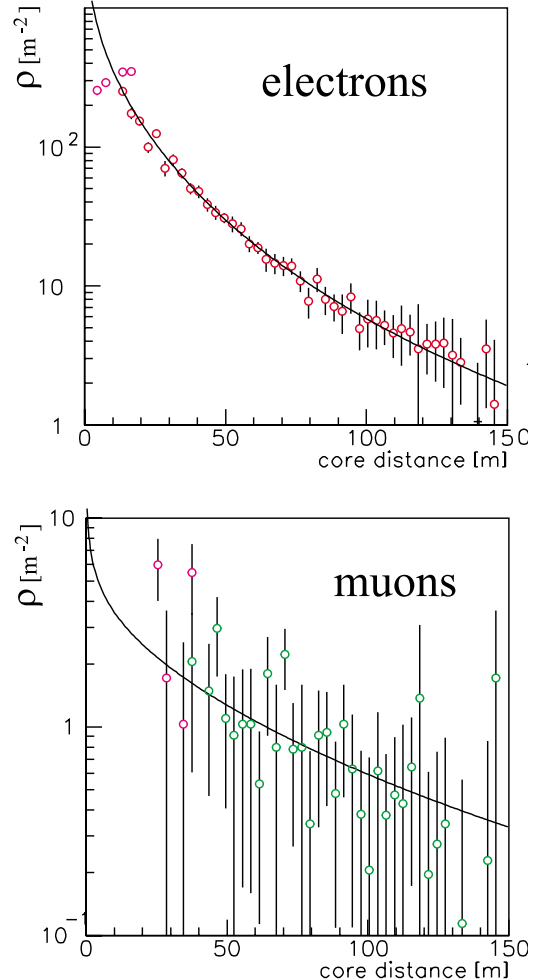


Figure 3: *Example of the measured particle densities of a single extended air shower as measured by the KASCADE detector array. The lines indicate the result of the fit of the NKG function to the measured densities.*

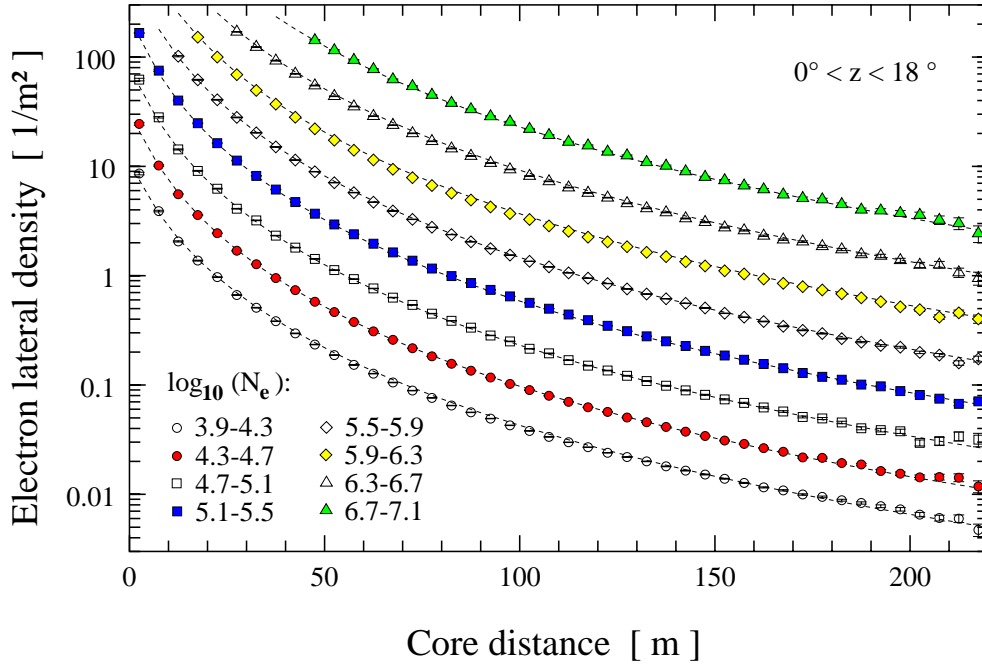


Figure 4: Mean electron lateral distributions for showers in the zenith angular range $10^\circ - 18^\circ$ grouped for different N_e (estimated per single shower) covering primary energies from ≈ 100 TeV to 100 PeV. The lines represent fits by the NKG function.

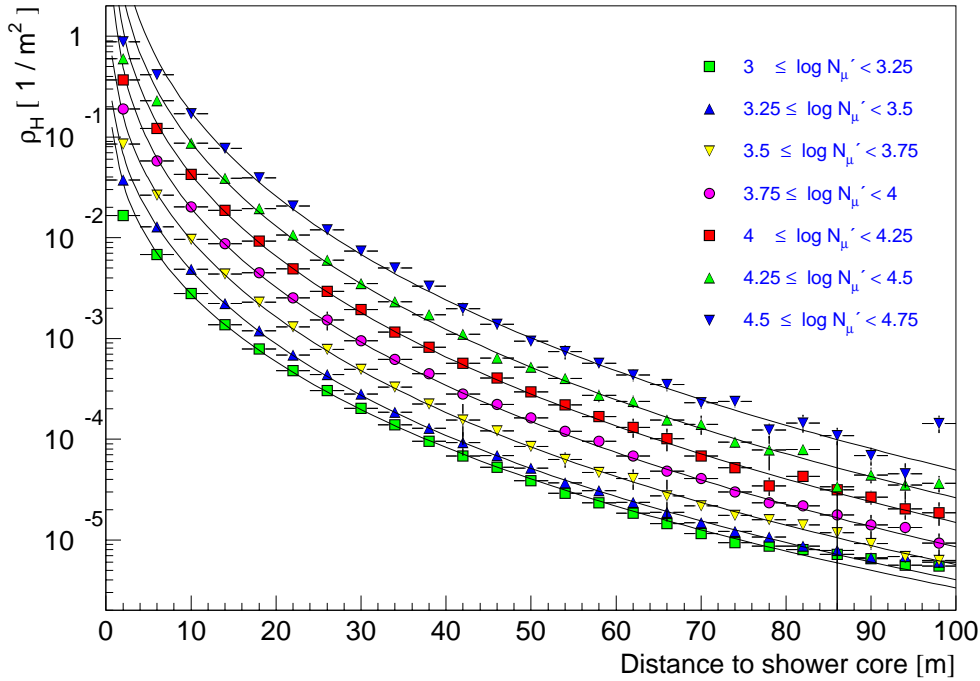


Figure 5: Mean lateral distribution of hadrons for different ranges in N_μ^{tr} for a hadron threshold of 50 GeV. The lines represent fits by the NKG function [21].

lateral distributions of hadrons for core distances up to 100 m (Fig.5). Due to the strong correlation of the hadronic to the electromagnetic component in the shower development the NKG function is well fitting the LDFs, too. But the Moliere unit has to be decreased to $R_m = 10$ m to fit the steep

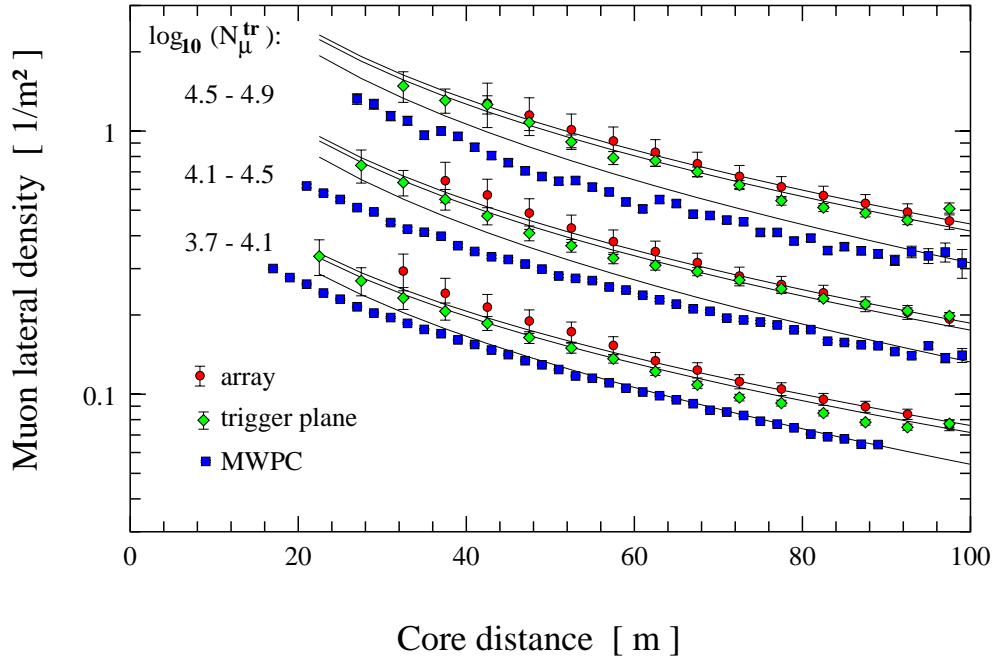


Figure 6: Mean lateral distributions of muons for three different energy thresholds for showers grouped in different ranges of N_{μ}^{tr} . The lines represent Greisen functions; it results from fits to the distributions from the array muons and expected distributions by the different energy thresholds using Monte Carlo simulations.

decrease of the lateral distribution.

In case of muons the KASCADE experiment with its multi detector setup has the possibility to measure muons with different energy thresholds:

1. For vertical showers the array muon scintillators register muons above $E_{\mu} = 250$ MeV at a total sensitive area of 622 m².
2. The scintillator layer of the central detector (trigger layer, 208 m²) allows muon measurements for $E_{\mu} > 400$ MeV.
3. A setup of two layers of multiwire proportional chambers (MWPC) at the basement of the central detector allows with a spatial resolution of ≈ 1.5 cm the reconstruction of muons with $E_{\mu} > 2000$ MeV. The total sensitive area of the chambers are 122 m².

A further component (a muon tunnel setup with towers of limited streamer tubes which is being built) will be able to track muons with a threshold of ca. 1000 MeV.

Fig.6 shows examples of the reconstructed mean lateral distributions for all three thresholds obtained with the different detector components. The different starting points of the distributions reflects the core distance where the punch-through corrections of the electromagnetic and hadronic EAS components have too large uncertainties. All muon density distributions in the range up to 100 m are describable by the functions mentioned above. The density distributions of the lowest muon threshold (array) are fitted by the so-called Greisen muon function (Fig.6). Using the muon content obtained by CORSIKA Monte Carlo simulations (QGSJet) expected lateral distributions for the other thresholds are calculated and included in the plot. It is seen, that the small differences between the threshold of

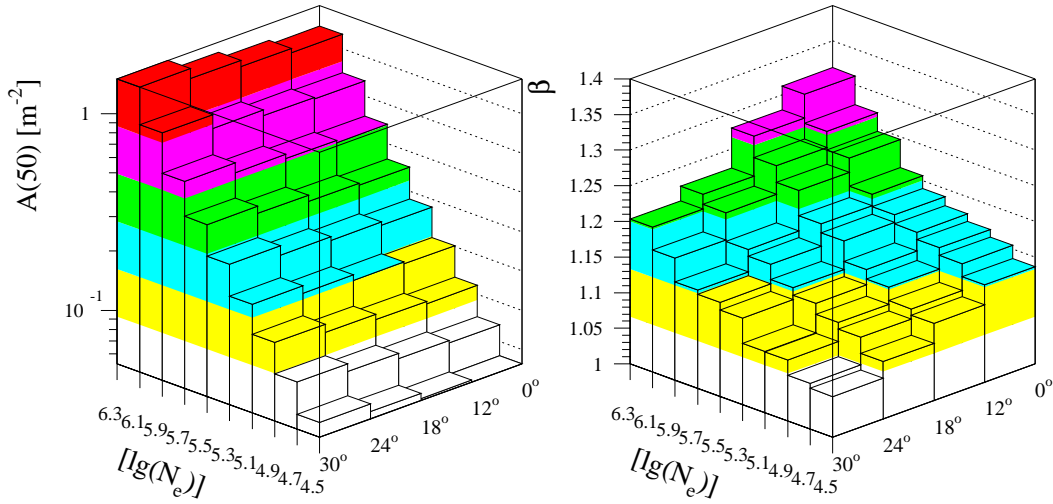


Figure 7: Dependencies of the normalization and slope parameters from the shower size and shower angle. Density distributions fitted by the "Hillas" function ($E_\mu = 250$ MeV).

trigger plane and array are reflected by the simulations. This is not valid for the muons measured by the MWPC system. Either the measurements have systematic uncertainties or the energy distribution of muons in the simulations do not reflect the reality. Different other observations prefer the latter argument of a unrealistic simulation of the EAS development [21], especially at higher primary energies, as seen in Fig.6.

For the following analysis the lateral muon density functions are fitted by the so called Hillas function:

$$\rho_\mu(r) \propto \left(\frac{r}{r_0}\right)^{-\beta} e^{-\frac{r}{r_0}} dr.$$

The chosen value r_0 is optimized by minimizing the chi-square for all distributions (all zenith angle and shower size ranges) [22]. It results for the different thresholds to $r_0 = 600$ m (250 MeV), $r_0 = 200$ m (400 MeV), and $r_0 = 100$ m (2 GeV). As free parameters of the fit the muon content at 50 m core distance ($A(50)$) as normalization parameter and the slope parameter β is chosen. Fig.7 shows the dependencies of these parameters from shower size and angle in case of the lowest threshold energy. As expected the muon content ($A(50)$) increase with larger shower size and zenith angle: Larger shower size im-

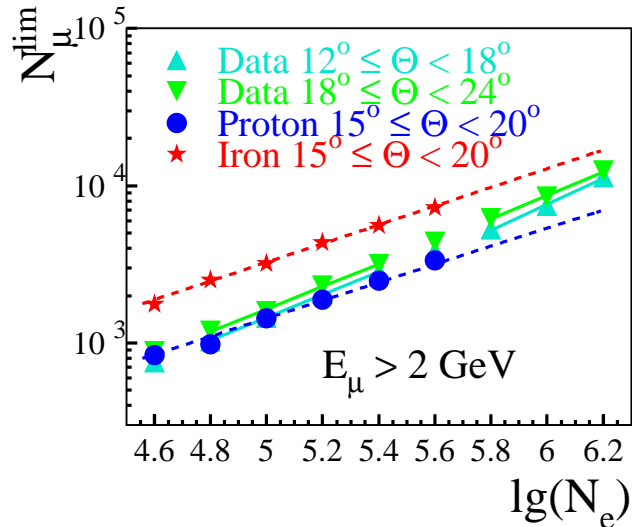


Figure 8: Correlation of the muon to electron number for high-energy muons of the KASCADE experiment compared with the result of detailed EAS simulations for different primary masses.

plies a higher primary energy, more inclined showers with same shower size have larger primary energy due to the higher absorption of the electromagnetic component in the atmosphere. The lateral distributions are steeper (increasing β) for smaller angles and larger sizes. As deeper the maximum of the shower development in the atmosphere (higher primary energy or more vertical) as deeper the muons are produced and as closer to the shower axes they reach the surface detectors. These are general features of the muon component of EAS and are found and confirmed by a lot of experiments [22].

The correlations between the electron number and muon number of EAS is known as a powerful mass estimator [23]. We investigate the correlation with help of the mean muon lateral density distributions by an integration of the Hillas function in a limited range of core distance (20m-100m). The resulting N_μ^{lim} is shown in Figure 8 (2 GeV threshold) versus the mean shower size N_e in comparisons with correlations obtained by detailed simulations for proton and iron induced primaries. The lines represent fits of power law functions. The data show a kink in the power law at the position of the knee at the KASCADE N_e size spectra, providing a change of the composition at the knee region. Investigating the mass composition at KASCADE uses more detailed multiparameter analyses, but as a confirmation or check of other results such a average view to the general features of the cosmic rays in the "knee" region is still useful.

4 Conclusions

The search for a global function describing the lateral distribution of particles in extensive air showers is motivated by the strong correlation of the total particle number to the primary energy of the incoming particle.

As the lateral density distributions at each experiment depend on the identification and energy threshold of the detected particles, on the range of the accessible core distance, on the shielding of the detectors, and on the energy, mass and angle of incidence of the primaries, a global function seems not possible and even not useful. Therefore comparisons of lateral distributions at different experiments seems to be very complicated.

In case of the KASCADE experiment all lateral distributions, measured for first time for electrons, muons at different thresholds and for hadrons, are describable by the NKG-function. But other functions historically used are in principle (for the muon lateral distributions) usable.

An estimation of particle numbers per single shower (i.e. fit of the lateral distribution and integration) is highly preferable to analyse the data on event-by-event methods [18]. Mean lateral distributions are used for consistency checks, mainly.

Acknowledgement

Thanks to Konrad Bernlöhner for reconstructing KASCADE lateral distributions in a very accurate way and to Janusz Kempa for the transmission of his large historical knowledge about the cosmic ray physics. The author will also appreciate Tina Asantiani for the educational discussions during the workshop.

References

- [1] D. Heck et al., FZKA 6019, Forschungszentrum Karlsruhe 1998
- [2] N.N. Kalmykov and S.S. Ostapchenko, Yad. Fiz. **56** (1993) 105

- [3] K. Greisen, Progress in Cosmic Ray Physics 3, North Holland Publ. (1956)
- [4] K. Kamata and J. Nishimura, Prog. Theoret. Phys. Suppl. **6** (1958) 93
- [5] K. Greisen, Ann. Rev. Nucl. Sci. **10** (1960) 63
- [6] T. Koneko et al., 14th ICRC (Munich) **8** (1975) 2747
- [7] T.K. Gaisser and T. Stanev, Phys. Rev. D **1** (1996) 122
- [8] M. Nagano et al., J. Phys. G: Nucl. Part. Phys. **10** (1984) 1295
- [9] S.N. Vernov et al., Proc. of the Moscow Cosmic Ray Conference (1960) Vol.II p.7 (English Edition).
- [10] C. Aguirre et al., J. Phys. G: Nucl. Part. Phys. **5** (1979) 139
- [11] A.M. Hillas et al, 11th ICRC (Budapest) **3** (1970) 533
- [12] G.B. Khristiansen et al., 15th ICRC (Plovdiv) **8** (1977) 148
- [13] J.N. Stamenov et al., TRUDY FIAN SSSR **109** (1979) 132
- [14] P.D. Acton et al., 21th ICRC (Adelaide) **9** (1990) 264
- [15] J. Kempa, Il Nuovo Cimento **31 A** (1976) 581
- [16] J. Unger, FZKA 5896, Forschungszentrum Karlsruhe 1997
- [17] H.O. Klages et al. - KASCADE Collaboration, Nucl.Phys.B (Proc.Suppl.) **52B** (1997) 92
- [18] A. Haungs et al. - KASCADE Collaboration, ANI Workshop 1999, these proceedings, p.31
- [19] J.H. Weber et al. - KASCADE Collaboration, Proc. 26th ICRC (Salt Lake City) 1999, HE 2.2.42
- [20] T. Antoni et al. - KASCADE Collaboration, in preparation for submitting to Astroparticle Physics, 1999
- [21] T. Antoni et al. - KASCADE Collaboration, Journ. Phys. G: Nucl. Part. Phys. **25** (1999) 2161
- [22] A. Haungs et al. - KASCADE Collaboration, FZKA 6263, Forschungszentrum Karlsruhe 1999
- [23] P.R. Blake and W.F Nash, J. Phys. G: Nucl. Part. Phys. **24** (1998) 217

Lateral Distributions of EAS Muons at Different Thresholds Energies, Bundles and Horizontal Muon Events

A.A. Chilingarian¹, A.V. Darian¹, V.S. Eganov¹, V.A. Ivanov^{1*}, N.M. Nikolskaya²,
V.A. Romakhin², V.V. Subbotin²

¹*Yerevan Physics Institute, Alikhanian Brothers St., 375036 Erevan, Armenia*

²*P.N. Lebedev Institute, Leninsky pr., Moscow, Russia*

The aim of the present analysis is the experimental determination of the ratio of average muon densities with threshold energies of 2.5 GeV and 5 GeV, respectively at different distances from the core of extensive air showers (EAS). It is shown that the measured values are consistent with expectations of Greisen's approximation. The muon lateral distribution for $E_\mu > 1$ GeV evaluated from the measurements by Greisen's approximation agree well with data of the EAS-TOP experiment for corresponding shower parameters. Additionally the possibility of the detection of muon bursts with the muon detectors of the GAMMA array is discussed.

1 Introduction

The lateral distribution of EAS muons depends from the energy thresholds with which the muons are registered by the particular detector facilities. For a determination of the N_μ/N_e ratio, to be comparable with the results of other experimental installations, the distributions should be related to a uniform threshold energy. The present experimental studies are prompted by the specific situation of the GAMMA installation [1] of the ANI Cosmic Ray Observatory on Mt. Aragats, Armenia, where the underground installation of muon detectors appears with different thresholds varying between 2.5-6.0 GeV. Actually a reliable muon detection and an accurate determination of the muon lateral distribution function (MLDF) for EAS is a delicate experimental task, involving a careful consideration of the experimental influences on the detection efficiency and mis-identification of muon events. Thus with too small and too widely spaced detector arrays the inherent EAS fluctuations do dominate the results by effects which are not taken into account by the parameterisations of the average behaviour. In addition high energy gamma rays or hadrons ("punch-through") penetrating near the shower axis and secondary particle production by electromagnetic and nuclear cascades in the absorber and detector material, faking or obscuring bundles, lead to difficulties in identifying muon events. Accompanied by detailed detector response studies the underground scintillation detector array would allow to study these influences [2].

For preparing the experimental basis of the MLDF studies the accumulated EAS data have been grouped along various ranges of the shower size N_e and the zenith angles of EAS incidence, and the muon densities $\rho_\mu(r)$ have been averaged over defined intervals of the distance r from the shower centre.

There are various forms of the MLDF en vogue for fitting the lateral distribution by adjusting the parameter values by the least-square method e.g. to fit the data.

The Greisen parameterisation [3]

$$\rho_\mu(r) = C \cdot r^{-n} \cdot (1 + r/r_0)^{-b}, \quad (1)$$

*corresponding author: ivanov@crdlx5.yerphi.am

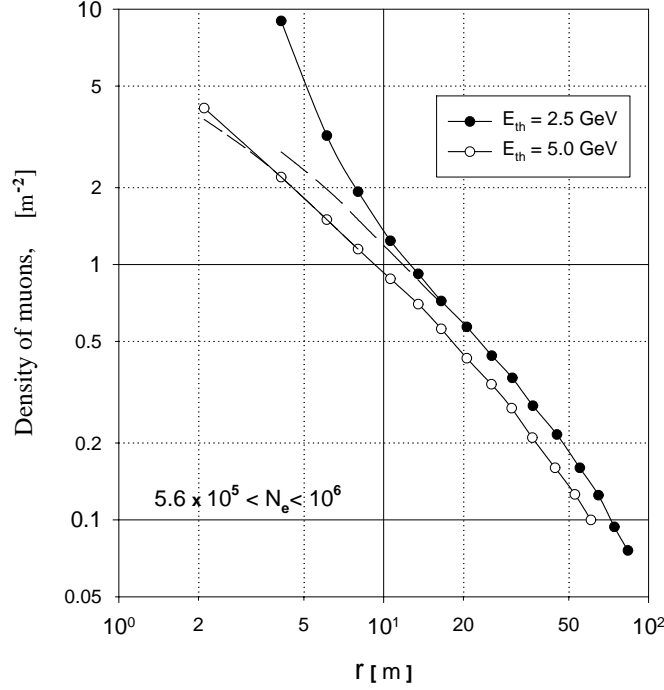


Figure 1: *Lateral density distributions of EAS muons for two different thresholds. The lines are drawn to guide the eyes. At small radii the experimental problems of muon detection near the shower axis are indicated. The dashed curves are fits for $r > 10$ m by the Greisen form.*

with the parameter values: $n = 0.5 - 0.75$, $r_0 = 280 - 460$ m and $b = 2.5$ is preferentially used. Alternatively the Hillas function [4] (with parameter values: $n = 0.45 - 0.86$, $r_0 = 80 - 600$ m)

$$\rho_\mu(r) = C \cdot r^{-n} \cdot \exp(-r/r_0), \quad (2)$$

has been used. Figure 1 displays an example.

The aim of the present studies is to determine the experimental ratio of the average muon densities with two energy thresholds and to relate the observations to results obtained with other thresholds.

2 The muon density ratio for different detection thresholds

In literature there are various experimental studies reported [5, 6, 7, 8] which result in parameterisations of the dependence of the total muon number $N_\mu(E_\mu; N_e)$ from the energy threshold E_μ and the EAS size N_e . The empirical form for the MLDF extracted from those studies are given by following expressions

$$\rho_\mu(r; E_\mu, N_e) = 14.4 \cdot r^{-0.75} \cdot (1 + r/320)^{-2.5} \cdot (51/(50 + E_\mu)) \cdot (3/(E_\mu + 2))^{0.14 \cdot r^{0.37}} \cdot (N_e/10^6)^{0.75} \quad (3)$$

for $1 < E_\mu < 20 \text{ GeV}$ and $20 < r < 100 \text{ m}$, (see ref. [5, 6]), and

$$\rho_\mu(r; E_\mu, N_e) = 1.4 \cdot 10^4 \cdot r^{-0.55 \cdot \varepsilon^{0.1}} \cdot (E_\mu + 250)^{-1.4} \cdot \exp(-r \cdot \varepsilon^{0.62}/80) \cdot (N_e/10^6)^{0.78} \quad (4)$$

for $5 < E_\mu < 500 \text{ GeV}$; $2.5 < r < 100 \text{ m}$ and $\varepsilon = (E_\mu + 2)/12$, (see ref. [8]).

Due to the constructive peculiarities of the underground arrangement of muon detection installation

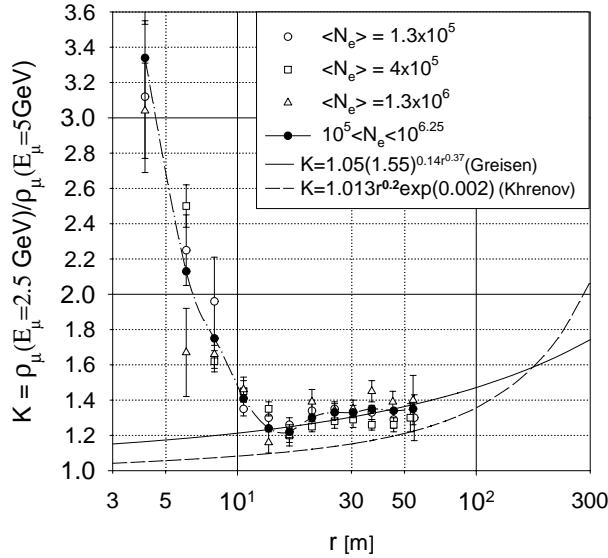


Figure 2: The lateral distribution of the ratio K of the muon densities for the energy thresholds $E_\mu = 2.5$ GeV and $E_\mu = 5.0$ GeV and for various EAS sizes as compared with expectations of parameterisations [8, 9].

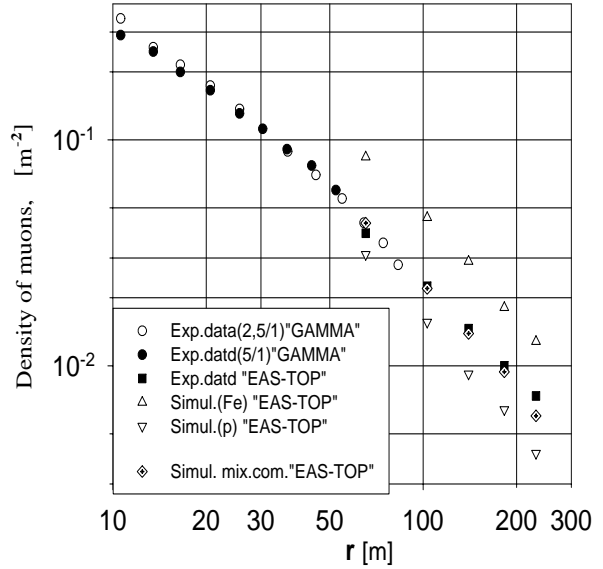


Figure 3: Comparison of the muon lateral distribution observed by the GAMMA and EAS-TOP [10] experiments and with simulations for $N_e = 10^5 - 10^{5.3}$.

of the hall and tunnel of the GAMMA array [1] the actual muon energy threshold varies between various groups of the detectors (in the hall from 4.7 to 6.0 GeV). In order to minimise systematic effects in the comparisons of the data with calculations according eq.3 two particular groups of detectors (located at the boundaries of the two underground units: hall and tunnel) are selected whose data are grouped in two samples of different well defined threshold energies (and the same detector area S). The two data samples are characterised by:

1. $\langle E_\mu \rangle \geq 2.5$ GeV; $5^\circ < \theta < 30^\circ$; $180^\circ < \varphi < 360^\circ$; $S = 15$ m²;
2. $\langle E_\mu \rangle \geq 5.0$ GeV; $5^\circ < \theta < 30^\circ$; $0^\circ < \varphi < 180^\circ$; $S = 15$ m².

Figure 2 shows the comparisons. The data at distances $r < 15$ m from the shower centre are certainly affected by above indicated detector effects not accounted for. For $R > 15$ m the Greisen parameterisation [9] fits fairly well. The data can be described by

$$K = 1.05 \cdot (1.55)^{0.14 \cdot r^{0.37}}. \quad (5)$$

and it proves to be superior to the alternative of Ref. [8]. There appears no significant dependence from N_e in the considered range.

In Figure 3 our results are scaled by the Greisen parameterisation to the energy threshold $E_\mu = 1.0$ GeV and compared with results of the EAS-TOP experiment [10] and to EAS simulations (in equivalent ranges of the zenith angles and N_e). Unfortunately the overlap and the lateral ranges of both experiments is small, but nevertheless indicative for the consistency.

The deviations of both GAMMA results at small radii may be explained by "punch-through" effects.

3 Muon bundles and horizontal muon events

During the investigation of the EAS muon density distributions, also the bundles and jets (or local showers) of penetrating particles, with several hundreds up to several thousands per m^2 have been detected. Examples of such events are displayed in Figure 4. The number of such events is less than 0.1 per cent of the total number of the registered EAS and their spatial distributions can be associated to muon jets, with a small number accompanying electromagnetic particles. For more detailed study of such anomalous muon jets a special "muon" trigger has been developed and implemented, permitting a more efficient multi-muon event selection. The observation of events of a similar character have been recently reported by the ALEPH group in CERN [11].

With the same trigger, apart from the muon bundles and jets, "aligned events" of intriguing character have been registered (Figure 4). These events can be explained by the horizontal muon flux, selected by the specific trigger conditions. The expected intensity of such events can be estimated from the data measured by horizontal muon spectrometers [12, 13] for zenith angles of $\approx 89^\circ$. The estimated result confirms this assumption with a good accuracy. On the other hand such events can be used to check the linearity of ADC codes, the average magnitude of which should correspond to energy deposit corresponding to ca. 20 particles traversing the scintillator in vertical direction ($100 \cdot \sec(\theta)/5 = 20 \sec(\theta)$).

Only "pure" events going without any accompaniment have been included in the data analysis, and the number of working detectors lying in the straight line should not be less than three. The relation between measured code (C) and corresponding number of particles (n_μ), is fitted by the expression:

$$C = 10 \cdot \ln(n_\mu) + 5.7. \quad (6)$$

Obtained distributions and the transition function "code - number of particles" are shown in Figure 5. It is obvious that "aligned events" really correspond to muons passing with large zenith angles, and that the ADC used in the experiment, gives a globally correct, unbiased estimation of number of particles (in particular in the interval of codes from 5 up to 64).

4 Summary and concluding remarks

The measured lateral distribution of $K(E_\mu = 2.5 \text{ GeV}/E_\mu = 5 \text{ GeV})$ can be empirically described by $K = 1.05 \cdot (1.55)^{0.14 \cdot r^{0.37}}$. The relation is recommended for further applications. For the more detailed and exact determination of the ratio $\rho_\mu(r, E_{\mu 1})/\rho_\mu(r, E_{\mu 2})$ with various threshold energies, it would be favourable to locate a part of muon detectors to the center of the hall in order to minimize the systematic errors arising from the details of the underground building structure. Particularly interesting would be an arrangement of a part of detectors at a different place, inside and under the

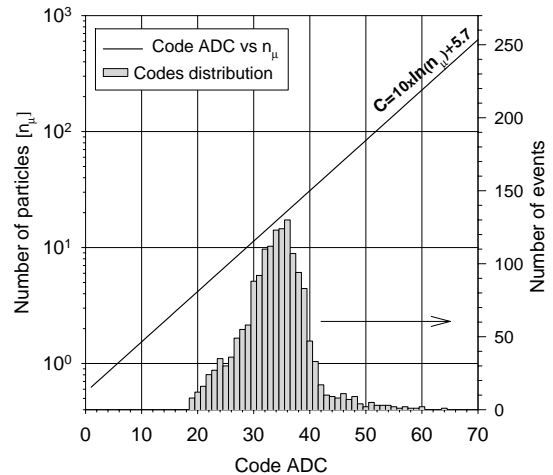


Figure 5: "Code ADC - Number of particles" transition function, and the distribution of the codes for horizontal muons.

magnet yoke of the uncompleted ANI muon spectrometer [14], in order to study both the MLDF and the energetic characteristics of the individual muon jets in the range of the threshold energies of 4.7, 7.0 and 10 GeV.

Moreover it would be of importance to set up the muon hodoscope by the trigger of the "MAKET" facility. The development of such a trigger would facilitate to determine the total number of the shower muons with improved accuracy, due to an extended range of the studied MLDF (from 15 up to 300 m). In addition, such a trigger would help to investigate methodical problems of studies of muon groups and their spatial distributions.

Acknowledgement

The authors are very grateful to Prof. Dr. H. Rebel and Dr. A. Haungs for carefully reading the manuscript and helpful comments. We thank also Dr. Kh. Sanosyan for the help in preparation of the manuscript. The work has been partly supported by the research grant No. 96-752 of the Armenian Government and by the ISTC project A-116.

References

- [1] A.A. Arzumanian et al., Proc.24th ICRC (Rome) **1** (1995) 482
A.A. Chilingarian et al., Proc. Workshop ANI 98, eds. A.A. Chilingarian, H. Rebel, M. Roth, M.Z. Zazyan, FZKA Report 6215, Forschungszentrum Karlsruhe (1998), p.27
See also ibid. H.-J. Mathes et al., p.91
- [2] M.Z. Zazyan and A. Haungs, Proc. Workshop ANI 98, eds. A.A. Chilingarian, H. Rebel, M. Roth, M.Z. Zazyan, FZKA Report 6215, Forschungszentrum Karlsruhe (1998), p.37
A. Haungs, F. Badea and M.Z. Zasyan: <http://www-ik3.fzk.de/~haungs/ares/ares.html>
- [3] K. Greisen, Annual Review of Nucl. Sci. **10** (1960) 63
- [4] A.M. Hillas, Nucl. Phys. B (Proc. Suppl.) **52B** (1997) 29
- [5] S. Hayakawa, Cosmic Ray Physics, Nuclear and Astrophysical Aspects, John Wiley and Sons (1969)
- [6] E.V. Bugaev, Yu.D. Kotov, I.L. Rozental, Cosmic muons and neutrinos, ATOMIZDAT Moscow (1970) 120 (in Russian)
- [7] J.C. Earnshaw et al., Proc. Phys. Soc. **90** (1967) 91
- [8] B.A. Khrenov, Thesis for the Ph.D. Degree of the MSU, Moscow (1986) 147 (in Russian)
- [9] S. Benett and K. Greisen, Phys. Rev. **124** (1961) 1982
- [10] M. Aglietta et al., Astroparticle Phys. **10** (1999) 1;
Preprint of EAS-TOP Coll., INFN/AE-96/16
- [11] CosmoLEP Collaboration, CERN COURIER Vol.39, Num.8, Oct.1999, p.31
- [12] S. Matsuno et al., Phys. Rev. **D 29** (1984) 1
- [13] T.L. Asatiani et al., Izvestiya AN USSR, Physics **49** (1985) 1377 (in Russian)
- [14] T.L. Asatiani, V.A. Ivanov, E.A. Mnatsakanian, VANT, Tech. of Phys. Exper. Iss. **2/8/**, Kharkov, USSR (1981) 77;
T.V. Danilova et al., Izv. AN Arm. SSR, Physics, 17, **3-4** (1982) 208

Simulation Study of the Lateral Distributions of the Muon and Electromagnetic EAS Components on Mt. Aragats Altitude

J.-N. Capdevielle¹, Kh.N. Sanosyan^{2*}

¹*LPCC, College de France, Paris, France*

²*Cosmic Ray Department, Yerevan Physics Institute, Yerevan, Armenia*

Various features of the lateral distributions of the muon and electromagnetic EAS components have been studied on basis of simulated EAS for different detection thresholds for the observation level of the Cosmic Ray Laboratory on Mt. Aragats. The Monte Carlo simulations use the CORSIKA program (version 5.62) with the QGSJET model as generator for the hadronic interactions.

1 Introduction

A thorough understanding, analyses in terms of EAS observables and even some calibration procedures of the data accumulated with the detector facilities [1, 2] operated in the ANI Cosmic Ray Laboratory on Mt. Aragats, Armenia, require the comparison with realistic Monte-Carlo simulations of the EAS development. These necessities are the motivation for a series of extensive Monte Carlo calculations for the case of the ANI observation level (3200m a.s.l., latitude: N40.47°, longitude: E44.18°) allowing a detailed study of various shower variables and of their correlations. In the present contribution results of the analysis of the simulated lateral distributions of various EAS components are communicated.

2 Simulation procedures

The EAS simulations used the Monte Carlo code CORSIKA (version 5.62) [3, 4] for calculating proton and iron induced showers for four different energy intervals: $(1.5 - 5.0) \cdot 10^5$ GeV, $5.0 \cdot 10^5 - 1.5 \cdot 10^6$ GeV, $(1.5 - 5.0) \cdot 10^6$ GeV, and $5.0 \cdot 10^6 - 1.5 \cdot 10^7$ GeV.

As generator of the high energy hadronic interactions the option of the QGSJET model [5] has been chosen, while for the low energies the GEISHA model has been invoked. The electromagnetic component is treated with the NKG approximation as well as optionally with the EGS4 procedure. In the latter case a thinning procedure [6] has been applied with a thinning factor of 10^{-4} . Effects due to thinning have been controlled by comparative calculations without thinning. Particles have been stored with energy thresholds above 0.3 GeV for hadrons, 0.1 GeV for muons and 3 MeV for electrons and gamma rays.

For the determination of the lateral distributions of the muons we consider two different muon energy thresholds of 2.5 GeV and 5 GeV. Within one bin of the primary energy the energy has been randomly chosen along the power law dependence of the spectrum with the spectral index of $\gamma = -2.7$. Similarly the angle of incidence is selected from the interval $0^\circ - 30^\circ$ in a way so that isotropic incidence is guaranteed.

It appears very crucial to take into account the effects of the magnetic field of the Earth. Introducing the coordinates of the Mt. Aragats station, the magnetic field components have been calculated

*corresponding author: khnko@crdlx5.yerphi.am

by the Geomagnetic Field Synthesis Program (Version 3.0) [7] with the results (1999): magnetic declination: 4d 41.1m, horizontal component: 25157 nT, vertical component : 41215 nT.

3 Lateral distributions

Lateral distributions of the simulated EAS have been calculated for circular radius bins of $\Delta r = 2$ m for distances of up to $r = 200$ m from the shower centre.

Figure 1 shows results for the muon lateral distributions of two different energy thresholds of muon detection. The values of the thresholds are suggested by the experimental situation of the underground muon detector installation on Mt. Aragats. Hardly surprisingly the intensity decreases with the energy threshold and increases with the primary energy and with the complexity of the primary particle. The energy dependence is separately displayed by normalised lateral distributions in Figure

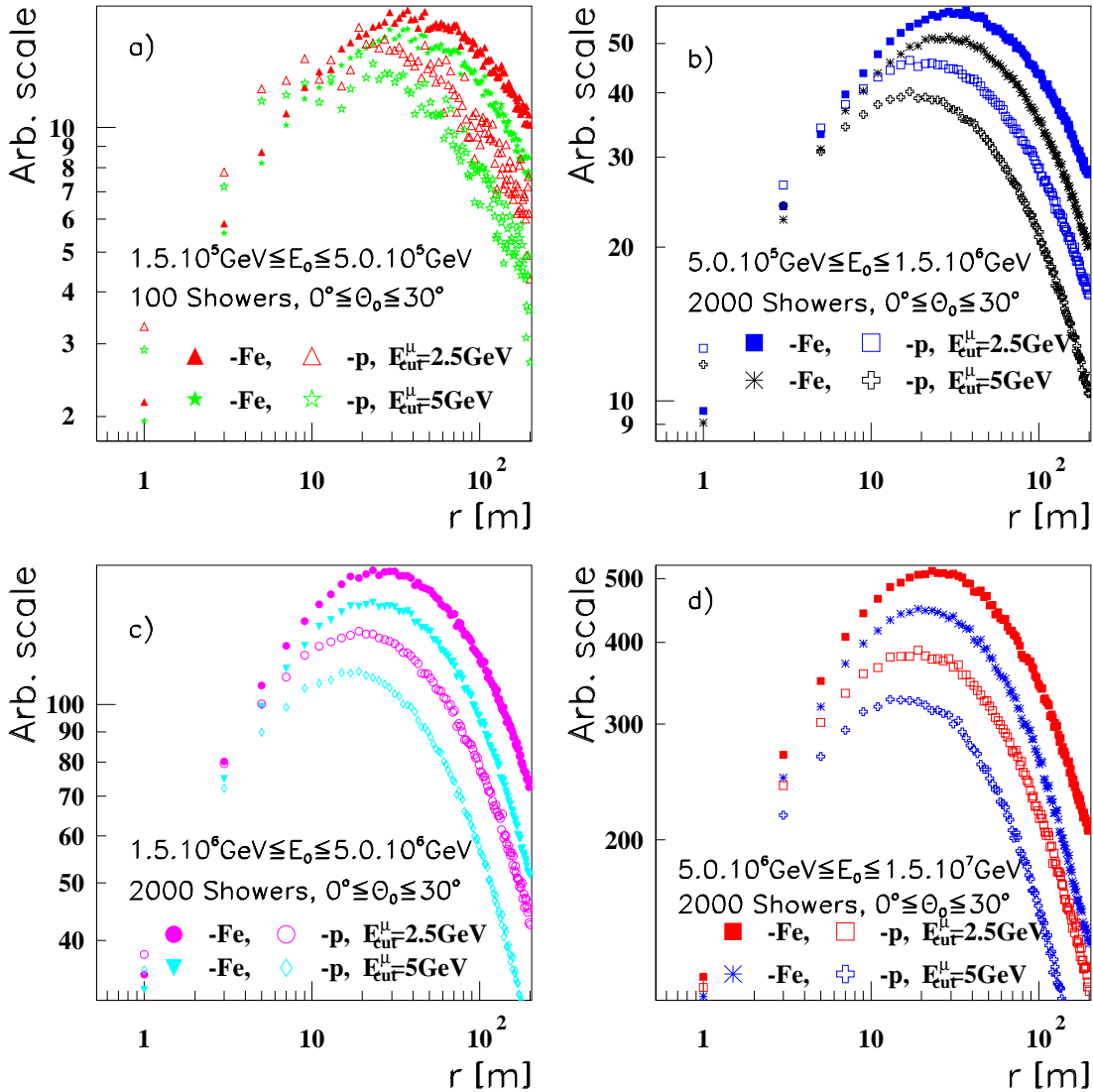


Figure 1: Lateral muon distributions for proton and Fe primaries of various energies and with different detection thresholds.

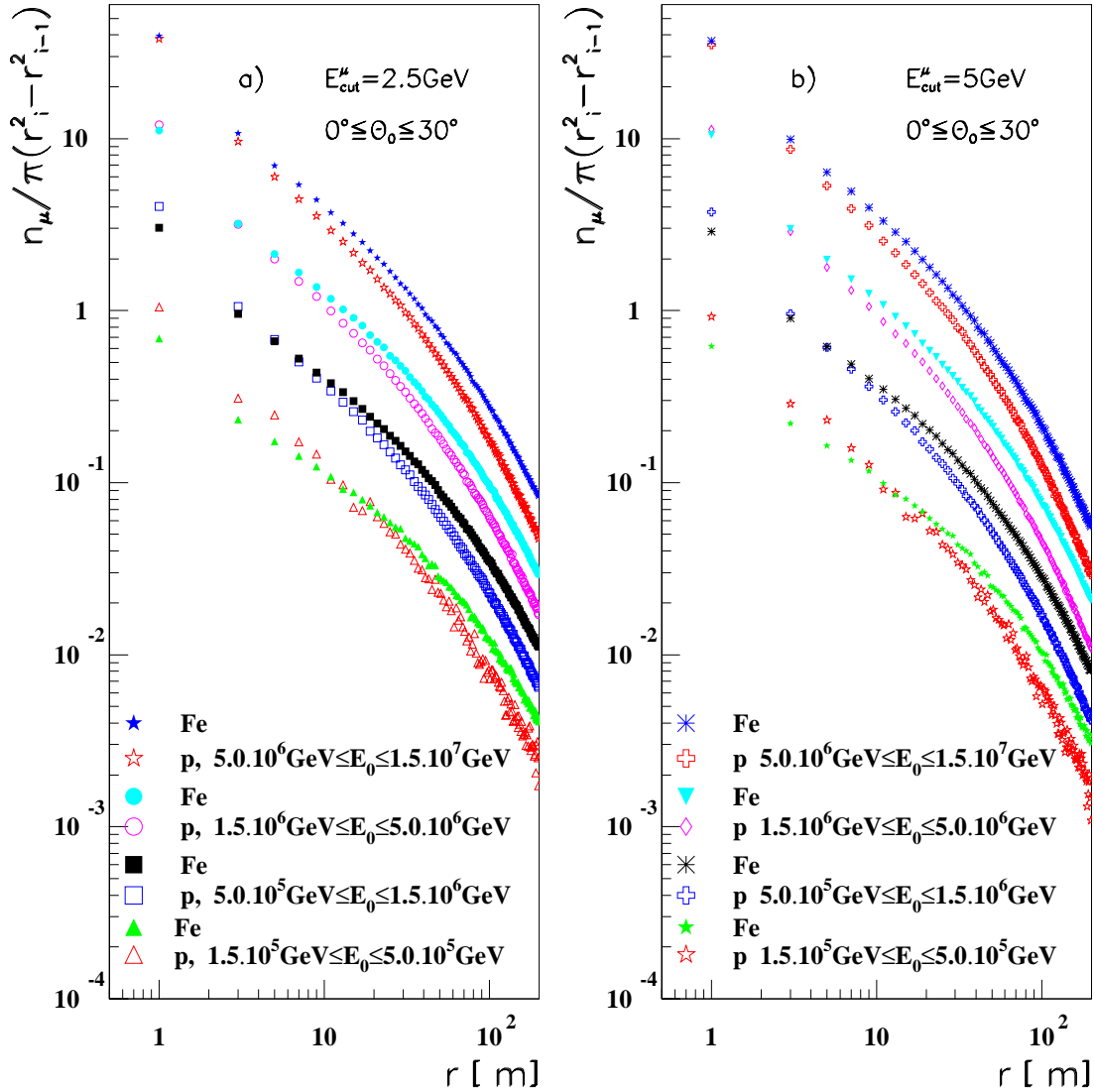


Figure 2: Muon lateral density distributions of proton and iron induced showers for various primary energies and two energy thresholds. Shown is the number n_μ of muons in a radial bin between r_{i-1} and r_i (i stands for the actual radius bin).

2. Some change in the slope of the distributions with energy is obvious, but also with the type of the primary. There appear "crossings" of the lateral density distributions at small radii for Fe and proton induced showers.

There is some interest in the ratio of the lateral muon density for different detection thresholds [8]. In Figure 3 the ratio is shown with 2.5 GeV and 5.0 GeV thresholds for p and Fe primaries of different energies.

The ratio increases with the distance from the shower centre faster for proton induced showers than for iron induced showers. The feature could already be inferred from Figure 1, showing the slower increase and the steeper decline of the higher energy EAS muons. The different rise for proton and Fe EAS may be explained by the fact that the average EAS development is determined by the energy per nucleon rather than by the total energy of the primary [9].

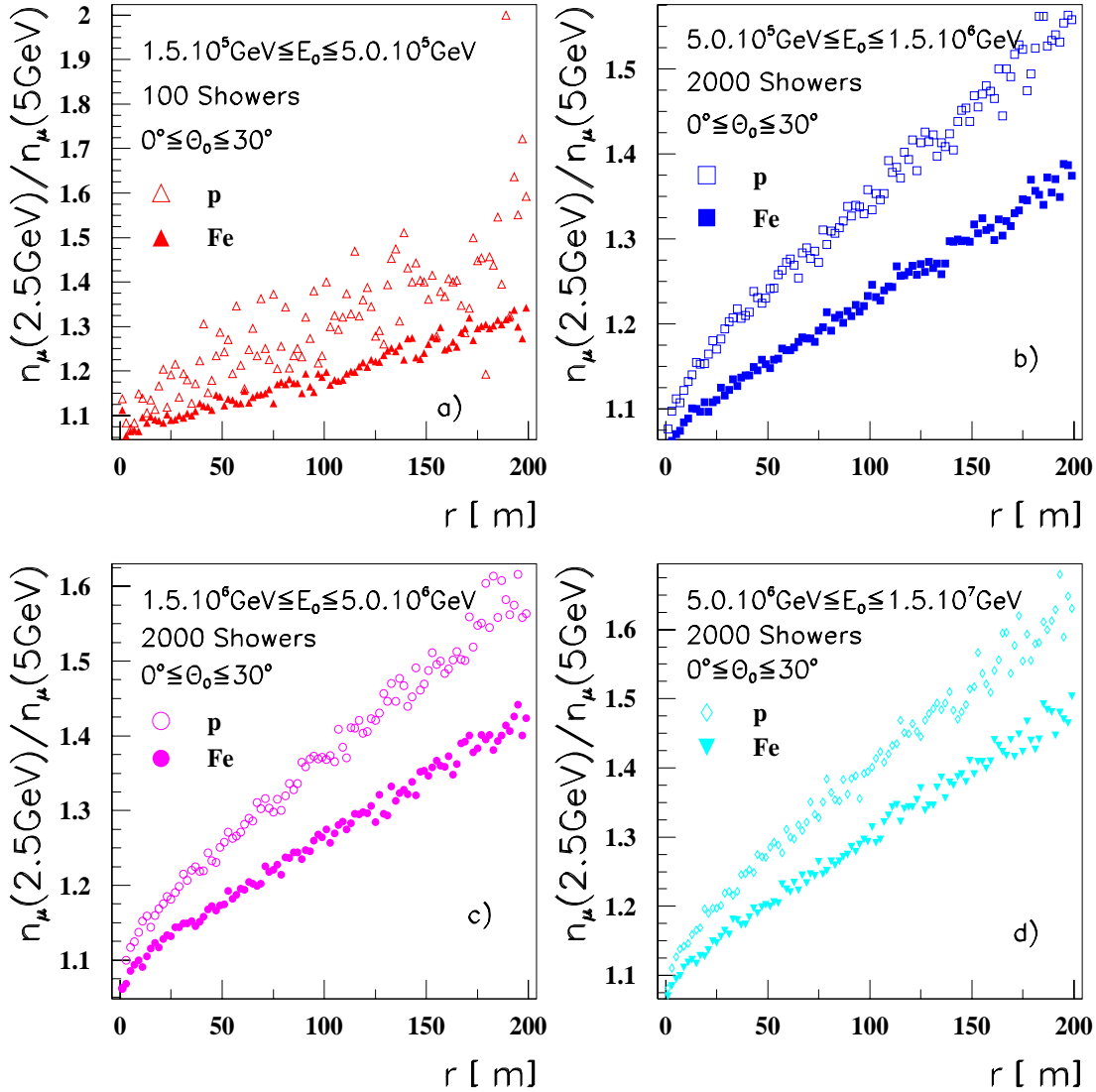


Figure 3: *The radial dependence of the ratio of the muon densities with two different detection thresholds (2.5 and 5.0 GeV) for proton and iron primaries.*

Figure 4 shows the lateral distributions of the ratio of the number of electrons to number of muons for different energies of the primaries and with different muon detection thresholds.

Again less surprisingly the ratio decreases due to a stronger concentration of the electromagnetic component at smaller radii.

Finally the distribution of the electromagnetic component is considered, in particular the ratio of photon and electrons (how it is predicted to appear at the particular observation level). This is shown for the above specified cases of different primary energies of iron and proton induced EAS.

The ratio is steeply decreasing with the radius, for protons steeper than for iron induced showers.

An energy dependence is not very pronounced. The well known fact of the dominance of the gamma quanta has experimentally prompted attempts to convert efficiently the gamma quanta in detectable electrons. Actually a quantitative knowledge of this ratio from simulations is of academic interest. For any comparison of experimental data the different detector responses of different set-ups would

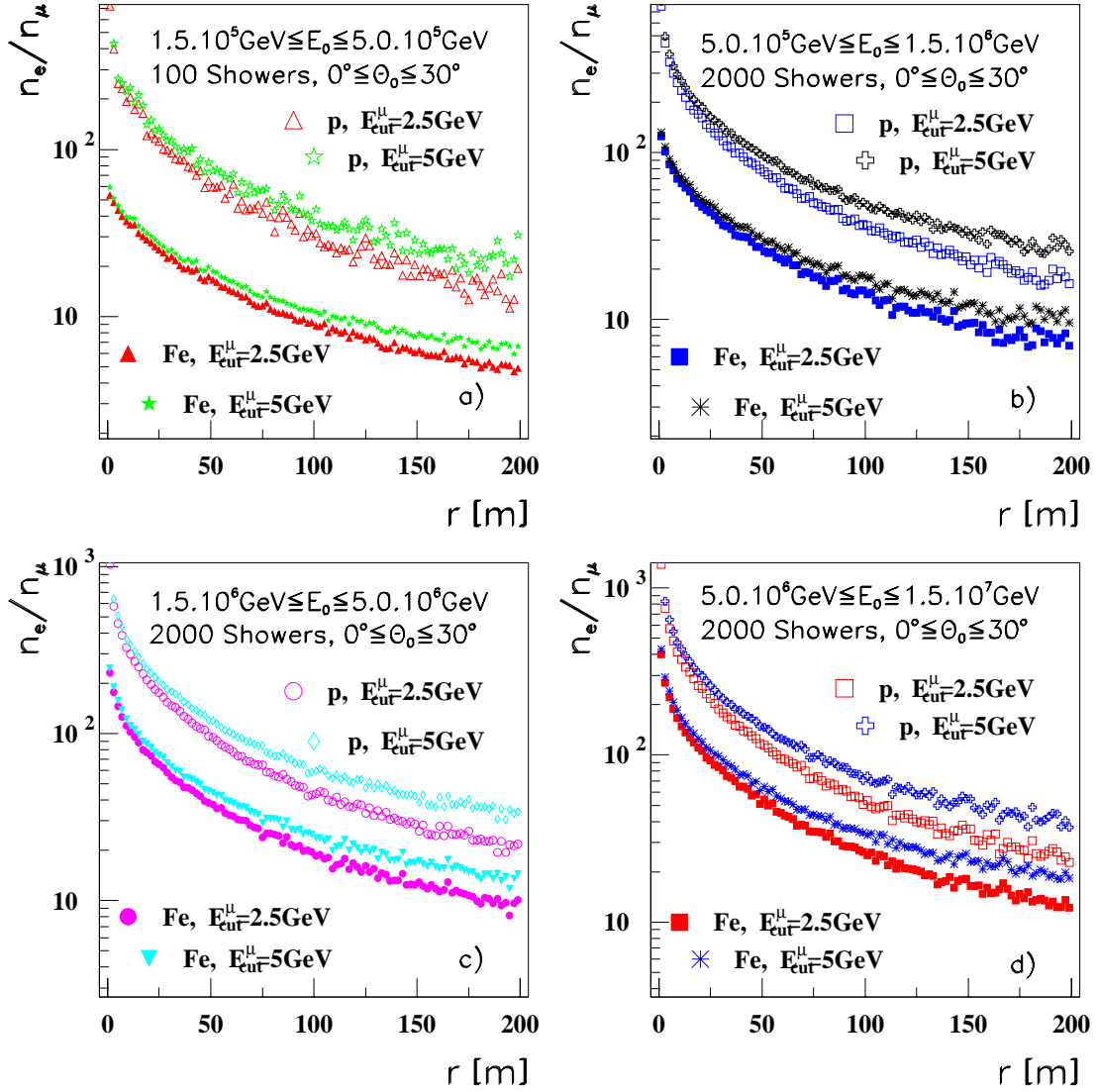


Figure 4: Lateral distributions of the ratio of the number of electrons to number of muons for different energies of the primaries and with different muon detection thresholds.

enter and influence the ratio.

4 Concluding remarks

With respect to the experimental possibilities for studies of the EAS muon component by the facilities installed underground in the ANI Cosmic Ray Laboratory on Mt. Aragats on high altitude, some features of the charge particle lateral distributions have been studied on basis of EAS simulations, in particular the distribution of the ratio of the number of muons at various thresholds. Actually this ratio may turn out as a further mass indicative observable in addition to the N_μ/N_e ratio. However, a *conditio sine qua non* of experimental studies of this kind is a detailed understanding of the detector efficiency and response to the detected particles. This quest implies the necessity of the development of a consistent detector simulation program, for which first steps for the ANI installations have been

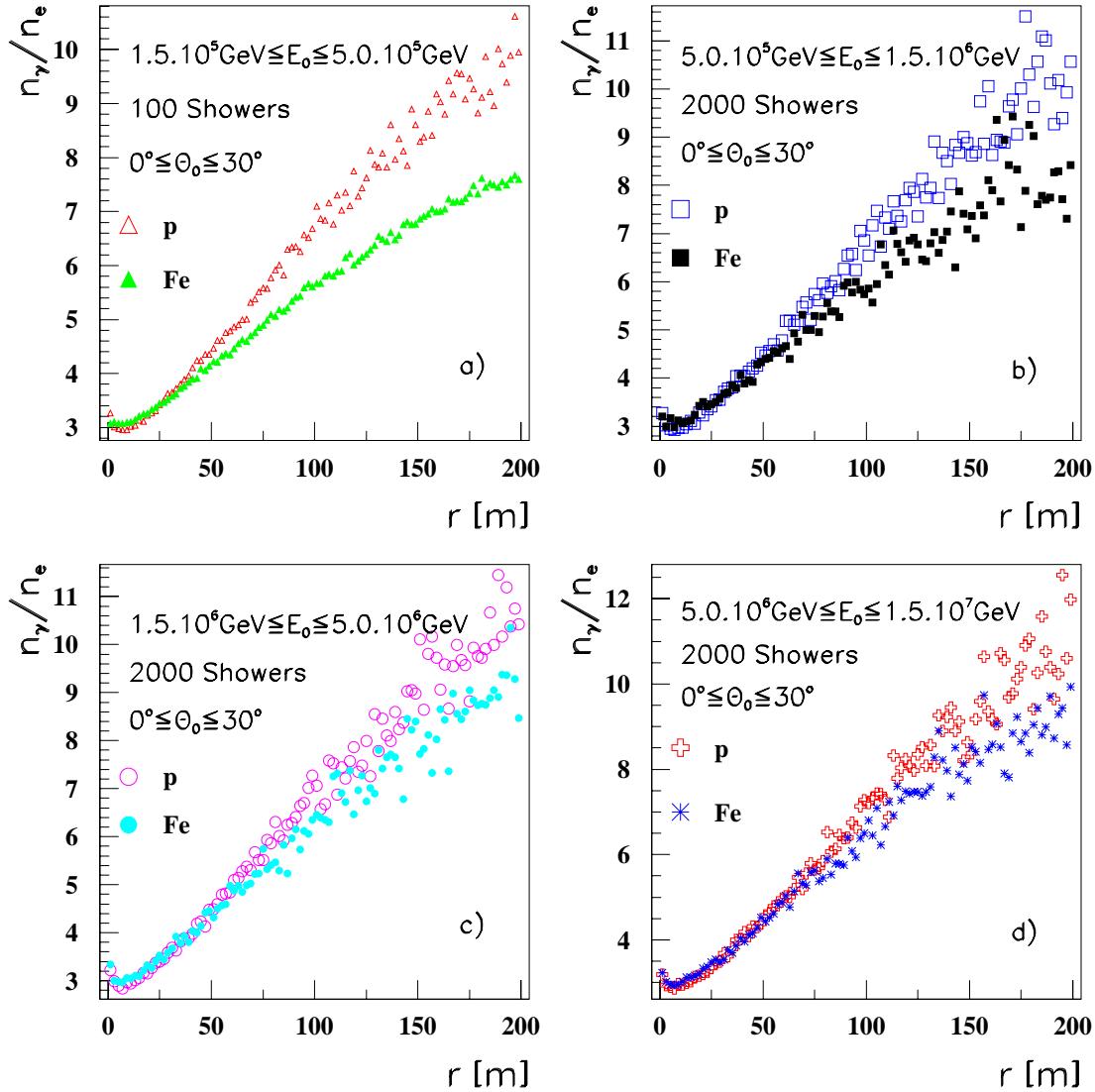


Figure 5: *The lateral distribution of the gamma/electron ratio.*

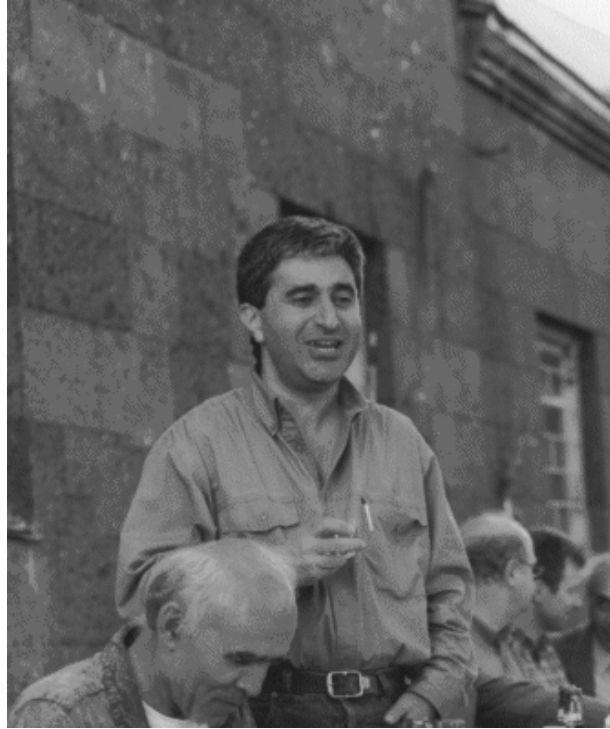
started by the ARES code [10]. Only by treating the CORSIKA simulations in this way a realistic comparison of the data and with results from other installations are useful and conclusive.

Acknowledgment

Kh.N.S. would like to thank Dr. D. Heck and Dr. J. Knapp for the kind introduction and familiarising him with many details of the CORSIKA code. We would like to thank Prof. Dr. A.A. Chilingarian, Dr. V.A. Ivanov and many colleagues of the ANI collaboration as well as our colleagues of the KASCADE group, in particular Prof. Dr. H. Rebel, Dr. A. Haungs and Dr. H.J. Mathes for many useful clarifications and stimulating discussions. The work has been partly supported by the ISTC project A116.

References

- [1] A. Chilingarian et al., ANI Workshop 1999, these proceedings, p.91
V.S. Eganov et al., ANI Workshop 1999, these proceedings, p.87
- [2] S.V. Blokhin, V.A. Romakhin and G.G. Hovsepyan, ANI Workshop 1999, these proceedings, p.111
A.A. Chilingarian et al., ANI Workshop 1999, these proceedings, p.53
- [3] J.-N. Capdevielle et al., KfK report 4998, Kernforschungszentrum Karlsruhe 1992
- [4] D. Heck et al., FZKA report 6019, Forschungszentrum Karlsruhe 1998
- [5] N.N. Kalmykov, S.S. Ostapchenko and A.I. Pavlov, Nucl.Phys.B (Proc.Suppl) **52B** (1997) 17
- [6] A.M. Hillas, Nucl. Phys. B (Proc. Suppl.) **52B** (1997) 29
- [7] Geomagnetic Field Synthesis Program: <http://www.ngdc.noaa.gov/seg/potfld/>
- [8] A.A. Chilingarian et al., ANI Workshop 1999, these proceedings, p.69
- [9] A.M. Hillas, Nucl. Phys. B (Proc. Suppl.) **28B** (1992) 67
- [10] A. Haungs, A.F. Badea and M.Z. Zazyan, ANI Workshop 1999, these proceedings, p.95



The EAS Electron Lateral Distribution as Observed with the MAKET-ANI Setup

A.A. Chilingarian, G.V. Gharagozyan, S.S. Ghazaryan, G.G. Hovsepyan,
E.A. Mamidjanyan, L.G. Melkumyan*, S.H. Sokhoyan
Yerevan Physics Institute, Cosmic Ray Division, Armenia.

The differential spectra of the electron density of Extensive Air Showers observed by the MAKET-ANI installation of the ANI Cosmic Ray Observatory are studied. The data stems from the registration period from August 1997 to March 1999 with $2.6 \cdot 10^6$ events and the shower size range $N_e \geq 10^5$. The investigations are focussed to a test of the Nishimura-Kamata-Greisen (NKG) lateral distribution function (LDF) at various radial distances from the shower axis. The LDF are fitted by NKG function in Greisen approximation.

1 Introduction

It is common praxis to describe the lateral distribution of the the electron density $\rho_e(R)$ of Extensive Air Showers (EAS) of the size N_e by modifications of the Nishimura-Kamata-Greisen form [1]. For studies of data of the MAKET ANI installation the following form has been adopted [2]:

$$\rho(R, N_e, s) = \rho_e(R, N_e, s) \left(\frac{R}{r_m} \right)^{-0.18} = F_{NKG}(R, N_e, s) \left(\frac{R}{r_m} \right)^{-0.18} \quad (1)$$

where R is the distance from the shower core; r_m is the Moliere unit (118 m at Mount Aragats), s - age of shower, N_e - EAS size, F_{NKG} is the Nishimura-Kamata-Greisen function [1], $(R/r_m)^{-0.18}$ is a factor taking into account the contribution of photons. For transformation of the response of the 5 cm thick scintillators into particle densities the procedure of ref.[3] is applied.

The present contribution reports on studies testing some details of the applicability of the NKG form for the experimentally observed shape of the lateral distribution function (LDF).

Using the data of the MAKET-ANI experiment the densities at the different distances from showers axis have been determined. The showers with lateral extensions up to the distances of 110-130m in direction to the peripheral point have been selected. Analysing about $5 \cdot 10^5$ events with EAS sizes $N_e \geq 1 \cdot 10^5$, the average lateral density $\langle \rho(R) \rangle$ of the charged particles for the different radial distances from the shower axes and for different EAS sizes N_e have been determined. In averaging of $\rho(r)$ also zero values of detector measurements in contrast to previous procedures [4], are taken into account. Therefore the results of ref.[4] get modified and corrected.

2 Data selection

The MAKET-ANI installation consists of 92 plastic scintillation detectors. 68 detectors with a thickness of 5 cm have an area of 1 m² each, the rest of 24 detectors are of 0.1 m² area. Two peripheral detector stations of 15 m² and 4 m² area, respectively, are located at 100 m and 70 m distance from the geometrical center of the installation (x_0, y_0) and are foreseen for precise measurements of electron-photon densities. The total area of the detectors is 70.4 m². The present analysis is based on data

*corresponding author : laura@crdlx5.yerphi.am

collected from August 1997 to March 1999 with an effective running time of nearly 8000 hours. The analysis is carried out for EAS selected with the conditions: $|x - x_0| \leq 20\text{m}$, $|y - y_0| \leq 10\text{m}$, for azimuth angles $\theta \leq 45^\circ$, $1 \cdot 10^5 \leq N_e \leq 5 \cdot 10^7$ and $0.3 \leq s \leq 1.7$. The basic EAS parameters (N_e , s , θ , φ , x , y) have been determined by the procedures described in ref.[5], using the CERN MINUIT computer package [6], for fitting to a Nishimura-Kamata-Greisen lateral distribution function [2] with an adjustable age parameter s . The angular coordinates θ and φ are derived from fast timing information.

3 Results

The correlations between $\rho(R)$ and N_e for the observed densities $\rho(R)$ at 50 m and 120 m distances from the showers axes are presented in Figure 1. Approximately a linear correlation of $\rho(R)$ on EAS size is observed (with a broad range of fluctuations) for the both distances.

The NKG function suggests that the $\frac{\rho_e(R)}{N_e}$ ratio is independent on N_e . In order to examine this feature at large distances of 50 m and 120 m radii, the $\langle \rho_e(R) \rangle / N_e$ ratio dependence on the showers

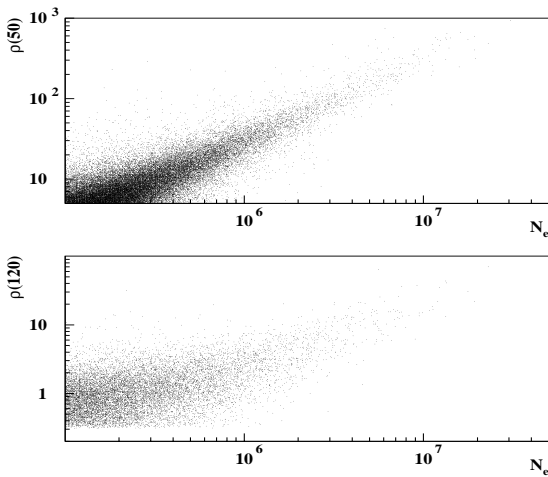


Figure 1: *Dependence of electron densities on shower size.*

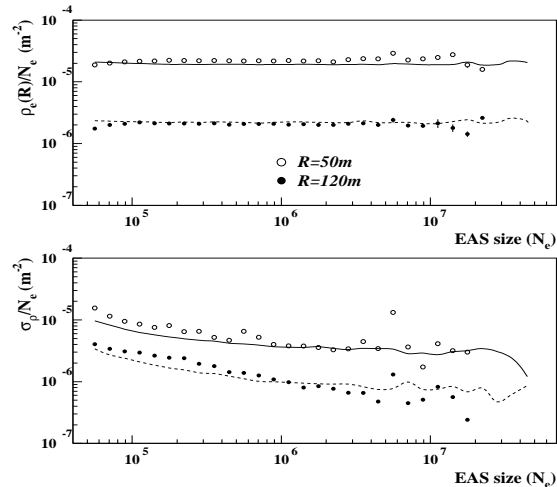


Figure 2: *The $\langle \rho(R) \rangle / N_e$ ratio vs the EAS size N_e (upper part) and the fluctuations (lower part).*

size and the uncertainties are shown in Figure 2. The predictions by the Nishimura-Kamata-Greisen function with Poissonian fluctuations are indicated by the dotted and dashed lines. The empty and filled circles correspond to 50 m and 120 m, respectively. A good agreement between experimental and theoretical curves is observed, proving that the NKG approximation is correct for 120 m and 50 m distances in the wide range of N_e .

The density spectrum can be expressed by the form [7]:

$$F(\rho_e) \sim \rho_e^{-(\gamma+1)} \quad (2)$$

in a large range of densities of $(1-1000) \text{ m}^{-2}$, where γ is the power index of the integral spectra. It has been shown that the size spectra have the same shape and slope as the density [7]. The densities of charged particles were derived by corrections of the actual detector measurements for the

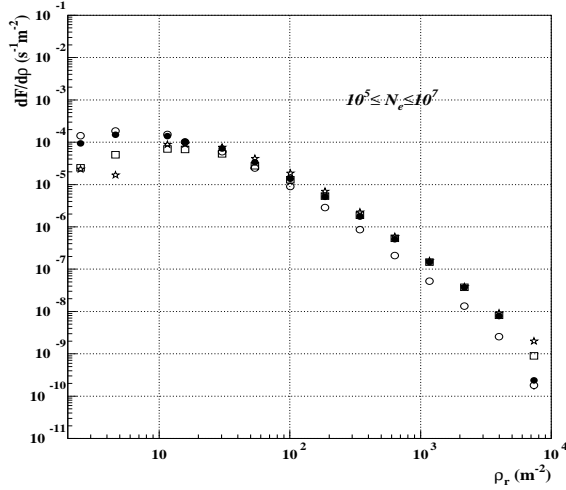


Figure 3: *Density spectra of four detectors at different locations in the detector array.*

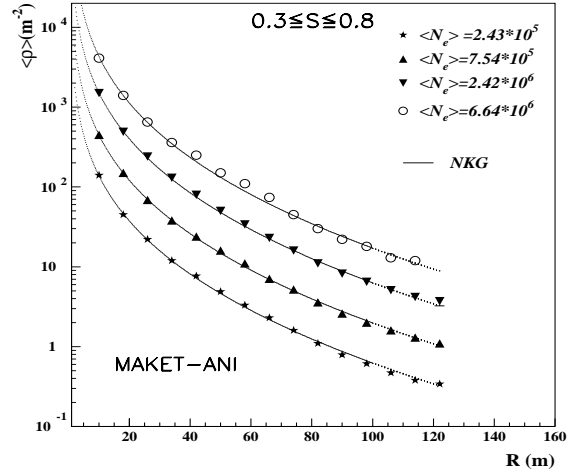


Figure 4: *Lateral distribution function for different shower sizes (young showers).*

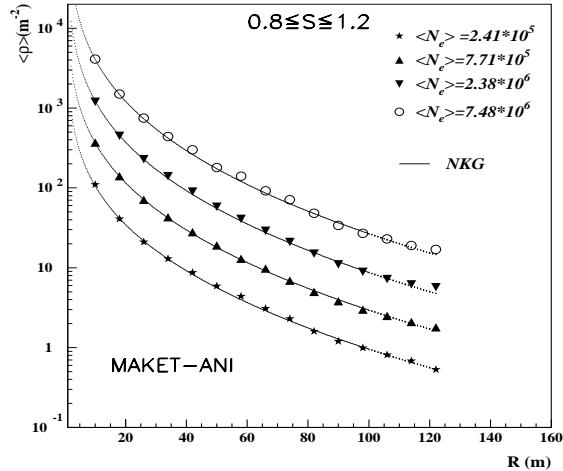


Figure 5: *Lateral distribution function for different shower sizes (mature showers).*

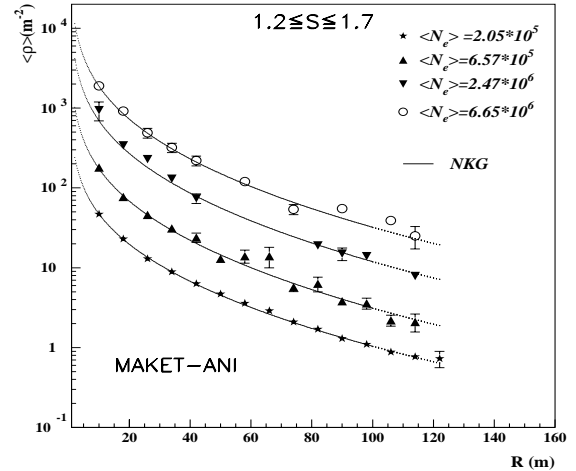


Figure 6: *Lateral distribution function different shower sizes (old showers).*

contribution of photons according to [3]. We have composed the differential spectra densities for each detector by using the obtained densities for the arbitrary chosen detectors located at the distances 10 m, 15 m, 25 m, 35 m from the center of the installation. The spectra from these detectors are shown in Figure 3. The spectral indices equal to 2.51 ± 0.1 and agree with slope values of refs.[8, 9]. For displaying the dependence on N_e the EAS collected in the data bank are divided into 4 equal logarithmic bins of electron sizes N_e and into radial $\Delta(R)$ bins of 4 m. For each (N_e, R) the mean particle density is obtained for each core distance bin, and the expected LDF by the modified Nishimura-Kamata-Greisen formula [1] have been calculated. In Figures 4-6 the LDF for the different EAS sizes are displayed. Dashed lines present the calculated NKG functions. In addition the dependence of ex-

perimental LDF on the shower age has been investigated for three age intervals of age: $0.3 \leq s \leq 0.8$, $0.8 \leq s \leq 1.2$ and $1.2 \leq s \leq 1.7$. The LDF of “old” showers appears to be flatter than the LDF of “young” EAS [10].

The relative errors of the (modified) NKG approximation appears to be ca. 3-4% at small distances and ca. 5-6% for large distances (> 80 m) from the EAS axis. This agreement is much better than claimed for the EAS-TOP detector setup [11].

4 Summary

The MAKET-ANI EAS data bank has been used to illustrate experimentally various features of the NKG form for the LDF of the electron component. The studies reveal a good general agreement and the good accuracy of the data, which are slightly modified as compared to previous communications [4] due to a refined calibration procedure of the detector signals in terms of particle densities.

Acknowledgments

The report is based on experimental results of the ANI collaboration. The MAKET-ANI installation has been set up in a collaborative project of the Yerevan Physics Institute (Armenia) and the Lebedev Physics Institute (Moscow). The continuous contributions and assistance of the Russian colleagues in operating of the installation and in the data analyses are gratefully acknowledged. We thank Dr. V. Romakhin for useful discussions and remarks.

One of the authors (L.G.M.) thanks A. Vardanyan and N. Gevorkyan for help in shaping of the paper and S.Ter-Antonyan for useful discussions.

The work has been partly supported by the research grant No. 96-752 of the Armenian Government and by ISTC project A116.

References

- [1] K. Greisen, Progress in Cosmic Ray Physics **3**, North Holland Publ. (1956)
- [2] V. Avakian et al., Soviet J. Nucl. Phys. **56**(9) (1993) 174 (in Russian)
- [3] S.V. Blokhin, V.A. Romakhin and G.G. Hovsepyan, ANI Workshop 1999, these proceedings, p.111
- [4] L. Melkumyan - ANI Collaboration, Proc. of the Workshop ANI 98, eds. A.A. Chilingarian, H.Rebel, M. Roth, M.Z. Zazyan, FZKA 6215, Forschungszentrum Karlsruhe 1998, 73
- [5] G.V. Gharagyozyan - ANI Collaboration, Proc. of the Workshop ANI 98, eds. A.A. Chilingarian, H.Rebel, M. Roth, M.Z. Zazyan, FZKA 6215, Forschungszentrum Karlsruhe 1998, 51
- [6] F. James, MINUIT Reference Manual, Version 94.1, CERN Program Library Long Writeup W506, CERN(1994)
- [7] G.B. Khristiansen, G.V. Kulikov, U.A. Fomin, Cosmic Rays of Super-high Energies, Atomizdat, 1975, 27 (in Russian)
- [8] D.S. Basak et al, Proceedings of 20th ICRC, Moscow, **5** (1987) 426
- [9] F. Ashton and A. Parvaresh, Proceedings of 14th ICRC, Munchen, **8**(1975) 2719
- [10] A.A. Chilingarian et al., ANI Workshop 1999, these proceedings, p.53
- [11] G. Agnetta et al. - The EAS-TOP Collaboration, Astroparticle Physics **10** (1999) 1

Experimental Studies of the Characteristic Features of the Soft EAS Component with the GAMMA Array

V.S. Eganov¹, A.P. Garyaka¹, E.V. Korkotian¹, R.M. Martirosov^{1*}, J. Procureur²,
H. Sogoyan¹, M.Z. Zazyan¹

¹*Yerevan Physics Institute, Alikhanian Brothers St., 375036 Erevan, Armenia*

²*Centre d'Etudes Nucleaires de Bordeaux-Gradignan, Universite de Bordeaux 1, France*

The main characteristic features of the EAS soft component are experimentally studied for $N_e \geq 5 \cdot 10^5$ by the GAMMA array on Mt.Aragats, Armenia. The dependence of the EAS observables on the experimental analysis procedures are discussed, and the results are compared with predictions of EAS Monte Carlo simulations of the programm CORSIKA. As energy identifier the selection parameter α_e with a modified and experimentally more practical definition is used. The use and the uncertainties of the application of this particular EAS parameter are commented. A good agreement between experimental observations and simulation is noted.

1 Introduction

The GAMMA array [1] is one of the major detector components of the ANI experiment on Mt. Aragats, Armenia. In the past years several modifications of the data processing and acquisition system have been made which led to a more reliable operation and more accurate measurements in studying the soft EAS component with determining the lateral density distributions and size spectra. In the present contribution some results are reported from the data collected during 2300 h operation time, observing $4 \cdot 10^4$ EAS with $N_e \geq 5 \cdot 10^5$ with the zenith angles of incidence $\Theta \leq 30^\circ$. For the studies of the EAS features we use the selection parameter α_e [2], which is assumed to be an energy identifier independent from the mass of the EAS primary. In order to facilitate a convenient experimental determination of this parameter, the definition of the selection parameter has been modified. Its application is illustrated and some open questions of its applicability are commented. The detector efficiency studies and some comparisons of the data with Monte Carlo simulations are based on the results calculated with the CORSIKA code (vers.5.20) [3] using the VENUS model as generator of the hadronic interactions.

2 Experiments

For a reliable determination of the charge particle densities the dynamical range of the ADCs of the data acquisition system has been extended to the range of $7 \cdot 10^3 - 10^4$. In addition efficiency factor K, relating the observed density (ρ_{seen}) to the true particle density ρ_{exact} , has been determined, taking into account the absorption, conversion and scattering effects of the detector housings (plastic roofs of the the detector boxes). Figure 1 displays the dependence of the K-factor from the distance r from the shower center and justifies the use of an average value of 1.25 . Figure 2 displays the lateral distributions and shows the agreement with the simulations.

*corresponding author: martir@lx2.yerphi.am

The integral spectrum (Figure 3) does not exhibit a sudden change in the slope so that the location of a knee is not directly obvious. In order to assign the comparable position, we look for the spectral intensity equal to the intensities observed for the knee in other experiments (EAS-TOP [4], KASCADE [5], see Table 1). It is for ca. $N_e = 1.6 \cdot 10^6$ in the spectrum observed in the ANI experiment.

Table 1: *Integral intensity at the knee position.*

Experiment	$I(\geq N_e^{knee})/10^{-8}$
EAS-TOP	9.9 ± 2.1
KASCADE	9.9 ± 2.0
GAMMA	11.0 ± 3.0

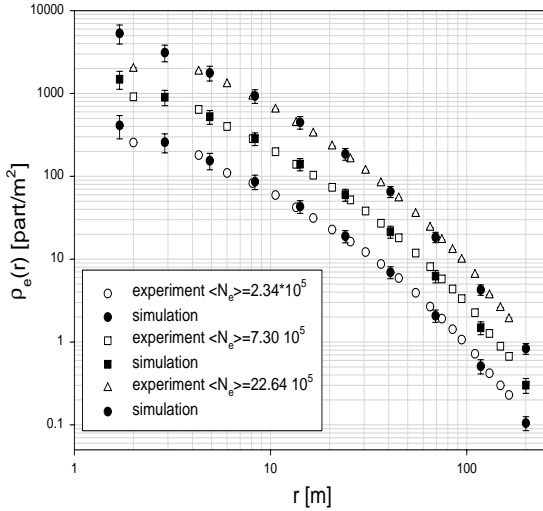


Figure 2: *Comparison of measured lateral distributions of different shower sizes with Monte Carlo simulations.*

3 Energy selection

Since the first introduction of the selection parameter α_e which had been justified [2] on basis of specific Monte Carlo simulations to be a mass-independent EAS energy identifier, the definition of this quantity has been changed several times [6,7]. The ingredients of the definition are the lateral density $\rho_e(r_\alpha)$ of the electromagnetic component at a particular distance r_α , the value $f_{NKG}(r_\beta, S_{r_x-r_y})$ of the Nishimura-Kamata-Greisen function at r_β , with an age value $S_{r_x-r_y}$ determined from the data by fitting the lateral range between r_x and r_y . With each definition specifying particular values of r_α , r_β ,

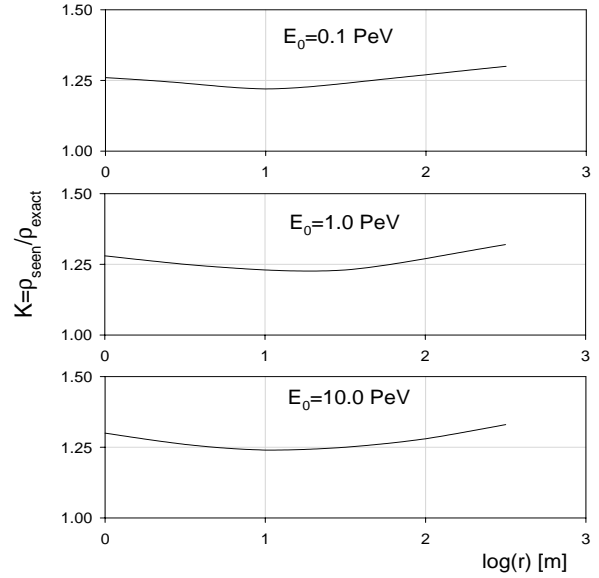


Figure 1: *The variation of the $K = \rho_{seen}(r)/\rho_{exact}(r)$ with the distance r from the EAS core for different primary energies.*

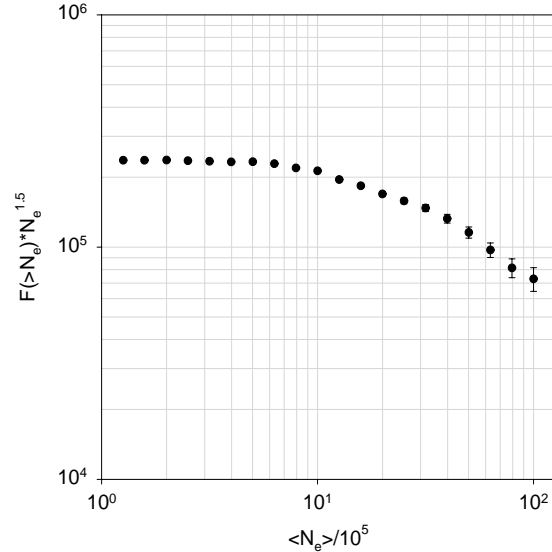


Figure 3: *Integral size spectrum measured with the GAMMA array.*

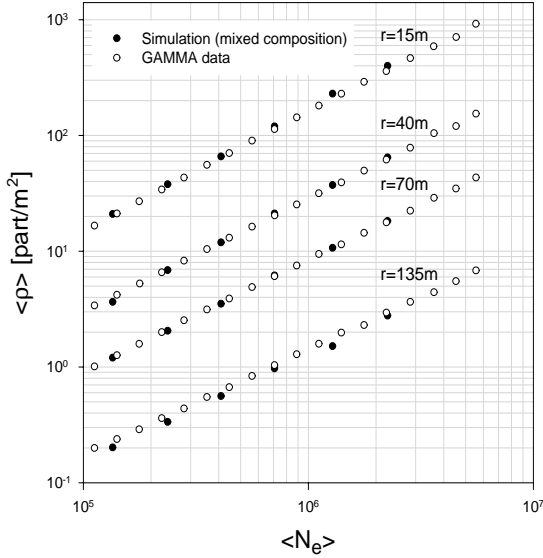


Figure 4: Lateral densities of the charge particle distributions at various distances from the shower axis increasing with N_e .

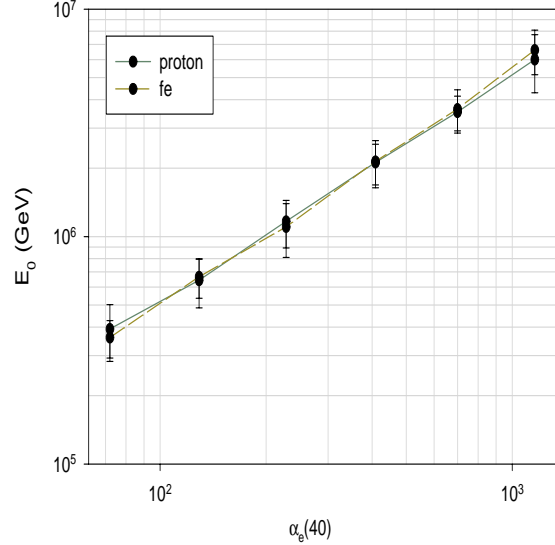


Figure 5: The relation between the primary energy of protons and iron nuclei with the parameter $\alpha_e(40)$ (simulation results).

r_x and r_y , Monte Carlo simulations prove that the combination $\alpha_e(r_\alpha) = r_\alpha^2 \rho_e(r_\alpha) / f_{NKG}(r_\beta, S_{r_x-r_y})$ is only dependent from the energy of the primary, but practically independent from the mass. So far this result get not influenced by the particular hadronic interaction model used for the simulations and by the simplifications of the real EAS appearance by the NKG form, though still not clearly explored, there must exist for any fixed energy an implicit mutual dependence of the parameters entering in $\alpha_e(r_\alpha)$. That means that for any choice of r_α the parameters of $f_{NKG}(r_\beta, S_{r_x-r_y})$ can be found in a way to conserve the energy selection quality. A previous definition with $r_\alpha = 135$ m proves to be experimentally inconvenient, since it requires measurements far from the shower axis, with statistical problems due to low densities and necessary corrections for the increasing contributions of muons. Figure 4 shows the dependence of the charged particle densities at particular distances r from the shower size. There are systematic deviations obvious between measurements and simulations for $r = 135$ m, while the agreement for $r = 40$ m is very good. For the simulations a mixed composition has been assumed (protons: 40%, He: 21%, light nuclei $< A > = 14 : 14\%$, medium heavy nuclei $< A > = 26 : 13\%$, and heavy nuclei $< A > = 56 : 12\%$).

Thus we defined $\alpha_e(40) = 40^2 \rho_e(40) / f_{NKG}(1, S_{15-70})$. The energy identifier quality is demonstrated with Figure 5. It results from simulation studies using the CORSIKA code (vers. 4.068) taking into account the conditions of the GAMMA array. The EAS have been simulated for energies between $10^5 - 10^7$ GeV along the primary spectrum. The error bars in Figure 5 represent the estimates of the uncertainties arising from the detector performance.

In order to illustrate the selection quality of the used $\alpha_e(40)$ and from the primary energy, respectively, of the simulated showers suggesting that the mass compositions are mapped by the fluctuations of N_e for fixed $\alpha_e(40)$, unless other type of fluctuations of the shower development or of experimental nature do obscure the effect.

Figure 7 compares $\alpha_e(40)$ with data determined with the GAMMA detector installation. Unfortunately due to the limitation of the used (old) version 4.068 and the unreliability of the used interaction model at high energies the simulations are limited to $\alpha_e(40) = 1000$. But a general good agreement between data and simulations can be tentatively noticed.

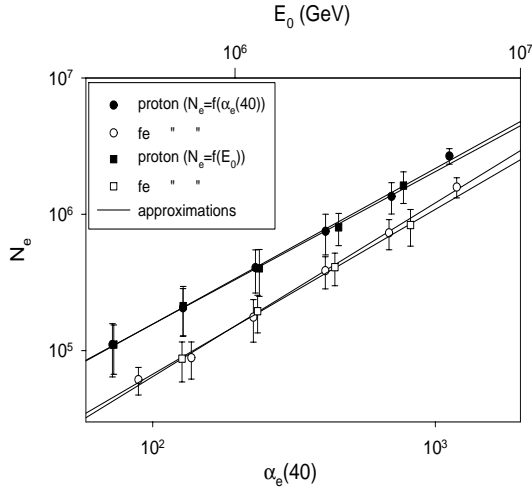


Figure 6: *EAS size as function of the parameter $\alpha_e(40)$ (lower scale) and of the energy E_0 of the primaries (upper scale), respectively (simulation results).*

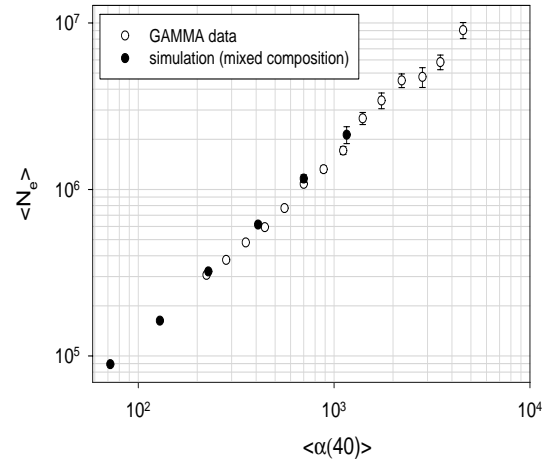


Figure 7: *EAS size as function of the parameter $\alpha_e(40)$ as extracted from the data of the GAMMA array compared with simulation results assuming a mixed composition.*

4 Conclusion

The studies of the characteristic features of the soft EAS component have been continued and the results of Ref.[8] are updated. Special attention has been focused to the application of the so-called α_e - parameter as energy indicator of the EAS. The concept and the definition has been justified on basis of Monte-Carlo simulations with the CORSIKA code, but restricted to the NKG description of the EAS and inferring the necessary local age parameter within this approximation. Actually there remain uncertainties on the properties of the α_e - parameter when more realistic considerations using EGS Monte Carlo simulations for the soft component are invoked. Additionally the dependence from the particular hadronic interaction model model, especially of the energy calibration of the α_e - parameter (by using more up-to-date versions of the CORSIKA code) is unclarified. Nevertheless phenomenological comparisons with data, so far possible, show a promising tendency.

References

- [1] S.A Arzumanian et al., Proc. 24th ICRC (Rome), 1 (1995) 482
A.A. Chilingarian et al., Proc. 16th ECRS (Alcala de Henares) (1998) 445
- [2] J. Procureur and J.N. Stamenov, Nucl. Phys. B (Proc. Suppl.) **39A** (1995) 242
- [3] D. Heck et al., FZKA report 6019, Forschungszentrum Karlsruhe 1998
- [4] M. Aglietta et al., Nucl. Phys. B (Proc. Suppl.) **75A** (1999) 251
- [5] K.H. Kampert et al., Proc. 26th ICRC, Salt Lake City, 3 (1999) 159
- [6] M. Brankova et al., Proc. of the Workshop ANI 98, eds. A.A. Chilingarian, H.Rebel, M. Roth, M.Z. Zazyan, FZKA 6215, Forschungszentrum Karlsruhe 1998, 69
- [7] M. Brankova et al., Proc. 16th ECRS (Alcala de Henares) (1998) 493
- [8] A.P. Garyaka for the ANI Collaboration, Proc. of the Workshop ANI 98, eds. A.A. Chilingarian, H.Rebel, M. Roth, M.Z. Zazyan, FZKA 6215, Forschungszentrum Karlsruhe 1998, 31

EAS Muon Characteristics in the Knee Region Measured with the GAMMA Array

A. Chilingarian¹, A.V. Darian¹, V.S. Eganov¹, A.P. Garyaka^{1*},
 V.A. Ivanov¹, E.A. Mamijanian², R.M. Martirosov¹, N.M. Nikolskaya², J. Procureur³,
 V.A. Romakhin², M.Z. Zazyan¹

¹ *Yerevan Physics Institute, Cosmic Ray Division, Armenia*

² *P.N.Lebedev Physics Institute, Moscow, Russia*

³ *Centre d'Etudes Nucléaires de Bordeaux-Gradignan, France*

EAS muons lateral distributions in various size intervals around the knee region, muon size spectra, and their dependences on electron sizes are presented as measured by the GAMMA array of the ANI Cosmic Rays Observatory on Mt.Aragats (3200m. a.s.l.) in Armenia. The data are compared with expectations of EAS simulations using the CORSIKA code and with data of other experiments.

1 Introduction

The determination of the energy spectrum and the mass composition of primary cosmic rays generating EAS is the main goal of the GAMMA experiment as well as of a number of other experiments located on different observation levels. The knee, which was found by measurements of the EAS electron size spectra [1], is of particular interest in view of its origin. The most natural hypothesis is a steepening of the primary cosmic ray spectrum as predicted by the diffusion model [2]. An alternative point of view is a change of properties of the hadronic interaction [3] to more rapid energy dissipation. There are also open questions about the position of the knee in the primary energy spectrum and the shape of the spectrum. Understanding the nature of the knee requires accurate measurements of the different EAS components. The muon component of EAS observed simultaneously with the electromagnetic component is sensitive to the mass composition, and it is expected to give information about the variation of the mass composition in dependence of the primary energy. As a first step on this way a detailed study of the mean characteristics of the muon component is necessary. In this paper we present experimental results obtained with the muon detectors of the GAMMA array, and we discuss some features of the knee as observed in the EAS muon component. We compare the measurements with model calculations and other experiments.

2 The Muon Detector and Data Treatment

The GAMMA array consists of two main parts: an array of surface detectors for the registration of the charged component of EAS and muon detectors. The surface part of the GAMMA array is described with results on the electromagnetic component in [4]. The spatial and angular coordinates of the shower axis are determined by the surface array. The muon detector setup of the GAMMA array [5, 6] consists of two parts with different thicknesses of the absorbers. The corresponding energy thresholds of the muons are 2.5 GeV and 5.0 GeV, respectively. Reconstructed showers with their cores inside of a circle of the radius of 40m, detected with an efficiency above 90%, are included in the following analysis. For these set of events we determine the muon density lateral distribution in

*corresponding author: alegar@jerewan1.yerphi.am

the range of core distances r up to 52 m for $E_\mu > 5.0$ GeV and up to 90 m for $E_\mu > 2.5$ GeV. In individual events the range of the accessible muon density measurements is smaller and depend on the position of the shower core. The lower limits on r are due to the punch-through particles of other types and estimated to 8 m and 15 m respectively. Additionally the determination of muon lateral distributions for larger intervals of r with events in the circle with radius of 70 m are possible. The corresponding upper limits of r are 70 and 110 m. The muon size spectrum as well as the muon size dependence on N_e will be reconstructed for events in circles with radii 40 m. Some essential changes were made in the method of the data evaluation. The correction of the transfer from the scintillation detector response to the incident charged particles number are treated in a way based on the shower simulations.

3 The experimental data

The average muon lateral distribution is shown in Figure 1 for the shower size interval $3.2 \cdot 10^5 - 5.6 \cdot 10^5$ and $\theta < 20^\circ$ for both muon energy thresholds. For $E_\mu > 5.0$ GeV it can be described by Hillas function with parameters which allow to approximate the Tien-Shan data [7]

$$\rho_\mu(r, N_e) = 0.95(N_e/10^5)^{0.8} r^{0.75} \exp\left(-\frac{r}{80}\right). \quad (1)$$

For $E_\mu > 2.5$ GeV in the range of distances 20-70 m the relation $\rho_\mu(2.5\text{GeV}) \approx 1.3\rho_\mu(5.0\text{GeV})$ is fulfilled. The Hillas function with adjusting above parameters describes the muon lateral distributions in ranges small shower sizes ($N_e < 2 \cdot 10^6$) good. For larger N_e the shape of the lateral distributions

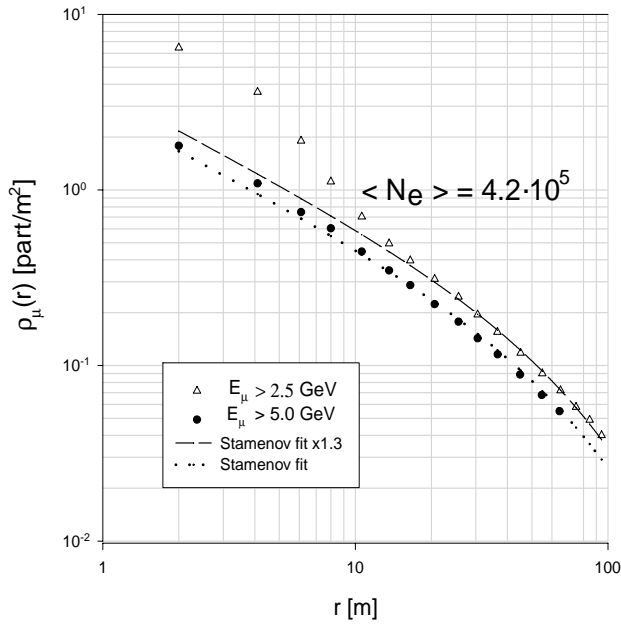


Figure 1: *Muon lateral distributions. The lines (Stamenov fit [7]) represent fits according to eq.(1).*

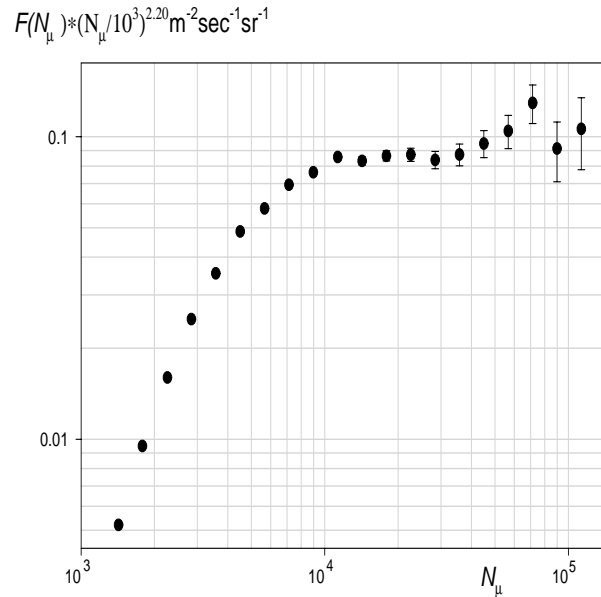


Figure 2: *Muon differential size spectra.*

does not change, but the N_e dependence become stronger. For smaller muon threshold energies effects of penetrating particles are seen up to 15 m core distance. The total number of muons N_μ is an integral of the lateral distribution over the whole range of r . The total number of muons in individual events is determined on the basis of experimental muon densities using the formula of the lateral probability distribution $w_\mu(r) = \rho_\mu(r, N_e)/N_\mu$ where the dependence on N_e is negligible - $N_\mu^{\text{exp}} = 1/K \sum \rho^{\text{exp}}(r_i)/w_\mu(r_i)$ where we sum up over all K muon detectors. As the measurements are only covering a limited range of r , the contribution of muon densities at large r for the total muon number has a not negligible uncertainty. We introduce therefore the so called *truncated* muon number following KASCADE [8] but with a slightly different definition: N_μ^{tr} is the number of muons in the core distance between 8 m and 52 m for $E_\mu^{\text{th}} = 5$ GeV. Here holds $N_\mu^{\text{tr}} = 0.31N_\mu$ for our simulation [9].

In Figure 2 the differential size spectra of N_μ , i.e. the total number of muons, is presented for $E_\mu^{\text{tr}} > 5$ GeV. A knee is seen at $N_\mu \approx 10^4$. The region of small N_μ up to $5 \cdot 10^3$ is strongly affected by threshold effects. It is not possible to determine accurately the power index of the spectra before the knee. After the knee it is equal to 2.20 ± 0.15 . In the region of $N_\mu \approx 6 \cdot 10^4$ there is a structure in the spectra. But because of small statistical accuracy we refrain from any speculation.

In Figure 3 the dependences of the mean number of muons and of the truncated number of muons with the mean electron size $\langle N_e \rangle$ are presented. At $\langle N_e \rangle$ up to the knee range these dependences can be described with the relation $\langle N_\mu^{\text{tr}} \rangle \approx \langle N_e \rangle^{0.79}$, followed by a slightly steeper increase. For illustration that better the dependence of $N_\mu \cdot N_e^{-0.79}$ with $\langle N_e \rangle$ is also shown in Fig. 3. Such behavior may indicate a primary spectrum with heavier composition after the knee. Also the CORSIKA results for the primary spectrum with power index equal to -2.70 and a constant mixed primary composition: proton - 40%, α -nuclei - 21%, light nuclei ($\langle A \rangle = 14$) - 14%, medium nuclei ($\langle A \rangle = 26$) - 13% and heavy nuclei ($\langle A \rangle = 56$) - 12% are shown. There is a good agreement for N_μ^{tr} in the region before the knee. The disagreement with the total muon number N_μ may indicate the problematic of extrapolations of the muon LDF by functional forms.

In conclusion the lateral distributions of the EAS muon component measured by the GAMMA array are in good agreement with the Tien-Shan results and can be reproduced by simulations using the

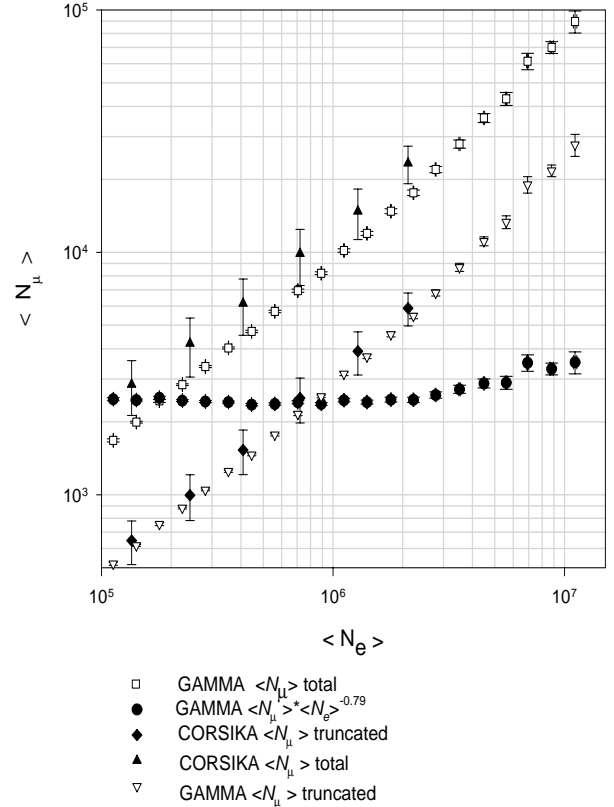


Figure 3: N_μ dependence on electron size.

CORSIKA code with a reasonable mixed mass composition.

Acknowledgement

The work was supported by the RFBR 96-02-18098 grant and by the grant 96-752 of the Armenian Ministry of Science and Education. We express our gratitude to all participants of the Workshop for valuable discussions.

References

- [1] G.V. Kulikov and G.B. Khristiansen, JETP **35** (1958) 35
- [2] G.T. Zatsepin et al., Izv. Akad. Nauk USSR, Seriya Phizika, **26** (1962) 685
- [3] S.I. Nikolsky, Nucl. Phys. B (Proc. Suppl.) **39A**(1995) 228
- [4] V.S. Eganov et al., ANI Workshop 1999, these proceedings, p.87
- [5] A.A. Chilingarian et al., Proc. 16th ECRS (Alcala de Henares) (1998) 445
- [6] A.A. Chilingarian et al., Proc. of the Workshop ANI 98, eds. A.A. Chilingarian, H. Rebel, M.Roth, M.Z. Zazian, FZKA report 6215, Forschungszentrum Karlsruhe, p.27
- [7] S.F. Abdrashitov et al. Proc. 17th ICRC(Paris) **6** (1981) 156
- [8] J.H.Weber et al. - KASCADE Collaboration, Proc. 26th ICRC (Salt Lake City) 1999, HE 2.2.42
- [9] A.F. Badea, private communication (1998)

The Aragats Event Simulation Tool ARES

A. Haungs^{1*}, A.F.Badea², M.Zazyan³

¹*Institut für Kernphysik, Forschungszentrum Karlsruhe, Germany*

²*Institute of Physics and Nuclear Engineering - Horia Hulubei, Bucharest, Romania*

³*Yerevan Physics Institute, Cosmic Ray Division, Armenia*

ARES (**AR**agats **E**vent **S**imulation) is a program for the simulation of the detector response of the scintillation detectors of the ANI experiment based on the detector simulation tool package GEANT. The first version for free and common use of the code (ARES version 1.01) is presented and a short introduction for beginners is given.

1 Introduction

For the understanding of the registered data in particle detectors used in modern accelerator and astroparticle experiments a detailed detector simulation is indispensable. Especially earth bounded extensive air shower experiments made a progress in accuracy over the last decade due to the usage of better particle detectors and electronics. Without a detailed detector simulation large uncertainties would still arise.

ARES is the simulation program for the detector response of the scintillation detectors of the ANI experiment at Mt. Aragats, Armenia [1]. It is based on GEANT 3.21 [2] with the description of the detectors used at ANI with unshielded electron detectors and muon detectors below a concrete and ground shielding. In the present version ARES describes the array of 150 muon detectors with their correct geometry including the housings and the shielding. ARES starts from single particles or particles obtained by the air shower simulation program CORSIKA [3] and calculates the energy deposit and arrival time of particles in each detector. Additionally the ADC value of the detectors are calculated including a simulation of the PMTs [4]. First physical results of using the ARES program are published at [5, 6, 7].

2 Download

The official homepage of ARES is

<http://www-ik3.fzk.de/~haungs/ares/ares.html>

For a first use of ARES, please visit this page and follow the instructions.

3 Rules for using ARES

A download of the ARES source is allowed, if attention is paid to the following rules:

- The use of ARES has to be referred (by this article) with the names of the ARES authors and the number of the used version.
- Any intrinsic changes of the program have to be proceeded to the authors to be confirmed and included in the official ARES.

*corresponding author: haungs@ik3.fzk.de

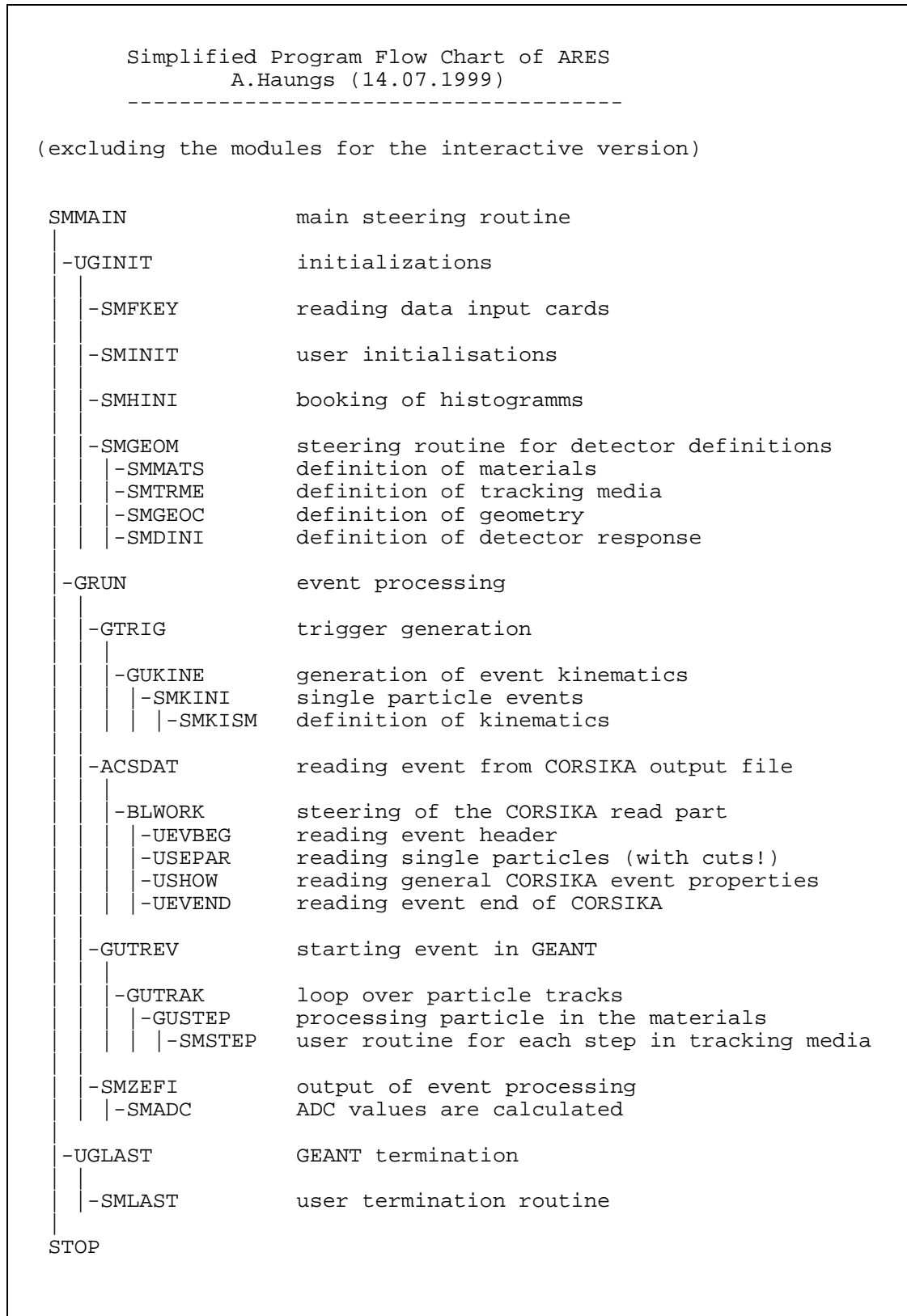


Figure 1: *The simplified flowchart of the ARES program.*

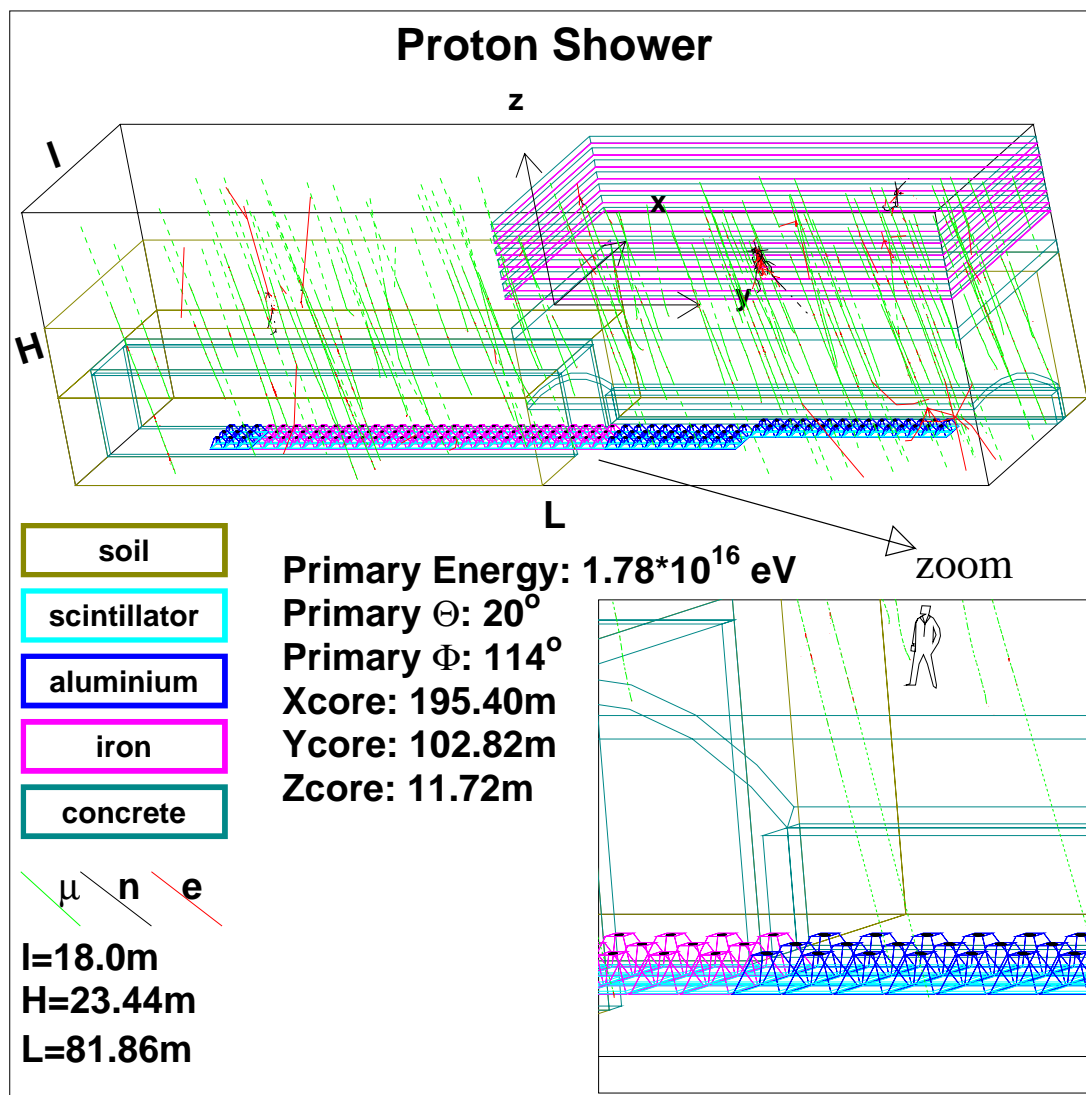


Figure 2: Example of using the interactive version of ARES.

4 Instructions for using ARES

Following files are achieved by a download of the ARES package:

README.html	a README file
Rules.html	rules for using ARES
flowchart.html	a simplified flowchart of ARES (Fig.1)
ares.cmz	the source of ARES
compares	compile and link script for LINUX version (batch).
comparesgra	compile and link script for LINUX version (graphic).
ares.input	commented steer cards for ARES
ares.car	the car file of ARES
ares.car.ps	a postscript file with the fortran source of ARES
areslogo.gif	the logo of ARES

ARES is written in FORTRAN77 and needs for a successful installation and execution the CERN program libraries including GEANT 3.21 [2].

From the same source (ares.cmz) a generation of a batch version and a interactive graphics version of ARES is possible.

The batch version produces as output a ntuple with different observables as well as a sample of histograms.

For the interactive version the user should have some knowledge in GEANT and its interactive part. An example of a possible output is given in Figure 2.

ARES is developed on a unix alpha workstation and on a LINUX PC (S.U.S.E. 5.2) parallel; for both machines there are macros available in ares.cmz (patch kumacs) to produce the executables. For the LINUX version additional compile and link scripts are available, which are called by the macros.

The present version is optimized for the batch version using the output (particles) from CORSIKA [3] extended air shower calculations looking for energy deposit and arrival time of particles at the muon detectors in the underground below the GAMMA installation of ANI.

For a first usage a simplified instruction is given at the README file on the Internet page (<http://www-ik3.fzk.de/~haungs/ares/ares.html>).

Acknowledgment

The authors would like to thank Ashot Chilingarian and in particular Heinigerd Rebel for initiating the ARES project. Two of the authors (A.B. and M.Z.) acknowledge for the kind hospitality in Forschungszentrum Karlsruhe during their research visits. The work has been partly supported by scientific - technical (WTZ) projects between Germany and Romania (RUM-014-97) and Armenia (ARM-002-98), respectively.

References

- [1] A. Chilingarian et al., Proc. 26th ICRC (Salt Lake City) 1999, HE 2.2.09
- [2] GEANT: CERN Program Library Long Writeups W5013 (1993)
- [3] D. Heck et al., FZKA report 6019, Forschungszentrum Karlsruhe (1998)
- [4] G. Hovsepian, private communication
- [5] M.Z. Zazyan and A. Haungs, Proc. of the Workshop ANI 98, eds. A.A. Chilingarian, H. Rebel, M. Roth, M.Z. Zazyan, FZKA report 6215, Forschungszentrum Karlsruhe (1998) 37
- [6] A.F. Badea et al., ANI Workshop 1999, these proceedings, p.99
- [7] M.Z. Zazyan et al., ANI Workshop 1999, these proceedings, p.105

ARES Simulations for the GAMMA Muon Underground Detector

A.F. Badea^{1*}, H. Bozdog¹, I.M. Brancus¹, A. Haungs², H.J. Mathes², H. Rebel²,
A.A. Chilingarian³, M.Z. Zazyan³

¹*Institute of Physics and Nuclear Engineering - Horia Hulubei, Bucharest, Romania*

²*Institut für Kernphysik, Forschungszentrum Karlsruhe, Germany*

³*Yerevan Physics Institute, Cosmic Ray Division, Armenia*

The simulation code ARES (**AR**agats **E**vent **S**imulation) is presented. ARES is developed for the simulation of the detector response of scintillation detectors of the extensive air shower experiment ANI. EAS Monte Carlo simulations for the particular case of shower cores positioned in an area centered at the MAKET-ANI surface array are performed using CORSIKA. The response of the muon underground detectors of the GAMMA array is simulated by ARES. Correlations between different shower observables are explored.

1 Introduction

The ANI experiment (3250 m a.s.l) consists of two detector arrays, the MAKET installation [1] and the GAMMA installation [2], with geometrical centres shifted by appr. 200 m. The muon detector system is installed underground below the GAMMA surface array, partially covered by a calorimeter building positioned in the middle of the array; the underground system consists of 150 plastic scintillator counters of 1 m² area and 5 cm thickness. Because of the sufficient large area of the muon detector system, a partitioning of the whole system (D30) in 3 subsystems D33 (40 plates), D32 (50 plates) and D31 (60 plates) could be introduced. This partitioning enables to study different correlations. It is also recommended for correlations (used for primary mass discrimination) when the shower core is positioned in certain zones of the GAMMA installation [3]; in such case these three partitions cover different radial intervals, each of them accessing particular intervals of the shower lateral distributions. Shower cores positioned inside the MAKET installation allows a good discrimination between different primaries (especially concerning muon arrival times) due to the large radial distance of the muon detectors from the shower core.

2 ARES Program

ARES (vers. 1.01/00 from 14.07.1999) [4] is the simulation program for the detector response of the GAMMA muon underground detector of the ANI experiment at Mt. Aragats (3250 m a.s.l.), Armenia. It is based on GEANT 3.21 [5] with the description of the detectors including the housings used at ANI as unshielded electron detectors and as muon detectors below a concrete and ground shielding. In the present version ARES describes the array of 150 muon detectors with their correct geometry and the shielding. ARES starts from single particles or particles obtained by the air shower simulation program CORSIKA [6] (version 4.6 in the present work, containing the high-energy interaction model VENUS [7], and using the NKG-approximation for the electromagnetic part of [8] the showers), and calculates the energy deposit and arrival time of particles (also secondary particles generated in the

*corresponding author: badea@muon2.nipne.ro

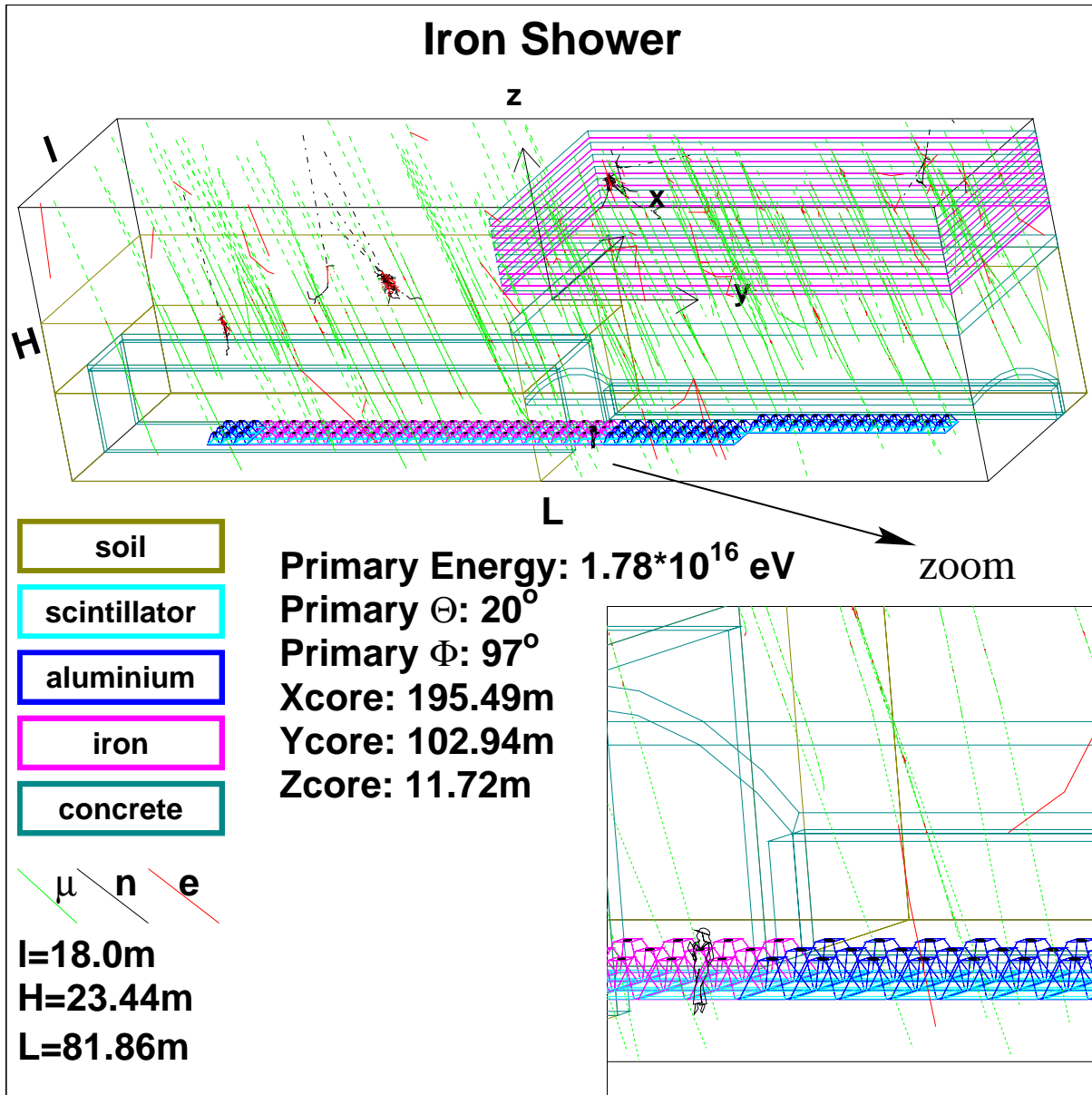


Figure 1: View of a iron shower in the muon detector. Centre of the shower is positioned in the *MAKET* installation.

absorber) in each detector. For inclined showers (zenith angle $\theta \neq 0^\circ$) corrections concerning arrival times of muons have been done; these arrival times are calculated in a plane through the position of the shower core and perpendicular to the shower axis. The correction is, in fact, only geometrical, the underground muons have practically the speed of light. The actual version of ARES does not take into account the response of electronics and the propagation of light inside the pyramidal houses of the scintillators. Figure 1 is an example of using ARES in a special graphic mode.

3 Monte-Carlo Simulations

In the present study EAS Monte-Carlo simulations using CORSIKA are performed. The shower core has been randomly positioned in a rectangle $16 \times 32 \text{ m}^2$ corresponding to the centre of MAKET-ANI. ARES detector simulations are performed for CORSIKA showers of primary protons and iron nuclei with fixed primary energy ($1.78 \cdot 10^{16} \text{ eV}$), but for two values of the zenith angle: $\theta = 0^\circ$ and $\theta = 20^\circ$. Approximately 500 showers have been simulated for each case.

It is important to specify the influence of δ -electrons at the detector signal produced by high energy muons before escaping from the concrete roof of the tunnel or from the concrete arch below the calorimeter; due to the distance between their production points and scintillator plates they can be enough deviated from the trajectory of the corresponding muons to hit a neighbouring detector faking a muon. A scintillator is considered as "fired" by the first particle (electron or muon) with

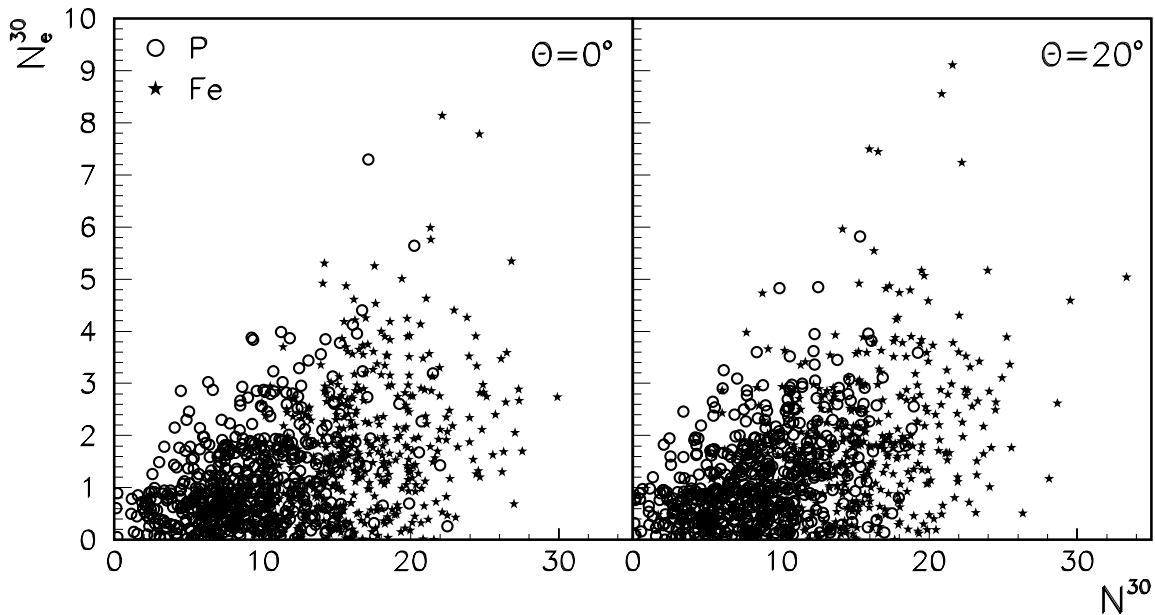


Figure 2: Number of detectors registering electrons (N_e^{30}) as a function of number of all hit detectors N^{30} . Each circle or star represents a single EAS.

energy deposit above 5 MeV. N^{30} represents the number of fired scintillators by one shower in all muon detectors of D30; N^{31} , N^{32} , N^{33} are the numbers of fired scintillators in the subdetectors D31, D32, and D33, respectively ($N^{30} = N^{31} + N^{32} + N^{33}$). Fig. 2 shows the level of contamination of signals by δ -electrons; the iron (1.5 mm thick) and aluminum (2.0 mm thick) pyramids housing the scintillator plates are not sufficient enough to absorb high-energy δ -electrons coming from above.

The finite resolution for the zenith angle θ of the shower and the time resolutions of the arrival time of the shower core and of the arrival times of single muons (δ -electrons) are ignored. ARES is able to reconstruct the (muon) arrival time distributions for each single shower relative to the arrival time of the shower core (so-called "global times": $\Delta\tau_1$ -arrival time of the first muon, $\Delta\tau_{mean}$ -mean arrival time, $\Delta\tau_{0.50}$ -median time, $\Delta\tau_{0.25}$ -first quartile, $\Delta\tau_{0.75}$ -third quartile) or relative to the arrival time of the first muon in the detector system ("local times"). Both, global and local times are calculated for the entire detector D30 and for the subdetectors D31, D32, D33. $\Delta\tau_1$, $\Delta\tau_{mean}$, $\Delta\tau_{0.50}$ is estimated

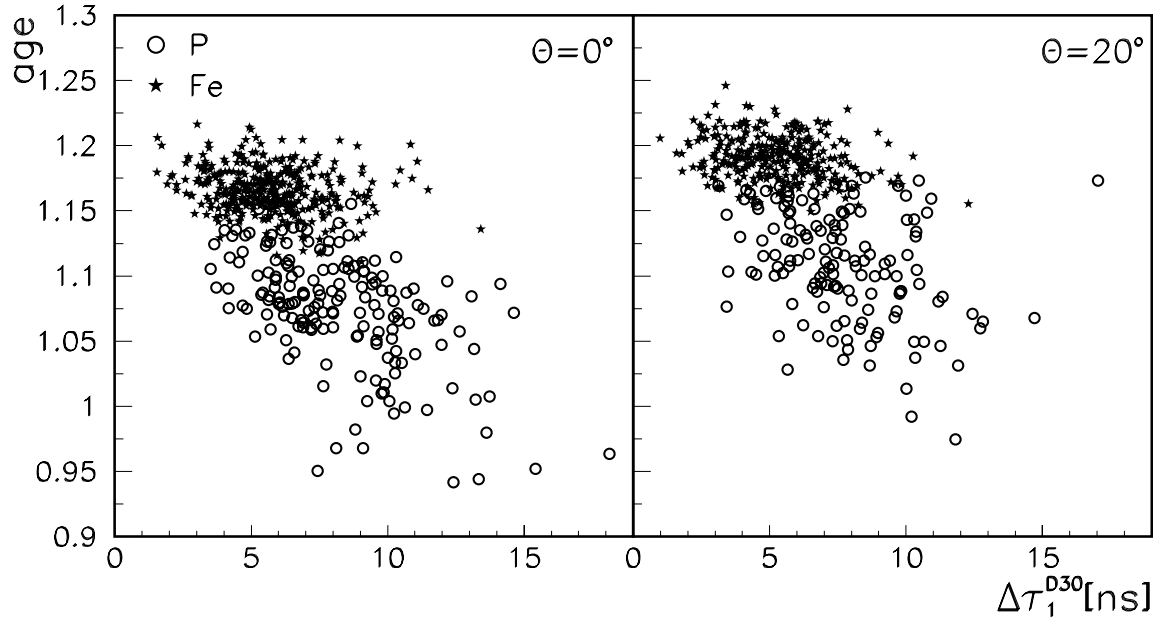


Figure 3: *Two-dimensional distribution of shower age vs. $\Delta\tau_1^{D30}$ for proton and iron induced EAS and for two values of the zenith angle ($\theta = 0^\circ, 20^\circ$). Primary energy: $E_0 = 1.78 \cdot 10^{16} \text{ eV}$.*

with a multiplicity condition:

$$N^{31} \geq 2 \text{ and } N^{32} \geq 2 \text{ and } N^{33} \geq 2 \implies N^{30} \geq 6 \quad (1)$$

i.e. at least 2 fired scintillator plates in each subdetector. The Multiplicity condition for estimating $\Delta\tau_{0.25}$ and $\Delta\tau_{0.75}$ is:

$$N^{31} \geq 4 \text{ and } N^{32} \geq 4 \text{ and } N^{33} \geq 4 \implies N^{30} \geq 12 \quad (2)$$

Fig. 3 shows the good discrimination feature for showers induced by proton and iron primaries in the twodimensional display: *shower age - arrival time of first muon in detector D30*. The correlation of the *shower size* with the *number of fired plates in detector D30* displays an excellent discrimination power between proton and iron induced showers (see Fig.4). Age and shower size are general shower parameters, which are reconstructible by a detector surface array like MAKET or GAMMA. For an analysis of the data in terms of the elemental composition of cosmic rays in a continuous work we have to specify, if the discussed variables (N_e , age, N^{30} and the $\Delta\tau$'s) are realistic from the experimental point of view.

4 Conclusions

High-energy δ -electrons produced by high energy muons and escaping from the concrete modifies the appearance of muons. Nevertheless an excellent discrimination between proton and iron primaries is observed, even when *number of "fired" detectors* instead of number of muons calculated from the signals in the scintillator plates are considered (Fig.4).

Concerning arrival times of muons (sometimes faked by δ -electrons): a discrimination between proton and iron primaries is favoured by large distances ($\approx 200\text{m}$) between muon detectors and the shower core positioned in the MAKET installation (Fig.3). Correlations of the *arrival time in one subdetector* with the *arrival time in another subdetector* (and also between number of muons in different subdetectors) [3] are not favoured because, for shower cores in the MAKET-ANI array all muon

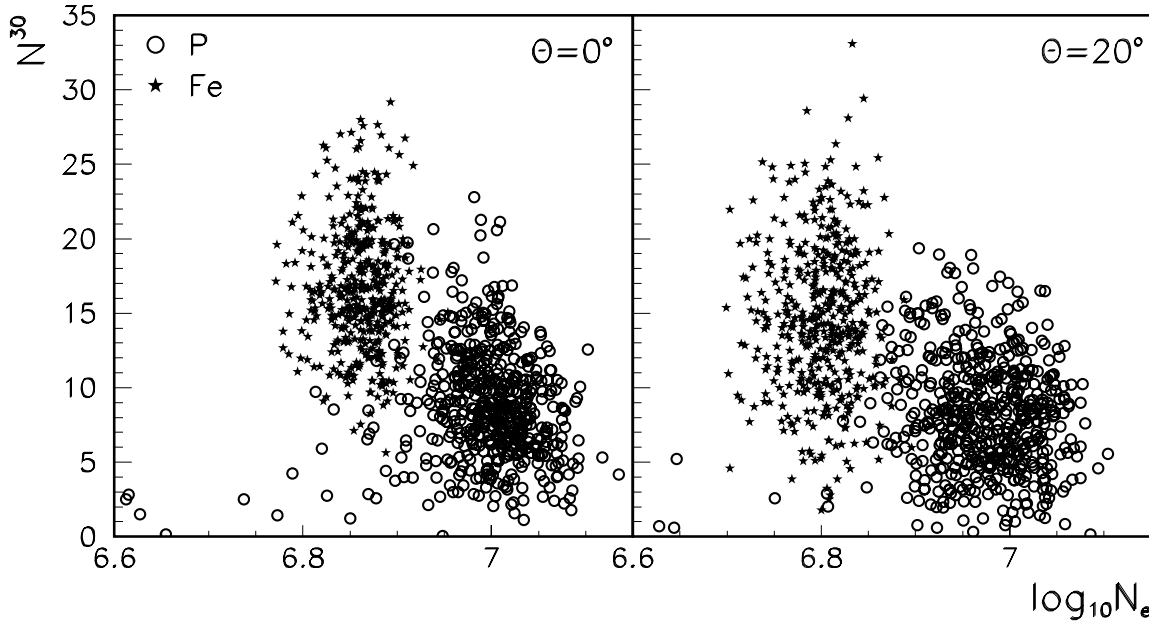


Figure 4: Number of fired plates in detector D30 (N^{30}) vs. the shower size (N_e) for two values of the zenith angle ($\theta = 0^\circ, 20^\circ$). Primary energy: $E_0 = 1.78 \cdot 10^{16} \text{eV}$.

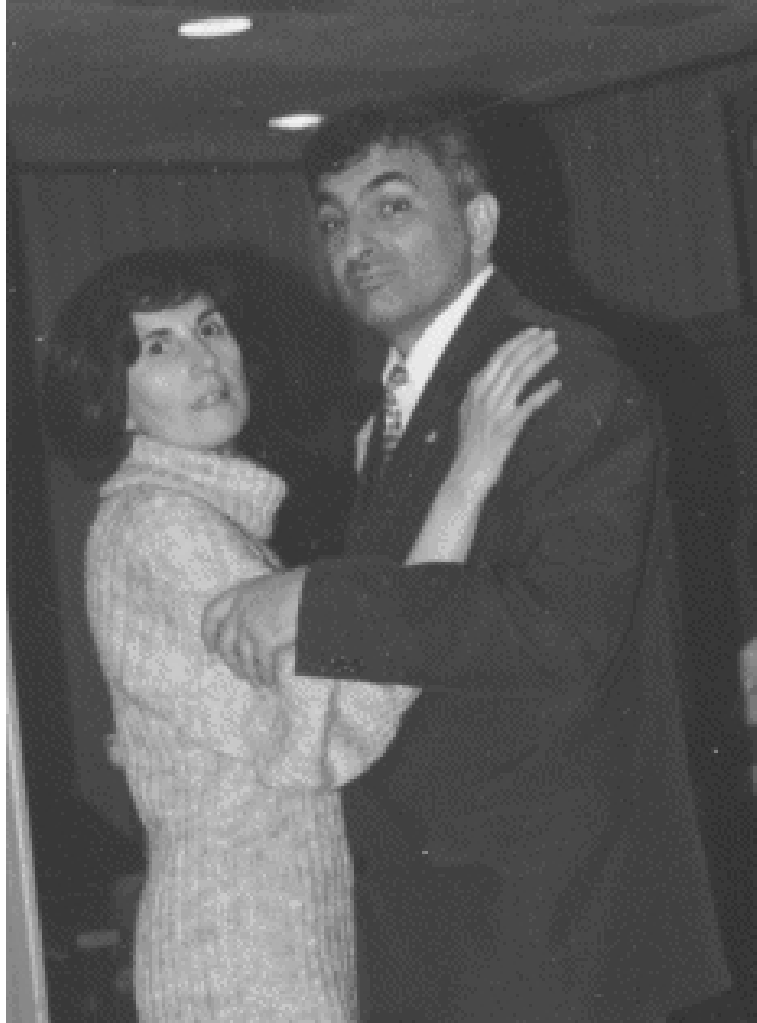
scintillators have rather the same distance to the shower axis. In addition, an aspect reducing the primary mass discrimination effect of arrival time distributions is the high energy threshold for muons penetrating into the scintillator plates of the underground muon detector [9].

Acknowledgement

Some of the authors would like to thank for the kind hospitality in Forschungszentrum Karlsruhe during their research visits. The work has been partly supported by scientific - technical (WTZ) projects between Germany and Romania (RUM-014-97) and Armenia (ARM-002-98), respectively.

References

- [1] G.V. Gharagozyan et al., Proc. of the Workshop ANI 98, eds. A.A. Chilingarian, H. Rebel, M. Roth, M.Z. Zazyan, FZKA 6215, Forschungszentrum Karlsruhe 1998, p.51
- [2] A.A. Chilingarian et al., Proc. of the Workshop ANI 98, eds. A.A. Chilingarian, H. Rebel, M. Roth, M.Z. Zazyan, FZKA 6215, Forschungszentrum Karlsruhe 1998, p.27
- [3] A.F. Badea et al., Proc. of the Workshop ANI 98, eds. A.A. Chilingarian, H. Rebel, M. Roth, M.Z. Zazyan, FZKA 6215, Forschungszentrum Karlsruhe 1998, p.77
- [4] A. Haungs, A.F. Badea and M.Z. Zazyan, ANI Workshop 1999, these proceedings, p.95
- [5] GEANT: CERN Program Library Long Writeups W5013 (1993)
- [6] D. Heck et al., FZKA-report 6019, Forschungszentrum Karlsruhe 1998
- [7] K. Werner, Phys. Rep. **232** (1993) 87
- [8] K. Greisen, Ann. Rev. Nucl. Particl. Sci. **10** (1960) 63
- [9] I.M. Brancus et al., FZKA-report 5835, Forschungszentrum Karlsruhe 1996



The Response of the EAS Muon Component in the GAMMA Detector Array

M.Z Zazyan^{1*}, A.F. Badea², A.P.Garyaka¹, A.Haungs³, R.M. Martirosov¹, H. Rebel³

¹*Yerevan Physics Institute, Cosmic Ray Division, Armenia*

²*National Institute of Physics and Nuclear Engineering - Horia Hulubei, Bucharest, Romania*

³*Institut für Kernphysik, Forschungszentrum Karlsruhe, Germany*

The response of the EAS muon component is studied by the detector simulation program ARES, developed for the GAMMA installation on Mt.Aragats (ANI Cosmic ray Observatory). The studies are directed to investigations of the features of the lateral distributions and the muon arrival time response. Comparisons with experimental data are presented.

1 Introduction

In order to interpret the results of EAS experiments the detailed modeling of the development of the EAS in the atmosphere and of response of the detector are required.

The response of the EAS muon component in the GAMMA installation [1, 2] is simulated by the detector simulation program ARES [3] based on the GEANT package [4] and specified to the actual layout of the installation, which consists of the surface part for the registration of the EAS soft component, a calorimeter building and the large muon underground detector to register the muon component.

The muon underground detector consist of two parts (see also [5]): 60 plastic scintillators (100*100*5 cm³) are placed in the underground hall below the ANI calorimeter building, and another 90 detectors are installed in the so-called tunnel. The detectors are built into aluminum or iron pyramid-shaped housings [6]. The thresholds for muon detection are $\approx 5\text{GeV}$ in the hall and $\approx 2\text{GeV}$ in the tunnel. The EAS simulations are performed using the CORSIKA version 5.62 [7] with NKG option and use of the high energy interaction model QGSJET and the GHEISHA for interactions at lower energies. Using CORSIKA data together with ARES program the response of the EAS secondary particles in the detectors is simulated to get the energy deposits and arrival times of each particle in the individual detector.

2 Muon Lateral Distribution

In the present analysis the air shower initiated by primary protons and irons with $E_0 = 10^{15}$ eV, $\theta = 0^\circ$ are considered. The shower core positions are varying randomly within the square of 60m*60m with the center in the middle of the calorimeter. This represents roughly the experimental shower selection.

The methodical procedure of the muon number estimation is described in [8]: to deduce the number of muons registered by each detector ("estimated" muon number) the sum of deposited energy in the detector has to be divided by factor of 9.5 MeV as a first approximation. This is compared with the

*corresponding author: mary@jerewan1.yerphi.am

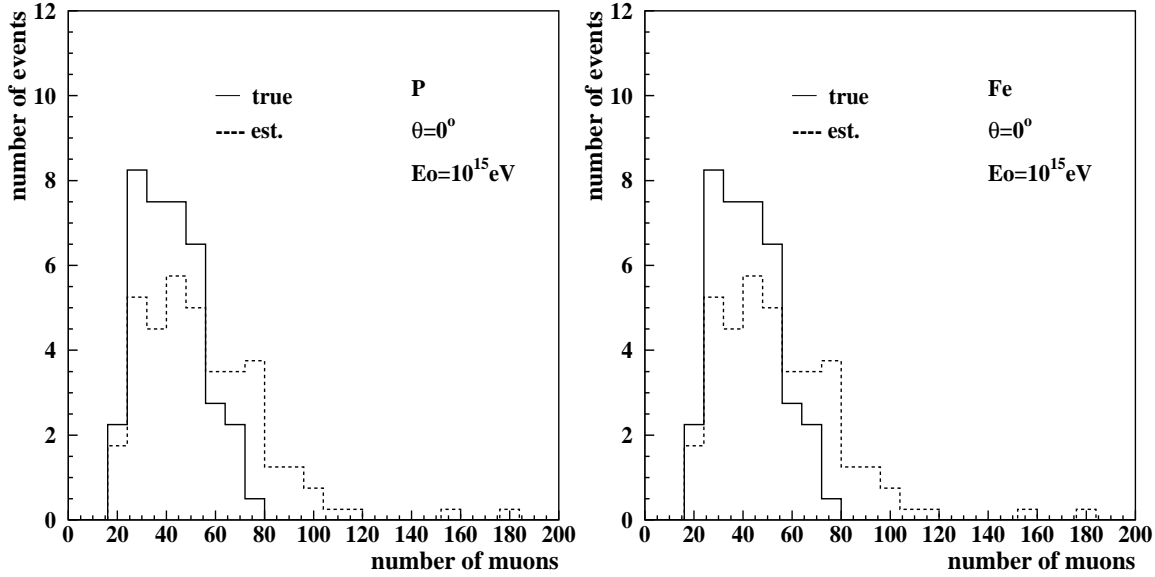


Figure 1: "True" and "estimated" muon numbers in all scintillators for proton and iron induced showers (simulated EAS with its core distributed in a square of 60m*60m around the center of the ANI calorimeter [5]).

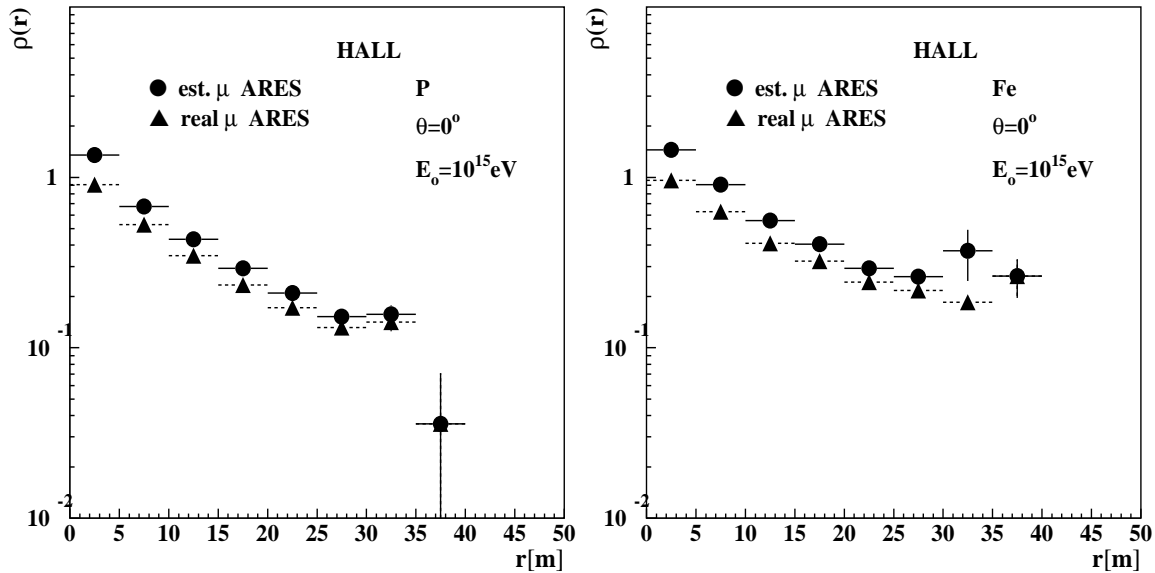


Figure 2: The lateral distributions of "true" and "estimated" muons in proton and iron induced showers for the hall detectors.

"true" muon number which is known due to the simulation procedure (see Fig.1). One can see some overestimation of muon number due to hadronic punch-through or due to high-energetic secondaries ("delta"- or "knock on"-electrons) produced in the shielding.

Using these muon numbers we can construct pseudo-experimental data (including primary energy of shower, angle of incidence, core coordinates and the energy deposits at each of the 150 detectors) from which we can calculate the muon lateral distribution function.

The lateral distributions of "true" and "estimated" muons in showers initiated by primary protons and iron nuclei with primary energy $E_0 = 10^{15}$ eV are presented in the Fig.2 and Fig.3 for the hall and tunnel detectors.

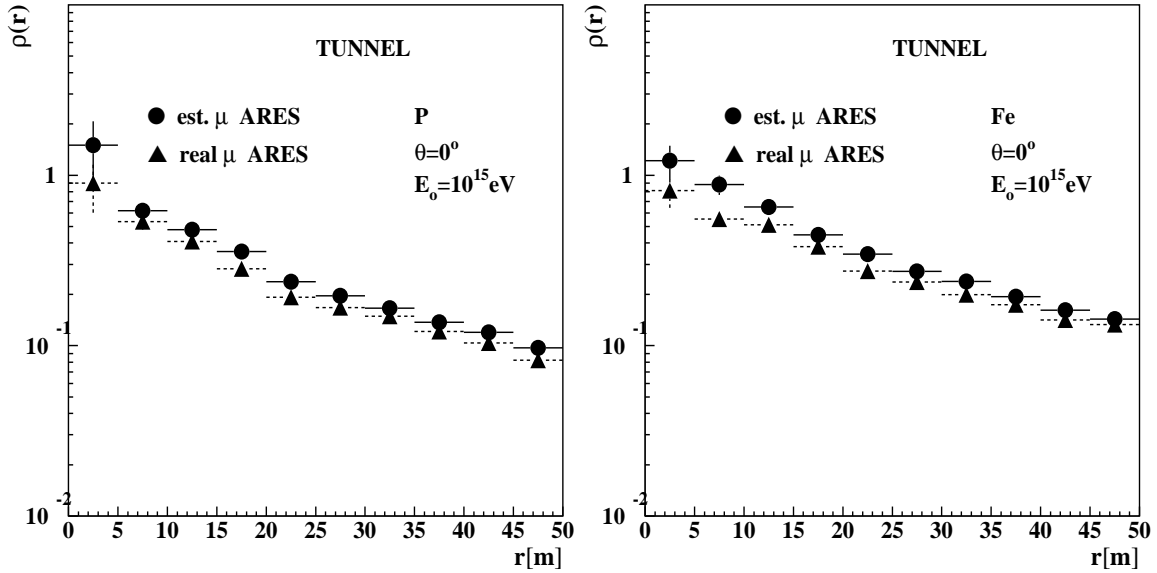


Figure 3: The lateral distributions of "true" and "estimated" muons in proton and iron induced showers for the tunnel detectors.

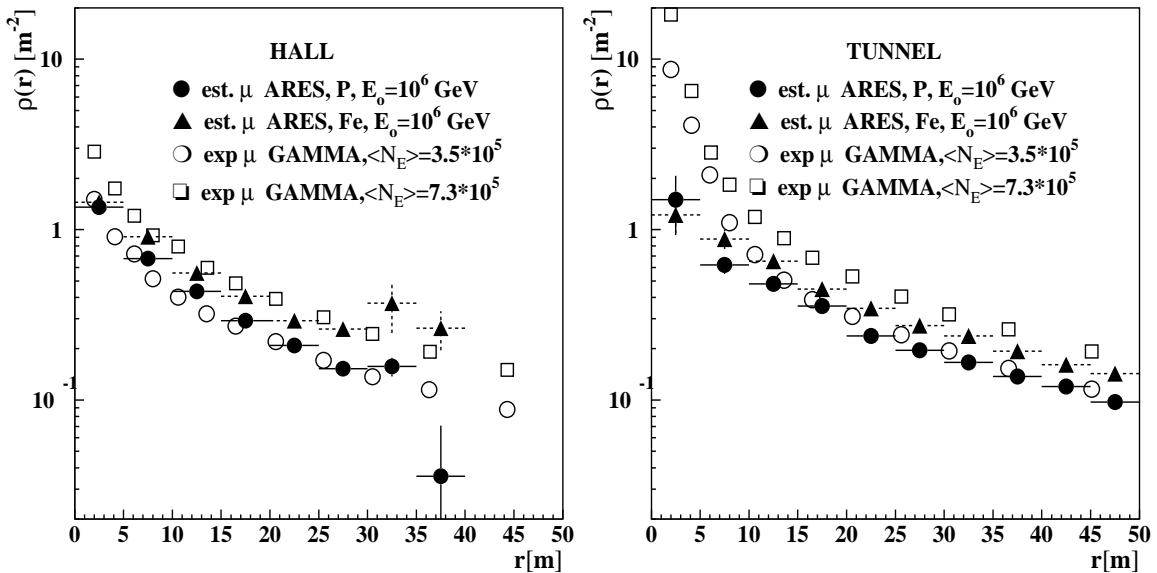


Figure 4: Simulated and experimental muon lateral distributions in the hall and tunnel detectors.

In Fig.4 the muon lateral distributions for proton and iron induced EAS are compared with the experimental data for two different shower size ranges. In each experimental sample classified along the shower size showers initiated by protons are prevailing. That is why there is a good agreement

between muon lateral distributions for proton induced EAS and data for $\langle N_e \rangle = 3.5 * 10^5$, which is the mean shower size for simulated proton showers. It has to be noted that this comparison is not correct for showers initiated by irons as far as in an EAS sample classified along the shower size the heavy primary induced EAS have a higher energies.

Some differences in the distributions could be due to the various factors, such as angles of incidence (in experimental sample it is $0 - 30^\circ$), fixed primary energy of simulated EAS, inaccurate description of uneven ground layer due to hilly place, the shower selection procedure (in the experiment we select the showers with axis inside the circle with the radius of 30m from the calorimeter center) et al. For the tunnel case the differences in simulated and experimental data below 10m are due to the punch-through of the electromagnetic EAS component which is not included in the simulation (CORSIKA with NKG-option). The shielding in case of the hall is thick enough to absorb this component in total.

3 Arrival Time Distributions of EAS Muon Component

For the investigation of the possibility to separate proton induced showers from iron induced showers in GAMMA experiment using the time distributions we considered the muon arrival time distributions [9] for two cases of shower positions - randomly within the calorimeter area ($X_{core} = -9m \pm 30m$, $Y_{core} = 20m \pm 30m$) and within the remote from the muon detector quarter of the calorimeter ($X_{core} = -24m \pm 15m$, $Y_{core} = 35m \pm 15m$).

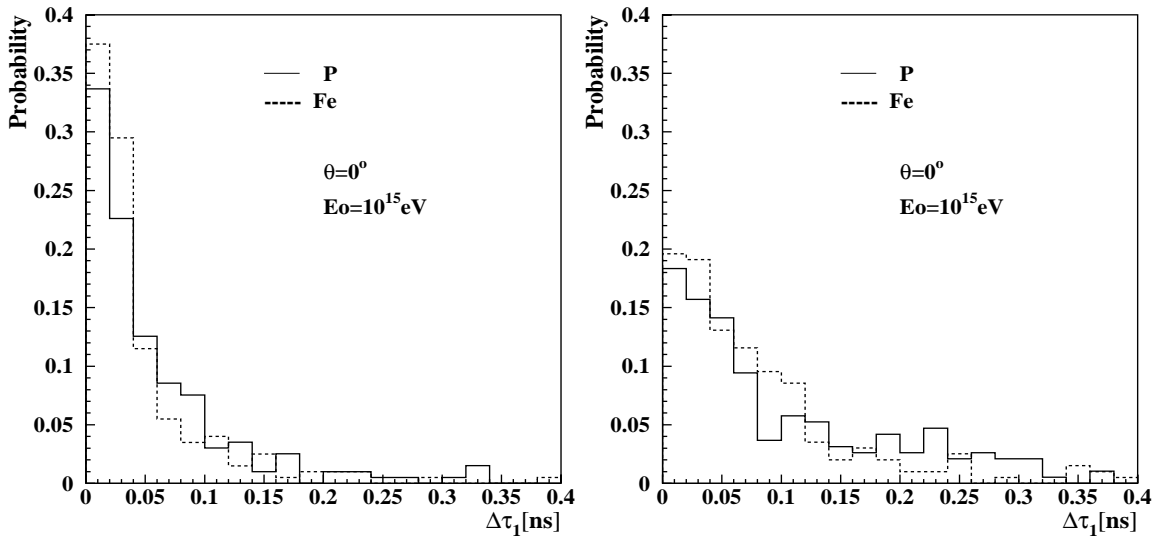


Figure 5: *The arrival time of the first muon in the muon detector for the showers randomly positioned within the calorimeter area (left) and within the area of remote quarter of the calorimeter (right).*

Fig.5 and Fig.6 show the distributions of the foremost muon and of the median values of the muon arrival times relative to the arrival of the core [10] for $E_0 = 10^{15}$ eV and $\theta = 0^\circ$. Of course, arrival time distributions depend on the primary energy E_0 , the inclination of the shower axis θ and the distance R_μ from the shower core. But one can see that it will be difficult to separate proton and iron induced showers with the distances from the muon detector to the shower axis available in the GAMMA installation.

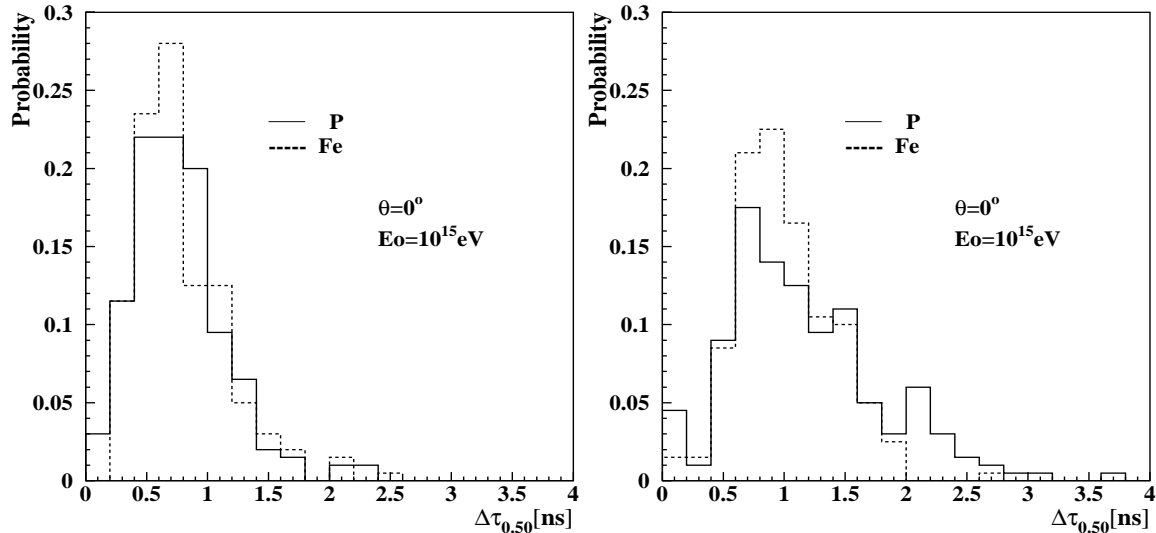


Figure 6: *The median muon arrival time in the muon detector for the showers randomly positioned within the calorimeter area (left) and within the area of remote quarter of the calorimeter (right).*

4 Conclusion

The detector simulation program ARES for GAMMA installation has been developed. The present studies examined that ARES works well.

In the future, the correct comparison of simulation results with experimental data will allow us to infer information on the mass of the primary particle.

Acknowledgement

We acknowledge the support of Yerevan Physics Institute, of IPNE Bucharest and of Forschungszentrum Karlsruhe to bring together the expertise of the authors. One of us (M. Zazyan) thanks J. Oehlschläger for the help in CORSIKA simulations.

References

- [1] S.A. Arzumanyan et al., Proc. 24th ICRC (Rome) 1 (1995) 482
- [2] A.A. Chilingarian et al., Proc. 16th ECRS (Alcala de Henares) (1998) 445
A.A. Chilingarian et al., Proc. of the Workshop ANI 98, eds. A.A. Chilingarian, H. Rebel, M. Roth, M.Z. Zazyan, FZKA 6215, Forschungszentrum Karlsruhe 1998, p27
- [3] A. Haungs, A.F. Badea, M.Z. Zazyan, ANI Workshop 1999, these Proceedings.
- [4] GEANT: CERN Program Library Long Writeup W5013, CERN (1993)
- [5] A.F. Badea et al., Proc. of the Workshop ANI 98, eds. A.A. Chilingarian, H. Rebel, M. Roth, M.Z. Zazyan, FZKA 6215, Forschungszentrum Karlsruhe 1998, p.77
- [6] H.J. Mathes et al., Proc. of the Workshop ANI 98, eds. A.A. Chilingarian, H. Rebel, M. Roth, M.Z. Zazyan, FZKA 6215, Forschungszentrum Karlsruhe 1998, p.91
- [7] D. Heck et al., FZK-Report 6019, Forschungszentrum Karlsruhe 1998

- [8] M.Z.Zazyan, A. Haungs, Proc. of the Workshop ANI 98, eds. A.A. Chilingarian, H. Rebel, M.Roth, M.Z. Zazyan, FZKA 6215, Forschungszentrum Karlsruhe 1998, p37
- [9] I.M. Brancus et al., FZKA-Report 6151, Forschungszentrum Karlsruhe 1998
- [10] A.F. Badea et al., ANI Workshop 1999, these proceedings, p.99

Calibration of Scintillation Detectors for the Aragats EAS Installation

S.V. Blokhin¹, V.A. Romakhin^{1*},
G.G. Hovsepyan²

¹*Lebedev Physics Institut of Russian Academy, Russia*

²*Yerevan Physics Institute, Cosmic Ray Division, Armenia*

The lateral distribution functions (LDF) of observed densities of particles measured by scintillation detectors with different thicknesses (5 cm, 1.5 cm and 1.0 cm) are investigated. Comparisons of the corresponding LDFs provide the possibility to reconstruct the "true" EAS particles density from the data measured with 5 cm thick scintillation detectors as used at the MAKET-ANI installation.

1 Introduction

In the investigations of the MAKET-ANI detector installations the lateral density distribution of the EAS particles is usually determined in the distance from 3 m to 100 m from the shower axis. The measured lateral distribution is fitted to Nishimura-Kamata-Greisen (NKG) form for the electromagnetic component of air showers:

$$\rho(r) = \frac{N_e}{r_m} C(s) F(r/r_m, s) \quad (1)$$

where $\rho(r)$ is the expected density at distance r from the EAS core position, N_e is the EAS size, $r_m = 118$ m (for the ANI altitude) is the Molière radius, s is the so called EAS age, and $C(s) = 0.366s^2(2.07 - s)^{1.25}$ [1].

If scintillation detectors are used for EAS particle density measurements, the experimentally registered densities have to be corrected to get the real particle density. Since the thickness of the plastic scintillation detector is finite, the particle density measured by 5cm thick plastic scintillators is affected by various effects, such as gamma ray conversions, nuclear interactions in the scintillator, absorption of low energy electrons etc. The difference between the experimentally observed density $\rho_{exp}(r)$ and the expected density $\rho_{true}(r)$ can be accounted by a function $R_{sc/ch}(r)$ which is estimated by an experimental calibration procedure [2-7] or by Monte-Carlo simulations [8].

2 Experimental determination of $R_{sc/ch}(r)$

The MAKET-ANI and GAMMA standard detectors are 5 cm thick plastic scintillators, which display a sufficiently large amplitude and timing resolution [9]. For the investigation of $R_{sc/ch}(r)$ at the MAKET-ANI installation two additional scintillation detectors with sizes of $30 \times 30 \text{ cm}^2 \times 1 \text{ cm}$ and $50 \times 50 \text{ cm}^2 \times 1.5 \text{ cm}$ have been used. For all scintillators the PM high voltage setting and tuning is performed in similiar way, as described in ref [10]. The thin scintillation detector is assumed to registrate an approximately correct particle density. Hence a comparison between the particle density measured with the thin detector and the density estimated with the standard detector ($100 \times 100 \text{ cm}^2 \times 5 \text{ cm}$) located at the same place in the EAS array is performed. The investigation uses samples of showers characterised by:

*corresponding author: romakhin@x4u.lpi.ruhep.ru

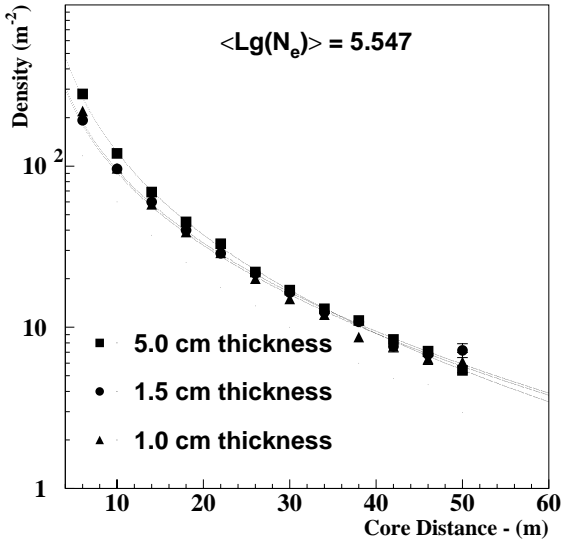


Figure 1: Average LDF for 5cm, 1.5cm and 1.0cm thick detectors. The parameters of the NKG form are presented in Table 1.

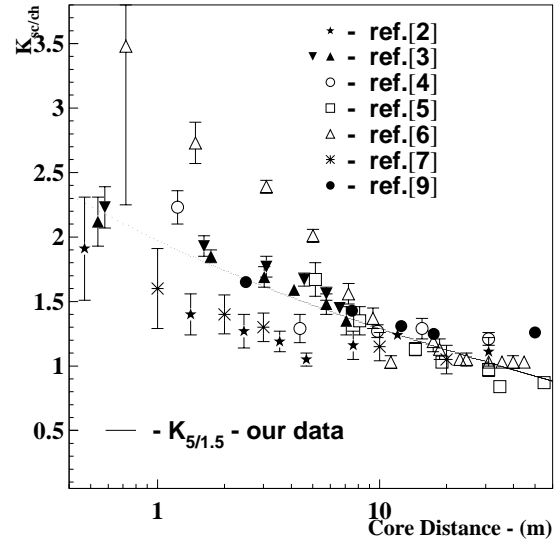


Figure 2: Experimental data obtained by calibration function for different installations. $K_{5/1.5}$ is defined by (2) from ratio of average LDFs for 5cm and 1.5cm thick detectors and $\langle \lg N_e \rangle = 5.547$.

- 1) EAS size: $1.5 \cdot 10^5 \leq N_e \leq 1 \cdot 10^6$;
- 2) age parameter $s \sim 0.3 \div 1.7$ and zenith angle $\theta < 30^\circ$;
- 3) EAS core position: $|x| \leq 24$ m and $|y| \leq 12$ m with x_0, y_0 as the coordinates of the geometrical center of the MAKET-ANI facility.

The LDF for the 5.0 cm, 1.5 cm and 1.0 cm detectors and for three EAS size intervals ($\langle \lg N_e \rangle = 5.324$, $\langle \lg N_e \rangle = 5.547$ and $\langle \lg N_e \rangle = 5.77$) are reconstructed (one of them is presented in Figure 1). The ratio of the NKG approximation for two detectors with different thicknesses (t_1 and t_2 in cm) leads to the calibration function:

$$K_{t_1/t_2}(r) = \frac{\rho_{exp}^{t_1}(r)}{\rho_{exp}^{t_2}(r)} \quad (2)$$

The calibration function measured for different EAS sizes and detector configurations (3.5 cm thick scintillator for [2], 5 cm for [3-5,7], 30 cm for [6]) are presented at Figure 2. The results of the present investigation are shown by the line on the same figure. In all quoted experiments for the calibration of scintillation detectors, the LDFs deduced by densities measured with standard detectors are compared with LDFs measured with detectors which have a low energy registration threshold and a low efficiency for γ conversion (gas counters at ref. [2-5], and a 0.3 cm thick scintillation detector at [7]). However, as shown in [11] the gas counters had a real threshold of 1-1.7 MeV (by housing, glass tubes etc.).

For our investigations we use thin plastic scintillators located in the same place as MAKET-ANI scintillators. The scintillators with thicknesses 5 cm, 1.5 cm and 1.0 cm are equivalent to 0.125, 0.038 and 0.025 radiation units, respectively. Assuming that, due to the relatively small thickness

Table 1: The parameters of NKG form (1) for three EAS size intervals for detectors of different thicknesses.

	N_e	age		N_e	age		N_e	age
5.0cm	$2.11 \cdot 10^5$	0.750	1.5cm	$1.99 \cdot 10^5$	0.901	1.0cm	$1.91 \cdot 10^5$	0.929
	$3.53 \cdot 10^5$	0.707		$3.19 \cdot 10^5$	0.886		$3.09 \cdot 10^5$	0.899
	$5.89 \cdot 10^5$	0.871		$5.02 \cdot 10^5$	0.871		$4.84 \cdot 10^5$	0.890

Table 2: Average of the experimentally shower parameters after correction with (5) and $\alpha = 0.18$.

	N_e	age
<i>Maket - ANI</i>	$1.87 \cdot 10^5$	0.927
	$3.00 \cdot 10^5$	0.903
	$4.81 \cdot 10^5$	0.894

of the scintillation detectors, processes of γ conversion and efficiency losses due a nonzero detector threshold linearly depend on the thickness of the detector, we obtain after simple transformations following expression (using 1.5 cm and 5 cm scintillators):

$$\rho_{true}(r) \approx \frac{1.5}{5 - 1.5} \cdot \rho_{exp}(r) \left(\frac{5}{1.5 K_{5/1.5}(r)} - 1 \right). \quad (3)$$

We check this relation with help of the data obtained by the 1 cm and 5 cm thick detector:

$$\rho_{true}(r) \approx \frac{1}{5 - 1} \cdot \rho_{exp}(r) \left(\frac{5}{K_{5/1}(r)} - 1 \right). \quad (4)$$

where $\rho_{true}(r)$ is the density of all charged particles and $\rho_{exp}(r)$ is the experimentally observed density at the 5 cm thick detector, $K_{5/1.5}(r)$ and $K_{5/1}(r)$ are defined by (2).

3 Results and Discussion

The EAS sizes and age parameters of the LDF give by eq.(1) are presented in Table 1 for the 5 cm, an 1.5 cm and 1 cm thick detector and for three intervals of N_e . We assume that the dependence of $R_{sc/ch}$ from the EAS core position follow the functional form [12, 13]:

$$R_{sc/ch}(r) = \frac{\rho_{exp}(r)}{\rho_{true}(r)} = \left(\frac{r}{r_m} \right)^{-\alpha}. \quad (5)$$

The values of the parameter α obtained from the fit to expression (5) are 0.15, 0.19 and 0.22 for the three N_e intervals.

To confirm this result we analyzed additionally the data of the 5 cm and 1.0 cm thick detectors. For this pair we obtain α values of 0.16, 0.18 and 0.21 respectively. This results agree with estimates of $\alpha = 0.18$ obtained by earlier investigations [12].

The experimental showers from the MAKET-ANI installation data bank have been recalculated using corrections (5) for $\alpha = 0.18$. The resulting average values of EAS size and age are presented at Table

2. The correction form (5) with $\alpha = 0.18$ satisfactorily approximates the observed mean values of the age parameter. The discrepancy of the observed age parameter does not exceed ± 0.03 depending on the EAS size.

References

- [1] V.S. Aseykin et al., Proc. of Lebedev Physics Institute **109** (1979) 3 (in Russian)
- [2] S. Kawaguchi et al., Proc. 12th ICRC (Hobart) 7 (1971) 2736
- [3] T.P. Amineva et al., Izv. AN USSR, Ser. Phys. **33** (1969) 1508 (in Russian)
- [4] A. Bakich et al., Proc. 11th ICRC (Budapest) 3 (1969), 501
- [5] V.A. Dadikin et al., Izv. AN USSR, Ser. Phys. **38** (1974) 1101 (in Russian)
- [6] V.A. Tizengauzen, Ph.D. Thesis, Baksan Neutrino Observatory, Institute for Nuclear Research, Moscow (1979) (in Russian)
- [7] T. Hara et al., Proc. 17th ICRC (Paris) 6 (1981) 52
- [8] J.H. Weber for the KASCADE Collaboration: Proc. 25th ICRC (Durban) 6 (1997) 153
- [9] T.V. Danilova et al., Izv. AN Arm. SSR, Ser. Phys. **17** (1982), 129 (in Russian)
- [10] G.Hovsepyan for ANI Collaboration, Proc. of the Workshop ANI 98, eds. A.A. Chilingarian, H.Rebel, M. Roth, M.Z. Zazyan, FZKA 6215, Forschungszentrum Karlsruhe 1998, p.45
- [11] A.I. Goncharov et al., Izv. AN USSR, Ser. Phys. **53** (1989) 330 (in Russian)
- [12] V.V. Avakyan et al., Yad. Fiz. **55** (1993) 174 (in Russian)
- [13] V.S. Murzin, Introduction of Cosmic Ray Physics, Moscow (1979) 275 (in Russian)

Some Comments on the Significance of Arrival Time and Angle-of-Incidence Distributions of EAS Muons

H.Rebel*

Institut für Kernphysik, Forschungszentrum Karlsruhe, Germany

In view of various approaches of installing efficient timing facilities in EAS detector arrays and current measurements of arrival time and angle-of-incidence distributions of EAS muons the information potential of such type of studies is discussed.

1 Introduction

Information about the longitudinal development of EAS (expressed by adequate parameters like the atmospheric depth X_m of the EAS maximum or the elongation rate) is of extreme interest and highly relevant for the task to disentangle the twin problem, which we are faced to in EAS physics: Determination of the nature of primary particles arriving from the cosmos and simultaneously of the nature of the hadronic interactions of these particles with the atmospheric nuclei at ultra high energies. Figure 1 displays the development of the total intensities (sizes) of the main EAS components as predicted by realistic Monte Carlo simulations. While the size of electromagnetic cascade develops to a well pronounced maximum (at the atmospheric depth X_m) with a subsequent decline when penetrating deeper in the atmosphere and the absorption processes are going to overcompensate the production of neutral pions, the muon cascade appears with a different shape, with a less pronounced decrease after reaching a maximum. Obviously the cascade curves for primary particles of different types have different shapes, in particular they differ in the position of the EAS maximum. However, we should be aware that the longitudinal development of single showers is subject of considerable fluctuations which obscure the differences when showers of different kinds are compared. In order to give an immediate impression about the strong fluctuations of the EAS development Figs. 2 and 3 display the size distributions of 10^{15} eV proton and iron induced EAS (from 1000 events of vertical incidence, simulated by CORSIKA with EGS), respectively for various observation levels. The fluctuations get obviously minimised for the atmospheric depth of

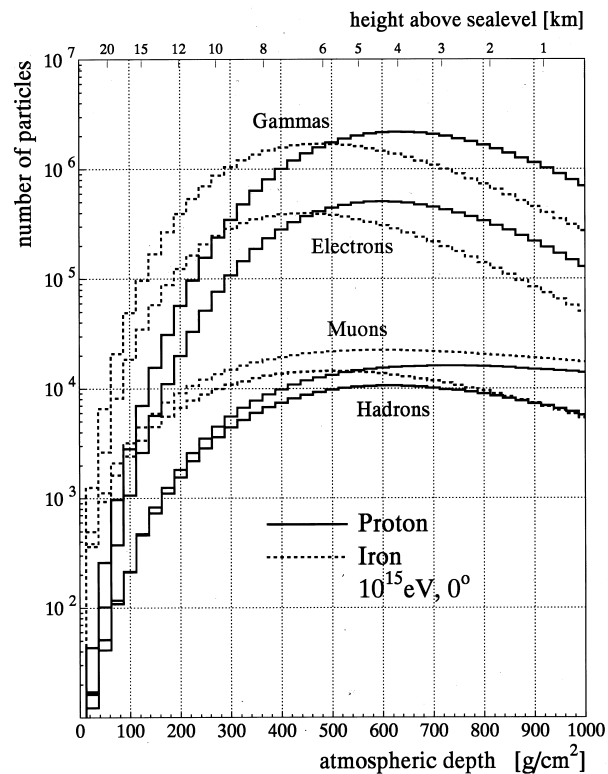


Figure 1: *The average longitudinal development of the various EAS components as predicted by Monte Carlo simulations using the CORSIKA code [1].*

*email: rebel@ik3.fzk.de

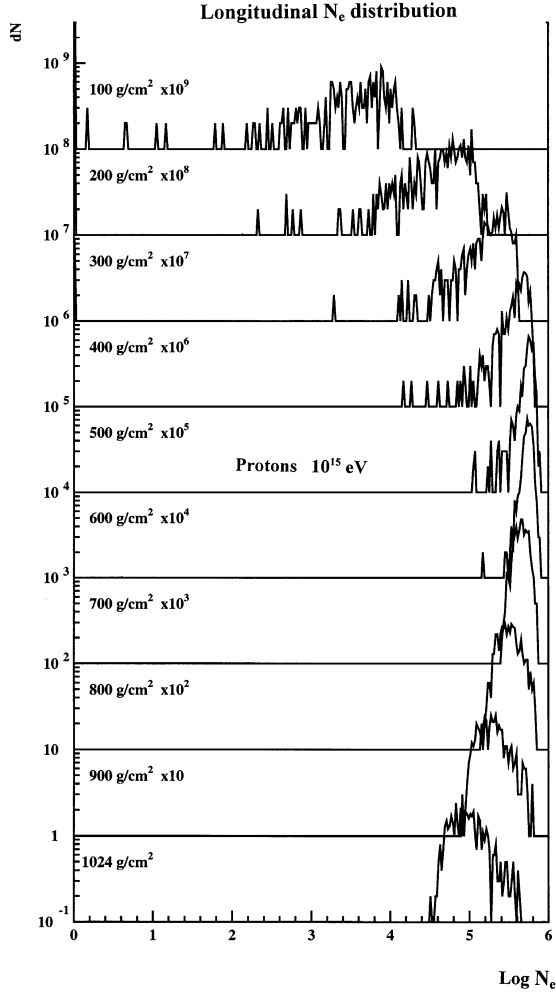


Figure 2: *Simulated N_e distribution for proton induced EAS with the primary energy of 10^{15} eV [2].*

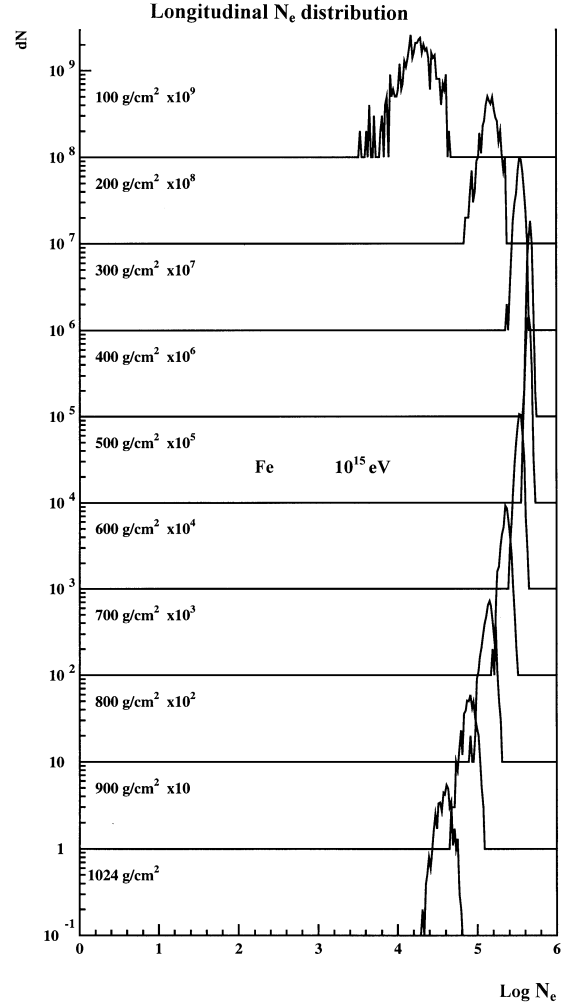


Figure 3: *Simulated N_e distribution for iron induced EAS with the primary energy of 10^{15} eV [2].*

500-600 gcm^{-2} .

The standard observables measured with ground based detector arrays inform merely about the actual state of the development of extensive air shower, just how it appears on the observation level. The sizes (N_e , N_μ) of the various components are deduced by integrating the more or less widely spread out lateral particle densities. The EAS muons e.g. which themselves or whose parents (charged pions and kaons) have acquired larger transverse momenta, are deflected to larger radial distances from the shower axis. The shape of the lateral distribution carries information about the status of the EAS development, expressed in parameterisations of the lateral charged particle distributions by the so-called age parameter. It quantifies the effect that the lateral charge particle distribution of a proton induced shower appears to be steeper than the distribution of an iron induced EAS of the same primary energy, just due a different longitudinal development.

There are historically well worked out attempts to infer some information about the average longitudinal development of the EAS variables near the observation level of the ground based detector

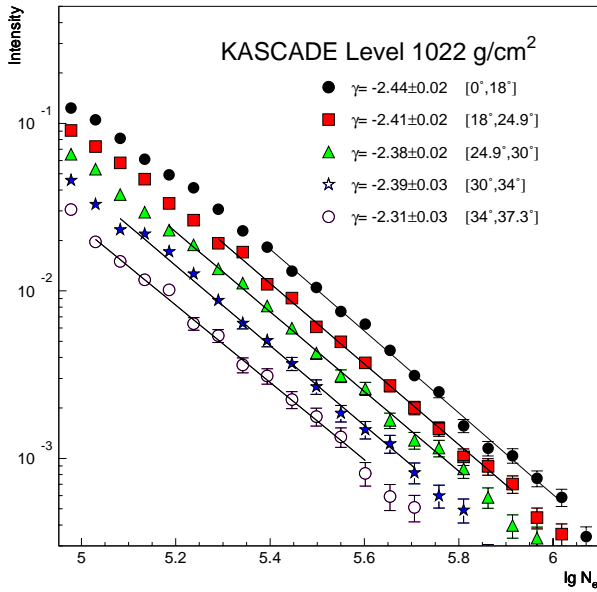


Figure 4: N_e spectra generated by EAS simulations from a primary energy spectrum $I \propto E^{-2.7}$ of protons at different observation levels and observed under different zenith angles of EAS incidence [3]. (γ represents the spectral indices of the N_e spectra.)

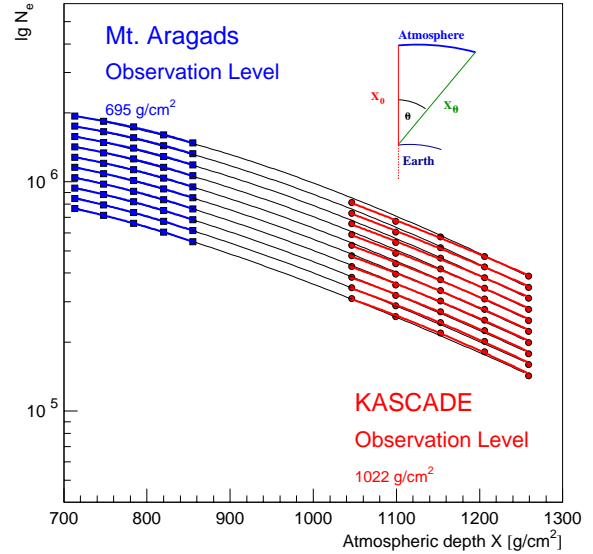


Figure 5: N_e cascades curves reconstructed along constant intensities of the N_e spectra observed under different zenith angles (see Fig.4).

array by observations under different zenith angles of EAS incidence, i.e. by observing the same class of showers after traversing different atmospheric depths X .

Figure 4 shows N_e spectra generated by EAS simulations (CORSIKA Monte Carlo simulations [1] with the NKG approximation) calculated from a primary energy spectrum $I \propto E^{-2.7}$ at different observation levels and observed under different zenith angles of EAS incidence [3]. From such spectra observed in various experiments (see Ref. [4]), relating equal intensities (more strictly equal primary energies identified by an adequate energy indicative EAS parameter) the cascade curves can be reconstructed (Fig.5). These cascade curves may be further analysed in terms of the attenuation of the shower development [4]. In a similar way the average age parameter observed under different zenith angles i.e. in different stages of the EAS development can be studied [5].

High-energy charged particles generate Cerenkov radiation which is strongly forward peaked and can be detected on ground. It is emitted by the shower cascade throughout the atmosphere and offers the possibility of measuring the total energy of the shower and of tracing the rate of build up the shower. Due to the changing refractive index and the characteristic Cerenkov angle the lateral distribution has a particular structure, and the shape of the distribution around 100 m gets sensitive to the height of emission. The light from the early part, where the energy of the particles are still very high and the scattering angles small is concentrated in a characteristic ring near 100 m. The resulting lateral distribution is the superposition from all heights and its shape depends on the shower development. If the shower maximum gets nearer to the ground, more light is produced near the shower core. That means the lateral distribution drops steeper, the closer the shower maximum approaches the detector. There is a correlation between the distance to the shower maximum and a slope parameter of the

Cerenkov light distribution $\rho_c = \rho_0 \exp(R \cdot \text{slope})$. The correlation proves to be independent from the type of the particle and the angle - of - shower incidence.

The information about the depth X_m of the shower maximum is related to information about the mass of the primary particle. The change of the position of the depth of the EAS maximum with the energy per decade, the so-called elongation rate is fairly constant. As consequence of the superposition model approximation i.e assuming that for the heavy primary (A) the X_{max} dependence scales with E/A , the mean atmospheric depth of the maximum depends only from the energy per nucleon of the primary. This is confirmed by simulations, but showing also considerable fluctuations, decreasing with the nucleon number A. With the average E/A deduced from X_m of maximum we gain information about the average mass, if independently the energy E of the primary can be determined [6].

Another efficient technique enabling the investigation of the longitudinal EAS development, in particular the distribution of X_{max} , relies on the excitation of nitrogen fluorescence in air by the passage of charged particles. By observation of the fluorescence light using large facilities like Fly's Eye [7] it is possible to reconstruct the size of EAS as function of the atmospheric depth, especially for high energy showers (for details see Ref.[7]).

Muons, associated with extensive air showers (EAS), carry valuable information on parent particles and reveal significant details of the production processes. Though the muon component is less copious and laterally more spread than the dominant electron gamma component, it reflects the properties of the parent particles and the development of the air shower cascade in a less distorted way. This is due the relatively direct coupling to the hadronic backbone of the EAS and due to the weak absorption and reduced Coulomb scattering of the muons, travelling through the atmosphere. From studies of the multiplicities at ground level or bundles of high energy muons observed deep underground, we may infer information about the first generations of interactions and of the leading shower particles. The following remarks will focus the attention to the particular information carried by the distributions of the arrival times of muons arriving at the detectors of ground-based arrays. They map the longitudinal development of the muon component, due to the fact that higher energy muons travel relatively undisturbed, like a light ray, through the atmosphere, so that their times of flight or angles of incidence do point to the loci of production [8, 8, 10]. Based on this feature the central detector of the KASCADE experiment [11] is equipped with a timing facility, a muon eye of 456 fast scintillation detectors to measure the muon arrival times relative to the arrival time of the shower core (global times) or relative to the arrival of the first muon in the detector (local times) [12]. Realising the great importance of the time dimension of shower variables for constraining the experimental information on the longitudinal EAS development and for controlling Monte Carlo simulations, the installation of a timing facility for the GAMMA array of the ANI Cosmic Ray Observatory on Mt. Aragats in Armenia has been proposed and advocated [13]. In following we consider some features of arrival time distributions, in particular with a closer look, of the EAS muon component.

2 Arrival time distributions of EAS particles

The particles of extensive air showers move nearly in the direction of the primary particle with velocities close the velocity of light. Transverse momenta and multiple scattering produce a lateral dispersion. Differences in the velocities and, in particular, in the path-length, when travelling through the atmosphere, are origin of a longitudinal dispersion of the air shower disc. This dispersion is reflected by the variation of the arrival times, for particles observed at a particular fixed arrival locus - this is the temporal structure i.e. the thickness of the shower disc -, as well as for particles of the extreme front (approximately, but with non-negligible fluctuations, represented by the arrival time of the first particle), observed at different distances from the shower centre. In the latter case the

relative arrival times reflect the shape (curvature) of the front and the direction of incidence of the shower.

We may quote Bassi, Clark and Rossi 1953 [14], who presented the first systematic experimental information about the time-structure of EAS and established the procedure to determine the arrival direction of EAS with the arguments:

”Particles in an extensive air shower, generated by a single high-energy particle incident on the top of the atmosphere, may be delayed with respect to one another at plane of observation because

- path lengths may differ as a result of scattering
- velocities may differ
- the axis of the shower may not be perpendicular to the plane of observation.“

Bassi et al. [14] determined the mean shower thickness (mean time delay) equivalent to 4-8 ns and the curvature of the front with a radius of more than 1300 m. For the penetrating component the curvature proves to be smaller, with a shower disc thickness equivalent to ca 8 ns, but with a mean value timely delayed by more than 10 ns compared to the electromagnetic component. The latter feature has been disproved: the muon disc walks *ahead* of the electromagnetic front.

Linsley and Scarsi [15] and Thielert and Wiedecke [16] systematically explored the lateral dependence of the shower thickness, expressed by the median delay time relative to the arrival time of the shower core. The increase of the time dispersion with the distance from the shower centre has been revealed. Since these early studies the time structure of the EAS charged particle component has been experimentally studied under various aspects. Walker and Watson [17, 18, 19] exploring the time structure of the charge particle component, and directed the interest to fluctuations, whose origin could be interpreted as fluctuations of the height of maximum of the shower development due to different masses of the primaries, as consequence of different interaction lengths of the primaries and the multiplicities, energy and momentum distributions of the secondaries [20]. More recently Agnetta et al. [21] and Ambrosio et al. [22, 23] presented detailed results about various dependences of the temporal structure of

EAS charged particles, based on measurements with the GREX/COVER-PLASTEX set-up [21]. The aspect that arrival time distributions of muons of higher energies do map the longitudinal shower development [24] has been pursued by detailed investigations of the temporal structure of the muon component with the underground water-Cerenkov-detector set-up of the Haverah Park experiment by Blake et al. [25]. They explored the dependence of the time-delay on the inclination θ of the

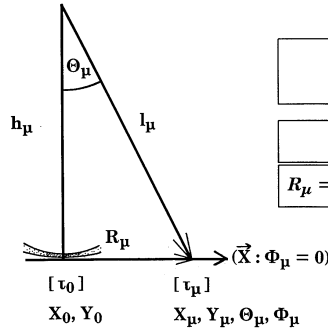
Advantages of muons:

- **Enhanced sensitivity to earlier stages of the EAS cascade**
- **Directly coupled to the nuclear cascade and not mediated by the e/y component like Č-photon**
- **”Seen” all the day, not only in clear and moonless nights**

$$\tau_{\mu} = f(\mathbf{E}_0, \mathbf{E}_{\mu}, \mathbf{R}_{\mu}, \Theta)$$

Muon delay time:

$$\begin{aligned} \Delta\tau_{\mu} &= \tau_{\mu}(\mathbf{R}_{\mu}) - \tau_{\text{core}} \\ &= l_{\mu} / \beta_{\mu} c - h_{\mu} / c \end{aligned}$$



$$h_{\mu}^{\tau} = \frac{R_{\mu}^2 - (c \Delta\tau)^2}{2 c \Delta\tau}$$

$$h_{\mu}^{tr} = R_{\mu} / \tan \Theta_{\mu}$$

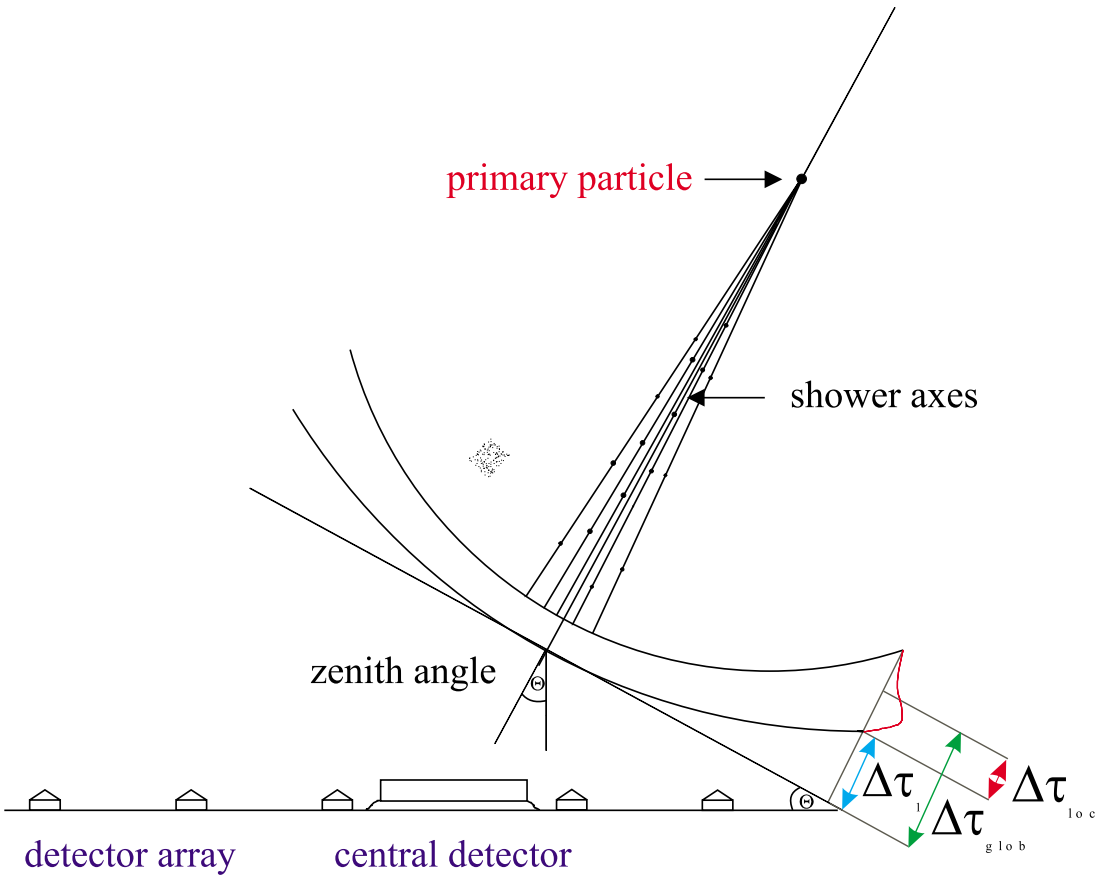
$$R_{\mu} = (X_{\mu} - X_0) \cos \Phi_{\mu} - (Y_{\mu} - Y_0) \sin \Phi_{\mu}$$

Mean arrival time $\Delta\tau$ and dispersion σ

Relative arrival time of the foremost muon

$$\Delta\tau_{\mu}^1 = \tau_{\mu}^1 - \tau_{\text{core}}$$

Figure 6: Relation of arrival-time and angle-of-incidence to muon production height.



- Single Shower: $\Delta\tau_1$ relative to the arrival of the core
 = shower front
 σ_1 fluctuations of the shower front
 $\{\Delta\tau_{0.50}^{loc}, \Delta\tau_{0.25}^{loc}, \Delta\tau_{0.75}^{loc}\}$: intrinsic structure
 = time spread = shower thickness
- Average Shower: $\{\langle\Delta\tau_{0.50}^{loc}\rangle, \langle\Delta\tau_{0.25}^{loc}\rangle, \langle\Delta\tau_{0.75}^{loc}\rangle\}$
 = average intrinsic time spread
 = average thickness
 $\{\sigma_{0.50}, \sigma_{0.25}, \sigma_{0.75}\}$ = dispersion of distributions
 of the quartiles of the single shower around
 the average

Figure 7: Air shower front and time profile.

shower axis, on the primary energy E_0 (or shower sizes N_e and N_μ , respectively), and on the distance R_μ from the shower core.

The experimental interest of this specific kind of EAS investigations is directed to measurements of EAS observables which represent the arrival time distributions, i.e. the distributions of various characteristic quantities T like the mean values, median values of the fluctuating individual distributions etc. and their dispersions. The variation of the mean of these quantities with the distance from the shower core R_μ represents the EAS time profile [11]. It depends on the energy E_0 , the mass M of the primary particle (reflected by adequate shower variables like N_e, N_μ), on the angle θ of shower incidence and additionally on biasing trigger and observation conditions: energy threshold E_{thres} and multiplicity n of the muon detection. The general interest is focussed to the arrival time distribution or to various characteristic parameters Q (mean value and dispersion e.g.)

$$Q_t = F(E_0/N_e, R_\mu; E_{\text{thres}}, m, \dots, M) \tag{1}$$

with a careful consideration of the biasing trigger, threshold conditions, the detection multiplicity m , and of the correlations with other shower variables.

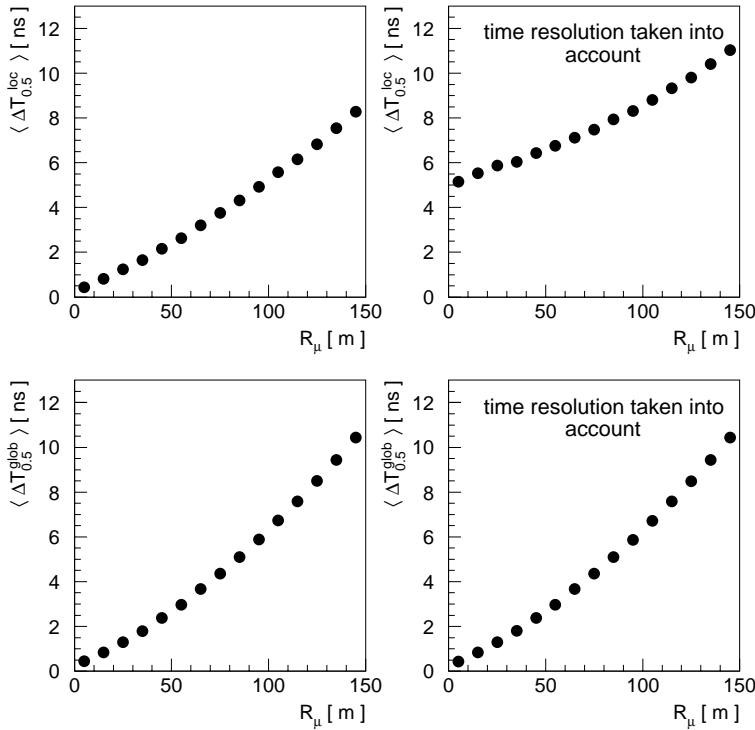


Figure 8: *The influence of laterally varying sample multiplicities of the single arrival time distributions on the global and local time profile of the EAS muon component without and with the detector resolution taken into account.*

vertical showers (the case, we consider for sake of simplicity). The relation shows that $\Delta\tau$ decreases with increasing height; it increases with the radial distance of the timing detector. There are some experimental philosophies to reconstruct, in a first step at least, the distribution of the production heights, which inform about the longitudinal shower development. In practical analyses, we consider the distributions of the mean, the median values ($\Delta\tau_{0.5}$) and other quartiles ($\Delta\tau_{0.25}, \Delta\tau_{0.75}$) of the

The measurements determine the time of arrival τ_μ of the muons relative to the arrival time τ_c of the EAS shower centre. This difference is traditionally called the muon delay time. We designate the distribution of these muon time delays as global arrival time distribution, which reflect the curvature of the shower disc. In a simplified geometrical consideration, neglecting the velocity dispersion, multiple scattering (geomagnetic effects) and the fact that the muon production loci can be displaced from the axis, it may be related to the production height. Strictly the arrival time of the muon is $T_\mu = \tau_0 + \tau_\mu$ where τ_0 includes the time of flight of the parent. The simplification assumes $\tau_0 = 0$, $\beta_\mu = 1$ and that the muon is produced on the shower axis.

This situation is sketched in Figure 6 for the simplified case of

single event distribution or of the first arriving muon ($\Delta\tau_1$). With respect to mass discrimination effects, it is preferable to analyse the measured distributions directly (without the detour of mapping the production height with limited accuracy).

Compared to the EAS muons, there are the much more abundant photons of the air-Cerenkov light. However, muons, though being less copious, exhibit some advantages, particularly since muons are directly coupled to the EAS development and can be observed day and night. In addition the time profile of the Cerenkov pulse maps the longitudinal development of $N_e(X)$ in a quite non-linear relationship between the height of emission and arrival times of Cerenkov photons. That is due the propagation of the optical photons under the influence of a changing refractive index.

Differently from global arrival time distributions $\Delta\tau^{glob}$ (see Fig.7), whose variation with the distance from the shower core characterises the curvature of the lateral particle distributions, the local time structure, determined relatively to the arrival of the foremost locally detected muon, reflects the intrinsic time structure and the spread relative to the front, the latter being defined by the arrival of the first muon. However, because of the relatively small number (sample multiplicity) of muons defining the observed single distributions, the local quantities are subject of various fluctuations, in particular of the fluctuation of the arrival of the first muon used as zero calibration point. As compared with the time delay distributions determined relatively to the (in principle) well defined arrival of the light front in the shower core, this fluctuation leads to a noticeable dependence of the local characteristic quantities from the muon multiplicity of the sample, as discussed in ref. [24]. Since the average multiplicity varies with the lateral distance from the EAS core, the observed local time distributions are superpositions of different multiplicities. Intriguing features arising from the effect that the time zero reference does not always reflect the extreme shower front, have already pointed out with KASCADE data in ref. [12] and get more pronounced, when combined with effect of the finite measuring resolution of the timing detectors (Fig.8).

Hence for a reasonable analysis of the arrival time distributions a correction procedure has been applied, removing the experimentally induced distortions by the fluctuations around the true reference point, in the observed data as well as in the detector simulations.

3 Shape of the arrival time distribution and the EAS time profile

In the following we illustrate some aspects with results of Monte Carlo simulations performed with the CORSIKA program [1] using the QGSJET model [26] for the case of the KASCADE experiment. The response of the KASCADE detector system and the timing qualities have been simulated using the CRES program, dedicatedly developed by the KASCADE group on the basis of the GEANT code [27]. The muons of the simulated EAS are tracked through the detector set up, and the timing response of the detectors are recorded for various core distances from the central detector facilities. Particularly, it should be noted that the timing depends on the energy deposit in the scintillation detectors. This effect slightly distorts the measured time distributions in the centre and could be corrected by introducing a corresponding correction procedure. For the presented examples we did not apply such a procedure to the experimental distributions and preferred to include this effect in the simulated distributions.

Figs. 9 and 10 display simulated median distributions of the arrival times for EAS corresponding to a $\log_{10} N_\mu^{tr}$ range of 3.7- 4.0. For the studies with the KASCADE experiment the so-called truncated muon number N_μ^{tr} , the muon intensity integrated between 40 and 200 m from the shower core, proves to be a good energy estimator. According to the suggestions of ref. [28] a mass composition H : O : Fe = 4 : 1 : 2 has been adopted. The simulated distributions do well follow the parameterisation by

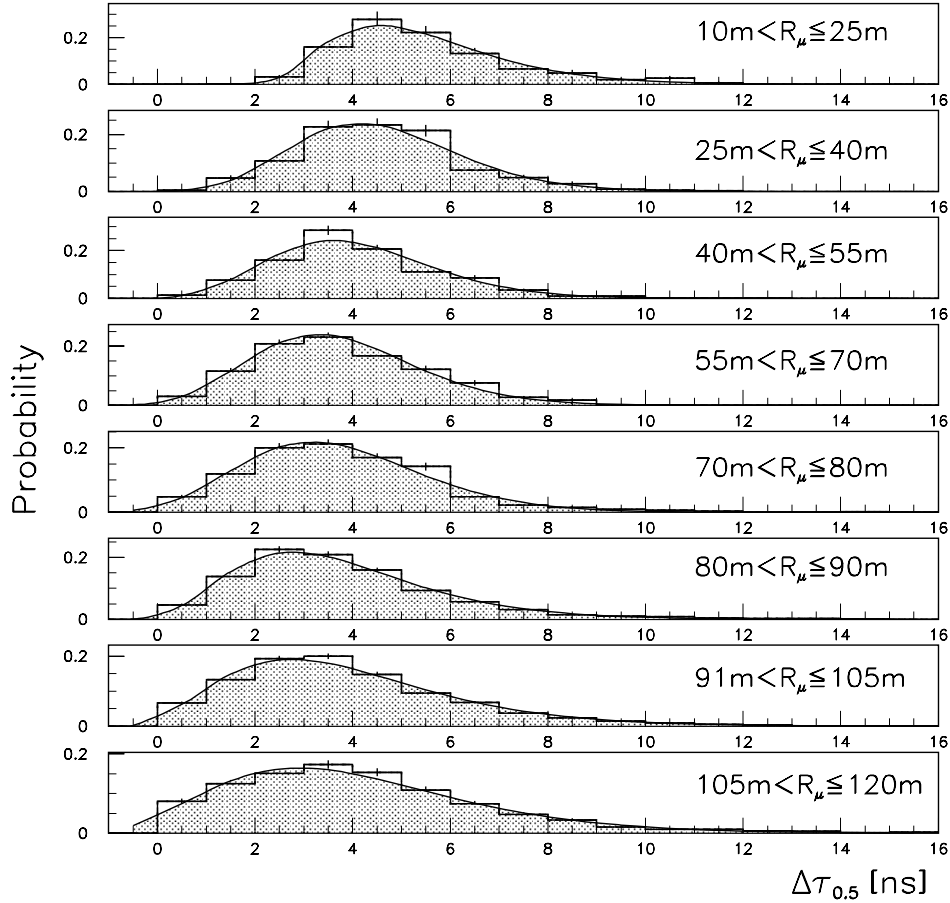


Figure 9: Simulated distribution of medians of $\Delta\tau_{0.5}$ the muon arrival time distributions observed for different distances from the EAS centre for a zenith angle range from $0^\circ < \theta \leq 15^\circ$ and $3.7 < \log_{10} N_\mu^{tr} \leq 4.0$.

the Γ - p.d.f. [29] (shown as lines in the figures).

$$\Gamma(T) = aT^b \exp(-cT) \quad (2)$$

with a mean value $\langle T \rangle = (1 + b)/c$ and the standard deviation $\sigma^\Gamma = (1 + b)^{1/2}/c$.

The simulations indicate a meager mass discrimination power, at least in a range of relatively low primary energies and when realistic conditions of the timing detectors are seriously taken into account. In Fig.11 simulated results for proton and iron induced EAS are shown. It shows that for the considered N_μ^{tr} range (corresponding to about $E_0 \approx 3 \cdot 10^{15}$ eV) and for radial ranges up to 80 m the median muon arrival times are close together for all primaries.

It is interesting to note that the simulated distributions reproduce the shift to increasing values at small R_μ , which is a consequence of the multiplicity effect, not corrected in the results shown for demonstration in Figs.9-11. Actually since the effect depends from the resolution of the timing detectors, for further discussions the influence of the lateral varying multiplicities, distorting the real profile should be removed. After a corresponding correction the profile exhibit fairly well a parabolic shape, for which an adequate parameterisation can be given (see ref.[12]).

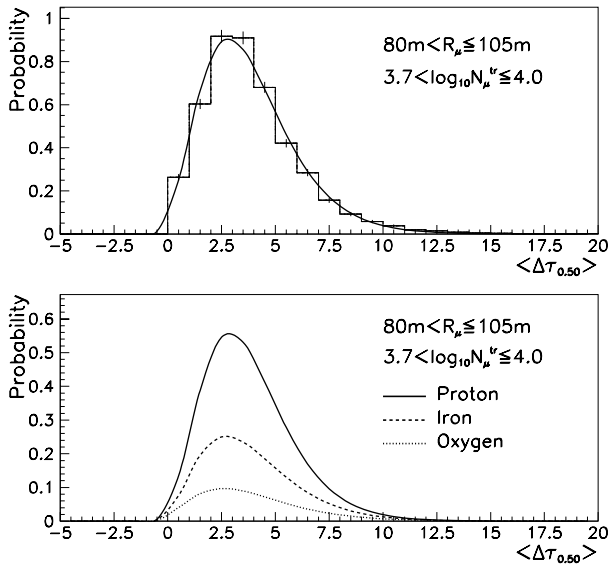


Figure 10: *Simulated distribution of medians $\Delta\tau_{0.5}$ of the muon arrival time distributions observed for a distance from the EAS centre $80 < R_\mu \leq 105\text{m}$, assuming a ratio of $H : O : Fe = 4 : 1 : 2$.*

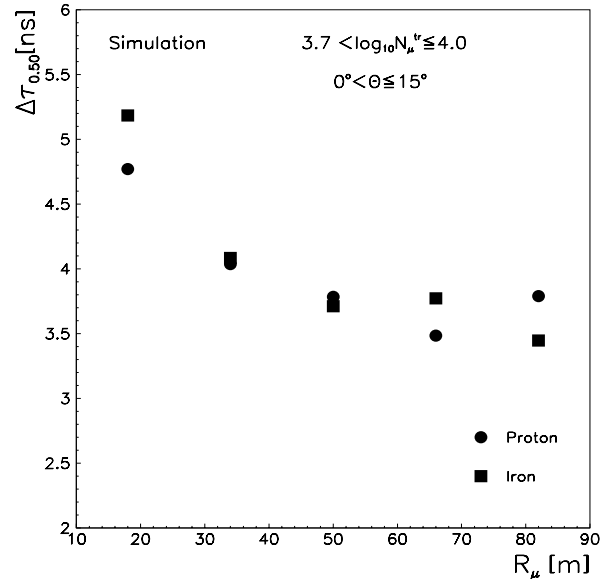


Figure 11: *Simulated median value time profiles $\langle\Delta\tau_{0.5}\rangle$, for proton and iron induced EAS (taking into account the detector response).*

4 Remarks on muon angle of incidence distributions

Analogously to the arrival time muon angle-of-incidence distributions can be studied. Due to experimental restrictions and necessary angular and location accuracies, experimental investigations are relatively scarce. In context with the so-called Time-Track Complementary principle [9] there is a discussion about the merits of such measurements. The basic assumption of tracking is the assumption that the production locus of the muon is the minimal distance of the reconstructed skew muon trajectory from the shower axis. This definition is somehow arbitrary so that the reconstruction result from the angular distribution - even if multiple scattering effects would be negligible - may differ from the time reconstruction. Obviously there is a strong correlation between the two kinds of distributions. The idea has been propagated to improve the accuracy by simultaneous measurements and to correlate the information. This has been put forward first by McComb and Turver in 1982 [30] and it has been later on ascribed to suggestions of Linsley [31]. Due to the strong correlation, however, the information about the longitudinal shower development extracted from both types of observations, is not complementary, it is substitutional. Using advanced statistical non-parametric methods for analysing multivariate distributions and invoking the Bayes theorem, it could be demonstrated [10] that the information content of arrival time and angle-of-incidence measurements are practically identical with respect to a mass discrimination of the primary cosmic ray particle. But it could be also shown that correlated observations of such distributions at different distances from the shower axis have more promising perspectives.

5 What do we learn from observations of EAS particle arrival time distributions?

The investigations of the shape of the particle arrival time distributions, especially when performed correlated with other shower observables (N_e , N_μ ,) on event-by-event basis, have different aspects, which be formulated by following items:

1. Understanding the **EAS structure**: the curvature and the thickness of the shower discs of the charge particle and muon components. The shape of the distributions of various adequate characteristic time quantities, the dependencies of their averages and dispersions from the distance R from the EAS centre (profiles) are represented by various phenomenological forms. Linsley, realising the increase of the EAS time spread with increasing R, suggested to use this effect on basis of a precisely determined parameterisation of the local shower profile of the charge particle component for an estimate of R of large EAS observed by small detector array, far from the shower core [32].
2. Signatures of the **longitudinal EAS development** mapped by the arrival time distributions, in particular for the muon component. Following an approach of John Linsley [33, 34] the dependence of the arrival time quantities from the zenith angle of shower incidence and from the primary energy may be related to the **elongation rate** and **fluctuations of the atmospheric depth of the shower maximum**. Studies which invoke comparisons with predictions of Monte Carlo simulations imply not only tests of the propagation procedures, but also of the high- energy interaction models used as generators of the Monte Carlo simulations. An exploration of the **sensitivities to features of the interaction models** and a comparison with data is of outmost current interest.
3. In addition to effects arising of the hadronic interaction features, revealing sensitivities to the **primary mass composition** is of similar interest [8]. Though differences in arrival time distributions due to differences of the primary mass of the cosmic particle inducing the EAS do prove to be small, arrival time distributions may play a guiding role in multivariate analyses of the EAS appearance in view of the mass composition of cosmic rays. The possibility of muon arrival time studies correlated event-by-event at different distances from the shower core is expected to enhance the information content [10].

Acknowledgement

I gratefully acknowledge various fruitful discussions about the topic with A. Haungs, M. Roth and R. Haeusler.

References

- [1] D. Heck, J. Knapp, J.N. Capdevielle, G. Schatz, T. Thouw, FZKA 6019, Forschungszentrum Karlsruhe (1998)
- [2] G. Schatz, private communication
- [3] M. Roth, private communication
- [4] A.A. Chilingarian et al., ANI Workshop 1999, these proceedings, p.43
- [5] A.A. Chilingarian et al., ANI Workshop 1999, these proceedings, p.53
- [6] J. Cortina, F. Aqueros, F. Lorenz, J.Phys.G: Nucl. Part. Phys. **23** (1997) 1733
- [7] P. Sokolsky, Introduction to Ultrahigh Energy Cosmic Ray Physics, Frontiers in Physics, Addison Wesley Publish. Company, Inc, 1989, p.65;
R.M. Baltrusaitis et al. Nucl. Instr. Meth. A **240** (1985) 410

- [8] H. Rebel, G. Völker, M. Föller, A.A. Chilingarian, *J. Phys.G : Nucl. Part. Phys.* **21** (1995) 451; H. Rebel, Proc.XV Cracow Summer School of Cosmology, Lodz, Poland, 15-19 July, 1996, ed. W.Tkaczyk, p.91
- [9] T.V. Danilova, D. Dumora, A.D. Erlykin, J. Procureur, *J. Phys.G : Nucl. Part. Phys.* **20** (1994) 961; *Physics of Atomic Nuclei (Yaderna Fizika)* **59** (1996) 109
- [10] I.M. Brancus, B. Vulpescu, H. Rebel, M. Duma, A.A. Chilingarian, *Astrop. Phys.* **7** (1997) 343; A.F. Badea et al., ANI Workshop 1999, these proceedings, p.99
- [11] K.H. Kampert et al.- KASCADE Collaboration, Proc. 16th European Cosmic Ray Symposium, Alcala, Spain: rayos cosmicos 98, 547, (1998), eds. J.Medina et al., Universidad de Alcala, Spain
- [12] I.M. Brancus et al.- KASCADE Collaboration, Report FZKA 6151(1998), Forschungszentrum Karlsruhe;
T.Antoni et al.- KASCADE Collaboration, *Astrop.Phys.*, to be published
- [13] H.J. Mathes et al., Proc. Workshop ANI 98, eds. A.A. Chilingarian, H. Rebel, M. Roth, M.Z. Zazyan, FZKA 6215, Forschungszentrum Karlsruhe 1998, p.91
- [14] P. Bassi, G. Clark and B. Rossi, *Phys.Rev.* **92** (1953) 441
- [15] J. Linsley, L. Scarsi and B. Rossi, *Phys.Rev.Lett.* **6** (1961) 485 ;
J. Linsley and L. Scarsi, *Phys.Rev.* **128** (1962) 2384
- [16] R. Thielert and L. Wiedecke, *Z.Phys.* **179** (1964) 199
- [17] A.J. Baxter, A.A. Watson and J.G. Wilson, *Can. Journ. Phys.* **46** (1968) S9
- [18] R. Walker and A.A. Watson, *Journ.Phys.G: Nucl.Phys.* **7** (1981) 1297
- [19] R. Walker and A.A. Watson, *Journ.Phys.G: Nucl.Phys* **8** (1982) 1131
- [20] H.E. Dixon and K.E. Turver, *Proc.R.Soc. London A* **339** (1974) 171
- [21] G. Agnetta et al., *Astrop. Phys.* **6** (1997) 301
- [22] M. Ambrosio, C. Aramo, L. Colesanti, T.V. Danilova and A.D. Erlykin, *Astrop. Phys.* **7**(1997)329
- [23] M. Ambrosio, C. Aramo, L. Colesanti and A.D. Erlykin, *Astrop. Phys.* **11**(1999)497
- [24] M.L. Armitage, P.R. Blake and W.F. Nash, *Journ.Phys.A: Math.Gen.* **8** (1975) 1005
- [25] P.R. Blake, W.S. Collis, M. Luksys, W.F. Nash and A.J. Septhon, *Journ.Phys.G: Nucl.Phys.* **16** (1990) 775
- [26] N.N. Kalmykov, S.S. Ostapchenko and A.I. Pavlov, *Nucl.Phys. (Proc. Suppl.)* **52B** (1997) 17
- [27] Application Software Group, GEANT-Detector Description and Simulation Tool, CERN, 1993
- [28] B. Wiebel-Sooth, P.L. Biermann and H. Meyer, *Astron. Astrophys.* **330** (1998) 389
- [29] C.P. Woidneck and E. Böhm, *J.Phys.A: Math.Gen.* **8** (1975) 997
- [30] T.J.L. McComb and K.E. Turver, *Journ.Phys.Soc.Japan* **51** (1982) 3087
- [31] J. Linsley, *Nuov. Cim.* **15C** (1992) 321
- [32] J. Linsley, *J. Phys.G: Nucl.Phys* **12** (1986) 51
- [33] J. Linsley, 15th ICRC (Plodiv, Bulgaria) **12** (1977) p.89
- [34] J. Linsley and A.A. Watson, *Phys.Rev. Lett.* **46** (1981) 459

Investigation of Relative Arrival Time Distributions of EAS Electron and Muon Component with the KASCADE Central Detector

W. Hafemann¹, R. Haeusler¹, F. Badea², I.M. Brancus²,
H. Rebel¹, H.-J. Mathes^{1*} for the KASCADE Collaboration[†]

¹*Institute for Nuclear Physics, IK III,
Forschungszentrum Karlsruhe, Germany*

²*National Institute for Physics and Nuclear Engineering,
Bucharest, Romania*

The Central Detector of the KASCADE experiment is equipped with two layers of scintillation detectors with different area coverage. The scintillators of both detector systems have a good timing resolution of about 1.6 ns.

With these two arrangements we performed extensive measurements of the arrival time differences at different energy thresholds of the electron and the muon component of EAS. The observed time structure of the shower profile is classified according to different EAS parameters. We furthermore present an analysis and comparison based on detailed MC simulations of the shower development. This comparison shows good agreement between experimental data and the expected behaviour of the different time distributions.

1 Introduction

Arrival time distributions of EAS particles reflect the longitudinal EAS development and provide information about the interactions driving the shower cascade. This is due to the fact that different primaries are characterized by differences in interaction lengths, transverse momentum, multiplicity and energy distributions of their secondaries. Especially, the muon component was studied under these aspects. Monte-Carlo simulations for EAS using the CORSIKA program [1] predict differences of the arrival time distributions of the electromagnetic and muon components (Fig.1), specifically showing, that the muon component arrives earlier with respect to the shower core and to the arrival time of the electro-magnetic component usually making up the so called shower front. In practice there are difficulties in exact determination of the cores arrival time, but the difference $\Delta\tau_{e-\mu} = \langle\tau_e\rangle - \langle\tau_\mu\rangle$ is an experimentally accessible quantity. In the present contribution we report about measurements of the relative

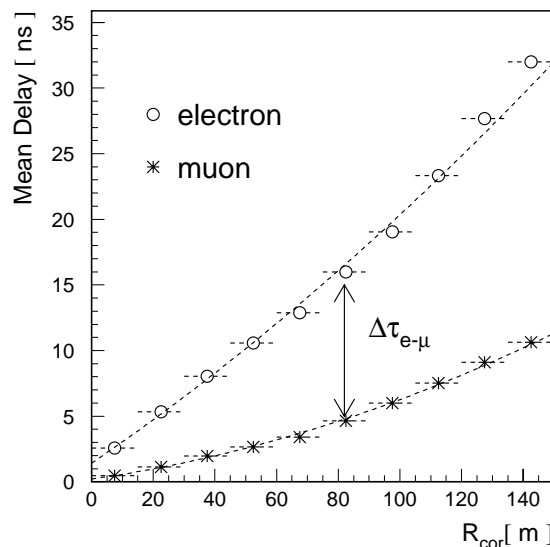


Figure 1: Mean arrival times of the electromagnetic and muon component for simulated EAS.

* corresponding author: mathes@ik3.fzk.de

† full collaboration list see at the end of these proceedings

time profile $\Delta\tau_{e-\mu}(R_{cor})$ for two different energy thresholds of the detected muons. The results are compared with predictions of Monte-Carlo simulations.

2 The Experimental Setup

For the measurements the timing and particle detection facilities of the KASCADE central detector [2] are used together with the KASCADE detector array which provides in the present analysis of the electro-magnetic EAS parameters. The specific features of the components of the KASCADE central detector are:

- The Topcluster, a detector array consisting of 50 scintillation detectors on top of the central detector, thus covering 7.5 % of the central detectors total area of about 320 m². It allows to measure arrival time and energy deposit of the first particle hitting a particular detector.
- The Triggerplane, making up the third active layer of the central calorimeter, measuring the energy and arrival times of particles passing this layer of scintillation detectors. They cover an area of about 64 %.
- The position sensitive multiwire proportional chambers (MWPC) underneath the basement of the central detector having a total area of 120 m² and therefore covering 41 %.

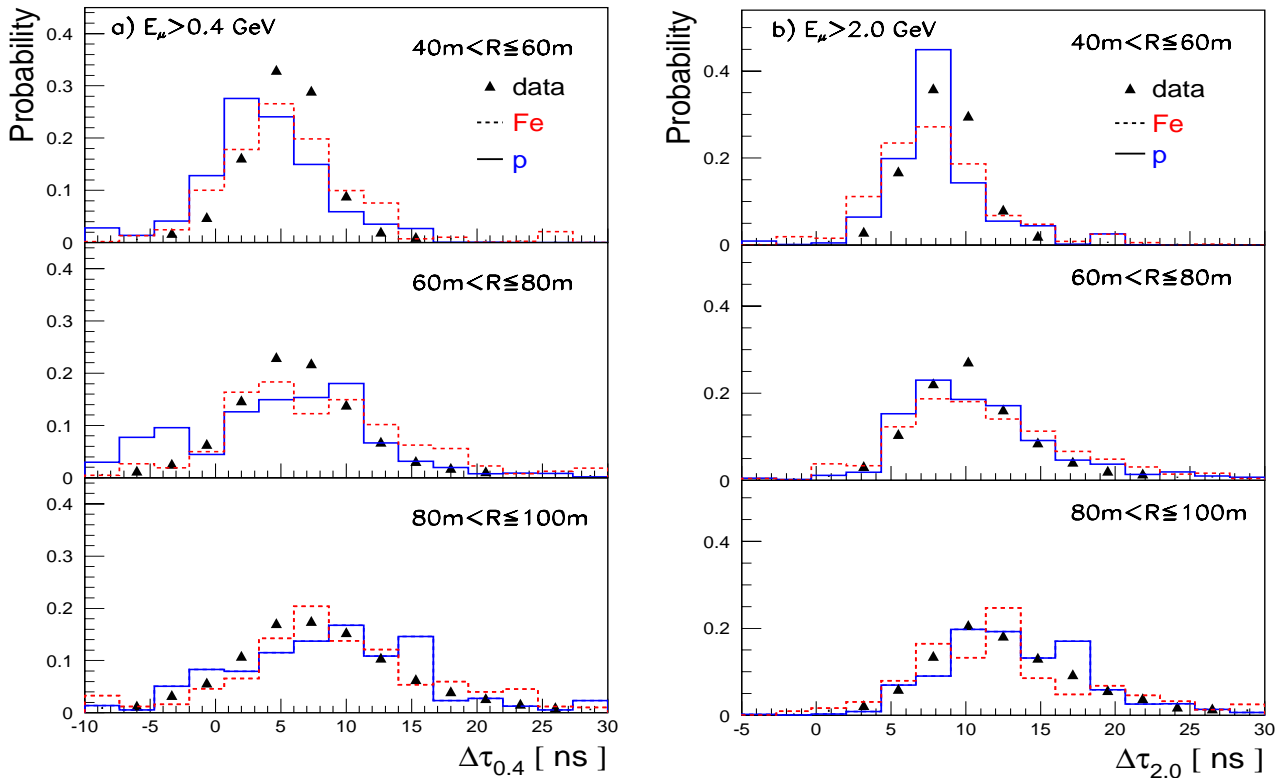


Figure 2: Distributions of relative arrival times of the electro-magnetic and muon components (of two different muon detection thresholds) as compared with EAS simulation predictions.

In particular the detection threshold for muons are about 0.4 GeV for the Triggerplane and 2.4 GeV for the MWPCs. This is due to the different amount of absorbing material between these detection

layers which is used to make up the hadron calorimeter of the experiment.

The measured arrival times in Topcluster and Triggerplane have to be corrected for two effects:

- (i) the timing signals are affected by the actual energy deposit due to the light production and the discriminator threshold (energy deposit effect),
- (ii) the timing signal depends from the number of particles simultaneously hitting the scintillator detectors (multiplicity effect).

Therefore these effects have to be corrected by procedures based on realistic detector simulations. This is particularly necessary for the Topcluster detectors as they encounter higher particle densities.

3 The Analysis of the Data

The analysis of the experimental data covers data taken in the period from October 1997 until August 1998 which sums up to about 20 million events. The cuts applied for these data are:

- core distances between 40 m and 100 m
- $\log_{10}(N_{\mu}^{tr})$ between 3.7 and 4.5
The energy estimator $\log_{10}(N_{\mu}^{tr})$ follows the relation: $\log_{10}(N_{\mu}^{tr}) \propto 0.9 * \log_{10}(E)$
- shower age between 0.8 and 1.8
- special selection:
 $\log_{10}(N_{\mu}) > 4.745 - 0.212 * \log_{10}(N_e)$

It has to be noticed that for the KASCADE case the number of muons N_{μ}^{tr} summed up between 40 and 200 m from the shower center is an energy identifier, nearly independent from the mass of the primary particle.

As the area coverage of each detector component is not full, particles of different type might be seen in one detection layer but not in another one. In addition particles of insufficient energy might be stopped in the absorbing material between each detecting layer.

Thus, the separation between signals originating from electrons from those induced by muons could not be done with 100 % efficiency and has to be estimated by Monte-Carlo simulations. The restrictions used for the electron-muon separation come mainly from additional conditions applied on the deposited energy and from the back tracing of the muons into Triggerplane or Topcluster using the MWPCs directional information or the shower direction. Finally about 65 % of the muons could be separated from electrons whereas the electrons are still contaminated by muons.

After all these conditions the remaining signals of the Topcluster are assigned to the electrons and the signals of the Triggerplane to muons above 0.4 GeV threshold. Furthermore, events are taken for the analysis only if they have at least 3 detector hits in the Topcluster and at least 3 detector hits in the Triggerplane or at least 3 hits in the Topcluster and at least 3 hits in the MWPCs. From the arrival times gained for one particle species the averaged quantities $\langle \tau_e \rangle$, $\langle \tau_{\mu(E_{\mu} \geq 0.4 GeV)} \rangle$ and $\langle \tau_{\mu(E_{\mu} \geq 2 GeV)} \rangle$ as well as the combined quantities

$$\Delta\tau_{0.4} = \langle \tau_e \rangle - \langle \tau_{\mu(E_{\mu} \geq 0.4 GeV)} \rangle \quad (1)$$

and

$$\Delta\tau_{2.0} = \langle \tau_e \rangle - \langle \tau_{\mu(E_{\mu} \geq 2 GeV)} \rangle \quad (2)$$

are calculated and used in the further analysis and comparisons.

4 A Comparison with Monte-Carlo EAS Simulations

The experimental data after the applied cuts and analysis procedure comprise approx. 200.000 EAS events. Results of the measurements are shown in Figs. 2 and 3 and compared to simulation results in different ranges of the energy indicated by the muon number N_μ^{tr} . The actual simulation calculations (based on the QGSJET model [3]) cover an energy range of $5 \cdot 10^{14} - 1 \cdot 10^{16}$ eV (divided in 5 overlapping energy bins for the three mass groups: H = protons, O = CNO group, Fe = heavy group) for an energy distribution with a spectral index of -2.7. They comprise a set of 2000 showers for each case. The response of the KASCADE detector system and the timing qualities have been simulated using the CRES program, which was a dedicated development of the KASCADE group mainly on basis of the GEANT code.

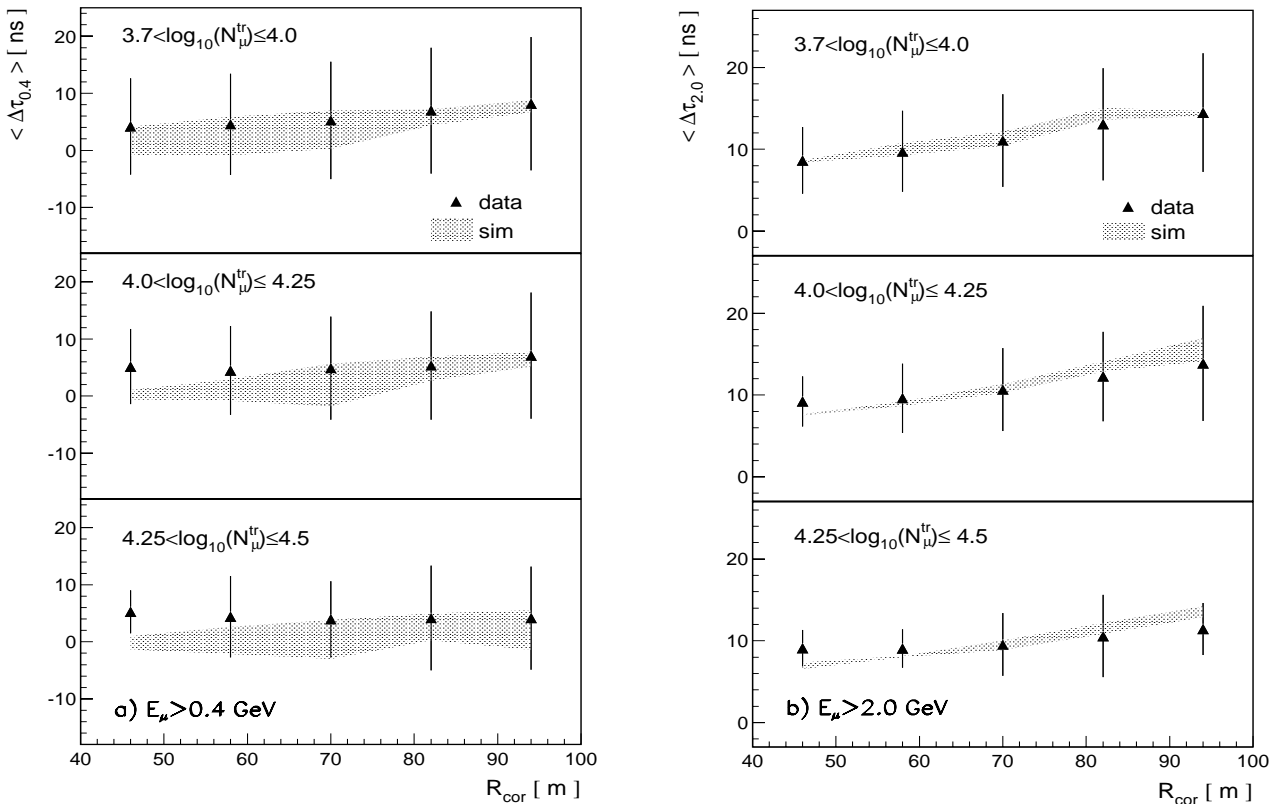


Figure 3: Comparison of the profiles of relative arrival times of the electro-magnetic and muon component with the predictions for simulated showers.

Fig. 2 displays such distributions of $\Delta\tau_{0.4}$ and of $\Delta\tau_{2.0}$, for $\log_{10} N_\mu^{tr} > 3.7$ (corresponding to a primary energy of about $E_{prim} > 2 \cdot 10^{15}$ eV) and for different distances from the EAS core. We notice the good agreement of the experimental data with the simulations, but significant differences between the different primaries in the relative arrival time distributions are not observed.

Fig. 3 presents the relative time profiles of $\Delta\tau_{0.4}$ and of $\Delta\tau_{2.0}$ for different $\log_{10} N_\mu^{tr}$ ranges. The data are compared with simulation results (which cover the range of proton and iron induced showers). For the low energy muon case there appears some slight disagreement. This might be an indication that at small distances, where the particle density is large, some problems with the corrections are still remaining.

5 Conclusion

The present experimental studies of the relative arrival times of the EAS muon and electro-magnetic component, give evidence for the different time profiles of the two EAS components and confirm former theoretical expectations. The comparisons of the data with Monte-Carlo simulations show a remarkably good agreement, but with missing any discrimination power for the mass of the cosmic ray primary.

Acknowledgement

The work has been partly supported by a grant of the Romanian National Agency for Science, Research and Technology as well as by a research grant (No.94964) of the Armenian Government and by the ISTC project A116. The collaborating group of the Cosmic Ray Division of the Soltan Institute of Nuclear Studies in Lodz and of the University of Lodz is supported by the Polish State Committee for Scientific Research (Grant No. 2 P03B 160 12). The KASCADE collaboration work is embedded in the frame of scientific-technical cooperation (WTZ) projects between Germany and Romania (No.RUM-014-97), Armenia (No. 002-98) and Poland (No.92-94).

References

- [1] D. Heck et al., FZKA-Report 6019, Forschungszentrum Karlsruhe (1998)
- [2] H.O. Klages et al. - KASCADE Collaboration, Nucl. Phys. B (Proc.Suppl.) **52B** (1997) 92;
A. Haungs et al. - KASCADE Collaboration, ANI workshop 1999, these proceedings, p.31
- [3] N.N. Kalmykov and S.S. Ostapchenko, Yad. Fiz. **56** (1993) 105



Linsley's Approach to infer Elongation Rate and Fluctuations of the EAS Maximum Depth from Muon Arrival Time Distributions

A.F. Badea¹, H. Rebel^{2†}, M. Zazyan³, I.M. Brancus¹, A. Haungs², and J. Oehlschläger²

¹*National Institute of Physics and Nuclear Engineering, Bucharest, Romania*

²*Forschungszentrum Karlsruhe, Institut für Kernphysik, Karlsruhe, Germany*

³*Cosmic Ray Division, Yerevan Physics Institute, Yerevan, Armenia*

An indirect approach to deduce the elongation rate D_e and the fluctuations of the atmospheric depth X_m of the EAS maximum from muon arrival time distributions has been scrutinized on basis of Monte Carlo simulations of the EAS development and of the longitudinal profile of various EAS parameters. Special attention is made to the behaviour of a scaling parameter relating the variations at the height of the shower maximum to the arrival time of muons at observation level.

6 Introduction

The early development of extensive air showers induced by high-energy cosmic particles, is critically influenced by the basic parameters of the particle-air interaction, i.e. by the mean free path, the interaction inelasticity and the multiplicity of secondary-particle production. A shorter initial free path, high inelasticity or high multiplicity can be also associated to a primary particle with high atomic number. The early stages, difficult to be directly observed, influence the position of the atmospheric depth of the maximum EAS development. Thus experimental studies which are able to observe the EAS maximum, like the observation of the fluorescence light of the atmospheric nitrogen do provide important information on the nature of the primary and of its interaction properties.

The average depth of the maximum X_m of the EAS development depends on the energy E_0 and the mass of the primary particle, and its dependence from the energy is traditionally expressed by the so-called elongation rate D_e defined as change in the average depth of the maximum per decade of E_0 :

$$D_e = dX_m/d\log_{10} E_0$$

Invoking the superposition model approximation i.e. assuming that a heavy primary (A) has the same shower elongation rate like a proton, but scaled with energies E_0/A

$$X_m = X_{init} + D_e \log_{10}(E_0/A)$$

or for a mixed composition, characterized by $\langle \log_{10} A \rangle$

$$\langle X_m \rangle = X_{init} + D_e (\log_{10} E_0 - \langle \log_{10} A \rangle)$$

As long as D_e is only weakly dependent from the energy, X_m shows practically a linear dependence from $\log_{10} E_0$, and any change in this dependence is indicative for a change either of D_e or of the composition ($\langle \log_{10} A \rangle$).

In 1977 [1, 2] an indirect approach studying D_e has been suggested. This approach can be applied to shower parameters which do not depend explicitly on the energy of the primary particle, but do

[†] corresponding author: e-mail: rebel@ik3.fzk.de

depend on the depth of observation X and on the depth X_m of shower maximum. EAS quantities like arrival times and their dispersions characterizing the time structure of the muon shower disc and mapping the longitudinal EAS development, are of this type. Actually the basic idea arises from the simple fact that the muon arrival time distributions reflect largely the time-flight of the muon travelling through the atmosphere i.e. being dependent on distance (path length) of the observation level X from X_m . Hence adequately defined arrival time parameters T do implicitly depend on the primary energy E_0 and the angle-of-EAS incidence Θ .

Prompted by recent experimental investigations of these dependences by the KASCADE collaboration [3, 4] we did scrutinize Linsley's approach on basis of Monte Carlo simulations of the EAS longitudinal development of the muon component. The interest in such studies arises from the question, how various influences of the muon propagation (Coulomb scattering e.g.) may obscure the information expected from the observation of muon arrival time distributions and if the basic assumptions involved are correct. From the calculated longitudinal profiles of the shower size N_e and the muon number N_μ the corresponding maxima $X_m^{(e,\mu)}$ and their fluctuations $\sigma(X_m^{(e,\mu)})$ are determined. These results are subsequently compared with the application of a procedure, essentially based on the relation between the variation of EAS time dispersion (characterised by various adequate moments T of the muon arrival time distributions like the mean or the median values e.g.) with the primary energy and the variation with the zenith angle of incidence.

7 Basic relations

The distribution of the EAS muon arrival times, measured at a certain observation level relatively to the arrival time of the shower core reflect the pathlength distribution of the muon travel from locus of production (near the axis) to the observation locus. The basic a-priori assumption is that we can associate the mean value or median T of the time distribution to the height of the EAS maximum X_m , and that we can express $T = f(X, X_m)$. Here X is slant depth at the observation level X_v (the vertical atmospheric thickness X_v)

$$\partial T / \partial \log_{10} E_0 |_X = D_e \partial T / \partial X_m |_X$$

The change of T with the energy E_0 at a given $X = X_v / \cos \Theta$ is proportional to the variation of T with X_m for a given energy. However, at observation level we do not observe $\partial T / \partial X_m$, which could be related, if specifying the function $f(X, X_m)$ and

$$F = -(\partial T / \partial X_m)_X / (\partial T / \partial X)_{X_m}$$

respectively. Thus

$$\partial T / \partial \log_{10} E_0 |_X = -F \cdot D_e \cdot 1 / X_v \cdot \partial T / \partial \sec \theta |_{E_0}$$

In order to derive from the energy variation of the arrival time quantities information about elongation rate, some knowledge is required about F , in addition to the variations with the depth of observation and the zenith-angle dependence, respectively.

In a similar way the fluctuations $\sigma(X_m)$ of X_m , may be related to the fluctuations $\sigma(T)$ of T

$$\sigma(T) = -\sigma(X_m) \cdot F_\sigma \cdot 1 / X_v \cdot \partial T / \partial \sec \theta |_{E_0}$$

with F_σ being the corresponding scaling factor for the fluctuation of F . In previous applications [5, 6] of this concept on basis of data measured with the Haverah Park water Cerenkov detectors simple assumptions have been made for two extreme forms of $f(X, X_m) = f(X - X_m)$ or $f(X, X_m) =$

$f(X/X_m)$ leading to $F = 1$ or $F = X/X_m$, respectively. At a closer look these assumptions appear to be not very convincing, since the arrival times are related directly only to the travel distances of the muons rather than to the differences in the traversed grammage of the atmosphere. That fact will complicate the dependence from X and X_m . We try to scrutinize this aspect on basis of detailed EAS Monte Carlo simulations.

8 Monte Carlo simulations

The simulations of the air shower development have been performed by use of the Monte Carlo air shower simulation program CORSIKA [7] (vers.5.621). The actual set of simulations calculations (based on the QGSJET model) comprise the EAS development of proton and iron induced EAS for three different primary energies (10^{15} eV, $3.16 \cdot 10^{15}$ eV, 10^{16} eV) and three different angles-of-incidence ($\Theta = 15^\circ, 25^\circ, 35^\circ$) with a set of 1000 simulated EAS for each case. The EAS quantities of interest are evaluated at six different observation levels, in the case of the EAS muons generally with two different energy thresholds of 0.25 and 2.0 GeV. The longitudinal profiles of the electromagnetic and the muon component develop differently. While the electromagnetic component exhibits a rela-

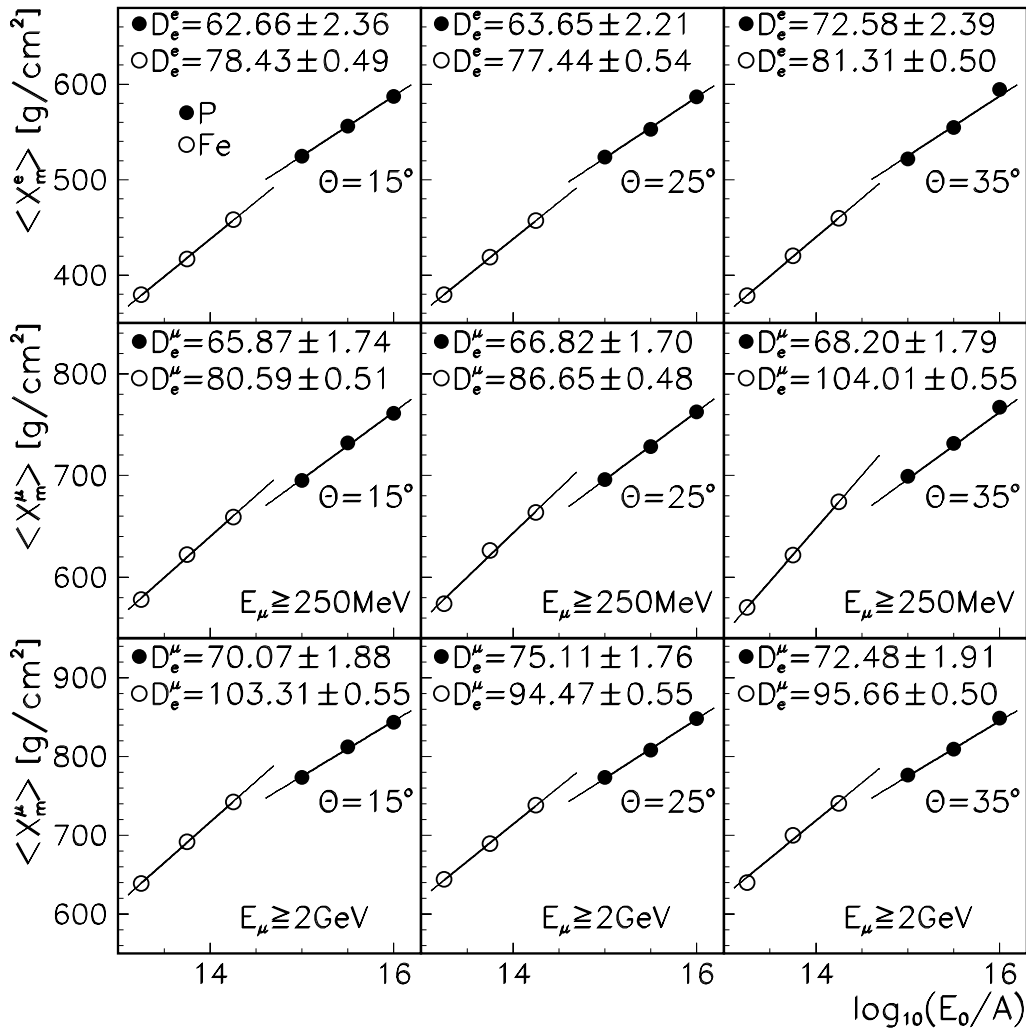


Figure 1: $D_e^{e,\mu} [g/cm^2/dec]$ for electromagnetic and muon components.

tively well pronounced maximum of the shower size N_e , characterized in the Greisen parametrisation by the shower age $s = 1$, the maximum of the penetrating muon component (N_μ) appears to be shifted deeper and rather shallow, since the muon losses, after reaching a kind of plateau of N_μ , are relatively small, especially for higher energy muons. As the maximum depths are not necessarily identical, we discriminate between X_m^e and X_m^μ , D_e and D_μ , respectively. The fluctuations $\sigma(X_m)$ (standard deviation of the X_m distributions) prove to be practically energy independent, but they are different for different cases: $\delta(X_m^e)(p) \approx 80 \text{ g/cm}^2$, $\delta(X_m^e)(Fe) \approx 17 \text{ g/cm}^2$, $\delta(X_m^\mu)(p) \approx 100 \text{ g/cm}^2$, $\delta(X_m^\mu)(Fe) \approx 30 \text{ g/cm}^2$. There is a trend of slightly increasing values D_e^e (60-70 g/cm/dec for protons) with the zenith angle, which can be understood as effect of the different path lengths of the particles traversing the same grammage layers at different zenith angles. Fig.1 illustrates the features of D_e . Though there are differences for different primaries, globally the superposition model appears to be a good approximation.

In deriving the muon arrival time distributions from the EAS simulations we restrict our considerations to the cases of distributions of the mean ($T = \Delta\tau_{mean}$) and median ($T = \Delta\tau_{0.5}$) arrival time of EAS registered relatively to the foremost muon in an interval of a distance from the shower core of $R_\mu = 90 - 110 \text{ m}$ with a detection multiplicity $n \geq 4$, for different energies E_0 and zenith angles Θ of incidence, and for different observation levels, especially for the level of the KASCADE experiment, Germany [3] on sea level and for the ANI installation on Mt.Aragats, Armenia (3250 m a.s.l.). The variations display a linear dependence, and $\epsilon_E = \partial T / \partial \log_{10} E_0|_{sec\theta}$ and $\epsilon_\theta = \partial T / \partial \log_{10} E_0|_{sec\theta}$ can be determined.

9 The scaling factor F deduced from arrival time parameters

Using the coefficients ϵ_E and ϵ_θ characterising the variation of the mean or median distributions with the energy and the angle of EAS incidence and adopting the value of the elongation rate, as predicted by the simulations, we infer for different observation levels and different primaries the values of the scaling parameter F, whose knowledge would be in turn a prerequisite to evaluate experimental data in terms of the elongation rate and fluctuations of the height of EAS maximum.

The results display a rather complex dependence of F from X, X_m , from the type of the primary (p or Fe: $F_{Fe} > F_p$) and from the energy threshold of the detected muons, varying between ($\approx 0.9 - 2.0$). Within all uncertainties and fluctuations of the results, eventually arising from the fact that the longitudinal development $T = f(X, X_m)$ can be never fairly expressed by a single form f for each observation level X_v , there may be a tendency with

$$F(X_v^1)/F(X_v^2) \propto X_v^1/X_v^2 \cdot \sec\theta \quad \text{and} \quad F(Fe)/F(p) \propto X_m(p)/X_m(Fe).$$

10 Summary

The relation between the arrival time observables and the changes of the longitudinal EAS profiles implies a scaling factor F, which depends from the height of the shower maximum, the observation level and zenith angle of EAS incidence. On basis of Monte Carlo simulations of the EAS development the ingredients for a determination of F have been deduced, and the variation of F has been studied for a number of cases. In the present status of our understanding we have to conclude that the scaling factor has a rather complex behaviour. It is affected by the EAS fluctuations and, though there are some trends, the dependences of average values are not yet established. In conclusion, unfortunately the Linsley approach does not provide a way to relate muon arrival time observations directly to the

elongation rate and fluctuations of X_m without invoking detailed Monte Carlo simulations.

Acknowledgement

We thank for the encouraging discussions with our colleagues of the KASCADE collaboration, in particular with A. A. Chilingarian, D. Heck, R. Haeusler and G. Schatz. Some clarifying remarks of M. Nagano and K. Honda are particularly acknowledged.

References

- [1] J. Linsley, Proc 15th ICRC (Plodiv, 1977), Vol.12, 89
- [2] J. Linsley and A.A. Watson, Phys. Rev. Lett. **46** (1981) 459
- [3] I.M. Brancus et al. - KASCADE Collaboration, FZKA Report 6151, Forschungszentrum Karlsruhe 1998
- [4] T. Antoni et al. - KASCADE Collaboration, Astrop. Phys. (1999), to be published
- [5] P.R. Blake et al., Journ.Phys.G: Nucl.Phys. **16** (1990) 775
- [6] R. Walker and A.A. Watson, Journ.Phys.G: Nucl.Phys. **7** (1981) 1297
- [7] D. Heck et al., FZKA Report 6019, Forschungszentrum Karlsruhe 1998

COLLABORATION LISTS

The ANI Collaboration

K.M.Avakian^a, A.A. Chilingarian^a, A.V. Daryan^a, V.S. Eganov^a, A.P. Garyaka^a, G.V. Gharagozyan^a, G.G. Hovsepian^a, V.A. Ivanov^a, N.V. Kabanova^b, S.S. Kazarian^a, E.A. Mamidjanian^a, R.M. Martirosov^a, L.G. Melkumian^a, N.M. Nikolskaya^b, S.I. Nikolsky^b, J. Procureur^c, V.A. Romakhin^b, S.H. Sokhoyan^a, V.V. Subbotin^b, S.V. Ter-Antonian^a, M.Z. Zazian^a

^aYerevan Physics Institute, Yerevan, Republic of Armenia

^bP.N. Lebedev Physical Institute, Moscow, Russian Federation

^cCentre d'Etudes Nucléaires de Bordeaux -Gradignan, France

The KASCADE Collaboration

T. Antoni^d, W.D. Apel^d, A.F. Badea^e, K. Bekk^d, K. Bernlöhr^d, H. Blümer^d, E. Bollmann^d, H. Bozdog^e, I.M. Brancus^e, A. Chilingarian^f, K. Daumiller^g, P. Doll^d, J. Engler^d, F. Feßler^d, H.J. Gils^d, R. Glasstetter^g, R. Haeusler^d, W. Hafemann^d, A. Haungs^d, D. Heck^d, T. Holst^d, J.R. Hörandel^d, K.-H. Kampert^{d,g}, H. Keim^d, J. Kempa^h, H.O. Klages^d, J. Knapp^g, H.J. Mathes^d, H.J. Mayer^d, J. Milke^d, D. Mühlenberg^d, J. Oehlschläger^d, M. Petcu^e, H. Rebel^d, M. Risse^d, M. Roth^d, G. Schatz^d, F.K. Schmidt^d, T. Thouw^d, H. Ulrich^d, A. Vardanyan^f, B. Vulpescu^e, J. Weber^d, J. Wentz^d, T. Wiegert^d, J. Wochele^d, J. Zabierowskiⁱ, S. Zagrómski^d

^dInstitut für Kernphysik, Forschungszentrum Karlsruhe, Germany

^eInstitute of Physics and Nuclear Engineering, Bucharest, Romania

^fCosmic Ray Division, Yerevan Physics Institute, Yerevan, Armenia

^gInstitut für Experimentelle Kernphysik, Univ Karlsruhe, Germany

^hUniversity of Lodz, Institute of Physics, Lodz, Poland

ⁱSoltan Institute for Nuclear Studies, Lodz, Poland

